Numerical Analysis of Pile Driving Dynamics

A thesis
submitted in fulfilment of the requirements
for the Degree of
Doctor of Philosophy
at the University of Western Australia
by
Andrew John Deeks

Department of Civil Engineering
University of Western Australia
1992

CONTENTS

1. INTRODUCTION

1.1 The context of this work

The use of foundation piles to support structures over water or soil with inadequate bearing capacity dates from pre-historical times. Although the use of cast in-situ piles has become popular in recent years, piles are commonly driven into the ground with some type of hammer.

Until the nineteenth century, the size and number of piles required to support a particular structure, and the hammer required to install those piles, were determined by rules of thumb and experience. As scientific engineering expanded, formulae for pile capacity and drivability were developed. Pile drivability formulae initially represented a correlation of empirical data, and later formulae were based on a combination of basic mechanics and empirical data.

Although the dynamics of pile driving were appreciated early this century, a practical method of solving the pile driving wave equation was not developed until the advent of digital computers. The method then developed employed an empirical model of the soil surrounding the driven pile. The one-dimensional wave equation is still the primary means of analysing pile drivability today. The last thirty years have seen various improvements made to the original method. Much additional data has been collected, allowing the empirical soil parameters to be refined, and the computational techniques have been improved. Because of the wealth of experience and data, the current techniques provide satisfactory solutions for most practical pile drivability problems today.

However, there are some cases, particularly in the offshore engineering field, in which piles of unusual size must be driven into soils which are uncommon on land. Since a large empirical database is not available, the parameters required for the standard wave equation analysis can be difficult to determine. This has motivated attempts to formulate a numerical model relying only on fundamental soil properties, which can be measured by standard geotechnical investigation methods. The finite element method has been used to analyse pile drivability occasionally, but the highly transient dynamics of the stress wave propagation and the non-linear behaviour of the soil cause such a solution to be computationally expensive.

Several models based on the one-dimensional wave equation and measurable soil parameters have been proposed. The finite element method has been used previously in attempts to verify these models, but the lack of a conclusive comparison in the literature suggests that these attempts have been less than successful. The coarseness of the finite element meshes used in these studies has led to some concern.

This thesis is a contribution to the process of finding a suitable one-dimensional model, based on measurable soil parameters, which adequately represents the pile driving process. The finite element method is used to accurately analyse the response of an ideal von Mises soil during a hammer blow on a full displacement pile. A one-dimensional model is developed which gives excellent agreement with the finite element results. In the process, doubt is cast on the accuracy of some of the finite element work previously reported in the literature, but the ability of one-dimensional wave equation models to represent pile driving behaviour is verified.

1.2 An outline of this thesis

A historical review follows this introduction, tracing the development of the analysis of pile driving dynamics through the literature. The thesis then follows the same route as the stress waves in a hammer/pile/soil system, commencing with the hammer system at the pile head, progressing to the propagation of axial waves in the shaft, then tracing the radiation of waves from the pile shaft, and finally considering the radiation of waves from the pile toe.

In Chapter 3 the hammer blow used to drive piles is examined. Analytical solutions are developed for a number of simple pile hammer models. These analytical solutions are shown to provide a convenient way of performing parametric studies of hammer performance. Studies of hammer separation and energy transmitted to the pile are included.

Chapter 4 formulates the equations governing the pile response. The finite element method and numerical time integration methods required to solve these equations are introduced. Soil plasticity is discussed, together with numerical methods for calculating non-linear response.

Chapter 5 examines the propagation of impact waves in a free-standing pile in detail. The effect of integration method, element size and type, and impulse shape on the accuracy of the solutions are investigated.

Chapter 6 considers the radiation of stress waves from the shaft of a pile embedded in an elastic soil. Plane strain shear waves emanating from a rigid pile are investigated first. A transmitting boundary for shear waves is derived. The effect of a finite pile stiffness is determined, and a one-dimensional model based on the transmitting boundary is developed. The radiation of dilation waves from the shaft is also investigated, and an appropriate transmitting boundary found.

The propagation of dilation waves from the pile toe is investigated in Chapter 7. Three-dimensional surface plots showing the propagating stress waves are presented. Existing one-dimensional base models are investigated, and a modified model developed. The complete elastic response of an embedded pile is computed and compared with results obtained by combining the new base and shaft models.

Chapter 8 deals with inelastic soil behaviour. Again, the transmission of shear waves from the shaft is investigated first. A variety of techniques for incorporating slip at the pile-soil interface into the finite element method and a one-dimensional model are considered. A one-dimensional model is again found to model the situation very well. The finite element method is used to model the inelastic penetration of the pile toe into the soil. Existing base models are compared to the finite element results. A new base model is developed. The response of the entire system is computed using finite elements, old one-dimensional models, and the new one-dimensional model.

Some examples of finite element analysis of pile driving available in the literature are analysed using the methods developed in this work, and the results are compared with the published results.

Conclusions, references, and figures follow.

2. PILE DRIVING ANALYSIS - A REVIEW

This chapter traces the development of rational pile driving analysis through the literature, identifying the major achievements. Although a mass of literature about pile driving formulae has formed over the years, only a few review articles will be identified. Similarly, much has been written about wave equation analysis in recent times, but only some key papers will be referred to in this chapter. Many other articles are referenced elsewhere in the thesis. The aims of the present study are stated at the end of this chapter.

2.1 The use of foundation piles

Foundation piles have been used to support structures over weak soils and water since prehistoric times. Early piles were made of wood. They were driven into the ground with various types of hammers. The city of Venice was built almost entirely on driven wooden piles (Legget, 1973). At that time, the hammer required to drive a particular pile was determined by experience, trial and error, and rules of thumb.

Piled foundations are still used extensively today, and, although cast in situ piles are now available, driven piles are still widely used.

2.2 Pile driving formulae

Pile driving formulae date back to the 1800's. The first formulae were purely empirical, and were valid over very limited ranges of soil and pile types. Dynamic formulae were later derived by treating the pile as a rigid body, equating the hammer energy (less various losses) to the energy required to push the pile through the ground. Reviews of the historical development of these formulae and comparisons between them have been performed regularly. Some examples are Terzaghi (1929), Dean (1935), and Chellis (1961).

2.3 Early progress in wave equation analysis

Although the differential equation for axial waves in a longitudinal bar was formulated and solved by St Venant in the 1850's (Timoshenko and Goodier, 1951), the presence of axial compression waves in piles during driving was first postulated by Issacs (1931). The existence of these waves was confirmed experimentally by Fox (1932). A method of analysis based on the wave equation was presented by Glanville et al (1938), but the simplifications required to permit manual solution did not allow satisfactory accuracy to be attained. Consequently, the approach did not find widespread acceptance, and pile formulae remained in common use.

However, the advent of the digital computer opened up new avenues for the solution of the wave equation. Smith (1960) published a numerical method for analysing pile driving problems using the wave equation. The pile and hammer are broken into a system of discrete springs and masses, and the surrounding soil is represented by dynamic reaction forces dependent on the pile displacement and velocity (Figure 2.1). The equations of motion of the discrete system are solved using the finite difference method.

In the original implementations of Smith's method, the dynamic resistance of the soil at the pile toe is modelled by a point force at the last pile node, the value of which is

$$R_t = \frac{R_t^u}{Q_t} u_t \ (1 + J \dot{u}_t) \qquad \text{for } u_t \le Q_t$$

$$R_t = R_t^u \ (1 + J \dot{u}_t) \qquad \text{for } u_t > Q_t \qquad (2.1)$$

where R_t^u is the ultimate static toe resistance, Q_t is the quake (which is the elastic ground compression before plastic behaviour commences), J is a damping constant, u_t is the toe displacement, and $\dot{u}_t$ is the toe velocity. The resistance of the soil along the pile shaft is represented by a discrete force at each pile node point, the magnitude of which is related to the nodal displacement and velocity by

$$R_S = \frac{R_S^u}{Q_S} u_S \ (1 + J' \dot{u}_S) \qquad \text{for } u_S \le Q_S$$

$$R_S = R_S^u \ (1 + J' \dot{u}_S) \qquad \text{for } u_S > Q_S \qquad (2.2)$$

where R_S^u is the ultimate static soil resistance summed over the shaft segment, Q_S is the quake required to utilise plastic deformation, J' is a damping constant, u_S is the pile node displacement, and $\dot{u}_S$ is the pile node velocity. Smith (1960) tentatively proposed quake and damping values for use in all soils (Table 2.1).

The viscous dashpots used in the original Smith model are non-linear, as indicated by equations (2.1) and (2.2). Smith introduced the damping factor J into the soil resistance because "obviously, the ground will offer more resistance to rapid motion than to slow motion" (Smith, 1960). He was, of course, correct. However, the damping was treated as an augmentation of the static response simply for convenience, with no theoretical justification. Goble et al (1975) modified the model by using a linear dashpot in place of the non-linear damping term. The equation for dynamic resistance along the shaft became

$$R_S = R_S^u \left(\frac{u_S}{Q_S} + J' \dot{u}_S\right) \qquad \text{for } u_S \le Q_S$$

$$R_S = R_S^u \left(1 + J' \dot{u}_S\right) \qquad \text{for } u_S > Q_S \qquad (2.3).$$

The equation for base resistance was modified in the same way. Computer programs implementing the Smith model in both the original form and the modified form are still used in engineering practice. Corte and Lepert (1986) have shown that the two forms give similar results.

In the twenty years following the publication of Smith's model, many computer programs were written incorporating the method, and the computational techniques were improved as computer capacity and speed increased. The development of these techniques has been reviewed by Goble et al (1980). The choice of quake and damping parameters was also the subject of much research. Coyle et al (1977) reviewed some of this work, and recommended parameter values slightly different from those of Smith (Table 2.1).

2.4 Recent advances

Although the method proposed by Smith has been used successfully for many years, the approach has some shortcomings. The empirical nature of the soil influence on the pile (equations (2.1) and (2.2)) is a major problem. The relationships between the pile motion and the soil reactions are not based on rigorous analysis of dynamic soil behaviour. Consequently, the quake and damping parameters cannot be associated with fundamental soil properties, and cannot be measured by standard geotechnical investigation techniques. Experience with the Smith method over the years has led to quake and damping parameters which can be used in normal pile driving situations with reasonable confidence. However, unusual situations can be encountered, especially in the offshore environment, in which reliable Smith parameters are difficult to estimate prior to driving.

The limitations discussed above, together with a general movement towards a more rigorous approach to geomechanics, have stimulated interest in alternative methods of analysis based on a rational understanding of soil behaviour.

The damping parameter J was originally associated with soil viscosity. However, laboratory studies into the strain rate and penetration velocity dependency of soil viscosity (Gibson and Coyle, 1968; Dayal and Allen, 1975; Litkouhi and Poskitt, 1980) consistently showed non-linear velocity dependence. Indeed, Randolph and Simons (1986) have examined the available data and found little evidence of velocity dependency once shaft velocity exceeds 0.1 m/s.

Following the analytical work of Novak (1977) and Novak et al (1978), Meynard and Corte (1984) conducted a laboratory investigation which led them to conclude that most wave attenuation in piles can be explained by radiation damping along the pile shaft, rather than soil viscosity. They used the work of Novak et al (1978) to show that radiation damping could be modelled by a viscous dashpot, and that the dynamic shear stiffness of the soil could be modelled by a spring. The spring and damping parameters are dependent mainly on the shear modulus and density of the soil.

2.4.1 Shaft model

The work of Meynard and Corte (1984) allowed the dynamic soil reaction along a pile shaft to be determined from basic soil properties. The association of the damping constant with radiation damping also led to a reconsideration of the structure of the soil model. In the original Smith model, a plastic slider was used in series with the spring, but not with the dashpot, as shown in Figure 2.2(a). Considering an elastic-perfectly plastic material, Simons and Randolph (1985) concluded that, since slip only occurs at the pile/soil interface, radiation damping cannot increase the shear stress above the yield stress, and so the plastic slider should be placed in series

with both the spring and the radiation dashpot (Figure 2.2(b)). Corte and Lepert (1986) reached the same conclusion after studying the multiple degree of freedom models of shear wave radiation presented by Holeyman (1984).

Randolph and Simons (1986) added an extra dashpot in series with the plastic slider to represent the rate dependency of the soil yield stress (Figure 2.2(c)). They stated that the damping constant of the extra dashpot is usually an order of magnitude less than the radiation damping constant. Corte and Lepert (1986) also considered the addition of such a dashpot, but dismissed it as unnecessary.

Nguyen et al (1988) modified the soil model shown in Figure 2.2(c) by varying the soil shear modulus with shear strain amplitude, using a relationship derived by Hardin and Drnevich (1972). They presented results which agreed well with field data, by did not show how significantly the variation of shear modulus affected their analysis.

Mitwally and Novak (1988) used the model shown in Figure 2.2(b), but varied the spring and damping coefficients to account for the effect of a weakened soil zone adjacent to the pile. They produced results which indicated that the computed shaft response could be significantly affected by a small zone of soil with reduced shear stiffness.

Warrington (1988) also implemented the model shown in Figure 2.2(b) in his ZWAVE program. He presented estimates of pile capacity from pile driving data which were of similar accuracy to CAPWAP.

2.4.2 Base model

Following the association of the viscous dashpots in the Smith model with radiation damping, Simons and Randolph (1985) used Lysmer's analogue to provide stiffness and damping values for the soil at the pile base which were dependent only on the shear modulus and density of the soil. The Lysmer analogue (Lysmer and Richart, 1966) allows approximation of the vertical vibration of a rigid footing on a semi-infinite half-space by replacing the half-space with a spring and a viscous dashpot in series.

Simons and Randolph did not alter the structure of the original Smith base model (Figure 2.2(a)). This base model was used by Novak and Mitwally (1988) in their demonstration of the effect of a weakened shear zone.

In their work discussed above, Nguyen et al (1988) used a base model with the plastic slider in series with both the spring and the dashpot, reasoning that the soil at the base behaves in a similar way to the soil along the shaft (Figure 2.2(b)). Warrington (1988) used the same model in his ZWAVE program.

Holeyman (1988) introduced a multiple degree of freedom model to represent the base response (Figure 2.3). His model uses a one-dimensional equivalent solid cone to simulate radiation damping. Plastic behaviour is included by specification of a power law stress/strain relationship for the discrete springs representing the soil cone. Holeyman presented analyses which showed reasonable agreement with field data.

2.7 Finite element studies

The first full finite element analysis of the pile driving problem was performed by Chow (1981). Smith and Chow (1982) compared a one-dimensional model based on the Smith (1960) method with an axisymmetric finite element model. The finite element mesh used by Chow is shown in Figure 2.4, and an example of the variation between the two models is shown in Figure 2.5. They neglected soil viscosity, and equated J to zero in the one-dimensional model. Consequently, the results obtained from the finite element model showed considerably less oscillation than the one-dimensional model, as the finite element model permitted radiation damping.

Simons (1985) performed similar axisymmetric finite element analyses, but compared the results with the improved one-dimensional model described by Simons and Randolph (1985). The mesh used by Simons is shown in Figure 2.6, and the pile head displacements computed with the finite element and one-dimensional models are shown in Figure 2.7. Since the improved one-dimensional model included the effect of radiation damping, the one-dimensional response is much smoother than that computed by Smith and Chow (1982). However, the finite element response shows significant oscillation.

Smith et al (1986) published further finite element results obtained with a refined mesh, which they claimed verified the accuracy of Chow's results. However, Figures 2.8 and 2.9 show significant differences in the displacement and force responses, although the permanent deformations and maximum forces are similar. At a time of approximately 18 milliseconds, the force calculated with the finer mesh is 180° out of phase with the coarse mesh. The calculated displacement responses during rebound are entirely different.

Coutinho et al (1988) reported the results of an axisymmetric finite element analysis of the driving of a cone-ended offshore pile. The mesh used is shown in Figure 2.10, and the results of the analysis presented in Figure 2.11. The simulation was stopped soon after the maximum toe displacement had been attained. No results were presented for the pile head displacement, and, with so little time integration, assessment of the accuracy of the model is difficult.

Mitwally and Novak (1988) also reported using axisymmetric finite elements to model pile driving. However, they concluded that, since finite element results depend mainly on the modelling of the pile soil interface, and in view of the computational cost of the method, shaft models are preferable.

2.8 The necessity for this study

Although some progress has been made in formulating a one-dimensional wave equation model of pile driving based on fundamental soil properties, much work is still to be done.

New models for the dynamic response of soil along the pile shaft have been formulated by a number of researchers. All of these models are based on the Novak's (1977) solution for harmonic oscillation of an axisymmetric soil disk under plain strain conditions, which was originally used to evaluate the response of a vibrating rigid pile. Verification of the applicability of such models to pile driving situations is required.

Three new base models were described above. There has been no significant comparison of these three models, and no conclusive demonstrations of the ability of any of them to accurately model the inelastic soil behaviour at the base of a pile.

The finite element method provides a way of finding approximate solutions to the equations of motion governing pile driving in idealised soils. One feature of the finite element method is that reasonable approximations of displacements can be produced long before the higher order derivatives have converged. However, the finite element method is prone to discretisation errors, particularly in dynamic and non-linear cases. Great care must be taken if accurate solutions to a problem as complex as pile driving dynamics are to be obtained. The published results of the finite element work reviewed above show some discretisation problems. The accuracy of these analyses is questionable.

2.9 The aims of this study

This study aims to use the finite element method to investigate pile driving in an ideal elastic/purely plastic (Von Mises) soil, producing solutions which are converged and accurate. The discretisation problems which are obvious in previous published work will be resolved. The accurate solutions will be used to find a one-dimensional model which adequately reproduces the behaviour of the ideal system. The one-dimensional model will be established from a purely analytical point of view, permitting the influence of real soil behaviour to be examined by other investigators.

3. HAMMER IMPACT

3.1 Introduction

Numerical analysis of the response of a pile during driving requires a model for the hammer system driving the pile. In the original Smith (1960) method, the hammer was modelled as lumped masses and springs. To simulate impact, the mass representing the hammer ram was given an initial velocity. More complex models have since been developed, especially for the modelling of diesel hammers (Goble and Rausche (1986), Rausche et al (1988)). However, Middendorp and van Weele (1986) have shown that relatively simple hammer models can provide adequate agreement with field data.

When examining the propagation of stress waves in a pile and in the surrounding soil, representing the influence of the hammer by a time-varying force at the pile head is advantageous, as a stress wave of known shape can be 'injected' into the pile. The changes in the stress wave during propagation can then be examined. However, the impact function should closely approximate the force created by the real hammer, otherwise the calculated behaviour may not accurately reflect the true behaviour.

The forces exerted on piles by simple hammer models can be computed analytically. The force caused by a hammer impacting directly on the top of a pile (Figure 3.1(a)) is well known (eg. Johnson, 1982). Randolph (1991) has presented an analytical solution for a model consisting of a ram impacting on a linearly elastic cushion seated directly on a pile (Figure 3.1(b)). As well as providing driving forces for pile drivability analyses, these analytical solutions also allow parametric studies of hammer performance to be performed rapidly.

This chapter presents solutions for some simple hammer models in new dimensionless quantities, including new analytical solutions for the models shown in Figure 3.1(c) and 3.1(d). The new solutions are shown to match field data extremely well. The potential of the analytical solutions to allow parametric analysis of hammer performance is illustrated by studies of ram separation, transmitted energy, and maximum impact force.

3.2 Ram/pile model

The simplest model of a pile hammer is that of a falling mass impacting directly on the top of a pile. The response of the pile to the impacting mass can be modelled by replacing the pile with a dashpot of equal impedance to the pile (Randolph, 1991). This impedance is given by

$$Z = \frac{E_p A_p}{c_p} \tag{3.1}$$

where E_p is the Young's modulus of the pile, A_p is the cross-section area of the pile, and c_p is the axial wave velocity in the pile.

The force exerted by the hammer on the pile can be obtained by analysing the system shown in Figure 3.1(a), where m_r is the mass of the ram, u_r is the displacement of the ram after it strikes the top of the pile, and v_o is the velocity of the ram when it strikes the pile. Dot notation will be used to represent differentiation with respect to time. The equation of motion for the ram is

$$m_r \ddot{u}_r + Z \dot{u}_r = 0 \tag{3.2}.$$

Defining a dimensionless time as

$$t^* = \frac{Z}{m_r} t \tag{3.3}$$

and a dimensionless velocity as

$$\dot{u}^* = \frac{du^*}{dt^*} = \frac{\dot{u}}{v_o} \tag{3.4},$$

the dimensionless displacement and acceleration are

$$u^* = \frac{Z}{m_r} \frac{u}{v_o} \tag{3.5}$$

and

$$\ddot{u}^* = \frac{d^2u^*}{dt^{*2}} = \frac{m_r}{Z} \frac{\ddot{u}}{v_o} \tag{3.6}.$$

Substituting these equalities into equation (3.2), a dimensionless equation of motion can be formed.

$$\ddot{u}_r^* + \ddot{u}^* = 0 \tag{3.7}$$

At a dimensionless time of zero (the instant the hammer strikes the pile), the dimensionless velocity of the ram is unity, and the displacement is zero. Applying these initial conditions, the solution to equation (3.7) can be found.

$$\dot{u}_r^* = e^{-t^*} \tag{3.8}$$

The force exerted on the pile is given by multiplying the pile impedance by the ram velocity.

$$f_p = Z\ \dot{u}_r$$

Since the appropriate non-dimensionalisation of force is

$$f^* = \frac{f}{Z\ v_o} \tag{3.9},$$

the dimensionless force exerted on the pile is simply

$$f_p^* = \frac{\dot{u}_r}{v_o} = \dot{u}_r^* = e^{-t^*} \tag{3.10}.$$

The dimensionless impulse function exerted on the pile by this pile hammer model is shown in Figure 3.2, denoted by an infinite cushion stiffness. At time zero the dimensionless force rises instantaneously to unity, and then decays exponentially with a non-dimensional time constant of unity.

3.3 Ram/cushion/pile model

The accuracy of the model described above can be increased by using a linear spring to model the effect of a cushion between the ram and the pile. The system then has two degrees of freedom, since the motion of the pile head can be different from that of the ram. The displacement of the pile head will be denoted by u_a, and the stiffness of the cushion spring by k_c. The model is illustrated in Figure 3.1(b).

The two equations of motion for this model are

$$m_r\ \ddot{u}_r + k_c\,(u_r - u_a) = 0 \tag{3.11}$$

and

$$Z\ \dot{u}_a + k_c\,(u_a - u_r) = 0 \tag{3.12}.$$

Using the dimensionless variables given in equations (3.3) to (3.6), these equations can be re-written as

$$\ddot{u}_r^* + k_c^*\ (u_r^* - u_a^*) = 0 \tag{3.13}$$

$$\dot{u}_a^* + k_c^*\ (u_a^* - u_r^*) = 0 \tag{3.14}$$

where

$$k_c^* = \frac{k_c\ m_r}{Z^2} \tag{3.15}.$$

Applying the Laplace transformation to equations (3.13) and (3.14) and solving simultaneously, the Laplace transform of the velocity at the pile head can be found.

$$\mathrm{L}\,\dot{u}_a{}^* = \frac{k_c{}^*}{s^2 + k_c{}^*\, s + k_c{}^*} \tag{3.16}$$

Factorising the quadratic denominator

$$\mathrm{L}\,\dot{u}_a{}^* = \frac{k_c{}^*}{(s + \frac{k_c{}^*}{2} + \mu)\,(s + \frac{k_c{}^*}{2} - \mu)} \tag{3.17}$$

where

$$\mu = \sqrt{\frac{k_c{}^{*2}}{4} - k_c{}^*} \tag{3.18}.$$

The inverse transform of equation (3.17) depends on the value of $k_c{}^*$. If $k_c{}^*$ is greater than 4, equation (3.17) becomes

$$\mathrm{L}\,\dot{u}_a{}^* = \frac{k_c{}^*}{2\mu}\left(\frac{1}{s + \frac{k_c{}^*}{2} - \mu} - \frac{1}{s + \frac{k_c{}^*}{2} + \mu}\right) \tag{3.19},$$

and performing the inverse transform yields

$$f^* = \dot{u}_a{}^* = \mathrm{e}^{-\frac{k_c{}^*}{2}t^*}\,\frac{k_c{}^*}{\mu}\sinh(\mu\, t^*) \tag{3.20}.$$

If $k_c{}^*$ is equal to 4,

$$\mathrm{L}\,\dot{u}_a{}^* = \frac{k_c{}^*}{\left(s + \frac{k_c{}^*}{2}\right)^2} \tag{3.21}$$

and

$$f_p{}^* = \dot{u}_a{}^* = t^*\,\mathrm{e}^{-\frac{k_c{}^*}{2}t^*} \tag{3.22}.$$

Finally, if $k_c{}^*$ is less than 4, μ is imaginary. Let

$$\mu' = \mu\,\mathrm{i} = \sqrt{k_c{}^* - \frac{k_c{}^{*2}}{4}} \tag{3.23}.$$

Equation (3.17) becomes

$$\mathrm{L}\,\dot{u}_a{}^* = \frac{k_c{}^*}{2\mu'\,\mathrm{i}}\left(\frac{1}{s + \frac{k_c{}^*}{2} - \mu'\,\mathrm{i}} - \frac{1}{s + \frac{k_c{}^*}{2} + \mu'\,\mathrm{i}}\right) \tag{3.24}$$

and

$$f_p{}^* = \dot{u}_a{}^* = \mathrm{e}^{-\frac{k_c{}^*}{2}t^*}\,\frac{k_c{}^*}{\mu'}\sin(\mu'\, t^*) \tag{3.25}.$$

The force in the cushion spring is equal to the force exerted on the pile. If k_c^* is less than 4, equation (3.25) indicates that the force will become negative after time t_s^*, where

$$t_s^* = \frac{\pi}{\mu'} \quad (3.26).$$

Since the cushion is not attached to the pile or the ram, negative stresses cannot develop in the cushion spring, so gaps will form and the ram will become separated from the pile. The force exerted on the pile after time t_s^* will be zero. Equation (3.25) is only valid for times less than or equal to t_s^*.

The dimensionless response of the ram/cushion/pile model is dependent solely on the dimensionless stiffness of the cushion, k_c^*. The effect of this stiffness on the response is shown in Figure 3.2. Finite stiffness of the cushion causes the force on the pile to have a finite rise time. A soft cushion causes a large rise time. As the cushion stiffness becomes large, the rise time decreases, and the solution approaches that for the ram/pile model.

3.4 Ram/cushion/anvil model

The hammer model can be further improved by introducing a finite anvil mass (Figure 3.1(c)). This does not change the number of degrees of freedom, but increases the complexity of the solution.

The two equations of motion governing the system are as follows, where m_a is the anvil mass.

$$m_r \ddot{u}_r + k_c (u_r - u_a) = 0 \quad (3.27)$$

$$m_a \ddot{u}_a + Z \dot{u}_a + k_c (u_a - u_r) = 0 \quad (3.28)$$

Again using the dimensionless variables given in equations (3.3) to (3.6), these equations can be re-written as

$$\ddot{u}_r^* + k_c^* (u_r^* - u_a^*) = 0 \quad (3.29)$$

$$\ddot{u}_a^* + \frac{1}{m_a^*} \dot{u}_a^* + \frac{k_c^*}{m_a^*} (u_a^* - u_r^*) = 0 \quad (3.30)$$

where k_c^* is given by equation (3.15), and the dimensionless anvil mass m_a^* is given by

$$m_a^* = \frac{m_a}{m_r} \quad (3.31).$$

Applying the Laplace transformation to equations (3.29) and (3.30) and solving simultaneously, the Laplace transform of the velocity of the anvil and the pile head can be found.

$$\mathrm{L}\, \dot{u}_a^* = \frac{\frac{k_c^*}{m_a^*}}{s^3 + \frac{1}{m_a^*} s^2 + k_c^* \left(\frac{1}{m_a^*} + 1 \right) s + \frac{k_c^*}{m_a^*}} \quad (3.32)$$

The anvil velocity and the force on the pile head can be found by factorising the cubic denominator and performing the inverse Laplace transform, as detailed in Appendix A. An expression of the following form is obtained. Expressions for the parameters F_p, c_1, c_2, ω, and ϕ are presented in the appendix.

$$f_p^* = \dot{u}_a^* = F_p \, e^{-c_1 t^*} \left(1 - e^{-c_2 t^*} \frac{\cos(\omega t^* - \phi)}{\cos \phi} \right) \quad (3.33).$$

The dimensionless force in the spring is given by

$$f_s^* = m_a^* \ddot{u}_a^* + \dot{u}_a^* \quad (3.34).$$

Differentiating equation (3.33), substituting into equation (3.34), and simplifying, the spring force can be expressed as

$$f_s^* = F_s \left(e^{c_2 t^*} - \frac{\cos(\omega t^* - \theta)}{\cos\theta} \right) \quad (3.35),$$

where F_s and θ are also specified in Appendix A.

The ram will separate from the top of the cushion when the spring force is zero, which occurs at time t_s^*, where

$$e^{c_2 t_s^*} = \frac{\cos(\omega t_s^* - \theta)}{\cos\theta} \quad (3.36).$$

An analytical solution for t_s^* cannot be found. For a certain range of anvil mass and cushion stiffness, ram separation does not occur. (This range is discussed in a subsequent section.) For those cases where separation does occur, equation (3.36) must be solved numerically to identify t_s^*.

For most combinations of dimensionless anvil mass and cushion stiffness, the cubic denominator in equation (3.32) has one real root and two imaginary roots, and the solution presented above applies. For a small range of combinations, the cubic denominator has three real roots, and different solutions must be used. In this case, equation (3.32) can be written in the following way.

$$L\,\dot{u}_a^* = \frac{a_0}{(s + b_1)(s + b_2)(s + b_3)} \quad (3.37)$$

When b_1, b_2, and b_3 are distinct, the solution is given by

$$f_p^* = \dot{u}_a^* = F_p \left(e^{-b_1 t^*} - A_p e^{-b_2 t^*} - B_p e^{-b_3 t^*} \right) \quad (3.38).$$

The force in the spring is

$$f_s^* = F_s \left(e^{-b_1 t^*} - A_s e^{-b_2 t^*} - B_s e^{-b_3 t^*} \right) \quad (3.39).$$

These solutions are developed in full in Appendix A, together with expressions for all the parameters.

However, if two of the real roots are the same, the solution is different again. When b_3 is equal to b_2, the solution becomes

$$f_p^* = \dot{u}_a^* = F_p e^{-c_1 t^*} \left(1 - e^{-c_2 t^*} (1 + b_2 t^*) \right) \quad (3.40)$$

$$f_s^* = F_s e^{-c_1 t^*} \left(1 - e^{-c_2 t^*} (1 + b_2 A_s t^*) \right) \quad (3.41),$$

as detailed in Appendix A.

For cases where b_1 is equal to b_3 or b_2, the above solution can be adjusted by interchanging subscripts. However, in a practical computer implementation of these analytical solutions, equations (3.40) and (3.41) are probably not needed, since a very small change in m_a^* or k_c^* will allow one of the solutions discussed previously to be used. Equations (3.40) and (3.41) are presented here for completeness.

When ram separation occurs, the equation of motion of the anvil is

$$m_a \ddot{u}_a + Z \dot{u}_a = 0 \quad (3.42)$$

or

$$m_a^* \ddot{u}_a^* + \dot{u}_a^* = 0 \quad (3.43).$$

The dimensionless velocity of the anvil at the time the ram separates will be denoted by v_s^*. The velocity of the anvil after separation is then given by

$$f_p^* = \dot{u}_a^* = v_s^* \, e^{-\frac{t^* - t_s^*}{m_a^*}} \tag{3.44}$$

The effect of the anvil mass on the force exerted on the pile head is shown in Figure 3.3 for a dimensionless cushion stiffness of 4. As the anvil mass increases, the time taken for the force to peak increases. The peak force also increases for a range of m_a^* values, but decreases after m_a^* exceeds a certain value. The anvil mass which leads to maximum peak force on the pile head is discussed in a later section.

3.5 Damped cushion model

The model above assumes that the cushion behaves as an elastic spring. However, in practice the cushion absorbs energy. This energy absorption is particularly significant for wooden and plastic cushions. To account for this energy loss, the cushion can be modelled as a linear spring in parallel with a dashpot (Figure 3.1(d)). This again increases the complexity of the solution, but does not introduce any extra degrees of freedom. Using c_C to represent the damping in the cushion, the equations of motion of the system are

$$m_r \ddot{u}_r + c_C (\dot{u}_r - \dot{u}_a) + k_C (u_r - u_a) = 0 \tag{3.45}$$

$$m_a \ddot{u}_a + Z \dot{u}_a + c_C (\dot{u}_a - \dot{u}_r) + k_C (u_a - u_r) = 0 \tag{3.46}$$

Again using the dimensionless variables specified in equations (3.3) to (3.6), these equations can be re-written as

$$\ddot{u}_r^* + c_C^* (\dot{u}_r^* - \dot{u}_a^*) + k_C^* (u_r^* - u_a^*) = 0 \tag{3.47}$$

$$\ddot{u}_a^* + \frac{1}{m_a^*} \dot{u}_a^* + \frac{c_C^*}{m_a^*} (\dot{u}_a^* - \dot{u}_r^*) + \frac{k_C^*}{m_a^*} (u_a^* - u_r^*) = 0 \tag{3.48}$$

where the dimensionless cushion damping c_C^* is given by

$$c_C^* = \frac{c_C}{Z} \tag{3.49}$$

Applying the Laplace transformation to equations (3.47) and (3.48) and solving simultaneously, the Laplace transform of the anvil velocity can be found.

$$\mathrm{L}\, \dot{u}_a^* = \frac{\frac{c_C^*}{m_a^*}\left(s + \frac{k_C^*}{c_C^*}\right)}{s^3 + \left(c_C^*\left(\frac{1}{m_a^*}+1\right)+\frac{1}{m_a^*}\right)s^2 + \left(k_C^*\left(\frac{1}{m_a^*}+1\right)+\frac{c_C^*}{m_a^*}\right)s + \frac{k_C^*}{m_a^*}} \tag{3.50}$$

Performing the inverse Laplace transform, the pile force and anvil velocity can be expressed in the same form as equation (3.33).

$$f_p^* = u_a^* = F_p \, e^{-c_1 t^*}\left(1 - e^{-c_2 t^*} \frac{\cos(\omega t^* - \phi)}{\cos \phi}\right) \tag{3.51}$$

The intermediate steps and expressions for the parameters are presented in Appendix B. The spring force can be found by applying equation (3.34), and is of the form

$$f_S^* = F_S \, e^{-(c_1+c_2)t^*}\left(e^{c_2 t^*} - A_S \frac{\cos(\omega t^* - \theta)}{\cos \theta}\right) \tag{3.52}$$

where the coefficients are also detailed in Appendix B.

The ram will separate from the top of the cushion when the spring force is zero, which occurs at time t_S^*, where

$$e^{c_2 t_s^*} = A_s \frac{\cos(\omega t_s^* - \theta)}{\cos\theta} \tag{3.53}$$

Again, this equation cannot be solved analytically. For those cases in which hammer separation occurs, the time for separation must be established numerically. The subsequent force response is then given by equation (3.44).

The above solution applies when the denominator has one real and two imaginary roots. If it has three distinct real roots, Appendix B shows that the solution can be expressed as

$$f_p^* = \dot{u}_a^* = F_p \left(e^{-b_1 t^*} - A_p e^{-b_2 t^*} + B_p e^{-b_3 t^*} \right) \tag{3.54}$$

The force in the spring is

$$f_s^* = F_s \left(e^{-b_1 t^*} - A_s e^{-b_2 t^*} + B_s e^{-b_3 t^*} \right) \tag{3.55}$$

When two of the roots are identical, the solution below applies (Appendix B).

$$f_p^* = \dot{u}_a^* = F_p e^{-c_1 t^*} \left(1 - e^{-c_2 t^*} (1 + \gamma t^*) \right) \tag{3.56}$$

$$f_s^* = F_s e^{-c_1 t^*} \left(1 - e^{-c_2 t^*} (A_s + \gamma B_s t^*) \right) \tag{3.57}$$

When the three roots are real, ram separation never occurs.

Figure 3.4 shows the effect of the dimensionless cushion damping on the solution for the case when k_c^* is 4 and m_a^* is 0.2. As expected, increased damping in the cushion decreases any oscillation of the force.

Figure 3.5 shows which of the above solutions must be used for different combinations of k_c^* and m_a^*. When there is no cushion damping, equation (3.33) must be used in the region with two imaginary roots. In the region with three distinct real roots, equation (3.38) applies, and along the dividing line between the two regions, equation (3.40) can be used. For non-zero values of c_c*, equation (3.51) applies in the region with two imaginary roots, equation (3.54) applies when there are three distinct real roots, and equation (3.56) should be used along the dividing line.

3.6 Matching field data

The ability of the analytical model to represent real pile driving hammers will be demonstrated by comparing two sets of field data to the analytical solutions.

In the first case, a BSP 357 hammer was used to drive a 762 mm diameter by 18.5 mm wall thickness pile with an impedance of 1750 kNs/m. The cushion was steel with a stiffness of 1.6×10^6 kN/m. The recorded variation of the pile head force with time is shown in dimensionless terms in Figure 3.6.

The specified ram and anvil masses for this hammer are 6860 kg and 850 kg respectively, yielding a dimensionless anvil mass of 0.124 and a dimensionless cushion stiffness of 3.653. Using these values in equation (3.33), which applies for zero cushion damping, yields the solution also plotted in Figure 3.6. The agreement between the analytical solution and the field data is excellent, suggesting that there is little damping in the cushion.

The second data set was obtained from a BSP HA40 hammer, driving a 762 mm diameter by 44 mm wall thickness pile with an impedance of 4000 kNs/m. In this case the cushion was Bongassi with a stiffness of 7.5×10^6 kN/m. The force measured at the pile head is shown in Figure 3.7.

The specified cushion stiffness, together with a ram mass of 39 300 kg and an anvil mass of 6000 kg, give a dimensionless cushion stiffness of 18.8, and a dimensionless anvil mass of 0.153. Equation (3.51) was found to best match the field data when a dimensionless cushion damping of 0.6 was used with a k_c^* of 25. The

4. PROBLEM FORMULATION AND SOLUTION TECHNIQUES

4.1 Introduction

This chapter presents the differential equations which govern the response of a pile embedded in a semi-infinite half-space to impact loading. Since these equations are too complex for general analytical solution, the equations are reformulated in a weak form to allow the solution to be approximated by a linear combination of a set of base functions. The finite element method is presented as a means of obtaining base functions sets which lead to banded symmetric matrices, and hence efficient numerical solution. Numerical integration of the finite element equations in time is discussed. Von Mises plasticity is introduced, together with numerical methods of solving the resulting non-linear equations.

4.2 Governing equations

A pile of circular cross-section embedded in a half-space, the properties of which vary only with depth, presents an axisymmetric problem. For simplicity, a pile of constant radius and a half-space with constant material properties will be considered. This idealised model is shown in Figure 4.1.

Assuming that both the pile and the half-space are elastic, the constitutive equations for the entire half-space (including the pile) in cylindrical coordinates are

$$\varepsilon_z = \frac{\sigma_z}{E} - \nu\frac{\sigma_r}{E} - \nu\frac{\sigma_\theta}{E}$$

$$\varepsilon_r = \frac{\sigma_r}{E} - \nu\frac{\sigma_z}{E} - \nu\frac{\sigma_\theta}{E}$$

$$\varepsilon_\theta = \frac{\sigma_\theta}{E} - \nu\frac{\sigma_r}{E} - \nu\frac{\sigma_z}{E}$$

$$\gamma_{rz} = 2(1+\nu)\frac{\tau_{rz}}{E} \qquad (4.1)$$

where ε_z, ε_r and ε_θ are the axisymmetric normal strains, γ_{rz} is the shear strain, σ_z, σ_r and σ_θ are the axisymmetric normal stresses and τ_{rz} is the shear stress. E is Young's modulus and ν is Poisson's ratio. The variation of these two parameters in axisymmetric space may be expressed as

$$E = \begin{cases} E_p & \text{for } -L \le z \le 0 \text{ and } r \le R \\ E_S & \text{for } z \le 0 \text{ and } r > R \text{ or } z < -L \\ 0 & \text{for } z > 0 \end{cases} \qquad (4.2)$$

and

$$\nu = \begin{cases} \nu_p & \text{for } -L \le z \le 0 \text{ and } r \le R \\ \nu_S & \text{for } z \le 0 \text{ and } r > R \text{ or } z < -L \\ 0 & \text{for } z > 0 \end{cases} \qquad (4.3)$$

where E_p is the elastic modulus of the pile, ν_p is the Poisson's ratio of the pile, E_S is the elastic modulus of the soil, ν_p is the Poisson's ratio of the soil, and R is the radius of the pile.

The constitutive relationships stated in equation (4.1) can be expressed in matrix form as

$$\sigma = \mathbf{D}\,\varepsilon \qquad (4.4)$$

where

$$\sigma = \begin{Bmatrix} \sigma_z \\ \sigma_r \\ \sigma_\theta \\ \tau_{rz} \end{Bmatrix}, \quad \varepsilon = \begin{Bmatrix} \varepsilon_z \\ \varepsilon_r \\ \varepsilon_\theta \\ \gamma_{rz} \end{Bmatrix}, \quad \text{and}$$

$$\mathbf{D} = \frac{E(1-\nu)}{(1+\nu)(1-2\nu)} \begin{bmatrix} 1 & \frac{\nu}{1-\nu} & \frac{\nu}{1-\nu} & 0 \\ \frac{\nu}{1-\nu} & 1 & \frac{\nu}{1-\nu} & 0 \\ \frac{\nu}{1-\nu} & \frac{\nu}{1-\nu} & 1 & 0 \\ 0 & 0 & 0 & \frac{1-2\nu}{2(1-\nu)} \end{bmatrix} \tag{4.5}$$

The local strains can be related to the displacements in the z and r directions (designated by u_z and u_r) with the following compatibility equations. Tensile strains and stresses are taken as positive in this chapter.

$$\varepsilon_z = \frac{\partial u_z}{\partial z}, \quad \varepsilon_r = \frac{\partial u_r}{\partial r}, \quad \varepsilon_\theta = \frac{u_r}{r}, \quad \gamma_{rz} = \frac{\partial u_z}{\partial r} + \frac{\partial u_r}{\partial z} \tag{4.6}$$

These equations can be expressed in matrix form as

$$\varepsilon = \mathbf{L}\,\mathbf{u} \tag{4.7}$$

where

$$\mathbf{u} = \begin{Bmatrix} u_z \\ u_r \end{Bmatrix} \quad \text{and} \quad \mathbf{L} = \begin{bmatrix} \frac{\partial}{\partial z} & 0 \\ 0 & \frac{\partial}{\partial r} \\ 0 & \frac{1}{r} \\ \frac{\partial}{\partial r} & \frac{\partial}{\partial z} \end{bmatrix} \tag{4.8}$$

The half-space will contain a initial stress field balancing the force gravity of gravity, and possibly containing locked in stresses. Since this stress field is self-equilibrating, and the system is assumed to be elastic, only the changes in stresses, strains, and displacements from this initial field will be investigated. All stresses, strains and displacements in the following equations are taken to be changes from the initial state.

The dynamic equilibrium equations can be found by considering the changing vertical and radial forces acting on an infinitesimal element in the pile or the half-space Figure 4.2 . Since the only changing external force present is the vertical force exerted by the hammer system, the equilibrium equations are

$$\rho r \frac{\partial^2 u_z}{\partial t^2} - r\frac{\partial \sigma_z}{\partial z} - \frac{\partial (r\,\tau_{rz})}{\partial r} - r f_z(z,r,t) = 0 \tag{4.9}$$

and

$$\rho r \frac{\partial^2 u_r}{\partial t^2} - \frac{\partial (r\,\sigma_r)}{\partial r} + \sigma_\theta - r\frac{\partial \tau_{rz}}{\partial z} = 0 \tag{4.10}$$

The external distributed stress (f_z) caused by the hammer impact load can be modelled as a time-varying stress uniformly distributed over the pile head. The external distributed stress in equation (4.10) can then related to the force impact functions (f_p) derived in Chapter 3 by the simple equation

$$f_z(t) = \begin{cases} -\dfrac{f_p(t)}{\pi R^2} & \text{for } r \le R \text{ and } z = 0 \\ 0 & \text{otherwise} \end{cases} \tag{4.11}$$

Prior to the ram striking the cushion, the displacements, velocities, and accelerations are zero at all points in the pile and half-space. The response of a pile to hammer impact can therefore be found if the system of second order linear differential equations represented by equations (4.9) and (4.10) together with equations (4.4) and (4.7) is solved, subject to the boundary condition represented by equation (4.11) and the initial conditions of zero displacement, velocity, and acceleration at all points.

Unfortunately, this equation set is too complex to be solved by analytical methods for the general case. The equations can be solved if certain simplifications are introduced, such as setting the soil stiffness to zero, leaving a floating pile, or making the pile infinitely long and infinitely stiff. However, for most realistic cases, only approximate solution is possible. Such approximate solutions are most conveniently obtained by numerical methods.

4.3 Weighted residual approximation

The weighted residual method allows an approximate solution for a set of differential equations to be found as a linear combination of a pre-defined set of basis functions. The method dates back to the last century, and is described fully by Finlayson (1972). The application of the weighted residual method to the differential equations governing pile driving will be described in this section.

The solution domain, which consists of the pile and the half-space, will be denoted by Ω. If the differential equations presented above are satisfied at every point in this solution domain, then for any function w, where

$$\mathbf{w} = \begin{Bmatrix} w_z(z,r) \\ w_r(z,r) \end{Bmatrix}$$

the following equation must also hold.

$$\iint_\Omega \left[w_z \left(\rho\, r \frac{\partial^2 u_z}{\partial t^2} - r \frac{\partial \sigma_z}{\partial z} - \frac{\partial (r\, \tau_{rz})}{\partial r} - r\, f_z \right) + w_r \left(\rho\, r \frac{\partial^2 u_r}{\partial t^2} - \frac{\partial (r\, \sigma_r)}{\partial r} + \sigma_\theta - r \frac{\partial \tau_{rz}}{\partial z} \right) \right] dr\, dz = 0 \qquad (4.12)$$

Since satisfaction of this equation is necessary but not sufficient for equilibrium, equation (4.12) is a weak form of the equilibrium conditions. Expanding and integrating by parts, and recognising that the stress changes from initial equilibrium at the domain boundaries are zero, equation (4.12) becomes

$$\iint_\Omega \left[w_z\, \rho \frac{\partial^2 u_z}{\partial t^2} + w_r\, \rho \frac{\partial^2 u_r}{\partial t^2} + \sigma_z \frac{\partial w_z}{\partial z} + \tau_{rz} \frac{\partial w_z}{\partial r} - w_z f_z + \sigma_r \frac{\partial w_r}{\partial r} + \sigma_\theta \frac{w_r}{r} + \tau_{rz} \frac{\partial w_r}{\partial z} \right] r\, dr\, dz = 0 \qquad (4.13).$$

The linear operators applied to the functions w are identical to those applied to the displacements to obtain the strains (equation (4.6)). Equation (4.13) can therefore be written in matrix notation as

$$\iint_\Omega \left[\rho\, \mathbf{w}^T \frac{\partial^2 \mathbf{u}}{\partial t^2} + [\mathbf{L}\ \mathbf{w}]^T\, \sigma \right] r\, dr\, dz - \iint_\Omega w_z f_z\, r\, dr\, dz = 0 \qquad (4.14).$$

Substituting equations (4.4) and (4.7), and applying the definition of f_z (equation (4.11)), equation (4.14) becomes

$$\iint_\Omega \left[\rho\, \mathbf{w}^T \frac{\partial^2 \mathbf{u}}{\partial t^2} + [\mathbf{L}\ \mathbf{w}]^T\, \mathbf{D}\, [\mathbf{L}\ \mathbf{u}] \right] r\, dr\, dz - \int_0^R w_z f_z\, r\, dr\, dz = 0 \qquad (4.15).$$

Now, if an approximation $\hat{\mathbf{u}}$ is used in place of the exact solution u, the equation above will not hold for every function w. For any particular w, the integrals in equation (4.15) will add to give a residual, which is a sum of the equilibrium errors caused by the approximation, weighted by the function w.

In the method of weighted residuals, an approximation $\hat{u}$ is sought as a linear combination of n base functions, $N_i(z,r)$. This approximation can be written as

$$\mathbf{u}(z,r,t) \approx \hat{\mathbf{u}}(z,r,t) = \sum_{1}^{n} \mathbf{N}_i(z,r)\, a_i(t) = \mathbf{N}\,\mathbf{a} \tag{4.16}$$

where **a** is an column vector of n unknown time dependant coefficients, and **N** is a column vector of n known base or shape functions. Since there are n unknown time dependant variables, n differential equations are required if a solution is to be obtained. A solvable system of equations can be formed by selecting n distinct weighting functions.

In general, each different set of weighting functions will lead to a different approximate solution. There are a variety of methods available for selecting weighting functions, including the Galerkin method, which uses the base functions as the weighting functions; point collocation, which satisfies the equilibrium equations exactly at n discrete points in the solution domain; and subdomain collocation, in which the integral of the error over each of n subdomains is equated to zero. The Galerkin method is particularly useful, as it often leads to symmetric matrices.

To apply the Galerkin method, each weighting function is equated to a shape function.

$$\mathbf{w}_i = \mathbf{N}_i \qquad i = 1 \ldots n \tag{4.17}$$

Equation (4.15) becomes a set of n equations, which, after substitution of equations (4.16) and (4.17), may be written as

$$\iint_{\Omega} \left[\rho\, \mathbf{N}^{\mathrm{T}} \frac{\partial^2(\mathbf{Na})}{\partial t^2} + [\mathbf{LN}]^{\mathrm{T}}\, \mathbf{D}\, [\mathbf{L(Na)}] \right] r\, dr\, dz - \int_{0}^{R} \mathbf{N}_z\, f_z\, r\, dr\, dz = 0 \tag{4.18}.$$

Since the coefficient matrix **a** is a function of time only, and the shape functions **N** are functions of position only, equation (4.18) can be rewritten as

$$\iint_{\Omega} \left[\rho\, \mathbf{N}^{\mathrm{T}}\mathbf{N}\, \frac{\partial^2 \mathbf{a}}{\partial t^2} + \mathbf{B}^{\mathrm{T}}\, \mathbf{D}\, \mathbf{B}\, \mathbf{a} \right] r\, dr\, dz - \int_{0}^{R} \mathbf{N}_z\, f_z\, r\, dr\, dz = 0 \tag{4.19a}$$

where

$$\mathbf{B} = \mathbf{L}\,\mathbf{N} \tag{4.19b}$$

or alternatively as

$$\mathbf{M}\,\ddot{\mathbf{a}} + \mathbf{K}\,\mathbf{a} = \mathbf{f} \tag{4.20}$$

with

$$\mathbf{M} = \iint_{\Omega} \rho\, \mathbf{N}^{\mathrm{T}}\mathbf{N}\, r\, dr\, dz \;, \quad \mathbf{K} = \iint_{\Omega} \mathbf{B}^{\mathrm{T}}\, \mathbf{D}\, \mathbf{B}\, r\, dr\, dz \tag{4.21}$$

and

$$\mathbf{f} = \int_{0}^{R} \mathbf{N}_z\, f_z\, r\, dr\, dz \tag{4.22}.$$

4.4 The finite element method

The finite element method is a type of weighted residual method. In the finite element method, the domain of interest is broken up into a number of discrete regions, or elements. Each element contains a number of nodes. Shape functions are formed by specifying a unit value at each node in turn, and holding the value at all other nodes at zero. The variation of the shape function between nodes is usually polynomial or linear, but other forms can be used. Nodes can be contained totally within one element, or shared by two or more adjacent

elements. An example of a small domain broken into triangular elements is shown in Figure 4.3, together with the associated linear shape functions.

The advantages of the finite element method are due to the way that the matrices in equation (4.15) can be assembled on an element by element basis. Because each shape function is only non-zero in a small region of the domain, many of the shape functions have no non-zero values in common, and this leads to sparsely populated matrices. If the equations are ordered carefully, considerable banding of the matrices can be achieved, leading to substantial economies in calculation time and computer memory requirements.

The finite element method for axisymmetric stress elements is usually formulated from virtual work principles (eg. Zienkiewicz (1977), Smith (1982)). The virtual work formulation leads to identical equations to those obtained above with the Galerkin weighted residual method.

4.5 Time integration

Finite element discretisation of the spatial solution domain leads to a set of n second order linear differential equations in time, with n time dependant variables (equation (4.20)). In general, this set of equations cannot be solved analytically, and must be numerically integrated forward in time from the instant the hammer ram strikes the cushion assembly. There are numerous numerical schemes through which this can be accomplished. Zienkiewicz (1977) has shown how most of these schemes can be derived using the weighted residual method. Some commonly employed schemes have been reviewed in detail by Bathe and Wilson (1976). This section briefly introduces three of the most widely used numerical time integration schemes.

In the *central difference scheme*, the displacement at time $t+\Delta t$ is related to the displacements at t and $t-\Delta t$ by

$$\mathbf{a}_{t+\Delta t} = \mathbf{M}^{-1} \left[\Delta t^2 \mathbf{f}(t) - (\Delta t^2 \mathbf{K} - 2\,\mathbf{M})\,\mathbf{a}_t - \mathbf{M}\,\mathbf{a}_{t-\Delta t} \right] \qquad (4.23).$$

Since the displacement at time $t+\Delta t$ is calculated from the equilibrium at time t, this scheme is called an explicit method. Solution of equation (4.23) requires inversion of the mass matrix (M). If the only non-zero terms in the mass matrix are on the diagonal, this is a trivial exercise. A mass matrix with only non-zero diagonal terms is a lumped mass matrix, since the physical interpretation is a model with mass concentrated only at the nodes. Such a mass matrix can be formed by judicious selection of the shape functions, which can be different from those used to form the stiffness matrix, and can be discontinuous, as derivatives of these functions are not required.

An explicit integration scheme such as that described above can save much computer time when used in conjunction with a lumped mass matrix. However, the scheme is only conditionally stable (Bathe and Wilson, 1976). Unconditional stability is only guaranteed when the time-step Δt is less than Δt_{crit}, where

$$\Delta t_{crit} = \frac{T_n}{\pi} \qquad (4.24).$$

T_n is the smallest natural period of the finite element system.

In the *constant-average-acceleration scheme* (Newmark $\beta = 1/2$), the displacement at time $t+\Delta t$ is found by considering the equilibrium at time $t+\Delta t$. Such methods are termed implicit. The new displacements are calculated at each time-step using the following equation.

$$\mathbf{a}_{t+\Delta t} = \left[\mathbf{K} + \frac{1}{4\Delta t^2}\mathbf{M} \right]^{-1} \left[\mathbf{f}(t+\Delta t) + \mathbf{M} \left(\frac{1}{4\Delta t^2}\mathbf{a}_t + \frac{1}{2\Delta t}\dot{\mathbf{a}}_t + \ddot{\mathbf{a}}_t \right) \right] \qquad (4.25)$$

This scheme is unconditionally stable and exhibits no numerical damping, but requires reduction of an effective stiffness matrix. Since this matrix is a linear combination of the stiffness and mass matrices, it always contains non-zero off-diagonal terms.

The *Wilson θ scheme* calculates the displacements at time $t+\theta\Delta t$, and then the displacements, velocities and accelerations at time $t+\Delta t$. The equilibrium conditions are satisfied at time $t+\theta\Delta t$, and so the method is implicit. Like the constant-average-acceleration method, reduction of an effective stiffness matrix is required. However, the scheme is only unconditionally stable when θ is greater than 1.37 (Bathe and Wilson), and exhibits numerical damping at high frequencies.

These time integration schemes will be compared in the next chapter.

4.6 Plasticity

The equations of motion formulated in the first section of this chapter were based on an elastic soil mass. However, pile driving involves inelastic deformation of the soil. There is a large variety of models of soil inelasticity available (eg. Chen and Baladi, 1985), but only the simplest will be used in the present work.

In the theory of plasticity, a yield surface in three-dimensional stress space defines the limit of elastic behaviour. The stress state cannot pass through the yield surface, and when it is on the yield surface, irrecoverable plastic strains can occur. If the direction of the plastic strain is always normal to the yield surface at the state of stress, the plastic flow is said to be associated.

The equation for the von Mises (1928) yield surface is

$$[{}^1/_2(\sigma_1-\sigma_2)^2 + {}^1/_2(\sigma_2-\sigma_3)^2 + {}^1/_2(\sigma_3-\sigma_1)^2 + 3\tau_{12}^2 + 3\tau_{23}^2 + 3\tau_{31}^2]^{1/2} - \sigma_y = 0 \qquad (4.26)$$

which forms a cylinder in three-dimensional stress space (Figure 4.4). The numerical subscripts represent the three coordinate axes, and σ_y is the von Mises yield stress. When combined with the associated flow rule, the von Mises model represents the behaviour of an undrained soil (Smith, 1982). There is no volume change during plastic flow, and the undrained shear strength is related to the von Mises yield stress by

$$s_u = \frac{\sigma_y}{2} \quad (4.27).$$

Equation (4.4) defines the relationship between stress and strain during elastic deformation. After yield, the relationship between stress increment and strain increment can be represented by

$$d\sigma = [\mathbf{D} - \mathbf{D}_p]\, d\varepsilon \qquad (4.28).$$

When the von Mises yield law is used with associated flow in axisymmetric coordinates (Yamanda et al, 1968), the matrix $\mathbf{D}_p$ is defined by

$$\mathbf{D}_p = \frac{3E}{2\sigma_y(1+\nu)} \begin{bmatrix} \sigma_z'^2 & \sigma_z'\sigma_r' & \sigma_z'\sigma_\theta' & \sigma_z'\tau_{rz} \\ \sigma_r'\sigma_z' & \sigma_r'^2 & \sigma_r'\sigma_\theta' & \sigma_\theta'\sigma_z' \\ \sigma_r'\tau_{rz} & \sigma_\theta'\sigma_r' & \sigma_\theta'^2 & \sigma_\theta'\tau_{rz} \\ \tau_{rz}\sigma_z' & \tau_{rz}\sigma_r' & \tau_{rz}\sigma_\theta' & \tau_{rz}^2 \end{bmatrix} \qquad (4.29).$$

The deviatoric stresses, represented by the dash, are

$$\sigma_z' = \frac{2\sigma_z - \sigma_r - \sigma_\theta}{3}, \quad \sigma_r' = \frac{2\sigma_r - \sigma_z - \sigma_\theta}{3}, \quad \text{and } \sigma_\theta' = \frac{2\sigma_\theta - \sigma_z - \sigma_r}{3} \qquad (4.30).$$

Since the matrix $\mathbf{D}_p$ is a function of stress, the set of differential equations represented by equation (4.20) becomes non-linear. Writing equation (4.18) in incremental form and substituting the plastic stress-strain relationship given by equation (4.28),

$$\iint_\Omega \left[\rho\, \mathbf{N}^T\mathbf{N} \frac{\partial^2 \mathbf{a}}{\partial t^2} + \mathbf{B}^T[\mathbf{D}-\mathbf{D}_p]\mathbf{B}\, \delta\mathbf{a} \right] r\, dr\, dz - \int_0^R \mathbf{N}_z\, \delta f_z\, r\, dr\, dz = 0 \qquad (4.31)$$

or

$$\mathbf{M}\, \ddot{\mathbf{a}} + \mathbf{K}\, \delta\mathbf{a} = \delta\mathbf{f} + \mathbf{f}_b \qquad (4.32)$$

where $\mathbf{M}$ and $\mathbf{K}$ are defined in equation (4.21),

$$\delta\mathbf{f} = \int_0^R \mathbf{N}_z\, \delta f_z\, r\, dr\, dz \qquad (4.33)$$

and

$$\mathbf{f_b} = \iint_{\Omega} \mathbf{B}^T \mathbf{D_p} \mathbf{B}\, r\, dr\, dz\, \delta\mathbf{a} \qquad (4.34).$$

The non-linear behaviour is now contained in the term $\mathbf{f_b}$, which represents the difference between the plastic response and the elastic response. Equation (4.32) is usually solved at a particular time t by using the Newton-Rhapson method (Zienkiewicz, 1977). This method commences by solving equation (4.32) without $\mathbf{f_b}$ to obtain an initial estimation of $\delta\mathbf{a}$. $\mathbf{f_b}$ is calculated using equation (4.34), and equation (4.32) is solved with this $\mathbf{f_b}$ to find a refined estimate of $\delta\mathbf{a}$. These two steps are repeated until $\delta\mathbf{a}$ and $\mathbf{f_b}$ do not change significantly. The process is illustrated graphically in Figure 4.5(a). The modified Newton-Rhapson method (Figure 4.5(b)) can be used to increase the rate of convergence of the iterative scheme. However, this method requires periodic recomputation and reduction of the tangential stiffness matrix, which offsets savings in iteration time. Consequently, the Newton-Rhapson method will be used in the work presented in this thesis.

To solve the pile driving equations, the iterative method described above must be used in conjunction with one of the numerical time integration methods described previously. When implicit integration is used, iteration must be carried out within each time step until the displacement changes converge.

4.7 Conclusions

This chapter derived the differential equations governing the response of a pile embedded in an elastic soil mass to hammer impact. Since these equations could not be solved analytically, the weighted residual method was introduced as a technique for obtaining an approximate solution. The finite element method was found to be a convenient way to obtain numerical solutions, and will be used in all the work which follows.

Techniques of numerical time integration were briefly described. These techniques will be investigated further in the next chapter.

The modifications to the governing equations caused by the assumption of von Mises plasticity were discussed, and the Newton-Rhapson methods were introduced as a method of solving the non-linear differential equation system. The standard Newton-Rhapson method was selected for use in the work which follows, since the modified Newton-Rhapson method requires repeated reduction of the structure stiffness matrix.

5. FINITE ELEMENT ANALYSIS OF THE PILE

5.1 Introduction

This chapter examines the propagation of impact waves in an elastic pile using the finite element method. The surrounding soil is ignored. The effect of impact wave shape, integration method, element type and node spacing on the convergence of the pile stresses is investigated. The level of discretisation required to produce accurate results is determined. The effect of radial inertia is examined, and the differences between the responses of solid and hollow piles are investigated.

5.2 The one-dimensional wave equation

An analytical solution to the equations of motion presented in Chapter 4

can be obtained when the following simplifications are made.

1. The soil surrounding the pile shaft has zero stiffness ($E_S = 0$).

2. The radial inertia term in equation (4.10) is ignored.

3. The axial stress and strain are taken as uniform across each cross-section.

4. The soil at the pile base has infinite or zero stiffness.

When these simplifications are applied to equations (4.1) to (4.10), the equation of motion in the vertical direction becomes

$$\rho \frac{\partial^2 u_z}{\partial t^2} - E_p \frac{\partial^2 u_z}{\partial z^2} - f_z = 0 \tag{5.1}$$

where u_z and f_z are functions of z and t only. Since f_z is only non-zero at $z = 0$, equation (5.1) is a one-dimensional wave equation over the rest of the pile. The equation can be rewritten as

$$\frac{\partial^2 u_z}{\partial t^2} - c_p{}^2 \frac{\partial^2 u_z}{\partial z^2} = 0 \tag{5.2}$$

where c_p is the axial wave velocity in the pile, defined by

$$c_p = \sqrt{\frac{E_p}{\rho_p}} \tag{5.3}.$$

Solution of this equation is trivial. A stress wave applied at $z = 0$ will propagate down the pile with velocity c_p. In this chapter, compressive stresses and strains are defined as positive. Since the wave travels in the negative z direction, the solution can be represented as

$$\sigma_z(z) = f_z\left(t + \frac{z}{c_p}\right) \tag{5.4}.$$

If the pile is of length L and the soil at the base of the pile is infinitely stiff, the stress wave will be reflected back up the pile after reaching $z = -L$. On returning to the top of the pile, the wave will be reflected back down the pile with a change in sign. Since no energy is radiated from the pile, this process will continue indefinitely. At any particular time, the axial stress in the pile can be obtained from the following equation, provided that the function $f_z(t)$ is taken as zero for negative t.

$$\sigma_z(z) = \sum_{i=1}^{n} (-1)^{i+1} \left(f_z\left(t + \frac{z-2(i+1)L}{c_p}\right) + f_z\left(t - \frac{z+2iL}{c_p}\right)\right) \tag{5.5}$$

This equation is valid in the time interval

$$\frac{2(n-1)L}{c_p} < t < \frac{2nL}{c_p}$$

If the soil at the base of the pile has zero stiffness, there will also be a change in sign after the wave is reflected from the base. For this case equation (5.5) becomes

$$\sigma_z(z) = \sum_{i=1}^{n} \left(f_z\left(t + \frac{z-2(i+1)L}{c_p}\right) - f_z\left(t - \frac{z+2iL}{c_p}\right)\right) \tag{5.6}$$

In the following sections, these exact solutions will be used to compare the abilities of several finite element schemes to accurately analyse the propagation of impact waves in a pile.

5.3 Rod elements

Since equation (5.1) only contains vertical motion, a finite element scheme with one vertical degree of freedom at each node can be used. The ability of three different elements to represent the behaviour of the pile will be investigated.

The first element contains two nodes. Linear shape functions are used to represent the variation in u_z between the nodes for the derivation of the stiffness matrix, and step functions are used to derive a lumped mass matrix. These functions are shown in Figure 5.1(a). This element leads to the formulation of Smith (1960), since it is equivalent to a spring of stiffness $EA/\Delta z$ between the nodes, and a mass of $\rho A \Delta z$ at each node. (A is the cross-sectional area of the pile, and Δz is the vertical distance between the nodes.)

The second element is also two-noded, but linear shape functions are used to derive both the mass and stiffness matrices (Figure 5.1(b)). A consistent mass matrix with off-diagonal terms is formed by this formulation. The stiffness matrix is the same as the element described above.

The third element has three nodes, and quadratic shape functions are used to derive the stiffness and mass matrices. These shape functions are shown in Figure 5.1(c).

Quadratic shape functions can represent a linear stress variation across an element exactly, whereas linear shape functions only allow constant stress within each element. However, this chapter will show that there is little difference between the accuracy of solutions obtained with linear elements and quadratic elements, providing the node spacing is not too large. For this reason, higher order polynomial shape functions will not be investigated. The increased complexity of these elements, especially when used in two-dimensional form, was anticipated to outweigh any slight numerical advantages. All previous finite element analysis of pile driving used quadratic shape functions.

5.4 The trial problem

All of the analyses presented in this chapter employed a pile with properties typical of offshore piles. The pile was taken to be 20 m long, and the base was rigidly supported. Typical hammer properties were also selected. The properties of the pile and the hammer system are shown in Figure 5.2. Similar pile and hammer properties were used by Simons (1985) and Smith and Chow (1982).

5.5 Hammer/pile impact

The first series of analyses was performed with the impact function caused by the hammer directly striking the top of the pile. This function was used by Simons (1985) in all his analyses. Each of the three elements described above was used with node spacings of 0.5, 0.25, and 0.125 m. Time integration was performed using the constant-average-acceleration method with a time-step of 0.1 $\Delta z/c_p$. Preliminary calculation had shown this scheme ensured any numerical errors due to the time discretisation were small when compared with those due to the spatial discretisation.

The two-noded lumped mass element was used first. Figure 5.3 shows the variation in axial force ($\sigma_z A$) along the pile 3 milliseconds after hammer impact. At this time the wave is three quarters of the way down the pile for the first time. The figure shows the axial force oscillating with a frequency which is dependent on the node spacing. The maximum stress exceeds the theoretical stress for all node spacings, with the finest mesh recording the highest stress. Figure 5.4 shows the variation in axial force when the stress wave is three quarters of the way down the pile for the third time. The accuracy of the solutions has clearly deteriorated. Figure 5.5 shows the variation of the force at the toe of the pile with time over the course of the analysis. The oscillations

observed in the spatial variation of axial stress are evident in the time variation of the toe force, and the peak force is overestimated on both the occasions that the wave front strikes the base. The variation of head displacement with time is shown in Figure 5.6. Despite the large oscillations occurring in the stresses and the toe force, the calculated head displacements are in close agreement with the theoretical solution, with some small erroneous oscillation evident at later times for the coarsest mesh.

This is a characteristic of the finite element method. Displacements may be estimated quite accurately with coarse meshes and shape functions which do not model the variation of internal force well. However, quantities which are related to derivatives of displacement, such as stress, are much harder to model accurately.

When the analyses were repeated with the two-noded consistent mass element, the results shown in Figures 5.7 to 5.10 were obtained. Figure 5.7 shows the axial stress 3 ms after impact. Compared with the results from the lumped mass analysis (Figure 5.3), the oscillation in the decaying portion of the wave is considerably reduced, and the maximum stress is underestimated rather than overestimated. The agreement between the exact solution and the finite element solution improves as the node spacing is reduced. However, whereas the lumped mass element showed little erroneous stress preceding the wave front, even after 19 ms, the consistent mass solution exhibits considerable leading stress oscillation, the period of which is a function of node spacing. Figure 5.8 shows that after 19 ms the solution has deteriorated considerably, with oscillation evident over the entire wave. The toe force (Figure 5.9) also shows much better agreement over the decaying portion of the wave with the exact solution than does the lumped mass solution, but considerable oscillation precedes the wavefront. This oscillation is of such magnitude that the head displacement is affected (Figure 5.10).

Smith and Chow (1982) refer to disagreement in the literature regarding the superiority or otherwise of lumped mass elements, but claim that consistent mass elements are clearly superior. The analyses presented here show that when a discontinuous impact force is applied, neither type of element is clearly superior. The consistent mass element represents the stress wave more accurately, but causes erroneous oscillating stress to precede the wavefront, to the extent that the resulting head displacement solution is actually worse than that predicted when lumped mass elements are used.

Figures 5.11 to 5.14 show the results obtained with the three-noded consistent mass element. These results only vary slightly from those obtained with the two-noded consistent mass element. There is a slight improvement in the representation of the peak stress, and the deterioration between 3 ms and 19 ms is less marked. The oscillation in front of the wave is slightly reduced, and consequently the head displacement is improved. However, the displacements are still not quite as good as those computed with the lumped mass element.

These analyses have shown that, of the three elements tested, the three-noded consistent mass element provided the best approximation of the stress distribution in the pile, together with reasonably good displacements. The analyses which follow will be performed mainly with this element, although one more set of analyses will be performed with a different impact function.and the two-noded consistent mass element to confirm the superiority of the three-noded element.

Despite the use of very fine meshes and three different types of element, the pile stresses obtained in the above analyses are poor approximations of the correct stresses. The problem lies not with the finite element approximation, but with the impact function. The accuracy of the finite element method depends on the ability of the elements to assume a shape which is a good approximation of the exact solution. The hammer/pile impact function contains a discontinuity in stress at the wavefront. The exact solution requires this discontinuity to propagate through every particle in the pile. In a finite element solution, the discontinuity should propagate through the elements. However, since the shape functions have C_1 continuity through the elements, the finite element mesh cannot accurately represent this propagation. There are specific finite elements available (Oden and Wellford, 1975) which accommodate travelling discontinuities, but such elements are only one-dimensional. Since the objective of the current project is to accurately model the complete pile driving process, adoption of such elements for the pile was not considered appropriate, as the problem of propagating the discontinuity would then be transferred to the soil.

An alternative approach is to use a hammer model which does not cause a stress discontinuity. The impulse functions for both the hammer/cushion and hammer/cushion/anvil models described in Chapter 3 are continuous. The effect of employing these impact functions is investigated in the following two sections.

5.6 Hammer/cushion impact

The shape of the hammer/cushion impulse function is indicated in Figure 3.2 ($k_c^* = 6.25$). The second series of analyses was performed using this impulse function and three-noded quadratic elements. The variation of axial force along the pile 3 ms after impact is shown in Figure 5.15. A significant improvement in accuracy over the

results shown in Figure 5.11 is evident. With the exception of the coarsest mesh, the only observable errors occur immediately in front of the wave. The axial forces 19 ms after impact are shown in Figure 5.16. Some deterioration in accuracy is evident, but the improvement over the results shown in Figure 5.12 is immense.

The improvement in accuracy carries over to the toe force and the head displacement (Figures 5.17 and 5.18). Again, the only significant errors occur immediately in front of the wave.

5.7 Hammer/cushion/anvil impact

Although the hammer/cushion impulse function is continuous, there is a discontinuity in slope at the front of the wave. The slope of the hammer/cushion/anvil impulse function is continuous at all times. This suggests that the hammer/cushion/anvil impact could improve the accuracy of the analysis even further.

The third series of analyses was performed with the hammer/cushion/anvil impulse function and three-node quadratic elements. The variation of axial force along the pile 3 ms after impact is shown in Figure 5.19. Only the coarsest mesh causes visible errors, and these errors are very small. The erroneous stress oscillation in front of the wave is almost eliminated. After 19 ms (Figure 5.20) there is minimal deterioration in accuracy, even with 0.5 m node spacing.

These observations can also be made of the variation of toe force and head displacement with time. For node spacings of 0.25 m and 0.125 m, the finite element solutions are virtually indistinguishable from the exact solutions.

After the investigation of hammer/pile impact solutions, three-node quadratic elements were selected over two-node linear elements. However, the results presented in that section did not conclusively show that the quadratic elements were superior. To establish this superiority, a set of analyses was performed using the hammer/cushion anvil impulse function with two-noded linear elements. The axial force after 3 ms is shown in Figure 5.23. A marginal decrease in accuracy over the results shown in Figure 5.19 is distinguishable. This loss of accuracy becomes more evident after 19 ms (Figure 5.24), and is also visible in the toe force and head displacement graphs (Figures 5.25 and 5.26).

The numerical experiments described above show that spatial discretisation errors are minimised when a continuous force impulse function, such as that resulting from a hammer/cushion/anvil impact, is used. If three-noded quadratic elements are used with 12 or more nodes in the rising portion of the wave, very accurate approximate solutions can be obtained.

5.8 Time integration methods

The analyses described above were performed with the Newmark $\beta = {}^1/_2$ method (the constant-average-acceleration method) and a very small time step ($0.1\Delta z/c_p$) to ensure that the time discretisation errors were much smaller than the spatial discretisation errors. This section turns attention to the different methods of time integration described in Chapter 4, and the effect of time-step size on the solution. The Newmark $\beta = {}^1/_2$ method will be referred to as the average acceleration method, the Wilson $\theta = 1.4$ method will be called the Wilson method.

To highlight the differences between the three selected methods of time integration, the hammer/impulse function was used with the coarsest element mesh ($\Delta z = 0.5$ m). Using a time step of $0.1\Delta z/c_p$, the responses presented in Figures 5.27 and 5.28 were obtained. There is little difference between the results obtained with the average acceleration and the central difference methods, while the Wilson method (due to its numerical damping) smooths some of the force oscillation. By 19 ms, the Wilson method has rounded off the wave shape significantly.

When the time step is reduced to $0.5\Delta z/c_p$, the oscillation in the central difference solution increases, while that in the average acceleration solution decreases (Figure 5.29). The numerical damping provided by the Wilson method increases, further attenuating the solution. After 19 ms, the peak pile force predicted by the Wilson method is less than 50% of the exact solution (Figure 5.30). This reduction is also evident in the toe force (Figure 5.31) and, to a lesser extent, in the head displacement (Figure 5.32).

In the preceding section, a hammer/cushion/anvil impulse applied to a pile model of three-noded quadratic elements with a node spacing of 0.25 m was shown to produce negligible discretisation errors. A set of analyses was performed with this model using a time step of $0.5\Delta z/c_p$ for each of the integration methods. Figure 5.33 shows that by 3 ms the Wilson method has caused a slight reduction in the maximum pile force, while the other two methods are in close agreement. After 19 ms the Wilson solution shows a maximum axial force 25%

less than the exact solution, while the central difference method shows increased oscillation in front of the wave (Figure 5.34). The force reduction due to the Wilson method is also evident in the toe force (Figure 5.35).

The analyses described show that the numerical damping in the Wilson method tends to smooth out higher frequency oscillations, but can cause significant attenuation of the stress wave. Although this may be acceptable in the analysis of real world problems, the aim of the present study is to obtain accurate solutions to the theoretical equations associated with pile driving. Consequently, a method containing such artificial numerical damping is not acceptable. The Wilson method was used by Smith and Chow (1982).

The explicit central difference method shows a tendency to amplify time discretisation errors when the problem contains frequencies which are close to the critical frequency. This method was used by Simons (1985), which partly explains the highly oscillatory results he obtained.

The average acceleration method shows no numerical damping, and is stable even for large time steps. For all the time-steps tested, the average acceleration results were as good as or better than the results of the central difference method. The explicit central difference method only possesses a computational advantage when lumped mass elements are used. However, when this is the case, smaller time-steps and node spacings are required to achieve accuracy equivalent to the average acceleration method.

For the reasons discussed above, the constant-average-acceleration method was selected for use in all the analyses which follow. The effect of time step on this method was examined using the accurate spatial discretisation presented previously and the hammer/cushion/anvil impact. Time steps of $\Delta z/c_p$, $0.5\Delta z/c_p$ and $0.1\Delta z/c_p$ were used.

Figure 5.37 shows little difference after 3 ms between the axial forces calculated using the different time steps. However, after 19 ms the largest time step shows noticeable errors (Figure 5.38). The error caused by the large time step is clearly visible in the graph of pile toe force (Figure 5.39), where the maximum force is 'missed'. However, there is little difference between the response predicted by time steps of $0.5\Delta z/c_p$ and $0.1\Delta z/c_p$ in any of the graphs, so a time step of $0.5\Delta z/c_p$ can be considered adequate for this problem.

5.9 The effect of radial inertia

In the first section of this chapter, assumptions were made that the radial inertia in the pile was negligible, and that the stress and strain were uniform across each cross-section. These assumptions allowed the one-dimensional wave equation to be obtained from the general equations presented in Chapter 4. This section will examine the validity of the assumptions.

Firstly, a solid circular pile will be considered. To include the vertical motion of the pile, each node is given two degrees of freedom. Three different elements are used to evaluate the effect of radial inertia on the response of the solid pile. The first two are three-noded elements with quadratic shape functions in the vertical direction and linear shape functions in the radial direction (Figure 5.41(a)). Plane sections are assumed to remain plane. The first element uses a consistent mass matrix for the vertical direction, but ignores the mass for the radial direction. The second element uses a consistent mass matrix for both directions. The third element is an eight-noded quadrilateral, which uses quadratic shape functions for all directions (Figure 5.41(b)). The stiffness and consistent mass matrices are found by integrating numerically, using four Gauss points (Zienkiwicz, 1977).

The first element closely approximates the radial displacement which accompanies the one-dimensional axial wave analysed in the previous sections. The second element is a first order approximation to the effect of radial inertia. The third element does not require plane sections to remain plane, but requires the hammer force to be distributed uniformly between the nodes at the top of the pile. Since plane sections are not required to remain plane, the third element is expected to most closely model the true effect of radial inertia.

A node spacing of 0.125 m was used for all meshes, with a time step of $0.5\Delta z/c_p$.

The results plotted in Figure 5.42 show that the addition of radial inertia slightly decreases the rise time of the axial force and fractionally delays the peak. The results obtained with the second three-node element are in reasonable agreement with those obtained with the eight-node element, but the eight-node element results show some additional oscillation in the decaying portion of the wave. Figure 5.43 shows that this force oscillation is associated with an oscillating radial displacement. The addition of radial inertia increases the maximum radial displacement by approximately 15%.

The above analyses modelled a solid pile. However, the effect of radial inertia may be more pronounced in a hollow pile, since the mass is concentrated at the edge of the pile. To model a tubular pile, three elements

analogous to those used above were selected (Figure 5.44). The first three-noded element allows radial movement, but neglects radial inertia. The second three-noded element includes radial inertia, but assumes plane sections remain plane, ignoring bending effects. The third element is eight-noded and uses quadratic shape functions for both directions. Bending and inertia in both directions are accounted for.

The properties of the elements were specified so that, for a wall thickness of 0.05 m, the pile impedance, stiffness, and axial wave velocity remained the same as those specified in Figure 5.1. Figure 5.45 shows the variation of axial force along the pile 3 ms after impact. Radial inertia is seen to have a much greater effect on the response of a hollow pile than on the response of a solid pile. The agreement between the three-noded and eight-noded radial inertia elements is not particularly good, suggesting that much of the difference is due to bending effects in the pile walls. The radial displacement of the eight-noded element model shows considerable oscillation (Figure 5.46). The toe force and head displacement graphs also show some variation between the two models, although the basic features are the same (Figures 5.47 and 5.48).

These two sets of analyses show that radial inertia affects the response of the pile, particularly when the pile is hollow. However, ignoring the radial inertia does not lead to gross errors, and reduces the amount of oscillation present in the travelling waves. In the case of hollow piles, the exact response of a particular pile is dependent on the wall thickness and the Poisson's ratio of the material, rather than just the pile impedance and wave velocity. In a study such as this, introduction of too many additional parameters is undesirable. Consequently, in the work which follows, the response of the pile will be modelled by three-noded elements which ignore the effect of axial inertia. This model will represent solid piles well, and hollow piles quite well.

5.10 Conclusions

A large number of numerical experiments have been performed to determine the appropriate element type, node spacing, integration type, and time-step size needed to accurately model the propagation of an impulse wave in a pile. The following conclusions have been drawn.

1. To obtain accurate results, a continuous impulse function with no slope discontinuity should be used, such as the hammer/cushion/anvil impulse presented in Chapter 3.

2. Three-noded quadratic rod elements with consistent mass matrices yield the most accurate results (of the three elements considered).

3. Very accurate results were obtained with 12 nodes in the rising portion of the wave, and 6 nodes gave adequate representation.

4. The constant-average-acceleration scheme is the most accurate and stable integration method of the three examined.

5. A time step of $0.5\Delta z/c_p$ is sufficient to give accurate answers.

6. Errors introduced by ignoring the effects of radial inertia are quite small, and an adequate representation of overall pile behaviour can be obtained by ignoring radial inertia and assuming plane sections remain plane. However, radial inertia and bending in thin-walled piles could significantly affect the shape of the reflected force often measured at the pile head during driving. This is an avenue for further research which will not be pursued in this thesis.

The analyses performed in this chapter assumed that the soil surrounding the pile had no stiffness and no mass. The next chapter examines the effect of finite stiffness and mass in the soil surrounding the soil shaft.

6. ELASTIC WAVE RADIATION FROM THE PILE SHAFT

6.1 Introduction

This chapter examines the propagation of elastic waves from the pile shaft into the surrounding soil. The plane strain shear and dilation waves are investigated first. A detailed investigation of finite element mesh truncation follows. Simplified models for plane strain shear and dilation wave transmission are developed in the course of this investigation. A finite element model is used to examine the effect of pile flexibility on the response, and the significance of dilation wave transmission investigated. Finally, the influence of soil under the pile toe on the shaft response is examined.

6.2 Shear wave transmission

Since the stiffness of a pile is usually far greater than the soil stiffness, as a first approximation the pile can be considered rigid (Novak, 1977). The soil surrounding the shaft will then be in a plane strain situation (Figure 6.1). Equation (4.9) can be combined with equations (4.4) and (4.6) to form an equation of motion for vertical displacement of the soil.

$$\rho_S r \frac{\partial^2 u_z}{\partial t^2} - G_S \left(r \frac{\partial^2 u_z}{\partial r^2} + \frac{\partial u_z}{\partial r} \right) - r f_z = 0 \tag{6.1}$$

The vertical displacement (u_z) is a function of r and t only. The external load (f_z) is only non-zero at the pile radius. When r is greater than R, equation (6.1) is a one-dimensional cylindrical wave equation, which can be rewritten as

$$\frac{\partial^2 u_z}{\partial t^2} = c_S^2 \left(\frac{\partial^2 u_z}{\partial r^2} + \frac{1}{r} \frac{\partial u_z}{\partial r} \right) \tag{6.2}$$

where c_S is the shear wave velocity in the soil,

$$c_S = \sqrt{\frac{G_S}{\rho_S}} \tag{6.3}.$$

This equation can be solved analytically for harmonic motion (Novak, 1977), or numerically for any exciting force. In the work which follows, three-node axisymmetric line elements with quadratic shape functions will be used to solve equation (6.2).

The propagation of axisymmetric shear waves from the pile was examined using a soil disk of unit thickness. Typical soil properties of G_S = 45 MPa and ρ_S = 2000 kg/m^3 were used. These properties are similar to those used by Simons (1985) and Smith and Chow (1982). The shear wave velocity in this soil is 150 m/s, which is much slower than the axial wave velocity in the pile analysed in the previous chapter.

The shear force applied to the soil disk by the pile was taken to have the same shape as the axial wave travelling in the pile. The ram/cushion/anvil impact of the hammer shown in Figure 5.2 was used to provide this shape. The distance between soil nodes required to ensure 12 nodes in the rising portion of the shear wave was considerably smaller than the pile node spacing, since the wave velocity was much slower. A node spacing of 0.0075 m was used. The axisymmetric disk and the corresponding finite element mesh are shown in Figure 6.2. The finite element mesh was extended to 3.25 m, and the analysis was stopped after 12 milliseconds to ensure that no erroneous boundary reflections interfered with the results.

Figure 6.3 illustrates the computed propagation of the shear wave away from the pile in terms of stress, and Figure 6.4 shows the propagation of the same wave in terms of total force. The total force was computed by integrating the stress over the cylindrical area at each radius. As the wave travelled away from the pile, the wave shape sharpened, and the peak force increased.

Researchers using finite elements to investigate pile driving (eg. Smith and Chow, 1982; Simons, 1985) have assumed that, since the stresses decrease as the wave travels away from the pile, satisfactory results can be obtained by increasing the radial node spacing in rough proportion to the radial coordinate, r. A typical mesh of this type is shown in Figure 6.2(c). The radial sizes of these elements are taken from Simons (1985).

The use of meshes with elements of varying radial size implies that dynamic analysis of piles can be accomplished with similar meshes to those used for static analysis. However, this is not the case. Although the stress wave decreases in magnitude in approximate proportion to $1/\sqrt{r}$ while travelling outwards, any reflected portion of the wave increases in magnitude when travelling back towards the pile, also in approximate proportion to $1/\sqrt{r}$.

If the size of the outer elements is increased, these elements may not be able to represent the travelling wave adequately. In this case, high frequency components of the wave will be reflected. As the reflected portion travels back towards the pile, the stress magnitude will grow, and significant distortion of the solution could occur.

As an example of this, the displacement of at the inner radius of the model shown in Figure 6.2(c) was calculated, and the response is plotted in Figure 6.5. The solution obtained previously from the accurate finite element analysis showed that the pile displacement should increase rapidly to a maximum, and then decrease relatively slowly. However, the response of the mesh with increasing radial element sizes shows considerable oscillation.

This investigation has shown that accurate analysis of a propagating shear wave can only be obtained with a mesh fine enough to represent the travelling stress wave correctly. Since the shear wave sharpens slightly as it travels away from the pile, the element size should be decreased as the radius increases, rather than vice versa. However, the sharpening is only slight, and results of sufficient accuracy can be obtained with a uniform mesh fine enough to give an adequate representation of the wave leaving the pile.

6.3 Dilation wave transmission

The expansion or contraction of a cylindrical cavity causes a wave of compression or tension to be transmitted radially. This wave may be termed an axisymmetric dilation wave. As the wave travels through the soil, stresses are generated both tangent and normal to the wave front. A pile subjected to a compressive axial wave will deflect in the radial direction, as discussed in the previous chapter. This causes an axisymmetric dilation wave to be transmitted into the soil.

Assuming plain strain, equation (4.10) can be combined with equations (4.4) and (4.9) to yield an equation of motion for the radial soil displacement.

$$\rho_S r \frac{\partial^2 u_r}{\partial t^2} - (2G_S + \lambda_S)\left(r\frac{\partial^2 u_r}{\partial r^2} + \frac{\partial u_r}{\partial r} - \frac{1}{r}u_r\right) - r f_r = 0 \qquad (6.4a)$$

Since f_r is only non-zero at the pile radius, elsewhere equation (6.4a) becomes

$$\frac{\partial^2 u_r}{\partial t^2} = \frac{2G_S + \lambda_S}{\rho_S}\left(\frac{\partial^2 u_r}{\partial r^2} + \frac{1}{r}\frac{\partial u_r}{\partial r} - \frac{1}{r^2}u_r\right) \qquad (6.4b)$$

Lame's constant for the soil (λ_S) is related to Young's modulus (E_S) and Poisson's ratio (ν_S) by

$$\lambda_S = \frac{\nu E_S}{(1+\nu_S)(1-2\nu_S)} \qquad (6.5).$$

If a displacement potential (ϕ) is defined by

$$u_r = \frac{\partial \phi}{\partial r} \quad (6.6),$$

then equation (6.5) can be rewritten as

$$\frac{\partial}{\partial r}\frac{\partial^2 \phi}{\partial t^2} = \frac{2G_S+\lambda_S}{\rho_S}\frac{\partial}{\partial r}\left(\frac{\partial^2 \phi}{\partial r^2} + \frac{1}{r}\frac{\partial \phi}{\partial r}\right) \qquad (6.7).$$

Integrating both sides with respect to r, a cylindrical wave equation in ϕ is obtained.

$$\frac{\partial^2\phi}{\partial t^2} = c_d^2 \left(\frac{\partial^2\phi}{\partial r^2} + \frac{1}{r}\frac{\partial\phi}{\partial r}\right) \tag{6.8}$$

The dilational wave velocity in the soil is

$$c_d = \sqrt{\frac{2G_s+\lambda_s}{\rho_s}} \tag{6.9}.$$

To investigate the propagating dilation wave, the soil disc and finite element mesh shown in Figure 6.2 were used. The hammer impulse function used to examine the shear wave propagation was applied again, but this time in the horizontal direction. Since the dilation wave velocity in the soil is 497 m/s, the node spacing was increased to 0.025 m, and the mesh was extended to 7.5 m to prevent any boundary reflection influencing the solution.

The calculated radial pile displacement is shown in Figure 6.6. Figure 6.7 shows the propagation of the dilation wave from the pile in terms of stress, and Figure 6.8 shows the same wave in terms of total force. Like the shear wave, the dilation wave sharpens as its distance from the pile increases, and the peak total force increases. However, unlike the shear wave, a region of tensile stress develops behind the wave as it travels away from the pile.

The displacements calculated with the mesh shown in Figure 6.2(c) (extended to 7.5 m) are also shown in Figure 6.6. Again, reflections caused by increasing the node spacings distort the solution.

Like the analysis of propagating shear waves, accurate analysis of propagating dilation waves requires a reasonably uniform mesh of sufficient fineness to model the shape of the wave transmitted from the pile.

6.4 Time-domain transmitting boundaries

In the two analyses described above, the mesh was extended far enough to ensure that the waves did not reach the boundary within the time domain of interest, preventing erroneous reflections. However, such a procedure is very limiting. Figure 6.5 indicates that the pile does not return to rest for some time, and so a much larger mesh would be required to correctly model the complete response. (In this case, the pile will never return to rest, but the analysis could be carried out until the pile was virtually at rest.) In static analyses, fixing the boundary at some point suitably distant from the region of interest allows calculation of accurate results. However, in dynamic analyses waves reflecting from a distant boundary can return with a significant amount of energy. Consequently, the finite element mesh must be truncated with a boundary which will not cause unrealistic reflection of impinging waves. There are many such boundaries available in the frequency domain, but problems involving non-linear behaviour of the solid are most readily solved in the time domain. Time-domain transmitting boundaries are therefore required for this study.

The various boundaries of this type which are in common use have been reviewed and compared by Wolf (1986). Most of these boundaries are formulated on the principle of no energy reflection from the boundary. However, such boundaries give inaccurate results when subjected to stress waves with non-zero time averages. In their paper introducing the viscous boundary (the most popular time-domain transmitting boundary), Lysmer and Kuhlemeyer (1969) warned that the boundary should only be used with loads having a vanishing time average. Loads which do not satisfy this requirement cause the finite element mesh to undergo rigid body motion. This restriction theoretically prevents the application of these boundaries to the pile driving problem. The inability of the boundary to support static load and the resulting rigid body motion prevent accurate calculation of residual stresses and absolute displacements. Nevertheless, other workers (Simons, 1985; Smith and Chow, 1982) have used boundaries which reflect no energy in the finite element analysis of pile driving, ignoring the rigid body motion.

More rigourous and generally applicable boundaries are available (see for example Engquist and Majda, 1979), but simplicity and ease of implementation has meant that the classical viscous boundary and related methods are still widely used. Frequency dependent transmitting boundaries for shear and dilation proposed by Novak (1977) and Novak and Mitwally (1988) will be discussed later.

6.4.1 A review of time-domain transmitting boundaries

Most of the transmitting boundaries reviewed by Wolf (1986) are derived on the assumption that no energy should be reflected by the boundary (ie. the boundary is a perfect absorber of energy). This is equivalent to

saying that the boundary transmits all the arriving energy into the far field, permitting no reflection from the far field. In the discussion which follows, such boundaries will be termed *zero reflection boundaries.*

The superposition boundary (Smith, 1974) is based on the principle that a free boundary reflects a wave of opposite sign to that reflected by a fixed boundary. The problem is duplicated, with a free boundary applied to one mesh and a fixed boundary applied to the other. Half of the exciting force is applied to each mesh, and the solutions are combined. The waves reflected from the boundary are of opposite signs and so cancel out. Since the reflected waves do not travel back into the mesh, usually only the part of the mesh adjacent to the boundary need be duplicated. As no energy is reflected, the superposition boundary is a zero reflection boundary.

The viscous boundary (Lysmer and Kuhlemeyer, 1969) is the simplest and the most widely used truncating boundary. The far field is replaced by distributed damping on the boundary, which absorbs almost all the energy in the impinging waves. The viscous boundary is discussed in detail in the next section. It is a zero reflection boundary in one dimension, and almost a zero reflection boundary in two dimensions.

The doubly asymptotic boundary (Underwood and Geers, 1981) converges to the correct solution as the frequency tends to zero, and also as the frequency becomes very large. A spring of appropriate stiffness is used so that, as the frequency tends to zero, the solution approaches the static solution. At high frequencies the effect of the spring is small in comparison with the effect of a dashpot, and so the second part of the solution consists of a viscous dashpot. The damping constant is identical to that used in the viscous boundary. The spring and the dashpot are combined in parallel. Since the boundary contains a spring, some energy is reflected back into the mesh.

In the paraxial method (eg. Cohen and Jennings, 1983) the boundary condition is expressed as a differential equation which only allows the propagation of waves outwards, preventing any reflection. Consequently, it is a zero reflection boundary.

The extrapolation method (Liao and Wong, 1984) prescribes the displacement of the boundary nodes by extrapolating from the displacements of adjacent nodes at preceding time steps. The waves are effectively allowed to travel through the boundary with minimal disruption. Consequently, the extrapolation method approximates a zero reflection boundary.

Several workers have compared two or more of the methods described above. Cohen and Jennings (1983) compared the paraxial method with the viscous method, and concluded that the paraxial method offered a slight increase in accuracy for a significant increase in complexity. Simons (1985) compared the superposition method with the viscous method, and found the two methods were in close agreement. Wolf (1986) used all the methods mentioned above to calculate the response of a semi-infinite bar on an elastic foundation subject to one cycle of sinusoidal loading, and compared the resulting approximations with an analytical solution. He found that, with the exception of the doubly asymptotic method, the different methods gave similar results. The doubly asymptotic method was found to cause significant reflection.

With the exception of the doubly asymptotic method, researchers have generally found the other methods are in close agreement. This should be expected, since they are all good approximations to a zero reflection boundary. Differences between them are an indication of their numerical efficiency, rather than their theoretical accuracy. The viscous boundary will now be examined in detail, since it will show characteristics common to all boundaries which model a zero reflection boundary.

6.4.2 Derivation of the viscous boundary

Consider a semi-infinite rod. The equation of motion for axial deformation of the rod may be derived by considering the dynamic equilibrium of an infinitesimal element. The x axis is taken to run along the axis of the bar, and the displacement at any point will be denoted by $u(x)$. Using E to denote Young's modulus and ρ to denote the density of the bar, the equation of motion may be written as

$$\frac{\partial^2 u}{\partial t^2} = \frac{E}{\rho} \frac{\partial^2 u}{\partial x^2} \qquad (6.10).$$

This is simply a one-dimensional wave equation in which the axial wave velocity c_p is given by

$$c_p = \sqrt{\frac{E}{\rho}} \qquad (6.11).$$

The viscous boundary is usually derived by considering the propagation of a harmonic wave (Lysmer and Kuhlemeyer, 1969), but an alternative derivation for a transient wave of arbitrary shape can be obtained with a method similar to that used by Booker (1985) to derive a transmitting boundary for a spherical dilation wave. A wave of arbitrary shape propagating along the bar in the positive x direction may be represented by

$$u(x,t) = f(x/c_p - t) \tag{6.12},$$

in which t represents the elapsed time.

Denoting the derivative of f with respect to the term in brackets by f', and treating compressive strains and stresses as positive, the strain (ε) and the stress (σ) at any point x may be expressed as

$$\varepsilon(x,t) = -\frac{\partial u}{\partial x} = -\frac{1}{c_p} f'(x/c_p - t) \tag{6.13}$$

and

$$\sigma(x,t) = E\,\varepsilon = -\frac{E}{c_p} f'(x/c_p - t) \tag{6.14},$$

At any particular x coordinate x_b, the derivative f' is identical in magnitude and opposite in sign to the time derivative $\partial f/\partial t$. The velocity at this point may therefore be expressed as

$$\frac{\partial u}{\partial t}(x_b,t) = -f'(x_b/c_p - t) \tag{6.15}.$$

Comparing equations (6.14) and (6.15), the stress at the boundary point can be related to the velocity at the boundary point as follows:

$$\sigma(x_b,t) = \frac{E}{c_p}\frac{\partial u}{\partial t}(x_b,t) = \rho\, c_p \frac{\partial u}{\partial t}(x_b,t) \tag{6.16}.$$

This is identical to the boundary restraint provided by truncating the bar and applying a viscous damper with damping constant $c = \rho\, c_p$.

A viscous boundary for shear wave propagation may be derived in a similar way. In the following equations τ represents the shear stress, G the shear modulus, and c_S the propagation velocity of the shear wave. The shear displacement at point x is represented by $v(x)$. The shear stress is

$$\tau(x_b,t) = \frac{G}{c_S}\frac{\partial v}{\partial t}(x_b,t) = \rho\, c_S \frac{\partial v}{\partial t}(x_b,t) \tag{6.17}$$

where

$$c_S = \sqrt{\frac{G}{\rho}} \tag{6.18}.$$

The viscous boundary can provide an exact model of wave transmission to the far field in any situation satisfying the one-dimensional wave equation.

6.4.3 Reflection from the far field

Axisymmetric situations involve geometrically attenuating waves. The wave equation for cylindrical shear waves is the same as the wave equation for axial waves in a wedge with linearly varying cross-sectional area, indicating that the waves attenuate at the same rate in both situations. Consequently, a simple one-dimensional bar of varying cross-sectional area can be used to illustrate the effect of a zero reflection boundary on geometrically attenuating waves.

Consider the application of an axial step load of stress intensity σ to the end of an infinitely long bar with constant cross-section. An axial stress wave will propagate down the bar at velocity c_p. The displacement of the end of the bar (u_0) may be calculated by integrating the strain over the length of the bar. At time t_1 the wave has only propagated to $x = c_p\, t_1$, so the integration need only be performed to this point.

$$u_0(t_1) = \int_0^{c_p t_1} \frac{\partial u}{\partial x} dx = \frac{\sigma}{E} c_p t_1 \qquad (6.19)$$

This equation shows that, after the step load is applied to the end of the bar, the end moves with constant velocity. The progress of the wave in the far field has no effect on the near field.

Now consider a bar consisting of two uniform cross-sections. When the wave reaches the point at which the cross-section changes, partial reflection will occur. Clearly, if this change in impedance occurs in the far field, truncating the problem to the near field with a zero reflection boundary will cause errors.

Suppose the cross-sectional area of the bar increases in small steps along the bar. Each time a wave reaches a change in impedance, part of the wave is reflected and part is transmitted. As the wave propagates into the far field, reflections from the cross-sectional changes will be transmitted back into the near field.

Now, if the cross-section of the bar varies in proportion to the distance from the end, and the steps between the impedance changes are reduced, in the limit the rod becomes a wedge with a continuous change in impedance (Figure 6.9(a)).

The equation of motion for axial waves in such a wedge is

$$\frac{\partial^2 u}{\partial t^2} = \frac{E}{\rho}\left(\frac{\partial^2 u}{\partial x^2} + \frac{1}{x}\frac{\partial u}{\partial x}\right) \qquad (6.20).$$

This equation can be solved numerically for a step excitation by Laplace transform or finite element methods. The propagation of the wave in a stepped bar (Figure 6.9(b)) can be solved by the method of characteristics.

Each length of constant cross-section is taken as an element. Each element has a unique impedance of $Z = EA/c_p$. Consequently, when a wave front passes through the interface between two elements, the magnitude of the transmitted wave will change, and a reflected wave will be generated. The magnitudes of the transmitted and reflected waves generated by a wave travelling from an element with impedance Z_1 to an element with impedance Z_2 may be computed by the following two formulae, in which v denotes the wave particle velocity (Randolph, 1989).

$$v_{transmitted} = \frac{2Z_1}{Z_1+Z_2} v_{incident} \qquad (6.21)$$

$$v_{reflected} = \frac{Z_1-Z_2}{Z_1+Z_2} v_{incident} \qquad (6.22)$$

All elements are the same length, so the time step is chosen so that the wave travels the length of an element in one time step. Whenever a wave front reaches the interface between two elements, an upwards travelling wave (up wave) and a downwards travelling wave (down wave) are generated. At any time, the up and down waves at a particular interface are dependant only on the values at the previous time of the down wave at the element interface immediately above, and the up wave at the interface immediately below. Using the subscripts u and d to represent up and down respectively, and numbering the interfaces as shown in Figure 6.9(c), the magnitudes of the up and down wavefronts at interface i can be computed with the following equations.

$$v_{d\,i}(t+\Delta t) = \frac{2Z_{i-1}}{Z_{i-1}+Z_i} v_{d\,i-1}(t) + \frac{Z_i - Z_{i-1}}{Z_{i-1}+Z_i} v_{u\,i+1}(t) \qquad (6.23)$$

$$v_{u\,i}(t+\Delta t) = \frac{2Z_i}{Z_{i-1}+Z_i} v_{u\,i+1}(t) + \frac{Z_{i-1} - Z_i}{Z_{i-1}+Z_i} v_{d\,i-1}(t) \qquad (6.24)$$

The variables in the scheme are the magnitudes of the up and down waves at each interface. The process can be initiated by introducing a step wave at the top of the wedge. The above equations can then be used for each interface at each time step. The velocity at the end of the bar can by found by summing the contribution of each wave front, and the displacement by integrating this velocity with time.

The results of several such analyses are shown in Figure 6.10. As the size of the elements is decreased, the solution approaches the exact solution for a wedge.

The above analyses show that a continuous variation of impedance can be modelled by a discrete series of impedance changes. Discrete changes in impedance in the far field cause a discrete series of reflections into the near field, so evidently a continuous variation in impedance results in continuous reflection from a wave front in the far field. If a zero reflection boundary is used to truncate the problem, preventing the reflection from the far field, the velocity of the end of the bar tends to a constant value. The results from an analysis with a truncated mesh are shown in Figure 6.11.

This study has shown that the rigid body motion of an axisymmetric finite element meshes truncated with zero reflection boundaries is caused by the prevention of far field reflection. Zero reflection boundaries are clearly inappropriate in such situations.

6.5 A transmitting boundary for axisymmetric shear waves

6.5.1 Derivation of a shear boundary

The viscous boundary condition is based on an expression which relates the internal stress at a particular point in a one dimensional medium to the velocity at that point (equation 6.16). This expression does not hold for the propagation of cylindrical waves. However, a similar expression can be found by considering the form of a travelling cylindrical wave.

A cylindrical shear wave travelling radially decreases in magnitude. An exact expression for the form of a cylindrical wave cannot be found, but (for intermediate values of wave front position) the form of a cylindrical wave may be closely approximated (Whitham, 1974) by

$$v(r,t) = \frac{1}{\sqrt{r}} f(r/c_S - t) \tag{6.25},$$

where v is used to represent the horizontal displacement.

The validity of this approximation is demonstrated in Figure 6.3, where the shear wave is shown to decrease in proportion to $1/\sqrt{r}$.

Denoting the derivative of f with respect to the term in brackets by f', the shear strain and the stress at any radius r may be found:

$$\gamma(r,t) = -\frac{\partial v}{\partial r} = \frac{1}{2r^{3/2}} f - \frac{1}{c_S \sqrt{r}} f' \tag{6.26}$$

$$\tau(r,t) = G\,\gamma = G\left(\frac{1}{2r^{3/2}} f - \frac{1}{c_S \sqrt{r}} f'\right) \tag{6.27}.$$

At any particular radius r_b, the derivative f' is identical in magnitude and opposite in sign to the time derivative $\partial f/\partial t$. The velocity at this point may therefore be expressed as

$$\frac{\partial v}{\partial t}(r_b,t) = -\frac{1}{\sqrt{r_b}} f'(r_b/c_S - t) \tag{6.28}.$$

Comparing equations (6.25), (6.27), and (6.28), the stress at the boundary point can be related to the boundary velocity and displacement as follows.

$$\tau(r_b,t) = G\left(\frac{1}{2r_b} v(r_b,t) + \frac{1}{c_S}\frac{\partial v}{\partial t}(r_b,t)\right) \tag{6.29}$$

$$= \frac{G}{2r_b} v(r_b,t) + \rho\, c_S \frac{\partial v}{\partial t}(r_b,t) \tag{6.30}$$

This is equivalent to a viscous dashpot with a distributed damping constant of ρc_S (identical to a viscous boundary) and a distributed spring constant of $G/2r_b$. This boundary equation is only approximate, relying on the accuracy of equation (6.25). When subjected to a static load, the new boundary predicts a limiting displacement as time tends to infinity. In contrast, the exact solution indicates no limiting displacement.

6.5.2 Response of the boundaries to hammer impact

The abilities of the viscous boundary and the new boundary to transmit plain strain shear waves were compared by analysing the problem shown in Figure 6.2(a). The hammer impulse function detailed previously was applied at the pile radius of 1 m. A mesh of the fineness shown in Figure 6.2(b) was used. A solution without truncation effects was calculated by extending the mesh to 7 m, preventing any boundary reflection before 40 ms.

The mesh was then truncated at a radius of 2 m with a viscous boundary. The effect of this truncation on the displacement at the pile is shown in Figure 6.12. Comparing the truncated solution with the solution resulting from the extended finite element mesh, the displacement of the truncated mesh is accurate until the wave reflected from the boundary returns to the pile at approximately 13 ms. The displacement subsequently tends to a constant value, instead of falling slowly to zero. This indicates that the entire mesh has undergone rigid body displacement.

When the mesh was truncated at 2 m with the new boundary, rigid body displacement was no longer observed. The displacement of the pile calculated with this truncation is also shown in Figure 6.12. After the wave reflected from the boundary reaches the pile, the displacement is slightly less than the correct solution. This is caused by the non-zero static stiffness of the new boundary. However, the new boundary approximates the correct behaviour much more closely than the viscous boundary.

A more severe test was performed by applying the boundaries directly to the side of the pile, eliminating the finite element mesh entirely. The displacements calculated in this way are shown in Figure 6.13. The viscous boundary caused a large rigid body displacement, but the new boundary estimated the maximum displacement extremely well. At larger times the new boundary slightly underestimated the displacement.

6.5.3 Exact solution for harmonic shear waves

An exact frequency dependent solution for harmonic axisymmetric shear waves has been presented by Novak (1977). When a long rigid pile is undergoing complex harmonic oscillation, the displacement and the shear stress at the pile radius (R) are related by a complex stiffness coefficient, which is a function of the angular frequency, ω.

$$\tau(R,t) = k_z(\omega)\, v(R,t) \tag{6.31}$$

The complex stiffness can be conveniently expressed in real and imaginary components as

$$k_z(\omega) = \frac{G}{2R}\left(S_{z1}(a_S) + \mathrm{i}\, S_{z2}(a_S)\right) \tag{6.32}$$

S_{z1} and S_{z2} are functions of the dimensionless frequency,

$$a_S = \frac{\omega R}{c_S} \tag{6.33}$$

and can be expressed in terms of Bessel functions of the first and second kind.

$$S_{z1}(a_S) = 2\, a_S \frac{J_1(a_S)\, J_0(a_S) + Y_1(a_S)\, Y_0(a_S)}{J_0^2(a_S) + Y_0^2(a_S)} \tag{6.34}$$

$$S_{z2}(a_S) = \frac{1}{\pi}\, \frac{4}{J_0^2(a_S) + Y_0^2(a_S)} \tag{6.35}$$

Dimensionless frequencies associated with the rising portion of the hammer impulse used in this chapter range up to approximately 20. Parameters S_{z1} and S_{z2} are plotted against dimensionless frequency in Figures 6.14 and 6.15.

6.5.4 Comparison of the new boundary with the harmonic solution.

The stiffness and damping terms of the new boundary can be combined to form a complex stiffness.

$$k_z = \frac{G}{2R} + \mathrm{i}\, \rho\, c_S\, \omega = \frac{G}{2R}\,(1 + \mathrm{i}\, 2a_S) \tag{6.36}$$

The real and imaginary stiffness parameters can then be identified.

$$S_{z1} = 1 \quad , \quad S_{z2} = 2\, a_s \tag{6.37}$$

These parameters are plotted against dimensionless frequency in Figures 6.14 and 6.15. The S_{z1} parameter of the new boundary is constant with frequency, and represents the limit approached by the Novak's S_{z1} as the frequency tends to infinity. Above a dimensionless frequency of 4, there is very little difference between the new boundary and the exact solution.

The difference between equation (6.35) and the S_{z2} of the new boundary is very small, especially at high dimensionless frequencies.

This comparison of the new boundary with the exact solution of Novak (1977) has shown that the new boundary accurately models the far field when the applied load contains high dimensionless frequencies. However, at lower frequencies the new boundary exhibits slightly too much in-phase stiffness.

6.5.5 Previous use of the harmonic solution

Meynard and Corte (1984) and Simons (1985) used the harmonic solution of Novak (1977) to obtain spring and damping constants for modelling radiation from a pile shaft (but not as a truncating boundary for finite element analysis). The constants were obtained by drawing a line of best fit through the plots of S_{z1} and S_{z2} provided by Novak (1977). The equivalent values obtained by Simons were

$$S_{z1} = 0.9 \quad \text{and} \quad S_{z2} = 2\, a_s \tag{6.38}.$$

Simon's S_{z1} was lower than the new boundary, because the plot of S_{z1} presented by Novak was for the range a_s = 0 to 3. Meynard and Corte obtained parameters identical to the new boundary.

6.5.6 Summary

A new shear boundary has been derived by considering the propagation of a wave of arbitrary shape and duration. Unlike the viscous boundary, the new boundary reflects some energy back into the near field, modelling the reflection from the far field occurring in the axisymmetric situation. Numerical experiments have shown that the new boundary out-performs the viscous boundary when subjected to transient waves. The effective dynamic stiffness of the new boundary under harmonic loading was compared with the exact solution, and the new boundary was found to provide an excellent model, particularly at high dimensionless frequencies. Even when the force was applied directly to the boundary, the computed response was close to the correct solution. The boundary can therefore be used to model shear wave transmission from piles without resorting to finite elements.

6.6 A transmitting boundary for axisymmetric dilation waves

6.6.1 Derivation of a dilation boundary

In equations (6.4) to (6.9), the equation of motion for axisymmetric dilation waves was shown to reduce to a cylindrical wave equation in a potential function ϕ, where

$$u = \frac{\partial \phi}{\partial r} \tag{6.39}.$$

As discussed in the section about cylindrical shear waves, an exact expression for the form of a cylindrical wave cannot be found, but can be approximated by

$$\phi(r,t) = \frac{1}{\sqrt{r}} f(r/c_d - t) \tag{6.40}.$$

The algebra which follows is based on Booker's (1985) solution for spherical dilation waves. Denoting the derivative of f with respect to the term in brackets by f', the displacement, strain and stress may be related to f at any radius r.

$$u(r,t) = \frac{\partial \phi}{\partial r} = \frac{-1}{2r^{3/2}} f + \frac{1}{c_d \sqrt{r}} f' \tag{6.41}$$

$$\sigma_r(r,t) = 2G\varepsilon_r + \lambda(\varepsilon_r + \varepsilon_\theta)$$

$$= (2G + \lambda)(\varepsilon_r + \varepsilon_\theta) - 2G\,\varepsilon_\theta \tag{6.42}$$

$$\varepsilon_r + \varepsilon_\theta = -\frac{\partial u}{\partial r} - \frac{u}{r}$$

$$= -\frac{\partial^2 \phi}{\partial r^2} - \frac{1}{r}\frac{\partial \phi}{\partial r}$$

$$= -\frac{1}{c_d^2}\frac{\partial^2 \phi}{\partial t^2} \tag{6.43}$$

$$\varepsilon_\theta = -\frac{u}{r} = \frac{1}{2r^{5/2}} f - \frac{1}{c_d r^{3/2}} f' \tag{6.44}$$

$$\sigma_r(r,t) = (2G + \lambda)\left(-\frac{1}{c_d^2}\frac{\partial^2 \phi}{\partial t^2}\right) - 2G\left(\frac{1}{2r^{5/2}} f - \frac{1}{c_d r^{3/2}} f'\right) \tag{6.45}$$

At any particular radius r_b, the derivatives of f with respect to time are the negative of derivatives with respect to its argument. The displacement, velocity, and acceleration at r_b may be expressed as

$$u(r_b,t) = \frac{-1}{2r_b^{3/2}} f(r_b,t) + \frac{1}{c_d\sqrt{r_b}} f'(r_b,t) \tag{6.46},$$

$$\frac{\partial u}{\partial t}(r_b,t) = \frac{1}{2r_b^{3/2}} f'(r_b,t) - \frac{1}{c_d\sqrt{r_b}} f''(r_b,t) \tag{6.47},$$

$$\frac{\partial^2 u}{\partial t^2}(r_b,t) = \frac{-1}{2r_b^{3/2}} f''(r_b,t) + \frac{1}{c_d\sqrt{r_b}} f'''(r_b,t) \tag{6.48}.$$

The second time derivative of the potential at r_b is

$$\frac{\partial^2 \phi}{\partial t^2}(r_b,t) = \frac{1}{\sqrt{r_b}} f''(r_b,t) \tag{6.49}.$$

The stress at the boundary can be found in terms of $f(r_b,t)$ by substituting equation (6.49) into equation (6.45).

$$\sigma_r(r_b,t) = (2G + \lambda)\left(\frac{-1}{V_d^2\sqrt{r_b}} f''\right) - 2G\left(\frac{1}{2r_b^{5/2}} f - \frac{1}{c_d r_b^{3/2}} f'\right)$$

$$= \frac{2G}{r_b}\left(u(r_b,t) - \frac{(2G+\lambda)r_b}{2G}\frac{1}{c_d^2\sqrt{r_b}} f''\right) \tag{6.50}$$

Differentiating this equation with respect to time,

$$\frac{\partial \sigma_r}{\partial t}(r_b,t) = \frac{2G}{r_b}\left(\frac{\partial u}{\partial t}(r_b,t) + \frac{(2G+\lambda)r_b}{2G}\frac{1}{c_d^2\sqrt{r_b}} f'''\right) \tag{6.51}.$$

Combining these two equations, all reference to the unknown function f can be removed. All quantities are evaluated at r_b.

$$\sigma_r + \frac{2r_b}{c_d}\frac{\partial \sigma_r}{\partial t} = \frac{2G}{r_b}\left(u + \frac{2r_b}{c_d}\frac{\partial u}{\partial t} + \frac{r_b^2}{c_d^2}\frac{2G+\lambda}{G}\frac{\partial^2 u}{\partial t^2}\right) \tag{6.52}$$

Equation (6.52) is independent of the form of the wave. Like the shear boundary derived above, this boundary condition approximates the effect of the far field.

6.6.2 Equivalent spring/dashpot/mass model

Unlike the boundaries discussed previously, equation (6.52) contains a time derivative of the boundary stress. The boundary can be used in a finite element analysis by integrating the boundary equations numerically in time. However, the boundary can be implemented more conveniently if it is represented by a spring/dashpot/mass model. The terms can then be assembled into the finite element matrices, as can the other boundaries. Wolf (1988) presents a spring/dashpot/mass model for spherical dilation waves. The model is shown in Figure 6.16. The axisymmetric dilation boundary can be modelled in the same way, but with different values for the mass, spring and dashpot.

The equations of motion for the model shown in Figure 6.16 are

$$k\,u_1 + c\,(\dot{u}_1 - \dot{u}_2) = f \tag{6.53}$$

$$m\,\ddot{u}_2 + c\,(\dot{u}_2 - \dot{u}_1) = 0 \tag{6.54}.$$

From equation (6.53)

$$\dot{u}_2 = \frac{1}{c}\,(k\,u_1 + c\,\dot{u}_1 - f) \tag{6.55}.$$

Differentiating with respect to time,

$$\ddot{u}_2 = \frac{1}{c}\,(k\,\dot{u}_1 + c\,\ddot{u}_1 - \dot{f}) \tag{6.56}.$$

Substituting equations (6.55) and (6.56) into (6.54), a single equation of motion can be formed.

$$f + \frac{m}{c}\dot{f} = k\left(u_1 + \frac{m}{c}\,\dot{u}_1 + \frac{m}{k}\,\ddot{u}_1\right) \tag{6.57}.$$

Equating equations (6.52) and (6.57), expressions can be found for the equivalent distributed stiffness, damping and mass.

$$m = 2\,\rho_s\,r_b\,,\quad c = \rho_s\,c_d\,,\quad k = \frac{2\,G_s}{r_b} \tag{6.58}$$

The values of the constants for spherical dilation waves presented by Wolf (1988) are

$$m = 4\,\rho_s\,r_b\,,\quad c = \rho_s\,c_d\,,\quad k = \frac{4\,G_s}{r_b} \tag{6.59}.$$

Inspecting equation (6.52), as time tends to infinity, all the time derivatives will tend to zero, leaving

$$\sigma_r = \frac{2G_s}{r_b}\,u_r \tag{6.60}$$

The spring constant derived in equation (6.58) can therefore be identified as the static spring stiffness.

Since the axisymmetric dilation problem has a static solution, a doubly asymptotic boundary can also be formulated. This boundary consists of the spring and dashpot in equation (6.58) placed in parallel. In the following section, the accuracy of the new boundary will be compared with the accuracy of the viscous boundary and the doubly asymptotic boundary.

6.6.3 Response of the boundaries to hammer impact

To compare the effectiveness of the boundaries, the plain strain axisymmetric disk shown in Figure 6.2(a) was used again. This time the hammer impulse was applied in the radial direction. Initially a Poisson's ratio of 0.45 was used, with a node spacing of 0.025 m. A solution with no truncation effects was computed by extending the mesh to 25 m, ensuring that no boundary reflection occurred before 40 ms.

Placing the truncating boundaries at a radius of 2 m, the displacements shown in Figure 6.17 were obtained. The viscous boundary gave better results than the doubly asymptotic boundary, but the new boundary approximated the effect of the far field far better than either of the other boundaries. As the dilation wave

propagated into the far field, the pile displacement became negative. This effect was only modelled correctly by the new boundary.

When the truncating boundaries were placed at the pile radius, the displacements plotted in Figure 6.18 were calculated. The viscous boundary caused non-zero terminal displacement of the pile, and the response of the asymptotic boundary was much too stiff. The new boundary gave a reasonable approximation of the response of the extended mesh, although the estimated maximum and minimum displacements were slightly high.

The response of an axisymmetric disc to radial impact is dependent of the Poisson's ratio of the soil. The analyses described above were performed with a Poisson's ratio of 0.45, which is common in pile driving situations. For completeness, the behaviour of the boundaries with a Poisson's ratio of 0.25 was also investigated. The displacements caused by truncating the mesh at a radius of 2 m are shown in Figure 6.19. Since the velocity of the dilation wave was reduced, the boundary reflections took longer to reach the pile, and the performance of all the boundaries was improved. The new boundary still provided the best approximation of the far field response.

The hammer impact was also applied directly to the boundary models at a radius of 1 m with a Poisson's ratio of 0.25. The displacements presented in Figure 6.20 were calculated. The new boundary modelled the response of the extended mesh extremely well. The response of the other two boundaries was still unsatisfactory.

6.6.4 Exact boundary for harmonic dilation waves

A transmitting boundary for harmonic axisymmetric plane strain dilation waves has been presented by Novak and Mitwally (1988).

The Novak boundary is specified in terms of a frequency dependent complex spring constant k_r. This complex stiffness can be written in terms of two parameters, S_{r1} and S_{r2}, which are functions of the dimensionless frequency of the load and the Poisson's ratio of the soil.

$$\sigma(R,t) = k_r(\omega,\nu)\, v(R,t) = \frac{G}{2R}\,(S_{r1}(a_s,\nu) + \mathrm{i}\, S_{r2}(a_s,\nu))\, v(R,t) \tag{6.61}$$

The parameters S_{r1} and S_{r2} can be expressed in terms of Bessel functions of the first and second kind, orders 0 and 1.

$$S_{r1}(a_s,\nu) = 1 - \frac{1}{2}\eta^2 a_d \frac{J_1(a_d)\,J_0(a_d) + Y_1(a_d)\,Y_0(a_d)}{J_1^2(a_d) + Y_1^2(a_d)} \tag{6.62}$$

$$S_{z2}(a_s,\nu) = \frac{1}{2}\eta^2 a_d \frac{J_0(a_d)\,Y_1(a_d) - Y_0(a_d)\,J_1(a_d)}{J_1^2(a_d) + Y_1^2(a_d)} \tag{6.63}$$

$$\eta = \sqrt{\frac{2(1-\nu)}{1-2\nu}} = \frac{c_d}{c_s} \tag{6.64}$$

$$a_d = \frac{a_s}{\eta} \tag{6.65}$$

The variation of S_{r1} with dimensionless frequency for various Poisson's ratios is shown in Figure 6.21, and the variation of S_{r2} is shown in Figure 6.22.

6.6.5 Comparison of the new boundary with the harmonic boundary

To compare the new boundary with the exact solution for harmonic waves, the complex stiffness of the boundary model shown in Figure 6.16 must be obtained. Expressing the complex stiffness in terms of two unknown real functions of the applied frequency and the model parameters, the system response can be expressed as

$$f(t) = (A(\omega,m,c,k) + \mathrm{i}\, B(\omega,m,c,k))\, u_1(t) \tag{6.66}$$

or

$$u_1(t) = \frac{A - i B}{A^2+B^2} f(t) \tag{6.67}$$

In the algebra which follows, the dependence of A and B on the model parameters and the excitation frequency is implied.

Although the second degree of freedom of the model does not enter into equation (6.66), the complex stiffness relating the second degree of freedom to the exciting force must be introduced to permit the functions A and B to be found. The complex stiffness of the second degree of freedom will be expressed in terms of real functions C and D, again dependent on the excitation frequency and the model parameters.

$$f(t) = (C(\omega,m,c,k) + i\, D(\omega,m,c,k))\, u_2(t) \tag{6.68}$$

or

$$u_2(t) = \frac{C - i D}{C^2+D^2} f(t) \tag{6.69}$$

The complex harmonic force applied to the system can be represented by

$$f(t) = f\, e^{i\omega t} \tag{6.70}$$

The time derivatives of the two degrees of freedom can then be found.

$$\dot{u}_1(t) = \frac{A - i B}{A^2+B^2} i\, \omega f\, e^{i\omega t} \tag{6.71}$$

$$\ddot{u}_1(t) = \frac{A - i B}{A^2+B^2} (-\omega^2 f\, e^{i\omega t}) \tag{6.72}$$

$$\dot{u}_2(t) = \frac{C - i D}{C^2+D^2} i\, \omega f\, e^{i\omega t} \tag{6.73}$$

$$\ddot{u}_2(t) = \frac{C - i D}{C^2+D^2} (-\omega^2 f\, e^{i\omega t}) \tag{6.74}$$

Substituting these equations into the equations of motion for the model (equations (6.53) and (6.54)),

$$\left(k \frac{A - i B}{A^2+B^2} + i\, c\, \omega \left(\frac{A - i B}{A^2+B^2} - \frac{C - i D}{C^2+D^2}\right)\right) f\, e^{i\omega t} = f\, e^{i\omega t} \tag{6.75}$$

$$\left(-m\, \omega^2 \frac{C - i D}{C^2+D^2} + i\, c\, \omega \left(\frac{C - i D}{C^2+D^2} - \frac{A - i B}{A^2+B^2}\right)\right) f\, e^{i\omega t} = f\, e^{i\omega t} \tag{6.76}$$

Dividing by $f(t)$, separating real and imaginary parts, and dividing the imaginary equations by i, four real equations in A, B, C and D result.

$$\frac{k\, A}{A^2+B^2} + c\, \omega \left(\frac{B}{A^2+B^2} - \frac{D}{C^2+D^2}\right) = 1 \tag{6.77}$$

$$\frac{-k\, B}{A^2+B^2} + c\, \omega \left(\frac{A}{A^2+B^2} - \frac{C}{C^2+D^2}\right) = 0 \tag{6.78}$$

$$\frac{-m\, \omega^2\, C}{C^2+D^2} + c\, \omega \left(\frac{D}{C^2+D^2} - \frac{B}{A^2+B^2}\right) = 0 \tag{6.79}$$

$$\frac{m\, \omega^2\, D}{C^2+D^2} + c\, \omega \left(\frac{C}{C^2+D^2} - \frac{A}{A^2+B^2}\right) = 0 \tag{6.80}$$

Solving these equations simultaneously yields the functions A, B, C and D.

$$A(\omega,m,c,k) = k\left(\frac{c^2 + \left(m^2 - \frac{mc^2}{k}\right)\omega^2}{c^2 + m^2\,\omega^2}\right) \tag{6.81}$$

$$B(\omega,m,c,k) = \frac{m^2\,c\,\omega^3}{c^2 + m^2\,\omega^2} \tag{6.82}$$

$$C(\omega,m,c,k) = k - m\,\omega^2 \tag{6.83}$$

$$D(\omega,m,c,k) = \frac{m\,k\,\omega}{c} \tag{6.84}$$

The functions C and D are of no interest, but A and B can now be related to the stiffness parameters, S_{r1} and S_{r2}.

$$k_r = A + \mathrm{i}\,B = \frac{2G_s}{r_b}(S_{r1} + \mathrm{i}\,S_{r2}) \tag{6.85}$$

From equation (6.58), the spring stiffness of the dilation boundary model is equal to the static stiffness $2G_s/r_b$, so

$$S_{r1} = \frac{A}{k} \quad \text{and} \quad S_{r2} = \frac{B}{k} \tag{6.86}.$$

Expressing the mass and damping coefficients as

$$m = \alpha\,\rho\,r_b \quad \text{and} \quad c = \beta\,\rho\,c_d \tag{6.87}$$

where, from equation (6.58), $\alpha = 2$ and $\beta = 1$, S_{r1} and S_{r2} can be found in terms of a_s and ν. The terms η and a_d are related to ν and a_s by equations (6.64) and equations (6.65).

$$S_{r1} = \frac{1 + \left(\left(\frac{\alpha}{\beta}\right)^2 - \frac{\alpha\eta^2}{2}\right)a_s^2}{1 + \left(\frac{\alpha}{\beta}\right)^2 a_d^2} \tag{6.88}$$

$$S_{r2} = \frac{1}{2}\,\frac{\frac{\alpha^2\eta^2}{\beta}\,a_d^3}{1 + \left(\frac{\alpha}{\beta}\right)^2 a_d^2} \tag{6.89}$$

These functions are plotted against a_s for various Poisson's ratios in Figures 6.21 and 6.22. Comparing these functions with the exact solutions obtained by Novak, the limits as a_s tends to zero and tends to infinity are identical. In between these limits, the new boundary provides a reasonable approximation of S_{r1}. The approximation is better for lower Poisson's ratios, and is always less than the exact solution. This corresponds with the observations made previously when the response of the boundary to impact loading was calculated. The approximation of S_{r2} is extremely good, especially at high dimensionless frequencies.

The new boundary provides a good approximation of the response of the far field to harmonic loads, although the displacement at low to mid-range dimensionless frequencies is slightly overestimated.

6.6.6 Matching the new boundary to the harmonic boundary

If the new boundary is subjected to harmonic loads of known frequency content, the accuracy of the approximation can be improved by adjusting the values of the stiffness and mass parameters. The values of S_{r1} and S_{r2} for the boundary can be matched to the exact quantities given by equations (6.62) and (6.63) for the

maximum excitation frequency. The boundary then provides better approximation over the lower frequencies than the unmatched boundary.

The matching can be performed by evaluating S_{r1} and S_{r2} at the desired dimensionless frequency, a_s'. The mass and damping coefficients required to match the new boundary at this frequency can then be found by solving equations (6.88) and (6.89) simultaneously, yielding

$$\alpha = 2 \frac{S_{r1}^2(a_s') + S_{r2}^2(a_s') - 2S_{r1}(a_s') + 1}{(1 - S_{r1}(a_s'))\, \eta^2\, a_d'^2} \tag{6.90}$$

$$\beta = \frac{1 - S_{r1}(a_s')}{S_{r2}(a_s')}\, a_d'\, \alpha \tag{6.91}$$

The stiffness parameters resulting from matching the boundary at $a_s = 5$ and $\nu = 0.45$ are shown in Figures 6.23 and 6.24,. The error at frequencies lower than 5 is reduced, but the error at higher frequencies is increased.

6.6.7 Summary

An approximate truncating boundary for plane strain axisymmetric dilation waves has been derived, and an equivalent distributed mass/spring/dashpot model obtained. When subjected to hammer impact loading, the new boundary was found to out perform the viscous boundary and the doubly asymptotic boundary. The new boundary performed well even when applied directly to the pile shaft, and could be used to represent dilation wave transmission from piles without resorting to finite elements.

The complex stiffness of the new boundary to harmonic excitation was derived, and was compared with the exact complex stiffness derived by Novak and Mitwally (1988). Although the boundary was found to represent the exact complex stiffness reasonably well, a method of improving the boundary for excitation of known harmonic content was also presented.

6.7 Shear interaction between layers

The analyses described so far in this chapter have treated each infinitesimal layer of soil independently, assuming no interaction occurred between the layers. When the pile is rigid, and there is no soil beneath the depth of the pile, this assumption is valid. However, since real piles have a finite stiffness, there will be some interaction between the soil layers. To determine the significance of this interaction, the propagation of a stress wave in a semi-infinite pile passing through a 5 m soil layer was considered.

Radial shear waves are caused by the axial wave moving down the pile. Each infinitesimal soil layer is excited before the underlying layer. Consequently, the underlying layer offers some vertical support. This causes vertical stress waves to propagate in the soil. The wave speed of axial waves in the soil is slightly greater than that of shear waves, and so the vertical size of the finite elements used to model the vertical wave propagation can be larger than the radial size. In the analysis which follows, eight-noded quadratic elements with four Gauss points were used. To allow approximately 6 nodes in the rising portion of the shear and axial stress waves, the radial size of the soil elements was 0.03 m, and the vertical size was 0.05 m.

Earlier in this chapter, a shear wave truncating boundary was shown to closely approximate the effect of an independent axisymmetric soil disc. Applying this boundary along the length of the pile shaft creates a one-dimensional model which closely approximates the effect of independent soil layers.

The finite element mesh and the one-dimensional approximation are shown in Figure 6.25. Analysis was carried out for 8 ms, and the pile displacement and force at the pile head and 5 m below the head were recorded. The displacements are presented in Figure 6.26, and the forces in Figure 6.27. The one-dimensional model yielded results which were extremely close to those resulting from the full finite element analysis, indicating that there was very little interaction between the soil layers. The minimal interaction between the soil layers was expected, as in all practical situations the axial stiffness of the pile is much greater than that of the soil.

6.8 Dilation wave transmission

The significance of dilation wave transmission from the pile was investigated using the finite element model of the surrounding soil described above. Rod elements with radial degrees of freedom but no radial inertia (Figure 5.41(a)) were used to model the pile. This model allowed interaction between the dilation and shear waves in the soil. However, the results of the analysis (Figures 6.26 and 6.27) showed no significant difference from those

obtained when the dilation wave transmission was ignored. The minimal influence of dilation wave transmission was expected, since the vertical soil displacement is much larger than the radial displacement.

6.9 Interaction with base

Near the pile base, the shear wave from the pile shaft interacts with the stress wave emanating from the pile base. The extent of this interaction above the pile toe was examined by analysing a 5 m pile embedded by varying amounts in a finite element mesh. The soil along the pile shaft above the mesh was modelled with the truncating shear boundary. Three of these models are shown in Figure 6.28. The truncating boundary closely approximates the situation of no interaction between the soil layers, so any difference between the complete finite element model and the partial model indicates substantial interaction between the shear wave and the base stress wave over the height of the mesh.

The analyses were performed for 6 ms. For each analysis, the displacement was recorded at the pile head and the force at the pile toe. The results are presented in Figures 6.29 and 6.30. These figures show that there was little change in the results when the truncating boundary was replaced by varying amounts of finite element mesh above the toe. Consequently, little interaction between the soil at the pile toe and the soil along the pile shaft is evident. The response of the soil under the pile toe can therefore be examined independently.

6.10 Conclusions

The investigation of axisymmetric plane strain shear and dilation waves revealed that as a stress wave travels away from a pile, the shape of the wave sharpens. Although the magnitude of the stress decreases as the wave travels, any reflections increase in magnitude as they approach the pile. Consequently, increasing the node spacing in proportion to the distance from the pile (in the manner often used for static pile analysis) is inappropriate, and was shown to lead to significant errors.

Since it is impractical in most cases to extend the finite element mesh to the maximum extent of stress wave travel, appropriate transmitting boundaries must be used to truncate the mesh. Most previous finite element work concerning pile driving used the standard viscous boundary to truncate the mesh. However, this boundary was shown to be unsuitable for use in axisymmetric situations. Alternative boundaries were presented for shear and dilation wave transmission. These boundaries were shown to accurately represent the behaviour of an extended finite element mesh, even when applied at the pile shaft with no finite element mesh.

The possibility of significant interaction between the shear layers along the length of the pile was investigated, but the interaction was found to be negligible. The effect of dilation wave transmission from the pile shaft was also found to be very small. Interaction between the shaft shear wave and the stress wave emanating from the pile toe was examined, but no significant influence was found.

This chapter showed that a truncating shear boundary applied along the length of a pile shaft is an excellent model of the elastic shear wave transmission, and that the dilation wave transmitted from the shaft can safely be ignored. In the next chapter, the elastic stress wave emanating from the pile toe will be examined in detail.

7. ELASTIC WAVE RADIATION FROM THE PILE TOE

7.1 Introduction

This chapter examines the propagation of elastic waves from the pile toe. The previous chapter showed little interaction between the shear waves radiating from the pile shaft and the stress wave generated at the pile toe. In simplified methods of pile analysis, the response of the soil at the pile toe is usually treated independently to the soil along the pile shaft (Figure 7.1). The pile toe is often modelled as a rigid circular footing on an elastic half-space (e.g. Simons and Randolph, 1986). This chapter commences with a finite element analysis of a rigid footing subjected to a typical hammer impact. Three-dimensional stress plots are produced to illustrate the propagation of stress waves in the soil mass, and the significant features are examined.

Analytical solutions for the response of a rigid circular footing to harmonic loads are then examined. These analytical solutions allow calculation of a frequency dependent complex compliance for the footing. Calculation of complex compliance and stiffness from a finite element mesh is considered, and a new method of obtaining the complex compliance from the response of a mesh to a transient load is introduced.

The effects of different truncating boundaries on the footing response and the compliance are examined, together with an investigation of the effect of Poisson's ratio of the soil. The effect of friction on the base of the footing is calculated.

Existing one-dimensional models of footing response are evaluated in terms of their complex stiffness. A new model is proposed which agrees well with the complex compliance and stiffness computed using finite elements over a wide range of dimensionless frequencies.

The effect of pile embedment is evaluated. The interaction of the soil reaction with the pile impedance is examined, and finally the elastic response of the entire pile/soil system is investigated.

7.2 Footing response to hammer impact

To examine the propagation of stress waves from a circular rigid footing, the impact force of the hammer shown in Figure 7.2(a) was applied to a massless rigid footing with a radius of 0.9 m bonded to a uniform elastic half-space with G_S = 45 MPa, ν_S = 0.45, and a density of 2000 kg/m^3. The finite element mesh shown in Figure 7.2(b) was used, truncated with standard viscous boundaries. As discussed above, such boundaries lead to rigid body motion of the mesh. However, the object of this analysis was to examine the stress waves in the soil, and so the long term response of the mesh was not important.

The propagation of stress waves in an axisymmetric half-space can be visualised when the stresses are plotted as surface graphs at regular time intervals. Figure 7.3 shows the relationship between the three-dimensional surface plots (presented subsequently) and the finite element mesh. Stresses were computed and plotted at the element Gauss points. The edge of the footing can usually be identified on the surface graphs by a stress spike.

Figures 7.4 to 7.7 present surface plots of the vertical, shear, radial, and Von Mises generalised shear stresses at times of 2, 4, 6 and 8 milliseconds. The Von Mises generalised shear stress ($\bar{\sigma}$) is related to the other stresses by

$$\bar{\sigma} = \sqrt{1/2(\sigma_z - \sigma_r)^2 + 1/2(\sigma_z - \sigma_r)^2 + 1/2(\sigma_z - \sigma_r)^2 + 3\tau_{rz}^2} \ .$$

Figures 7.4 to 7.7 clearly show the propagation of two distinct waves with different velocities, identifiable as the dilation wave (or P-wave) and the shear wave (or S-wave). Although a surface (or Rayleigh) wave must be present, distinguishing this wave from the shear wave is difficult, as the two wave velocities are approximately the same (Lysmer and Kuhlmeyer, 1969).

The dilation wave has two notable features. Firstly, the wave travels downwards from the footing, and only shows a small amount of radial dispersion. The stresses at the side boundary caused by the dilation wave are small. This is indicated by both the vertical and generalised stress plots. Consequently, reflections from the side boundaries of the mesh are determined by the shear wave travel time, rather than the dilation wave travel time. The concentration of the dilation wave beneath the footing is also evident in Figures 7.8 and 7.9, which show the variation of vertical stress with depth at radii of 0 m and 0.9 m respectively. There is little attenuation of the peak stress as the wave travels, but the magnitude of the stress under the edge of the footing is approximately one third of the stress under the centre of the footing.

Secondly, as the dilation wave travels, a region of tensile stress forms behind the wave. This is consistent with the propagation of the cylindrical dilation wave presented in Figure 6.8. The tensile stress can be seen most easily in Figure 7.8, but is also evident as a hollow behind the dilation peak in Figure 7.4. The similarity of these dilation waves suggests that, at least to some extent, the base response will be similar to the response of the dilation boundary discussed in the previous chapter.

The dilation wave hits the edge of the mesh at 4 ms, and is subsequently absorbed. Conceptually, the wave propagates into the far field.

Unlike the dilation wave, the shear wave shows a more uniform distribution in all directions. A large stress concentration occurs at the edge of the footing when the impact force is large, and the shear wave appears to radiate from this area. The distance taken for the shear wave to rise to a maximum determines the minimum node spacing. Figure 7.5 graphically illustrates the steep gradient of the shear wave. The magnitude and gradient of the shear wave travelling vertically are similar to the shear wave travelling radially, suggesting that the node spacing in both directions should be similar. Figures 7.10 and 7.11 show that gradient of the wave does not decrease with distance from the footing, but, like the cylindrical shear wave, appears to increase slightly. This supports the earlier observation that the size of the finite elements should not decrease with distance from the footing.

Figure 7.6 shows that most of the radial stress is associated with the dilation wave, and is highest in the soil underneath the footing. A small amount of radial and vertical stress is associated with the shear wave.

The propagation of the waves viewed in terms of the Von Mises generalised shear stress is significant, as this stress is limited by the Von-Mises yield criteria. Figure 7.7 shows that the the shear wave causes significant generalised stress over a much larger area than the dilation wave. At a radius of 0 m, the generalised stress associated with the shear wave is slightly larger and of longer duration than that associated with the dilation wave (Figure 7.12(a)), and, at a radius of 0.9 m, most of the generalised stress is associated with the shear wave (Figure 7.12(b)). These facts will become significant in the next chapter, when a new model for inelastic base response is constructed.

The pile and hammer properties used for all examples presented above have been based on those used by Simons (1985) and Smith and Chow (1982). However, the combination of a large diameter pile with a sharp impact wave requires a large finite element mesh, as illustrated by the analysis above. While the sharp wave leads to the excellent visual separation of the shear and dilation waves evident in Figures 7.4 to 7.7, the time taken to perform the computations is large. The time taken to analyse such a problem can become impracticably long when inelastic soil behaviour is taken into account. To alleviate this problem, a different combination of pile and hammer properties will be used in some of the analyses which follow. These properties are shown in Figure 7.13, and the impact force created by this hammer/pile combination is plotted later in Figure 7.17(b). The rise time of 3 ms allows a much coarser mesh than the previous rise time of 1 ms.

7.3 Analytical solutions for harmonic footing response

The response of a circular rigid footing to a complex harmonic loading has been tackled analytically by several researchers. Bycroft (1954) obtained an approximate solution by assuming that the stress distribution under a dynamic footing was the same as that under a static footing. Such an approximation is valid at low dimensionless frequencies, but breaks down at high frequencies. The vertical stresses on the footing analysed in the first part of this chapter are plotted at 2, 4, 6 and 8 milliseconds in Figure 7.14, along with the static stress distribution for the impact force at 2 milliseconds. The impact load gives rise to significant tensile stresses over some sections of the footing which are not present in the static stress distribution.

Lysmer (1965) obtained another approximate solution by modelling the footing as a series of concentric rings carrying uniform stress, and equating the displacement of each ring to the footing displacement. Robertson (1966) presented an expression for the solution involving the Fredholm integral equation, and evaluated the functions at low dimensionless frequencies using a power series expansion. Shah (1968) solved the integral equation of Robertson numerically, evaluating the compliance of a rigid footing over a large range of dimensionless frequencies. Similar evaluation was performed by Luco and Westmann (1971), who presented plots of vertical compliance for several values of Poisson's ratio.

The analytical solutions referenced above only relate to a smooth rigid circular footing on a uniform half-space. The complex compliance cannot be expressed in terms of elementary functions, and numerical evaluation of the complex Friedholm equation must be performed. Such a procedure is cumbersome, and the use of approximate polynomial expressions is common (eg. Novak, 1977).

7.4 Fourier analysis of transient response

The steady state response of a circular rigid footing to a harmonic load can be determined with the solutions referenced above. Lysmer and Richart (1966) showed how Fourier series analysis can be used to determine response to transient loads. This procedure will be reviewed briefly, as it will be used as the basis of a new method of determining the compliance of a finite element mesh.

Lysmer and Richart (1966) reason that, since the footing system is strongly damped, the transient force can be represented by a continuous series of alternating force pulses, as shown in Figure 7.15(a). Provided that the distance between each pulse is large enough that the response of the footing to one pulse dies out before the next occurs, the response is a series of alternating displacement pulses, as shown in Figure 7.15(b). Since there is no interaction between consecutive pulses, the displacement pulse corresponding to a particular force pulse is the same as the transient response of the footing to that pulse alone. If a transient force pulse of $F(t)$, which dies out to zero before time T, is specified, a Fourier series can be found for the corresponding pulse train.

$$F(t) \approx \sum_{n=0}^{N} c_{fn} \cos\left(\frac{(2n+1)\pi}{T} t + \psi_{fn}\right) \tag{7.1}$$

As N approaches infinity, the series becomes exact, but if N is sufficiently large, a good approximation can be achieved. Lysmer and Richart (1966) provide a guide for choosing N and T. The coefficients c_{fn} and ψ_{fn} can be obtained from the following equations. If the force function is known at a number of discrete points in time, numerical evaluation of the integrals is trivial.

$$c_{fn} = \sqrt{\alpha_{fn}^2 + \beta_{fn}^2} \tag{7.2}$$

$$\psi_{fn} = \tan^{-1} \frac{-\beta_{fn}}{\alpha_{fn}} \tag{7.3}$$

$$\alpha_{fn} = \frac{2}{T} \int_0^T F(t) \cos\left(\frac{(2n+1)\pi}{T} t\right) dt \tag{7.4}$$

$$\beta_{fn} = \frac{2}{T} \int_0^T F(t) \sin\left(\frac{(2n+1)\pi}{T} t\right) dt \tag{7.5}$$

The dimensionless frequency corresponding to each term in the Fourier series is simply

$$a_n = \frac{(2n+1)\pi R}{c_S T} \tag{7.6}.$$

Since the system is linear, the footing response to each term in the Fourier series can be computed independently, and the results combined. If the system flexibility is available as a frequency dependent complex compliance, the response for each frequency component can be determined. The series representing the displacement is presented in equation (7.7), where F_1 and F_2 are the coefficients of real and imaginary flexibility respectively, and k_{static} is the static footing stiffness.

$$u_z(t) \approx \sum_{n=0}^{N} \frac{c_{fn}}{k_{static}} \left(F_1(a_n) \cos\left(\frac{(2n+1)\pi}{T} t + \psi_{fn}\right) - F_2(a_n) \sin\left(\frac{(2n+1)\pi}{T} t + \psi_{fn}\right)\right) \tag{7.7}$$

7.5 Footing compliance from finite elements

The complex compliance of a rigid footing can be approximated using a finite element model of the footing and the half-space. When the footing is subjected to a complex harmonic force of $F_0 e^{i\omega t}$, each degree of freedom

oscillates at the same frequency, but with different amplitudes and phase angles. The displacement, velocity, and acceleration of the j^{th} degree of freedom can be expressed as

$$u_j(t) = (a_j(\omega) + \mathrm{i}\, b_j(\omega))\, F_0\, e^{\mathrm{i}\omega t} \tag{7.8},$$

$$\dot{u}_j(t) = (\mathrm{i}\omega a_j(\omega) - \omega b_j(\omega))\, F_0\, e^{\mathrm{i}\omega t} \tag{7.9}$$

and

$$\ddot{u}_j(t) = -(\omega^2 a_j(\omega) + \mathrm{i}\, \omega^2 b_j(\omega))\, F_0\, e^{\mathrm{i}\omega t} \tag{7.10}.$$

The matrix equation of motion is

$$\mathbf{K}\, \mathbf{u}(t) + \mathbf{C}\, \dot{\mathbf{u}}(t) + \mathbf{M}\, \ddot{\mathbf{u}}(t) = F_0\, e^{\mathrm{i}\omega t}\, \mathbf{f} \tag{7.11},$$

where $\mathbf{f}$ contains unity for the excited degree of freedom, and zero for all others. Substituting equations (7.8) to (7.10) and dividing by $F_0\, e^{\mathrm{i}\omega t}$, a complex equation in the frequency dependent vectors $\mathbf{a}(\omega)$ and $\mathbf{b}(\omega)$ is formed.

$$\mathbf{K}\, \{\mathbf{a}+\mathrm{i}\mathbf{b}\} + \omega\, \mathbf{C}\, \{\mathrm{i}\mathbf{a}-\mathbf{b}\} - \omega^2\, \mathbf{M}\, \{\mathbf{a}+\mathrm{i}\mathbf{b}\} = \mathbf{f} \tag{7.12}$$

Breaking this equation into real and imaginary parts, two real equations are formed.

$$\mathbf{K}\, \mathbf{a}(\omega) - \omega\, \mathbf{C}\, \mathbf{b}(\omega) - \omega^2\, \mathbf{M}\, \mathbf{a}(\omega) = \mathbf{f} \tag{7.13}$$

$$\mathbf{K}\, \mathbf{b}(\omega) + \omega\, \mathbf{C}\, \mathbf{a}(\omega) - \omega^2\, \mathbf{M}\, \mathbf{b}(\omega) = \mathbf{0} \tag{7.14}$$

These equations can be combined to form one matrix equation. If equation (7.14) is multiplied by -1 before combining, the harmonic stiffness matrix which results retains symmetry.

$$\begin{bmatrix} \mathbf{K}-\omega^2\mathbf{M} & -\omega\mathbf{C} \\ -\omega\mathbf{C} & \omega^2\mathbf{M}-\mathbf{K} \end{bmatrix} \begin{Bmatrix} \mathbf{a} \\ \mathbf{b} \end{Bmatrix} = \begin{Bmatrix} \mathbf{f} \\ \mathbf{0} \end{Bmatrix} \tag{7.15}$$

The coefficients $\mathbf{a}$ and $\mathbf{b}$ can be found by solving this system of equations. To optimise the numerical solution of these equations, a and b coefficients should be ordered alternately, minimising the profile of the matrix. Denoting the degree of freedom associated with the vertical displacement of the footing by m, the complex flexibility coefficients are simply

$$F_1(\omega) = \frac{a_m(\omega)}{k_{static}} \qquad \text{and} \qquad F_2(\omega) = \frac{b_m(\omega)}{k_{static}} \tag{7.16}.$$

This method of calculating complex compliance from a finite element mesh is essentially the same as that proposed by Lysmer and Kuhlmeyer (1969) and used by others (eg. Chow (1985)). However, the method has a number of drawbacks. Firstly, equation (7.15) contains twice as many unknowns as the corresponding finite element formulation, and the band of the matrix in equation (7.15) is twice as wide as the band of the stiffness matrix, so a large amount of computer time and memory may be required. Secondly, equation (7.15) must be solved for each frequency at which the coefficients F_1 and F_2 are required.

Another serious drawback is the large influence that the truncating boundary has on the solution. Inspection of equation (7.15) reveals that the interaction between the $\mathbf{a}$ and $\mathbf{b}$ coefficients is caused solely by the system damping matrix. If the material damping of the soil mass is neglected, the only damping is provided by the transmitting boundary. If there is no damping on the boundary, the coefficients $\mathbf{b}$ become zero, and the response is always in phase with the oscillating load. This effect is independent of the extent of the finite element mesh.

If the method is used to evaluate the steady state effectiveness of transmitting boundaries, the inordinate influence of the boundaries could be justified. However, solutions obtained in this manner must be viewed with suspicion, as the steady state nature of the solutions can hide significant behaviour traits. The inability of the standard viscous boundary to correctly model response to transient loads is not immediately evident when this type of analysis is used. More significantly, proponents of the above method often use different meshes for each frequency at which the analysis is undertaken, specifying the element size and boundary distances in terms of the wavelength of the shear waves. This means that the phase difference between the boundary reflections and the footing force is maintained at a constant value, which may hide the true extent of the boundary errors. Both

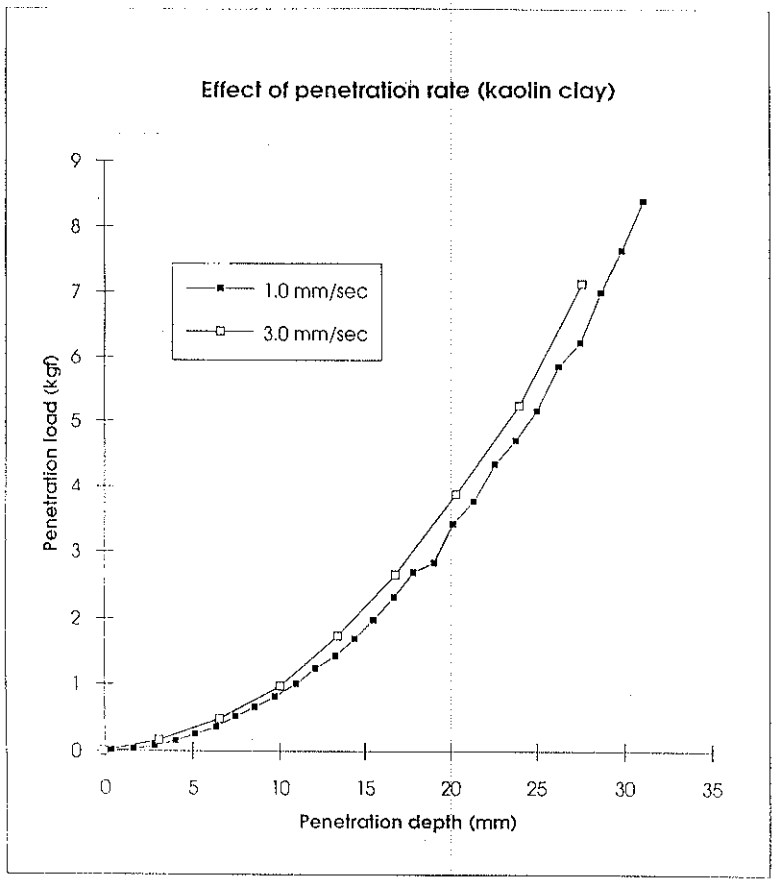

Figure 2: Effect of penetration rates on load - penetration curves for Kaolin clay

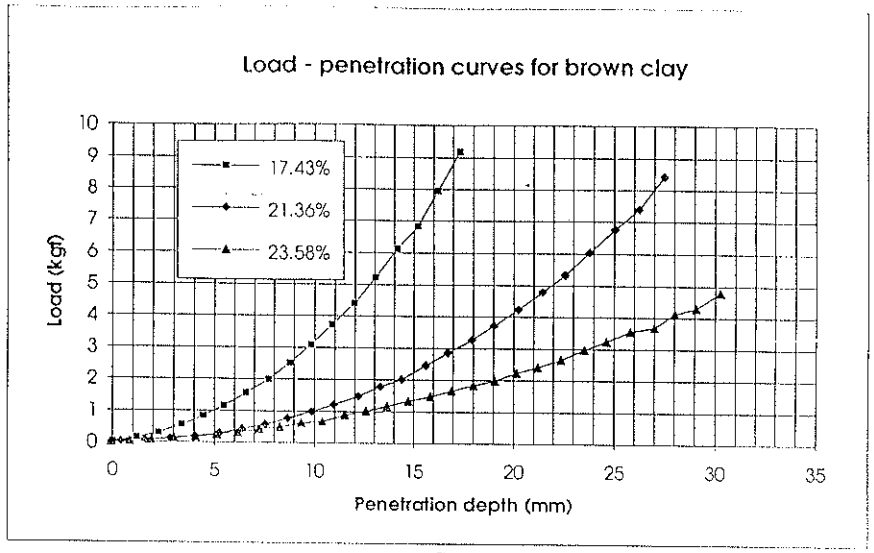

a

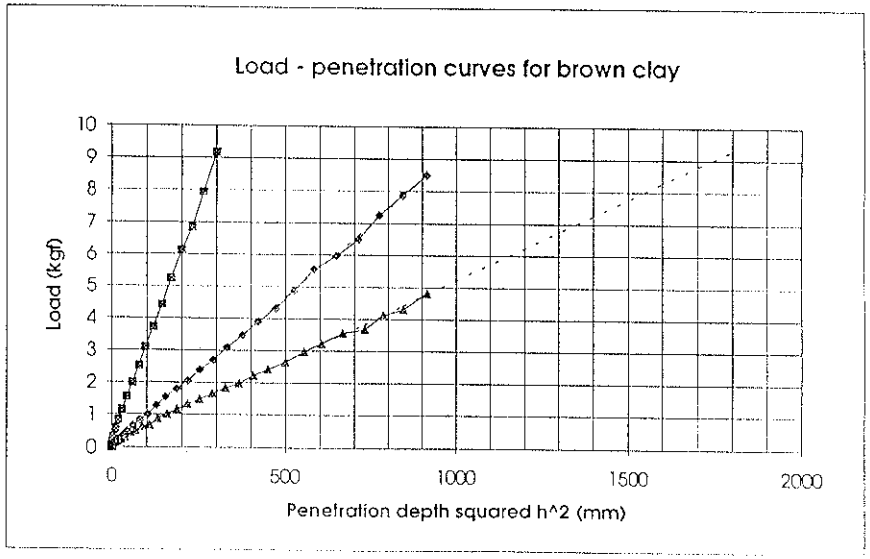

b

Figure 3a) Penetration load versus penetration depth and
b) penetration depth squared for Brown clay.

Lysmer and Kuhlmeyer (1969) and Chow (1985) calculate three points on the footing compliance curves with three different meshes, and draw smooth lines through these points.

The mesh shown in Figure 7.16(a) was used to compute the footing compliance over the standard dimensionless frequency range of 0 to 2 at intervals of 0.02. The calculated compliance curves are presented in Figure 7.16(b). The performance of the viscous boundary is worse than Chow's (1985) results indicate. When doubly asymptotic boundaries were used in place of the viscous boundaries, the computed compliance showed resonant peaks at several frequencies (Figure 7.16(b)). Later in this chapter, the doubly asymptotic boundary will be shown to out-perform the viscous boundary when the footing is subjected to a transient load. Consequently, this method of computing complex compliance does not reflect the ability of a finite element model to represent transient response.

7.6 An alternative method

To overcome the shortcomings of the procedure described above, an alternative method of computing footing compliance from a finite element analysis is proposed. This technique uses the response of a finite element mesh to transient loading to derive complex compliance, inverting the Lysmer and Richart procedure for computing transient response using Fourier series. A transient force is applied to the finite element model of the footing and soil, and the footing displacement is calculated by numerical time integration of the finite element equations. Time integration is carried out until all significant dynamic behaviour has ceased. The time period required for this to occur becomes T in Figure 7.15. A Fourier series is then formed for the force using equations (7.1) to (7.5), and for the footing displacement (u_z) using the equations below. Since numerical time integration yields the displacement at regular time intervals, numerical integration of equations (7.20) and (7.21) is trivial.

$$u_z(t) \approx \sum_{n=0}^{N} c_{un} \cos\left(\frac{(2n+1)\pi}{T} t + \psi_{un}\right) \tag{7.17}$$

$$c_{un} = \sqrt{\alpha_{un}^2 + \beta_{un}^2} \tag{7.18}$$

$$\psi_{un} = \tan^{-1} \frac{-\beta_{un}}{\alpha_{un}} \tag{7.19}$$

$$\alpha_{un} = \frac{2}{T} \int_0^T u_z(t) \cos\left(\frac{(2n+1)\pi}{T} t\right) dt \tag{7.20}$$

$$\beta_{un} = \frac{2}{T} \int_0^T u_z(t) \sin\left(\frac{(2n+1)\pi}{T} t\right) dt \tag{7.21}$$

Once Fourier series have been obtained for both the force and the displacement, the magnitude (b_n) and phase shift (θ_n) of the complex compliance can be obtained at each frequency represented in the series. The dimensionless frequencies can be computed with equation (7.6), and the magnitudes and phase shifts are given by equations (7.22) and (7.23).

$$b_n = \frac{c_{fn}}{c_{un}\, k_{static}} \tag{7.22}$$

$$\theta_n = \psi_{un} - \psi_{fn} \tag{7.23}$$

The real and imaginary flexibility coefficients can then be calculated, and the stiffness coefficients can be obtained from equations (7.26) and (7.27) if required.

$$F_1 = b_n \cos \theta_n \tag{7.24}$$

$$F_2 = b_n \sin \theta_n \tag{7.25}$$

$$S_1 = \frac{1}{b_n} \cos \theta_n \tag{7.26}$$

$$S_2 = \frac{-1}{b_n} \sin \theta_n \tag{7.27}$$

At higher dimensionless frequencies, the calculated approximations of b_n and θ_n have been observed to contain erroneous oscillation with dimensionless frequency. These functions can be smoothed using a point-averaging algorithm over sufficient points to cover the period of the oscillation. The smoothing should be applied before the flexibility and stiffness coefficients are calculated, otherwise significant oscillation of these parameters can occur.

The accuracy of the new method will be demonstrated using the simple two degree of freedom mechanical system shown in Figure 7.17(a). The complex compliance of this system can be obtained analytically. (This complex compliance is derived later in equations (7.30) to (7.34).) The complex compliance can also be calculated using the new method. Comparing the two solutions gives an indication of the accuracy of the new method.

The hammer impulse shown in Figure 7.17(b) was applied to a numerical model of the system, and the response was computed by integrating the equations of motion using the constant-average-acceleration method. The response is shown in Figure 7.17(c). A time step of 0.05 ms was used, and the response was computed for 30 ms. To obtain sufficient resolution of low frequency response, T was taken as 324 ms and N as 270. The resulting Fourier series approximations for force and time are also shown in Figures 7.17(b) and 7.17(c). There is no significant difference between the Fourier approximations and the original functions.

The computed magnitude and phase shift of the compliance are shown in Figure 7.18, together with the smoothed functions obtained by using an 11-point smoothing algorithm. The compliance computed from the smoothed magnitude and phase shift shows no appreciable difference from the analytical compliance (Figure 7.19).

To further verify the accuracy of the new method, the method was used to compute the complex compliance of a smooth circular rigid footing on a semi-infinite half-space, and the results compared with a published solution. The finite element mesh shown in Figure 7.20 was used to compute the response of the footing to the hammer impulse plotted previously in Figure 7.17(b). The boundaries were located sufficiently far away to prevent any boundary influence before the footing returned to rest. The flexibility coefficients obtained for a Poisson's ratio of 1/3 are plotted in Figure 7.21, together with those obtained by Luco and Westmann (1971). The calculated compliance agrees well with the published compliance.

The new method requires the frequency content of the force pulse applied to the footing to be well distributed over the frequency range of interest. Higher frequencies must be given higher weighting to maintain accuracy. When these requirements are satisfied, the new method can produce superior results to the method described in the previous section. The new technique is substantially cheaper in computer time, as the number of equations is smaller and the compliance for a large number of frequencies is obtained from one analysis. In addition, the finite element analysis can be performed with a standard dynamic finite element analysis program without customisation. The Fourier analysis can then be performed on the output displacement function and input force function to obtain the compliance. This analysis is trivial enough to be programmed in a spreadsheet macro language, or BASIC, by someone with a rudimentary knowledge of programming.

In the work presented here, the complex flexibility and stiffness obtained by the new method will be used to compare the effects of different boundaries, to examine the effect of friction on the base of the footing, and to compare different mechanical footing models. The potential of the method extends beyond this, permitting calculation of the compliance of footings of arbitrary shape on soils with varying elastic properties. However, more work must be done to establish the optimum input pulse, and to determine the source of the oscillating error. This error is possibly due to the slight frequency shift caused by the time integration procedure.

7.7 Finite element boundaries

Using the mesh shown in Figure 7.20 for inelastic computations is not practical, as too much computer time is required. The mesh must therefore be terminated with transmitting boundaries. Previous finite element analyses of pile driving problems have usually used a two-dimensional version of the standard viscous boundary.

Generalising from the one-dimensional viscous boundaries discussed in Chapter 6, Lysmer and Kuhlemeyer (1969) proposed a viscous boundary for two dimensions expressed by the following two equations.

$$\sigma = a \rho c_p \frac{\partial u}{\partial t} \tag{7.28}$$

$$\tau = b \rho c_s \frac{\partial v}{\partial t} \tag{7.29}$$

σ and u are normal to the boundary, while τ and v are tangential.

These boundary conditions only approximate the effect of the far field. The constants a and b may be selected by attempting to optimise the energy absorption of the boundary. Proceeding on a trial and error basis, Lysmer and Kuhlemeyer (1969) found that setting the constants to $a = b = 1$ gave good energy absorption, providing the incident angle of the wave approaching the boundary was not too small.

White *et al* (1977) presented a rational procedure for maximising energy transmission, which allows computation of a and b for any Poisson's ratio. (The values of the constants were found to vary slightly with Poisson's ratio.) They termed the resulting boundary conditions a *unified boundary*. However, the increase in efficiency over using unit values for a and b was shown to be less than one percent.

Although derived for propagation of plane waves in two dimensions, the two-dimensional viscous boundary has often been demonstrated using the axisymmetric problem of a vibrating rigid circular footing on a semi-infinite half-space (eg. Lysmer and Kuhlemeyer, 1969; Chow, 1985). However, White *et al* (1977) calculated optimum values of a and b for the absorption of cylindrical waves. They found that a and b are dependant on the ratio of the boundary radius to the wave length, and are therefore frequency dependent. For large boundary ratios, a and b approach the values obtained for two-dimensions. The difference between the axisymmetric unified boundary and the viscous boundary is generally very small.

The referenced literature has demonstrated that the viscous boundary may be used in two-dimensional and axisymmetric problems with zero time-average loads. The paraxial and superposition methods are theoretically superior to the viscous boundary in two dimensions, but have been shown to yield little improvement in practice (Cohen and Jennings, 1983; Simons, 1985).

In Chapter 6 the geometric attenuation of axisymmetric waves was shown to cause reflection from the far field. Consequently, application of perfect transmitting boundaries to meshes such as that shown in Figure 7.16(a) cause rigid body motion when the applied load has a non-zero time average. Such rigid body motions have been identified by Mitwally and Novak (1988).

The impulse force caused by the hammer shown in Figure 7.13 was applied to the mesh in Figure 7.16(a) truncated with viscous boundaries. The computed displacement is compared with that calculated using the extended mesh of Figure 7.20 in Figure 7.22. The permanent displacement at the end of the time integration is due to the rigid motion of the mesh. The new method of computing complex compliance cannot be used with a mesh which undergoes rigid body motion.

In the previous chapter, transmitting boundaries were derived for plain strain axisymmetric shear and dilation waves. The derivations depended on explicit expressions for the travelling waves. The surface plots presented in the first section of this chapter show that the attenuation of the travelling waves under a rigid footing is complex, and equivalent expressions cannot be found. However, the transmission of shear and dilation waves from the side of the mesh can be modelled with the boundaries for plane strain cylindrical waves derived in Chapter 6.

The base of the mesh is more difficult. Figure 7.4 showed that the vertical stress wave travelling downwards from the rigid footing shows little attenuation and dispersion, and is practically a one-dimensional axial wave. Consequently, the wave is effectively absorbed by a viscous boundary. To test these boundaries, the hammer in Figure 7.13 was applied to the mesh in Figure 7.16(a), as before. This time the plane strain boundaries were applied to the sides of the mesh, and a viscous boundary was applied at the base. In Figure 7.22 the resulting displacement is compared with the displacement calculated with the extended mesh. The purely viscous base boundary allows too much vertical displacement, and evidently should have some in-phase stiffness.

One way of providing finite stiffness on the base boundary is to use a doubly asymptotic boundary of the type described in Chapter 6. The static stiffness of a circular footing with a radius equal to that of the finite element mesh can be applied as a uniformly distributed spring across the base of the finite element mesh. The improvement obtained by adding this stiffness is shown in Figure 7.22.

An alternative base boundary can be obtained by treating the vertical dilation wave as spherical cavity expansion. The mechanical model shown in Figure 6.4 can be used with the parameters provided by Wolf (1988) for

spherical cavity expansion. The stiffness of this boundary lies between the viscous and the doubly asymptotic boundaries. The results obtained using this base boundary are also presented in Figure 7.22.

The spherical cavity expansion base boundary and the doubly asymptotic base boundary show only a slight improvement over the viscous base boundary. However, there is a distinct difference between the response of the truncated mesh and the extended mesh at large times. Figure 7.22 shows the time taken for the dilation wave to reflect from the base boundary and return to the footing, and the time taken for the shear wave to reflect from the side boundary and return to the footing. In the time between the return of the dilation wave from the base and the return of the shear wave from the side, the response of the truncated and extended meshes are similar, indicating that all the base boundaries behave quite well. However, once the shear wave returns from the side boundary, the responses of the truncated and extended meshes become quite different.

In Chapter 6, the plain strain boundaries were shown to perform very well. The apparent reflection of the shear wave from this boundary was explained by Lysmer and Kuhlmeyer (1969), who showed that a viscous boundary does not totally absorb the surface Rayleigh wave, which propagates at approximately the same velocity as the shear wave. They derived a boundary for the absorption of Rayleigh waves, but the boundary is highly dependent on excitation frequency. Like the viscous boundary, the plane strain boundaries are unable to totally absorb this wave.

Fortunately, the Rayleigh wave travels relatively slowly, and so, for a mesh of reasonable size such as that in Figure 7.16(a), the significant dynamic response is complete before the errors caused by the reflected wave become evident. In pile driving, the permanent inelastic deformation occurs at small times when the base force is relatively high. Consequently, the reflected Rayleigh waves will not significantly affect the computed force response, or the predicted set.

The new method for computing the complex compliance of a finite element mesh can be used to compare the effectiveness of different truncating boundaries. The effect of the truncating boundaries on the compliance of the Figure 7.16(a) mesh is shown in Figure 7.23. Unlike the compliances computed by the old method (Figure 7.16(b)), the compliances for boundaries with in-phase stiffness do not exhibit resonant peaks. The different base boundaries have little effect on the computed flexibility, as most of the error is due to the reflected Rayleigh wave.

7.8 The effect of footing friction

The rigid footing compliances referenced previously were calculated for a smooth rigid circular footing, which develops no shear stress on the base of the footing. A pile is usually embedded, which limits the vertical movement beneath the pile, and significant shear stresses can be developed between the pile base and the soil. Luco and Westmann (1972) show that the compliance of a rigid strip is slightly altered when bond between the footing and the half-space is taken into account. To determine the significance of this effect on a circular footing, the compliance of a rigid circular footing bonded to a half-space was calculated using the mesh of Figure 7.20 and the new method of computing compliance.

The effect of bonding on the complex compliance is shown in Figure 7.24. The difference between the bonded and un-bonded cases is so small that the degree of bonding beneath the pile toe can be ignored. In all subsequent analyses, the footing representing the pile base will be assumed to be fully bonded to the under-lying soil.

7.9 The effect of Poisson's ratio

The results of Luco and Westmann (1971) indicated that Poisson's ratio has a significant influence on the complex flexibility of a smooth circular rigid footing. To determine the effect of Poisson's ratio on the response of the pile base, complex compliances were computed out for a rough circular footing on soil with Poisson's ratios of 0.25, 0.33, 0.40, and 0.45. The results are presented in Figure 7.25. There is little difference between the complex compliances computed for Poisson's ratios of 0.25 and 0.33, but as Poisson's ratio is increased to 0.45, the in-phase stiffness at high dimensionless frequencies becomes negative.

During pile driving, the Poisson's ratio of the soil is typically in the range 0.45 to 0.5, as the soil response is predominantly undrained.

7.10 Simplified modelling of footing response

To simplify analysis of the dynamic response of rigid footings, Lysmer and Richart (1969) proposed a one-dimensional model consisting of a spring and slider in parallel. This model is shown in Figure 7.26(a). Lysmer and Richart used the complex compliance of a half-space model with a Poisson's ratio of $^1/_3$ to compute

equivalent spring and damping constants. Although these parameters were dependent on dimensionless frequency, constant values were selected which gave reasonable agreement with the half-space model. Because the variation of complex compliance with Poisson's ratio is quite small, Lysmer and Richart suggested that the model be used for all values of Poisson's ratio. This suggestion has largely been followed, and all rational models of pile driving dynamics have employed base models derived from Lysmer's analog (eg. Simons and Randolph, 1986).

Another mechanical model of dynamic footing response has been presented by Wolf (1988). This model is shown in Figure 7.26(b), and contains an additional degree of freedom, an additional dashpot, and two lumped masses. With the exception of the added mass at the footing, this model is a combination of the models for axisymmetric shear and dilation wave transmission presented in the previous chapter. Wolf derived parameters for the model by matching the complex compliance of the model to the computed compliance of a half-space over a limited range of dimensionless frequencies. The parameters are presented in Figure 7.26(b) as functions of Poisson's ratio.

Figure 7.27 compares the complex compliance of these two models with that computed by the finite element method for a rough footing on a soil with a Poisson's ratio of 0.45. Although the general shape of the curves is similar, there is significant variation between the models at higher frequencies.

The differences are more apparent in Figures 7.28 and 7.29, which plot the real and imaginary stiffness parameters. The real stiffness of the Wolf model is in close agreement with the finite element computation at low frequencies, but the high frequency response is very poor. The constant spring stiffness of the Lysmer model poorly approximates the variation of the in-phase stiffness with dimensionless frequency. Both models only approximate the out of phase stiffness component well at low frequencies.

Since the impact waves caused by pile driving hammers have significant high frequency content, the simplified base models described above may perform poorly under pile driving conditions. This was confirmed by subjecting models of the base of the pile shown in Figure 6.25 to the impact of the hammer in Figure 5.2. The calculated footing displacements are compared with those calculated with finite elements in Figure 7.30. Both models yield footing displacements which are significantly different from the finite element results.

A better base model can be formed by matching the complex stiffness of the model shown in Figure 7.26(b) to the complex stiffness obtained by finite element analysis. To accomplish this, the complex stiffness of the model must be calculated in terms of the model parameters.

The equations of motion for the model are

$$m_0 \ddot{u}_1 + c_0 \dot{u}_1 + c_1(\dot{u}_1 - \dot{u}_2) + k u_1 = f(t) \tag{7.30}$$

$$m_1 \ddot{u}_2 + c_1(\dot{u}_2 - \dot{u}_1) = 0 \tag{7.31}.$$

The parameters can be non-dimensionalised in the following way.

$$\alpha_0 = \frac{m_0}{k}\left(\frac{c_S}{R}\right)^2 \quad \alpha_1 = \frac{m_1}{k}\left(\frac{c_S}{R}\right)^2 \quad \beta_0 = \frac{c_0}{k}\left(\frac{c_S}{R}\right) \quad \beta_1 = \frac{c_1}{k}\left(\frac{c_S}{R}\right) \tag{7.32}$$

The complex stiffness coefficients can then be found in terms of the dimensionless frequency, a_S, using the procedure detailed in equations (6.66) to (6.86).

$$S_1 = \frac{1 + \left(\left(\frac{\alpha_1}{\beta_1}\right)^2 (1 - \alpha_0 a_S^2) - (\alpha_0 + \alpha_1)\right) a_S^2}{1 + \left(\frac{\alpha_1}{\beta_1}\right)^2 a_S^2} \tag{7.33}$$

$$S_2 = \frac{\left(\beta_0 + \left(\frac{\alpha_1}{\beta_1}\right)^2 (\beta_0 + \beta_1)\, a_S^2\right) a_S}{1 + \left(\frac{\alpha_1}{\beta_1}\right)^2 a_S^2} \tag{7.34}$$

The complex stiffness was calculated using the new finite element method for Poisson's ratios of 0.25, 0.33, 0.40, and 0.45. At each Poisson's ratio, the values of α_0, α_1, β_0, and β_1 which best fitted equations (7.33) and (7.34) to the finite element stiffness over a wide range of dimensionless frequencies were found by trial and error. α_0 and β_0 were found to be independent of Poisson's ratio, with

$$\alpha_0 = 0 \quad \text{and} \quad \beta_0 = 0.8 \tag{7.35}$$

α_1 and β_1 were found to vary with Poisson's ratio. The computed values are plotted against Poisson's ratio in Figures 7.31 and 7.32. The parameters can be approximated by the following equations, which are also plotted in Figures 7.31 and 7.32.

$$\alpha_1 = 0.63 - 3.6\ \nu + 6\nu^2 \tag{7.36}$$

$$\beta_1 = 1.58 - 10.3\ \nu + 19\nu^2 \tag{7.37}$$

The difference between the parameters of new model and those of Wolf's (1988) model is caused by the matching of the new model over a larger range of dimensionless frequencies. An example of the improved fit to the complex flexibility and stiffness parameters achieved by the new model is shown in Figures 7.27, 7.28, and 7.29 for a Poisson's ratio of 0.45.

When the new model is used to model the base of the pile shown in Figure 6.25, the calculated displacement is much closer to the finite element results than the other models (Figure 7.30).

7.11 The effect of embedment

Some preliminary results detailed in Chapter 6 indicated that little interaction occurred between the soil at the pile base and the soil surrounding the shaft. To investigate the interaction in more detail and in more general terms, the complex compliances of a series of rigid piles with various embedments were computed using the new finite element method. The finite element meshes are shown in Figure 7.33(a). The meshes were truncated with a doubly asymptotic base boundary, and plane strain side boundaries.

To determine the effect of the interaction, the compliances of the one-dimensional models shown in Figure 7.33(b) were also computed. Comparing the compliance of each model with the appropriate finite element compliance, the agreement between the two was found to be independent of the pile embedment (Figure 7.34). This supports the previous conclusion that little interaction occurs between the soil surrounding the shaft and the soil beneath the base. The displacements of the piles are shown in Figure 7.35. The simplified models agree well with the finite element results.

The shear wave travelling from the base along the surface of the half-space beneath the pile is in phase with the shear wave travelling from the pile shaft in the layer above the half-space. Consequently there is little stress on the adjoining surface, and little interaction. However, this conclusion is only valid for elastic analysis. When the inelastic response of the system is examined in the next chapter, the effect of embedment will have to be re-evaluated, since the plastic mechanism could be affected by the overlying soil.

7.12 The effect of pile interaction

In the examples presented above, a hammer impact force was applied directly to a weightless rigid footing, and the displacement was computed. In pile-driving applications, the impact force propagates down the pile as an axial stress wave, and reflects from the soil at the pile base. The amount of force generated in the soil and the magnitude of the stress wave reflected back up the pile depend not only on the dynamic properties of the soil at the base, but also on the impedance of the pile.

Randolph (1990) has shown that the velocity at the base of the pile (v_b) is related to the downward travelling wave (F_d), the base resistance (Q_b) and the pile impedance (Z) by the following equation.

$$v_b = \frac{2F_d - Q_b}{Z} \tag{7.38}$$

By simple algebra, the base force can be related to the downward travelling wave and the base velocity.

$$Q_b = 2F_d - Z v_b \tag{7.39}$$

These equations show that the effect of the pile on the base response can be modelled by attaching a dashpot of impedance Z to the footing, and then applying twice the hammer force to the footing. Both the displacement at the pile base and the force exerted on the soil can then be computed.

The response of the base of the pile shown in Figure 7.36 was computed with the effect of the pile impedance included in this way, using a finite element model, the Lysmer base model, the Wolf base model, and the new base model. The resulting forces and displacements are shown in Figures 7.37(a) and 7.37(b). The agreement between the force predicted by the finite element solution and the force predicted by the new base model is extremely good, whereas the forces predicted by the other models are considerably different. Correct modelling of this force response is extremely important, as it affects the reflected force wave, which is often recorded at the pile head during pile driving.

7.13 Overall pile response

The shaft and base response of the pile have been examined separately, and interaction between the two has been shown to be small. The effect of the improved base model on the overall elastic response of a pile is now demonstrated. The pile shown in Figure 7.36 was analysed. Analyses were performed using the full finite element mesh shown in Figure 7.38(a), and using one dimensional models consisting of the shear transmitting boundary along the shaft and the three base models described above (Figure 7.38(b)). The displacements and base forces calculated when the the pile was subjected to a blow from the hammer of Figure 5.2 are shown in Figures 7.39 and 7.40. The displacements and base force resulting from the improved one-dimensional model are practically the same as those calculated using finite elements, and are significantly better than the one-dimensional models incorporating the other base models.

7.14 Conclusions

The stress waves emanating from a rigid footing on an elastic half-space were examined in detail, and two distinct wave types were observed. The dilation wave was seen to propagate vertically downwards from the footing, showing little geometric attenuation or horizontal dispersion. The shear wave was found to give rise to a reasonably uniform stress hemisphere propagating from the footing.

Computation of the response of a circular rigid footing to harmonic loads was considered, and a new technique for computing complex stiffness and flexibility from a finite element analysis was developed. The new technique was shown to provide answers which agreed well with published solutions.

Two-dimensional transmitting boundaries were investigated, and the standard viscous boundary was found to adequately absorb the dilation wave, although a doubly asymptotic boundary was found to provide more accurate displacement approximations. The shear boundary developed previously was found to cause erroneous reflections of the Rayleigh surface wave. Published boundaries for Rayleigh wave absorption were found to be frequency dependent, and so the side boundary of the mesh was located far enough from the footing to prevent erroneous reflections interfering with the short term response of the base.

The effects of footing friction and Poisson's ratio of the soil on the complex compliance of a rigid footing were evaluated. Friction between the soil and the underside of the footing was found to alter the dynamic response only slightly, while Poisson's ratio was found to have more significant effect.

Simplified mechanical models of dynamic footing response were examined. An improved model was constructed by matching the complex stiffness of the Wolf (1988) model to that obtained by finite element analyses for a variety of Poisson's ratio over a large range of dimensionless frequencies. The new model was found to provide better agreement with finite element results than existing models.

The effect of embedment was examined, and the response of an embedded rigid pile was found to be modelled adequately by combining the new base model with an appropriate length of shaft transmitting boundary. This indicates that little interaction occurs between the soil surrounding the shaft and the soil at the base of the pile.

Finally, a simplified model consisting of a one-dimensional pile, the shear transmitting boundary placed along the pile shaft, and the new base model was found to represent the elastic behaviour of a complete finite element model extremely well.

The effect of soil inelasticity will be considered in the next chapter.

8. SOIL INELASTICITY

8.1 Introduction

The preceding chapters of this thesis have dealt with the elastic dynamics of pile driving. However, a key part of the pile driving process is the inelastic response of the soil, which leads to permanent set of the pile. This chapter examines the effect of soil inelasticity on pile driving dynamics, using the Von Mises model of soil inelasticity described in Chapter 4.

Slip at the pile shaft/soil interface is considered first. The effect of interface elements on the dynamic finite element response is investigated, and an improved interface element with internal damping is proposed. At the same time, the effect of a weakened soil layer adjacent to the pile is examined. Plastic sliders are implemented in the implicit time-stepping scheme. One-dimensional and finite element models of slip at the pile/soil interface are compared.

The inelastic penetration of a circular rigid footing into a half-space under hammer impact is examined. Three-dimensional surface plots of the stress waves propagating from the footing are presented. Existing one-dimensional models for the inelastic response of a rigid footing are reviewed, and a new model is proposed. The models are compared with finite element results for a variety of hammer, pile, and soil combinations.

The response of a complete finite element model of a pile and the surrounding soil is compared with the response of a simple model consisting of a one-dimensional pile, the shaft model, and the new base model. The effect of re-driving is also examined, and the residual stresses in the pile and the surrounding soil are computed.

The methods developed in the current work are used to analyse two pile-driving examples presented in the literature. The new results are compared with the published results.

8.2 Shaft/soil interface

Chapter 6 established that the shear waves propagating from the shaft are substantially cylindrical, and that interaction between adjacent soil layers can be ignored. The magnitude of the stress in the shear waves propagating from the shaft decreases in rough proportion to $1/\sqrt{r}$, so the maximum shear stress occurs in the soil adjacent to the pile shaft. Since the normal and radial stresses near the shaft are small in comparison with the shear stress, in an ideal Von Mises soil the shear strength of the bond between the pile and the surrounding soil can be related to the Von Mises yield stress and the undrained shear strength of the soil, s_u, by the following equation.

$$f_s = \frac{\sigma_y}{\sqrt{3}} = \frac{2}{\sqrt{3}} s_u$$

In the ideal model, slip between the shaft of the pile and the surrounding soil will occur when the shear stress reaches f_s, which will be referred to as the shaft friction.

The inclusion of inelasticity in the finite element method was reviewed in Chapter 4. The integration of the body loads over the elements (equation (4.34)) is usually performed numerically using Gauss-Legendre . The excess generalised shear stress is computed at each Gauss point, and integrated over each element to find the contributions to the body loads at the nodes (f_b).

Yielding along the pile shaft/soil interface is highly localised. If the inelastic soil behaviour is computed using standard eight-noded soil elements adjacent to the pile, the computed results may be inaccurate, as the Gauss points will not be on the pile/soil interface. In the limit, as the element size tends to zero, the solution converges to the theoretical solution, but extremely small elements are necessary to produce accurate results. Thin-layer interface elements and joint elements are commonly used in the static analysis of similar situations. These elements have been reviewed by Leong (1991).

8.2.1 Interface elements

Thin-layer interface elements are similar to standard inelastic elements. The deformation within the element is described by continuous shape functions. Zienkiewicz et al (1970) describe a six-noded thin-layer element, while Desai et al (1984) describe an eight-noded element. The stress-strain relationship within the element can be

distinct from the surrounding soil, and can be highly non-linear. Newton-Rhapson iteration is often used to compute the inelastic behaviour of interface elements.

In a material with a Von Mises yield law, the accuracy of a finite element scheme using thin-layer elements depends on the thickness of the elements. Theoretically, all inelastic deformation occurs in an infinitesimal soil layer adjacent to the pile. As the soil elements tend to zero thickness, the computed solution becomes exact. However, as the interface elements become much thinner than the elements representing the surrounding soil, the relative stiffness of the interface elements becomes large. This can lead to ill-conditioning of the structure stiffness matrix, and can increase the number of Newton-Rhapson iterations necessary for convergence. Because the static solution is often insensitive to the elastic stiffness of the interface elements, this stiffness is often artificially reduced to promote convergence (Zienkiewicz et al, 1970).

While thin-layer interface elements model a thin soil layer adjacent to the interface, joint elements attempt to model a joint between adjacent finite elements. The joint element is either given an arbitrary small thickness (Ghaboussi et al, 1973), or has zero thickness (Toki et al, 1981). In a Von Mises soil, the joint should be rigid until the shear stress across the joint reaches the undrained shear strength of the soil. The joint should then permit relative slip between the adjacent elements to limit the transmitted shear stress to the soil shear strength. This type of rigid/plastic joint element can be implemented either by reconstructing the stiffness matrix each time a joint becomes plastic, or by assigning an arbitrary (large) stiffness to the joint and using an iterative scheme to account for the inelastic behaviour (Toki et al, 1981).

The application of thin interface elements to dynamic soil-structure interaction has been considered by Zaman et al (1984). Such elements were also used by Chow (1981) and Smith et al (1985). To avoid the high natural frequencies present in elements with high stiffness and low mass, the interface element mass is usually neglected. Despite this, interaction between the high interface stiffness and adjacent elements possessing mass can create natural modes with high resonant frequencies in the finite element mesh. Partly to counter this effect, Chow (1981) and Smith et al (1985) added interface damping on the basis of the viscous soil damping of the Smith (1960) model. Such damping is inconsistent with elastic-perfectly plastic soil behaviour.

Beltyschyko et al (1976) have implemented inter-nodal slip in an explicit time-integration scheme. The force between two adjacent nodes is assigned a limit. Once the force would exceed this limit, the two nodes are permitted to move independently, and the force between the nodes is set to the limiting value. In effect this is a two-node rigid/plastic joint element. The method can only be used in an explicit time-integration scheme.

A similar scheme for inter-nodal slip was used by Simons (1985) in his finite element analysis of pile driving. Simons also adopted some interface damping to improve the appearance of his results, justifying such inclusion by reference to Chow's work.

Toki et al (1981) implemented a joint element in an implicit time-integration scheme by providing the joint with high elastic stiffness and using load transfer iteration.

8.2.2 Comparison between thin-layer and joint elements

The shaft/soil interface in a Von Mises soil should ideally have zero thickness, and should exhibit rigid/perfectly plastic behaviour. The scheme proposed by Beltyschko et al (1976) can accomplish this when an explicit time-integration algorithm is used. However, when an implicit time-integration method is used, the structure stiffness matrix must be adjusted each time a rigid/plastic joint yields or closes. This adjustment can be performed efficiently using the method of Deeks et al (1984). The change in stiffness can then be found without reducing the entire stiffness matrix (Deeks and Clyde, 1992).

The pile driving problem involves not only slip between the pile shaft and the surrounding soil, but also significant plastic soil flow around the pile toe. Unlike the shaft/soil slip, the inelasticity of the soil at the pile toe is not contained within a narrow band, and cannot be modelled with joint or interface elements. The plastic flow is spread through the soil elements, and the response must be computed using the initial stress method and Newton-Rhapson iteration or a similar scheme.

If the response of the soil at the pile toe is calculated with an iterative scheme, the computer programming can be minimised by computing the slip at the pile/soil interface by the same scheme. This approach was used in the work which follows. However, in the calculations reported later in this chapter, considerably more iterations were needed to account for the shaft/soil inelasticity than were needed to correctly compute the response of the soil at the pile toe. The reason for this was the high relative stiffness of the interface elements compared with the other components of the model. Implementation of a separate direct solution scheme for the pile/soil interface in future work could be advantageous.

To allow the initial stress scheme to be implemented for the pile/soil interface, the joint elements must have finite elastic stiffness. There is no practical difference between a joint element with finite stiffness and a thin-layer interface element. The thickness of the thin-layer element is always small in relation to the dimensions of the problem, so the small distance between the nodes on either side of the interface will not affect the solution.

The simplest form of interface element is a stiff spring connecting two adjacent nodes. The simplest rigid/plastic interface element can be represented by a stiff spring in series with a plastic slider. The behaviour of higher order interface elements can be understood by studying this simple form.

When the initial stress method is used to compute the response of an interface element, decreasing the element stiffness improves the convergence of the initial stress method, but reduces the accuracy of the solution. The static elastic response of a problem is usually used to determine a stiffness which achieves sufficient accuracy within a reasonable time.

8.2.3 The effect of varying the interface stiffness

The effect of interface stiffness on the soil and structure dynamics was not considered in the work referenced above. The researchers have assumed that when the interface elements are stiff enough to avoid excessive static deformation error, the elements will not significantly affect the dynamic response of the system. In Chapter 6, the dynamic stiffness of the soil surrounding the pile shaft was found to be significantly stiffer than the static stiffness, particularly at high dimensionless frequencies. In order to quantify the effect of interface stiffness on dynamic response, an investigation was undertaken using the plane strain propagation of shear waves from a pile shaft, considered in Chapter 6. In this investigation, the soil was separated from the pile shaft by an elastic spring. The stiffness of this spring (k_i) was non-dimensionalised with respect to the limiting dynamic shear stiffness of the soil disk, as indicated by equation (8.1). The model is shown in Figures 8.1(a) and 8.1(b).

$$k^* = \frac{k_i}{2R/G_S} \tag{8.1}.$$

The complex stiffness of a soil disk subjected to plain strain shear harmonic oscillation was presented by Novak (1977), and was stated in equation (6.32). In the current model, the soil disc is connected to the pile shaft by a spring representing an interface element. The flexibility of the combined system may be obtained by adding the complex flexibilities of the spring and the soil disc. Since the interface spring has no imaginary component, the dimensionless flexibility of the system is

$$F_{s1} + i F_{s2} = F_{z1} + \frac{1}{k^*} + i F_{z2} \tag{8.2},$$

where F_{s1} and F_{s2} represent the dimensionless flexibility of the system, and F_{z1} and F_{z2} represent the dimensionless flexibility of the soil disc.

The dimensionless complex system stiffness can be found by inverting the flexibility.

$$S_{s1} + i S_{s2} = \frac{F_{z1} + \frac{1}{k^*}}{(F_{z1} + \frac{1}{k^*})^2 + F_{z2}^2} - i \frac{F_{z2}}{(F_{z1} + \frac{1}{k^*})^2 + F_{z2}^2} \tag{8.3}$$

The interface spring stiffness effects both the real and imaginary components of the system stiffness. The variation of the real and imaginary stiffness parameters with the interface spring stiffness is shown in Figures 8.2(a) and (b) for dimensionless frequencies from 0 to 10. Although having little effect at very low frequencies, the interface spring dramatically increases the real stiffness at high dimensionless frequencies, and reduces the coefficient of imaginary stiffness. This behaviour can be explained when the soil disc is replaced with the shear transmitting boundary (Figure 8.1(c)). At high frequencies the dashpot representing the radiation damping is extremely stiff, and so the interface spring responds as if connected to a rigid boundary. A spring connected to a rigid boundary oscillates in phase with the applied force. This tendency is most evident when the interface spring stiffness is weak. When the dimensionless interface stiffness is 2 and 5, Figure 8.2(a) shows that, at high frequencies, the real spring stiffness tends towards the interface spring stiffness, while the imaginary (out of phase) stiffness tends towards zero.

The dimensionless stiffness of a thin-layer interface element may be easily shown to be related to the thickness and stiffness of the soil layer by

$$k^* = \frac{2\,\frac{G_m}{G_s}}{\ln\left(1 + \frac{t}{R}\right)} \tag{8.4}$$

where t is the thickness of the layer, R is the radius of the pile, G_S is the shear modulus of the surrounding soil, and G_m is the shear modulus of the interface layer surrounding the pile.

The variation of k^* with t/R is shown in Figure 8.3 for $G_m = G_S$. A thickness of as little as $0.02R$ (2 mm for a 500 mm diameter pile) results in a interface stiffness of approximately 100, which is enough to significantly affect the response at high dimensionless frequencies. The effect of reducing G_m is shown in Figure 8.4, and will be considered later.

8.2.4 Appropriate interface stiffness

Although the addition of a sufficiently stiff interface element does not significantly affect static response, the study above shows that the effect on the dynamic response can be quite dramatic, unless the element is extremely stiff. An interface element capable of better performance under dynamic conditions can be constructed by considering the flexibility of the system.

In the following discussion, the soil adjoining the interface will be referred to as the far field. Under static conditions, the interface element will not cause significant error if the combined real flexibility of the far field and the interface is similar to the real flexibility of the far field alone. In other words, when the ratio of the system flexibility and the far field flexibility is approximately unity. This will be the case when the ratio of the interface flexibility and the far field flexibility is small, and hence the interface stiffness is large. Using F_{i1} to represent the flexibility of the interface, these requirements can be written as

$$\frac{F_{s1}}{F_{z1}} = \frac{F_{z1} + F_{i1}}{F_{z1}} \approx 1 \tag{8.5},$$

$$\frac{F_{i1}}{F_{z1}} \approx 0 \tag{8.6}.$$

Under dynamic conditions, the ratio of the complex flexibilities of the system and the far field must also be approximately unity. This cannot be achieved unless the interface flexibility has an imaginary component (F_{i2}).

$$\frac{F_{s1} + \mathrm{i}F_{s2}}{F_{z1} + \mathrm{i}F_{z2}} = \frac{F_{z1} + F_{i1} + \mathrm{i}(F_{z2} + F_{i2})}{F_{z1} + \mathrm{i}F_{z2}} \approx 1 \tag{8.7}$$

Unless the ratio F_{i2}/F_{z2} is the same as F_{i1}/F_{z1}, there will be a phase shift in the system flexibility at high frequencies. If the two ratios are equal, the error in the imaginary flexibility will be the same as the error in the real flexibility. This error will be small if

$$\frac{F_{i1}}{F_{z1}} = \frac{F_{i2}}{F_{z2}} \approx 0 \tag{8.8}.$$

Equation (8.8) will be satisfied if the ratio of the imaginary stiffness of the interface element and the imaginary stiffness of the far field is the same as the corresponding real stiffness ratio, and both ratios are large. The stiffness and flexibility of the far field can only be found precisely for simple problems, but since the interface flexibility is always far smaller than the far field flexibility, the flexibility ratios can vary slightly without effecting the results.

The effect of adding this damping to the interface spring was investigated using the problem discussed above. To compute the interface damping, the complex stiffness of the far field was approximated by the truncating shear boundary presented in Chapter 6, and the corresponding dimensionless interface damping equated to the dimensionless interface stiffness.

$$c^* = \frac{c}{2\pi R \rho_S c_S} = k^* \tag{8.9}$$

The real and imaginary components of the system stiffness are shown in Figure 8.5(a) and (b). The improvement over an interface element with only real stiffness is dramatic. For k^* greater than 20, there is no discernible error in the real stiffness, and little error in the imaginary stiffness.

To examine the effect of interface damping on the response, the hammer impact used to examine the propagation of shear waves in Chapter 6 was applied to the finite element mesh shown in Figure 6.2(b). However, this time an interface element with $k^* = 21$ was placed between the pile and the soil. This is equivalent to a thin-layer element with $t/R = 0.1$. Analyses were performed with and without interface damping, and without an interface element. The calculated pile displacements are shown in Figure 8.6. The results obtained using the interface element with damping are indistinguishable from those obtained without any interface element, while those obtained by using the interface element without damping are completely different , especially at small times.

This study leads to the conclusion that thin layer interface elements or joint elements with finite stiffness should only be used in dynamic analyses when accompanied by sufficient internal damping. The function of this damping is not to dissipate energy, but to prevent unrealistic reflection from the interface/mesh intersection at high dimensionless frequencies.

The interface damping described here can be used with any of the joint or interface elements described in the literature which have finite elastic stiffness. A damping matrix can be formed by factoring the terms of the elastic stiffness matrix appropriately.

8.2.5 The effect of a weak interface layer

The driving of a pile disturbs the surrounding soil. This disturbance can significantly reduce the soil stiffness in the immediate vicinity of the pile. Novak and Sheta (1980) have analysed the effect of a zone of soil with reduced shear stiffness on the dynamic response of the pile. They obtained a theoretical solution for the frequency dependent complex shear stiffness of this system, representing the weakened soil layer by a spring. The mass of the thin layer was neglected to prevent reflections from the internal boundary between the regions of different stiffness. The analytical solution suggested that the radiation damping of the pile could be substantially reduced by a surrounding zone of weak soil.

Providing the zone of weakened soil is small in comparison to the pile, the Novak model is well represented by combining the far field solution for a pile radius of R with a spring of the stiffness shown in Figure 8.4. For the example presented by Novak and Sheta (1980), in which $t/R = 0.1$ and $G_m/G_s = 0.1$, a dimensionless spring stiffness of 2.1 provides results which are virtually identical to those published. This suggests that the reduced radiation damping indicated by this solution is partially due to the neglect of mass in the weakened zone, and the consequent phase shift in the response.

To investigate this further, a finite element model including a weakened zone equivalent to the example of Novak and Sheta (1980) was constructed. Analyses were performed with the weakened zone represented by finite elements with the same density as the surrounding soil, with the weakened zone represented by a spring, and with the weakened zone represented by a spring and dashpot in parallel. The results are shown in Figure 8.7.

The finite element solution shows the stress wave bouncing backwards and forwards inside the weakened zone, reducing in magnitude due to radiation damping. When the mass of the weakened zone is neglected (and the weakened zone modelled by a spring), the response at short times is quite different from the finite element response. When the weakened zone is represented by a spring and a dashpot, the initial slope is identical to the initial slope of the finite element response, but the wave reflection in the weakened layer is eliminated. The response of the damped weakened zone appears to be a smoothed version of the finite element solution.

Since the soil surrounding the pile must have mass, but the change in stiffness is unlikely to be sharp enough to cause the wave reflection computed with finite elements, the actual response of the soil is probably best represented by the damped weakened zone model. The reduction in radiation damping caused by a weakened zone is therefore more likely to be represented by Figure 8.5(b) than 8.2(b), and is probably less dramatic than would be anticipated from the work of Novak and Sheta (1980).

8.2.6 Soil/pile interface modelling

In a Von Mises soil, the soil and the pile shaft should be separated with continuously distributed rigid plastic sliders. In a numerical model, discrete rigid/plastic sliders can be used to separate the pile model from the soil model at discrete points. To allow solution by the initial stress method, these simple two-node interface elements must have finite stiffness. As discussed above, this stiffness should have both real and imaginary components. The simplest possible element therefore consists of a spring and dashpot in parallel, connected in series with rigid/plastic slider, as shown in Figure 8.8.

The complex stiffness of the spring/slider combination should be high enough to prevent distortion of the solution, but low enough to permit reasonable convergence when the slider action is calculated by the initial stress method. Since slip only occurs in the z direction, the radial degrees of freedom either side of the interface element can be rigidly linked together.

This interface element can be used between the pile and the soil in both the finite element model and the one-dimensional model. However, unless direct calculation of the soil nodal displacements, velocities and accelerations is required, the stiffness of the interface element can be ignored in the one-dimensional model, and the excess body force applied only at the pile node, as shown in Figure 8.9. Since the elastic stiffness defined by the soil model is much smaller than the interface stiffness, convergence of the Newton-Rhapson iteration is then considerably quicker.

When rigid/plastic sliders are used in a time-stepping integration scheme, the commencement and cessation of sliding are possible sources of error. Sliding usually commences within a time-step. At the beginning of the time-step the slider force is less than the yield force, and at the end of the time-step the force is greater than the yield force. When initial stress iteration is used, the force at the end of the time-step is always limited by the yield force, and the commencement of sliding taken into account implicitly. However, when the interface possesses both stiffness and damping, the separation time and the relative velocity of the two nodes at the separation time are needed to determine when sliding action ceases.

A plastic slider will close when the sliding velocity decreases to zero. If the interface has no damping, the sliding velocity is equal to the relative velocity of the two nodes, since there will be no change in spring deformation while the force is held constant. However, if the interface possesses both stiffness and damping, the slider velocity will be affected by the internal response of the element. Referring to Figure 8.8, the equation of motion for the internal spring and dashpot can be solved to find the slider velocity ($\dot{u}_S$). At any time after sliding commences, the slider velocity is determined by the equation

$$\dot{u}_S = (\dot{u}_2(t) - \dot{u}_1(t)) - (\dot{u}_2(t_S) - \dot{u}_1(t_S))\, e^{-\frac{k_i}{c_i}(t - t_S)} \qquad (8.10),$$

where t_S is the time at which sliding commenced, k_i and c_i are the interface stiffness and damping, and $\dot{u}_1$ and $\dot{u}_2$ are the nodal velocities. When the constant-average-acceleration method is used to perform the time integration, a close approximation to the separation time can be obtained from the nodal velocities and the slider force at the end of the time-step in which the yield force was exceeded, and the average nodal accelerations within the time-step.

$$t_S = t_2 - \frac{k_i(\dot{u}_2(t_S)-\dot{u}_1(t_S)) \pm \sqrt{(k_i(\dot{u}_2(t_S)-\dot{u}_1(t_S))^2 - 2k_i a\,(f(t_2)-f_y)}}{k_i\, a} \qquad (8.11)$$

The time at the end of the step is represented by t_2, the force is the slider is represented by f, the yield force is f_y, and the average relative acceleration of the nodes is

$$a = {}^1/_2\,(\ddot{u}_2(t_1) - \ddot{u}_1(t_1) + \ddot{u}_2(t_2) - \ddot{u}_1(t_2)) \qquad (8.12).$$

The sign of the square root term is selected to ensure that the separation time falls between t_1 and t_2. Once this time has been determined, the relative velocity of the nodes at separation is simply

$$\dot{u}_2(t_S) - \dot{u}_1(t_S) = \dot{u}_2(t_S) - \dot{u}_1(t_S) + a\,(t_2 - t_S) \qquad (8.13).$$

These equations allow the time at which sliding should cease to be determined accurately. However, this time is also usually inside a time-step. Unless an adjustment is made, the slider could be removed too early or too late. If the slider is not removed at the correct time, the velocity of the slider is not zero, and a small equilibrium error is introduced when the velocity is set to zero. This error can be reduced considerably by decreasing the slider force over the time-step so that the slider velocity becomes zero at the end of the time-step. This can be achieved by iteratively satisfying the equation

$$f(t_2) = f_y - {}^1/_2\,(\dot{u}_S(t_1) + \dot{u}_2(t_2) - \dot{u}_1(t_2))\, k_i\, \Delta t - (\dot{u}_S(t_1) - \dot{u}_2(t_2) + \dot{u}_1(t_2))\, c_i \qquad (8.13).$$

Unless the above adjustments are implemented, accurate results can only be obtained when the integration time-step is considerably smaller than that necessary to solve the elastic problem. When the adjustments are used, accurate results can be obtained with the same time-step.

8.2.7 Comparing the models

To compare the inelastic response of the simplified shaft model and the finite element model, the semi-infinite pile used to compare the elastic response was employed (Figure 6.25). Interface elements were placed between the pile shaft and the surrounding soil in both models. The dimensionless stiffness and damping of these elements was 20, and the shear strength (f_s) was 100 kPa.

The calculated displacements at the pile head and at the bottom of the soil layer are shown in Figure 8.10. The axial force in the pile at the pile head and at the bottom of the soil layer are shown in Figure 8.11. The results obtained from the simplified model are virtually identical to those obtained from the finite element model. Since there is no significant interaction between the soil layers when soil inelasticity is included, the vertical dimension of the soil elements surrounding the shaft need only be sufficiently small to accurately represent the axial wave in the pile, rather than small enough to represent vertical waves in the soil.

8.3 Toe penetration

8.3.1 Finite element modelling

The effect of soil inelasticity on the travelling waves under a circular rigid footing was investigated by applying the hammer impact force shown in Figure 8.12(a) to the finite element model shown in Figure 8.12(b). This hammer impact has a longer rise time than that used to investigate elastic wave propagation at the beginning of Chapter 7, and so the travelling waves are less sharp, and a coarser element mesh can be used.

Figure 8.13 shows the generalised stress in the soil at 2 ms intervals. Soil inelasticity limits the generalised shear stress to 1 MPa. The wave velocity indicates that the major part of the plastic behaviour is associated with the shear wave. The final plot in the series shows the residual soil stresses after all dynamic action has ceased.

8.3.2 The effect of pile embedment

Section 7.11 showed that the elastic response of the soil at the pile toe could be separated from the response of the soil along the shaft, and treated as a rigid footing on a half-space. However, inelastic penetration of the pile toe requires the formation of a plastic mechanism in the soil, while soil inelasticity along the shaft is confined to the pile/soil interface. Soil above the pile toe will therefore affect the failure mechanism, as indicated in Figure 8.14(a). In practice, the static failure load of an embedded circular footing in an undrained soil is often taken to be 9 s_u, while the failure load of surface footing is often taken to be 6 s_u .

The effect of embedment on the dynamic inelastic behaviour was investigated by comparing the response of a surface footing to the response of footings embedded by 2R and 4R. A dashpot was used to account for reflection of the wave back up the pile, and twice the impact load applied to the footing, as described in Section 7.12. The finite element models are presented in Figure 8.14(b). Anticipating that the inelastic footing response would be a function of the static failure load, the shear strength for the soil containing the embedded footings was taken as 330 kPa, while the shear strength for the soil under the surface footing was taken as 500 kPa, giving all footings static failure loads of approximately 2.15 MN.

The response of each footing to static loading was computed, and is shown in Figure 8.15. The behaviour of the two embedded footings was similar, especially at loads near the failure load. The failure load of the surface footing (on the stronger soil) was close to that of the embedded footings. The static failure load indicated by the finite element meshes is slightly larger than the assumed failure load of 2.15 MN, as expected.

The hammer impact shown in Figure 8.12(a) was then applied to all three meshes. The displacements of the embedded footings and the surface footing are shown in Figure 8.16(a), while the forces exerted on the footings are shown in Figure 8.16(b). Up to the time that the maximum displacement is attained, there is very little difference between the responses, supporting the proposition that the dynamic response is mainly a function of the static footing failure load. The difference between the footing embedded by 2R and that embedded by 4R is negligible.

The force exerted on the footing by the soil mass initially increases above the static failure load, but then falls below this failure load, although plastic soil deformation is still occurring. The reduction of the base force below the static failure load during inelastic penetration can be partly attributed to the effect of the dilation wave. Studies presented in the previous chapters indicated that as a dilation wave travels, a region of tensile stress develops behind the wave. This tensile stress effectively pulls the near field in the direction of the travelling dilation wave for a short period of time. In the case of the wave propagating from the pile toe, the tensile region

behind the travelling wave reduces the stresses in the soil beneath the pile, and hence the force exerted on the pile. The confining stress surrounding the plastic zone is also reduced, and so the vertical load required to produce plastic penetration is reduced.

The force on the surface footing is slightly larger than the force on the embedded footings during the later stages of plastic penetration. Consequently, when plastic behaviour ceases, the rebound of the surface footing is slightly greater.

The larger force on the surface footing supports the proposition that the dilation wave reduces both the footing force and the vertical load to produce penetration. Since the yield stress of the soil under the surface footing was larger than the yield stress of the soil surrounding the embedded footings, and the stress reduction caused by the dilation wave is not significantly affected by the embedment, the stress reduction is relatively larger for the embedded footings.

8.3.2 One-dimensional modelling

The base model originally used by Smith (1960) to model the inelastic base response is similar to that shown in Figure 8.17(a). Simons and Randolph (1985) used Lymer's analogue (Lysmer and Richart, 1969) to provide values for the spring and dashpot constants based on the fundamental soil properties of shear modulus and density. They identified the slip load of the plastic slider with the ultimate static failure load. Nguyen et al (1988) used a similar model, but relocated the position of the plastic slider to that shown in Figure 8.17(b). They used the same stiffness and damping values as Simons and Randolph.

A more complex model of inelastic footing response was proposed by Holeyman (1985). This model replaces the half-space beneath the footing with an equivalent conic solid. The cone angle is computed to ensure that the elastic response of the cone is virtually identical to the response of Lysmer's analogue. The cone is truncated with Lysmer's analogue for a footing of equal radius to the cone base. The equivalent solid is divided into one-dimensional elements of varying cross-section, as shown in Figure 8.18. The stress-strain relationship for each of these axial elements is approximated by a hyperbolic curve (Holeyman, 1988).

In Chapter 7, a new model for the elastic response of a rigid circular footing was developed. This model provided significantly better agreement with finite element results than Lysmer's analogue. The model will now be modified to include the effect of soil inelasticity. Following from the lead of the Smith models described above, a plastic slider with a slip load equal to the static failure load will be introduced.

There are three possible locations at which this slider could be introduced. These are marked A, B and C on Figure 8.19(a). Placing a slider at location A will limit the force exerted on the footing to the static failure load. The finite element results presented in Figure 8.16 indicate that the force rises significantly higher than the static failure load, so this location will not be used. Preliminary results published by Deeks and Randolph (1991) indicated that placing the slider in position C would result in an under estimation of the inelastic deformation.

Placing the slider at position B can be justified by the above observations regarding the propagation of stress waves within the half-space. The dilation wave rapidly travels away from the footing in the vertical direction. Although the dilation wave may cause soil plasticity, the time period during which inelastic displacement occurs is small. The amount of permanent displacement associated with the dilation wave is therefore also small. The plastic slider should not, therefore, be placed in series with the auxiliary mass and dashpot, as these are identified with the dilation wave. The standard spring and dashpot largely represent the response to the shear wave, which causes most of the plastic deformation. Once a plastic mechanism is formed, the force exerted on the footing can only increase if soil viscosity effects are included. These effects have been neglected in the work reported in this thesis. Since the force on the footing cannot be increased by radiation damping after a plastic mechanism has formed, the slider should be in series with both the spring and the dashpot. The slider should therefore be positioned at B, as shown in Figure 8.19(b).

As was noted above, the tensile stress region following the dilation wave reduces both the stress on the footing and the stress required to produce plastic deformation. The auxiliary mass and dashpot in the model account for the reduction of footing stress. Once the velocity of the auxiliary mass is larger than the footing velocity, the auxiliary dashpot exerts a tension on the footing. However, a method for modelling the reduction in the stress required to cause plastic deformation is not immediately evident. The reduction must be related to the tension caused by the dilation wave. The effect of reducing the plastic slider slip force in proportion to the tension in the auxiliary dashpot will be evaluated.

There is no viscosity in the ideal soil currently under consideration. However, in real soils the effect of soil viscosity on the dynamic failure could be modelled by placing an extra dashpot in series with the plastic slider, as also shown in Figure 8.19(b).

The new model will give correct static response (as will the other simplified models) and, compared with the other models, will give superior elastic response to transient loads. In the following sections, the ability of the new model to model the dynamic inelastic response will be investigated.

8.3.3 Comparison of methods

In Chapter 7, the elastic response of each of the models to a pulse of general shape was evaluated by examining the frequency dependent complex flexibility and stiffness, and comparing them with those obtained by accurate analysis. Since a pulse of arbitrary shape can be modelled as a combination of harmonics, and the system is linear, the general accuracy of the models was established. However, when inelastic soil behaviour is involved, the system is non-linear, and such a general measurement of accuracy cannot be obtained.

Since the accuracy of the elastic response of each model has already been evaluated, the additional factors which could affect the inelastic response are the ratio of maximum footing load to static failure load, the ratio of soil shear strength to soil shear modulus, and the pile impedance. The pile impedance can be non-dimensionalised by dividing by the radiation damping constant. The effect of each of these factors was examined by analysing a variety of problems. The finite element mesh and each combination of hammer, soil, and pile properties are shown in Figure 8.20.

All the arrangements were analysed using the finite element method, and using the simplified models described above. The new model with a plastic slider force equal to the static failure load will be denoted as *new model 1*, while the same model with the plastic slider force reduced by the tension in the auxiliary dashpot will be denoted as *new model 2*.

The footing displacements for arrangement A in Figure 8.20 are presented in Figure 8.21(a), and the forces in Figure 8.21(b). The new models show the footing force exceeding the static failure load, and subsequent plastic action occurs at a force less than the static failure load. This behaviour is evident in the finite element results, but not in the other simplified models. The maximum force predicted by the Smith model (1) is considerably higher than the finite element force, while the displacement is significantly lower. The results of the Holeyman model and the modified Smith model are in close agreement, but neither show the variation in footing force predicted by the finite element analysis. The modified new model, in which the plastic slider slip load is reduced by the tension in the auxiliary dashpot, shows better agreement with the finite element results than the standard new model.

The effect of the ratio of maximum force to static failure load was examined by analysing the same problem with twice the hammer load (arrangement B in Figure 8.20). The forces and displacements calculated with the different models are shown in Figure 8.22. The differences between the models noted above are still evident. The finite element results fit between the new model and the modified new model, although the models slightly underestimate the peak force. This analysis indicates that, providing the maximum hammer force is significantly higher than the static failure load, the model responses are not significantly affected by this ratio. During pile driving, the hammer forces in the pile are usually significantly higher than the static failure load of the pile base.

Deeks and Randolph (1991) have shown that, when the ratio of applied force and static failure load is close to unity, the Holeyman model predicts the finite element displacements better than the other models. This is because the hyperbolic stress-strain relationship used in Holeyman's model permits inelastic deformation to occur before the static failure load is reached. Such deformation is not permitted by any of the other models. However, in practical pile driving problems most inelastic deformation takes place after the static failure load is exceeded.

The effect of pile impedance was examined by considering two extremes. Firstly, the influence of the pile was disregarded entirely, and the hammer load was applied directly to the footing (arrangement C in Figure 8.20). This represents a pile impedance of zero. The footing was given a mass of 8000 kg (equivalent to the anvil mass) to prevent unrealistic acceleration under the prescribed impact load. Secondly, a pile impedance of 10 MNs/m was used, representing the upper end of practical pile impedances (arrangement D in Figure 8.20). The results from the arrangement C are shown in Figure 8.23, and from arrangement D in Figure 8.24.

When no pile impedance is used, all the models except the original Smith model yield results which are similar to the finite element model. However, the results of the new model are significantly closer than the other models. When the pile impedance is 10 MNs/m, the same differences between the models and the finite element results are still evident, showing that the models account quite well for the pile impedance. The finite element results fall between the results of the new model and the modified new model.

The effect of the soil strength/stiffness ratio was examined by increasing the soil strength by a factor of three (arrangement E in Figure 8.20). The hammer force was doubled to ensure sufficient inelastic penentration. The computed displacements and force are shown in Figure 8.25. The effect of the soil/strength ratio can be seen by contrasting these results with those shown in Figure 8.22, which were obtained for the same hammer blow and a static failure load of 2.15 MN. The effectiveness of the models is not affected. The modified new model best represents the finite element results.

The effect of a sharper hammer blow was investigated by using the original footing and soil strength and increasing the cushion stiffness to halve the rise time of the hammer force (arrangement F in Figure 8.20). The resulting displacements and forces are shown in Figure 8.26. Again, the same differences between the models can be observed. While slightly underestimating the peak force, the modified new model best fits the finite element results.

The foregoing investigations have shown that the new models are significantly better than existing base models, yielding results which are in close agreement with results obtained from accurate finite element analysis. This agreement has been shown to extend over a broad range of problems. The differences between the new model and the modified new model were only apparent at large times, and the forces computed from the finite element models were often found to fall between the forces computed with the two new models. Consequently, although the results of the modified new model were generally better, the simpler new model can be used with only slight reduction in accuracy.

8.4 Overall pile response

The foregoing analyses have established the accuracy of the simplified shaft model and the new base models. The effect of combining the shaft and base models will now be examined, and compared with a complete finite element model.

Due to computer capacity limitations, the short pile shown in Figure 8.27(a) was analysed. The response was computed using the finite element mesh of Figure 8.27(b) and the simplified model shown in Figure 8.27(c). Both of the new base models were used.

The results obtained for a single hammer blow are shown in Figure 8.28. The results from the new one-dimensional models are very close to those computed with the finite element model. The model with the modified new base (designated as 1D model (b)) gave slightly better results than the model with the standard new base (1D model (a)). However, both models gave good representation of the significant features of the displacement and force responses.

8.5 Repeated driving and residual stresses

The abilities of the one-dimensional models to represent residual stresses in the soil and the pile were examined by subjecting the same pile to three hammer blows, preserving the permanent displacements and residual stresses between each blow.

The displacements and forces are presented in Figure 8.29. The simple models again gave results which are very close to the finite element results. The model with the modified new base gave a better approximation to the displacement. However, by the third blow the finite element force response was closer to the model with the standard new base.

The variation of residual axial force along the length of the pile is shown in Figure 8.30 for each blow. Again, the results from the simple models are very close to the finite element results. During the first blow, the model with the modified base predicted the residual axial force better. However, by the third blow the standard new base model was superior. The residual soil stresses surrounding the pile after three blows were computed from the finite element analysis, and are shown in Figure 8.31.

The behaviour of the finite element model falls between the model with the standard new base and the model with the modified new base. At higher blow counts, the error in the standard base model is reduced. In practical pile driving problems, the pile is driven from the surface, so residual soil stresses surround the pile at every hammer blow except the first. Consequently, the simple version of the new base model should be adequate in most applications, and will be used in the comparisons which follow.

8.6 Comparison with other analyses

This thesis has shown that much care must be taken to ensure that finite element analysis of pile driving yields accurate results. Some analyses presented in the past have not taken this care. As an illustration, the problem presented by Simons (1985) was re-analysed using a finite element mesh of appropriate fineness, and using the new one-dimensional model. The pile, hammer, and soil parameters are shown in Figure 8.32(a), and the mesh used in the present analysis is shown in Figure 8.32(b). The finite element mesh used by Simons was shown in Figure 2.6. The work reported above has shown that the shear transmitting boundary together with a plastic slider represents the effect of soil along the pile shaft extremely well, so this boundary was used along the pile shaft to reduce the size of the finite element mesh.

The displacement at the pile head computed by the different methods are shown in Figure 8.34. Simon's finite element results are far worse than those he obtained with a simplified one-dimensional analysis. The difference between the new one-dimensional model and the current finite element analysis is small.

The problem used by Chow (1981) was also analysed. The pile is shown in Figure 8.34(a), and the finite element mesh in Figure 8.34(b). Chow's mesh was shown in Figure 2.4. The results are shown in Figure 8.35. The new one-dimensional model and the current finite element analysis are in close agreement, but the only similarity with Chow's results is the permanent displacement.

8.7 Conclusions

This chapter examined the effect of inelastic soil behaviour on pile driving dynamics. Slip between the pile shaft and the surrounding soil was modelled by using interface elements with complex stiffness, as interface elements with only in-phase stiffness were found to interfere with the elastic response of the system. The differences between a finite element model of the shaft response and a one-dimensional model with the shear transmitting boundary separated from the pile by plastic sliders were found to be negligible.

The effects of inelasticity on the stress waves emanating from a rigid footing were examined by finite element analysis. Existing simplified base models were reviewed, and two alternative models were formed by modifying the new elastic base model to include soil plasticity. The base models were compared with finite element results for a range of pile driving problems, and the new models were shown to be more accurate than the other models. The accuracy of the new models was shown to be insensitive to pile embedment, applied force to static failure load ratio, soil strength ratio, pile impedance, and force rise time.

A complete pile/soil problem was then analysed, using a finite element model and new one-dimensional models. The new models consisted of a one-dimensional pile with the shear transmitting boundary separated from the shaft by plastic sliders, and the new base models. The new models were shown to agree well with the finite element analysis. During repeated blows, the model incorporating the standard version of the new base model was found to perform slightly better than the model with the modified version, justifying the adoption of the simpler version.

Two pile driving problems available in the literature were analysed, and the new simplified model was shown to give closer agreement with accurate finite element analysis than the published finite element solutions.

9. SUMMARY AND CONCLUSION

9.1 Synopsis

Dynamic soil-pile interaction models used in practical field applications must be 'correct' for ideal conditions, otherwise no faith can be placed in soil parameters deduced from such models. Conversely, without models based on measurable soil parameters, predictive dynamic pile analysis must rely on empirical soil-pile interaction models. In a contribution to the development of a model based on fundamental soil parameters, this thesis has presented a detailed study of dynamic soil-pile interaction in a simple (ideal) soil. The study proceeded in a methodical manner through hammer impact, stress wave propagation in the pile, elastic shear wave radiation from the shaft, elastic wave radiation from the toe, the effect of soil inelasticity on the wave radiation, and finally the analysis of the complete pile-soil system. In the process, a simplified model was developed which represents the behaviour of the ideal system extremely well, laying the basis for simplified models that may be calibrated in future work for field application.

This chapter presents a summary of the contents of the thesis, including the major findings and conclusions. The summary is followed by a section identifying areas in which further work could be performed, and concluding remarks.

9.2 Summary

Following a literature review, an analytical study of some simple drop hammer models was performed. The equations of motion of the hammers were written in a new dimensionless form, and the force exerted on the pile solved analytically for each model. Two of these analytical solutions are new. Comparisons with field data were presented, demonstrating the ability of the new solutions to represent real hammers. Unlike numerical models of the pile hammer system, the analytical solutions allow parametric studies of hammers performance to be carried out quickly and easily. Studies of ram separation, transmitted energy, and maximum transmitted force were presented to illustrate this ability.

The propagation of axial stress waves within a pile was then studied using the finite element method. The major conclusions from this study were that a continuous impulse function should be used to represent the hammer impact, and that the node spacing be small enough for the finite element mesh to adequately represent the sharply rising wave-front. Unless these conditions were maintained, the travelling stress wave was found to give rise to spurious high frequency oscillation. A study of time integration schemes concluded that the Newmark constant-average acceleration method most faithfully represented the response of the discrete finite element mesh. Errors introduced by ignoring the effects of radial inertia were found to be quite small, and an adequate representation of the pile behaviour was achieved by ignoring radial inertia and assuming plane sections remained plane.

The radiation of elastic shear and dilation waves from the pile shaft was then studied. The deformation of the soil along the shaft was found to be essentially plane strain, as the axial wave velocity in the pile was much higher than either the shear wave velocity or the dilation wave velocity in the soil. An investigation of the propagating axisymmetric plane strain waves revealed that both the shear and dilation waves sharpen as they propagate away from the pile. Consequently, increasing the size of the finite elements away from the pile was found to cause significant erroneous reflection.

Truncation of the finite element meshes with a standard viscous boundary was found to lead to rigid body motion. A new derivation of a transmitting boundary for transient axisymmetric plane strain shear waves was presented. This boundary consists of a spring and a dashpot. The boundary was shown to give excellent agreement with an extended finite element mesh, even when applied directly to the pile shaft. A similar boundary was derived for axisymmetric plane strain dilation waves. A new equivalent mechanical model for this boundary was also derived. Again, the boundary was shown to give good agreement with a finite element mesh, even when applied directly to the pile shaft.

Little interaction between the soil adjacent to the pile shaft and the soil beneath the pile toe was found, so the radiation of waves from the pile toe was initially examined by considering the response of a rigid circular footing on a semi-infinite half-space. The stress waves emanating from a rigid footing subject to hammer impact were examined. The dilation wave was found to propagate downwards, with little geometric attenuation of horizontal dispersion. The shear wave was found to form a reasonably uniform stress hemisphere propagating from the footing.

The response of a rigid footing to harmonic loads was examined, and a new technique for computing the frequency dependent complex stiffness and flexibility from one finite element analysis was proposed. In this technique, a multi-frequency transient load is applied to the footing, and the displacement computed at discrete time intervals until the footing returns to rest. Fourier series representing both the applied force and the computed displacement are formed, and the complex flexibility is calculated for each discrete frequency in the series. The technique was shown to provide answers which agreed well with analytical and published solutions.

Simplified mechanical models of dynamic footing response were considered. An improved model was constructed by matching the complex stiffness of the footing model with the complex stiffness computed by finite element analyses for a variety of Poisson's ratios over a large range of dimensionless frequencies. When subjected to impact loads, the new model was found to give closer agreement with finite element results than existing models.

The elastic response of an embedded rigid pile was found to be adequately modelled by combining the new base model with an appropriate length of shaft transmitting boundary, indicating that little interaction occurs between the soil surrounding the shaft and the soil beneath the pile toe. A simplified model consisting of a one-dimensional pile, the shear boundary applied along the pile shaft, and the new base model was found to represent the elastic behaviour of a complete finite element model extremely well.

The effect of soil inelasticity was then examined. Slip between the pile shaft and the surrounding soil was modelled using interface elements. Interface elements with only in phase stiffness were found to interfere with the response of the elastic system. A new interface element with complex stiffness was proposed. This interface element was shown to considerably reduce the distortion of the elastic solution.

The response of a finite element shaft model with interface elements between the pile and the soil was shown to be well represented by a one-dimensional model with the shear transmitting boundary separated from the pile by plastic sliders.

The elastic model for the soil at the pile base was extended to include inelastic behaviour by the insertion of a plastic slider with a yield force equal to the static failure load. The new model was found to reproduce the results of finite element analyses significantly better than existing models. In particular, the force exerted on the pile was found to initially rise above the static failure load, and then drop below the failure load while plastic deformation continued. The new model was the only model which reproduced this behaviour. The accuracy of the new model was found to be insensitive to pile embedment, ratio of applied force to static failure load, soil strength ratio, pile impedance, and force rise time.

A complete pile/soil problem was analysed using a finite element model. These results were found to be reproduced extremely well by a simplified model consisting of a one-dimensional pile, the shear transmitting boundary separated from the shaft by plastic sliders, and the new inelastic base model. Two pile driving problems from the literature were analysed, and the new model was found to give closer agreement with accurate finite element analysis than the published solutions.

9.3 Further work

This thesis has shown that a simplified model can represent the driving of a closed ended pile in a Von Mises soil extremely well. However, there are a number of areas in which more work can be done.

An analytical solution for a hammer model with cushion damping was presented in Chapter 3. This cushion damping could be chosen so that the solution represented field data very well. Research needs to be conducted into the equivalent cushion damping present in a range of practical hammer systems, so that the solution can be used to model the hammer in practical problems.

In Chapter 5, the radial motion of the pile wall was found to have only a small effect on the overall pile response. However, for a thin-walled pile, the radial motion was found to change the shape of the propagating wave quite significantly. This could affect the reflected force often measured at the pile head during driving. A full study of the effect of radial pile motion on the stress wave is required. The models developed in this thesis for shear, dilation, and base wave transmission could be used to represent the soil. Full finite element models of a range of thin-walled piles could then be studied, and comparisons made with field measurements.

A new method for computing the complex compliance of footings from a finite element analysis was proposed in Chapter 7. This method could be developed further, as it has the potential to compute the compliance of footings for which analytical solutions are not available.

In Chapter 8, standard interface elements were found to cause significant distortion of the elastic solution, and an improved interface element with complex stiffness was proposed which could overcome this problem. The interface element was only used in a basic two-noded form. The element could be formulated in more general terms, and applied to a variety of dynamic structure soil interaction problems.

The new base model was shown to reproduce the finite element results extremely well. An experimental study into inelastic base response could be undertaken to verify the theoretical predictions. The effect of a different soil type on both the finite element response and the experimental response could be examined.

A detailed study correlating the complete pile driving model with a wide range of field data should be performed, determining whether the new model provides a significant practical improvement over the existing models.

The study reported in this thesis was limited to closed ended piles. Since doubt has been raised regarding the accuracy of previously published finite element results, a detailed study of the dynamic response of an open-ended pile should be undertaken. The soil surrounding the pile shaft could be modelled with the shaft model presented above, and finite elements used to represent the soil plug and the soil immediately surrounding the pile toe. The mesh could be truncated with the transmitting boundaries described in this thesis.

9.4 Concluding remarks

A detailed study of pile driving dynamics has lead to an improved model of pile-soil interaction which represents the theoretical behaviour of a pile in an ideal soil extremely well. More complex finite element models can only achieve greater accuracy than the improved model when great care is exercised. The new model is a promising alternative to empirical models in current use, and, once calibrated with field data, should find widespread application.

REFERENCES

Bathe, K.J. and Wilson, E.L. (1976). *Numerical Methods in Finite Element Analysis*, Prentice-Hall Inc., New Jersey.

Beltyschko, T., Chiapetta, R.L., and Bartel, H.D. (1976). 'Efficient large scale non linear transient analysis by finite elements.' *Int. J. Num. Meth. Engineering*, vol. 10, 579-596.

Bettess, P. (1977). 'Infinite elements.' *Int. J. Num. Meth. Engg*, vol. 11, 53-64.

Booker, J. (1985). Private communication to M.F. Randolph.

Bycroft, G.N. (1954). 'Forced vibrations of a rigid circular plate on a semi-infinite elastic space and on an elastic stratum.' *Phil. Trans. of the Royal Society of London*, vol. 248, series A, no. 948, 327-368.

Chellis, R.D. (1961). *Pile Foundations*, McGraw Hill.

Chen, W.F. and Baladi, G.Y. (1985). *Soil Plasticity: Theory and Implementation*, Elsevier, Amsterdam.

Chow, Y.K. (1981). *Dynamic Behaviour of Piles*, PhD Thesis, University of Manchester.

Chow, Y.K. (1985). 'Accuracy of consistent and lumped viscous dampers in wave propagation problems.' *Int. J. Num. Meth. Engg*, vol. 21, 723-732.

Cohen, M., and Jennings, P. C. (1983). 'Silent boundary methods for transient analysis.' In *Computational Methods for Transient Analysis*, (eds. Belytschko, T., and Hughes, T. J. R.), Elsevier, Amsterdam.

Corte, J.-F., and Lepert, P. (1986). 'Lateral resistance during driving and dynamic pile testing.' *Third Int. Conf. on Numerical Methods in Offshore Piling*, Nantes, 19-33.

Coutinho, A.L.G.A., Costa, A.M., Alves, J.L.D., Landau, L. and Ebecken, N.F.F. (1988). 'Pile driving simulation and analysis by the finite element method.' *Third Int. Conf. on Numerical Methods in Offshore Piling*, Nantes, 3-15.

Coyle, H.M., Lowery, L.L.Jr., and Hirsch, T.J. (1977). 'Wave equation analysis of piling behaviour.' In *Numerical Methods in Geotechnical Engineering*, (eds Desai, C.S., and Christian, J.T.), McGraw Hill.

Dayal, U., and Allen, J.H. (1975). 'The effect of penentration rate on the strength of remoulded clay and sand samples.' *Canadian Geotechnical J.*, vol.12, 336-348.

Dean, A.C. (1935). *Piles and Pile Driving*, Crosby, Lockwood & Son.

Deeks, A.J. and Clyde, D.H. (1992). 'Efficient solution of piece-wise linear structures.' Submitted for publication.

Deeks, A.J. and Randolph, M.F. (1991). 'Evaluation of the inelastic response of an axisymmetric foundation to impact loading.' *Proc. 7th Int. Conf. Computer Methods and Advances in Geomechanics*, Cairns, vol. 1, 735-740.

Deeks, A.J., Patnaikuni, I., and Clyde, D.H. (1984). 'Flexibility revisited.' *Ninth Aust. Conf. Mech. Structures and Materials*, Sydney.

Desai, C.S., Zaman, M.M., Lightner, J.G., and Siriwardane, H.J. (1984). 'Thin-layer interface element for interfaces and joints.' *Int. J. Num. Anal. Meth. Geomech.*, vol. 8, 19-43.

Engquist, B., and Majda, A. (1979). 'Radiation boundary conditions for acoustic and elastic wave calculations.' *Comm. Pure App. Math.* vol. 32, 313-357.

Finlayson, B.A. (1972). *The Method of Weighted Residuals and Variational Principles.* Academic Press.

Fox, E.N. (1932). 'Stress phenomena occurring in pile driving.' *Engineering*, vol. 134, 263-265.

Ghaboussi, J., Wilson, E.L., and Isenberg, J. (1973). 'Finite element for rock joints and interfaces.' *J. Soil. Mech. and Found. Div.*, ASCE, vol. 99, no. 10, 833-848.

Gibson, G.C., and Coyle, H.M. (1968). 'Soil damping constants related to common soil properties in sands and clays.' Report No. 125-1, Texas Transport Institute, Texas A and M University.

Glanville, W.H., Grime, G., Fox, E.N., and Davies, W.W. (1938). 'An investigation of the stresses in reinforced concrete piles during driving.' British Building Research Board, Technical Paper 20.

Goble, G.G. and Rausche, F. (1986). *WEAP86 program documentation in 4 Vols*, Federal Highway Administration, Office of Implementation, Washington D.C.

Goble, G.G., Likins, G.E.Jr., and Rausche, F. (1975). 'Bearing capacity of piles from dynamic measurements.' Final report, Dept of Civil Engg, Case Western Reserve University.

Goble, G.G., Rausche, F., and Likins, G.E.Jr. (1980). 'The analysis of pile driving - a state-of-the-art.' *Int. Seminar of the Application of Stress-Wave Theory on Piles*, Stockholm.

Hardin, B.O. and Drnevich, V.P. (1972). 'Shear modulus and damping in soils: design equations and curves.' *J. Soil Mech. Found. Engg*, ASCE, vol. 98, no. SM7, 667-692.

Holeyman, A.E. (1985). 'Dynamic non linear skin friction of piles.' Comptes-rendus Symposium, *Penetrability and Driveability of Piles*, San Franciso, 173-176.

Holeyman, A.E. (1988). 'Modelling of dynamic behaviour at the pile base.' *Third Int. Conf. on the Application of Stress Wave Theory to Piles*, Ottawa.

Issacs, D.V. (1931). 'Reinforced concrete pile formulas.' *Trans. Inst. Engineers Aust*, XII, pp 305-323.

Johnson, W. (1972). *Impact Strength of Materials.* Arnold, London.

Legget, R.F. (1973). *Cities and Geology*. McGraw Hill.

Leong, E.C. (1991). *A Study of Internal and External Shaft Friction of Piles.* PhD thesis, University of Western Australia.

Liao, Z. P., and Wong, H. L. (1984). 'A transmitting boundary for the numerical simulation of elastic wave propagation.' *Soil Dyn. Earthq. Engg*, vol. 3, 174-183.

Litkouhi, S. and Poskitt, T.J. (1980). 'Damping constants for pile driveability calculations.' *Geotechnique*, vol. 30, no. 1, 77-86.

Luco, J.E. and Westmann, R.A. (1971). 'Dynamic response of circular footings.' *J. Eng. Mech. Div.*, ASCE, vol. EM5, 1381-1395.

Luco, J.E. and Westmann, R.A. (1972). 'Dynamic response of a rigid footing bonded to an elastic half space.' *J. App. Mech.*, ASME, vol. 39, 527-534.

Lysmer, J. (1965). *Vertical Motion of Rigid Footings.* PhD thesis, University of Michegan.

Lysmer, J., and Kuhlemeyer, R. L. (1969). 'Finite dynamic model for infinite media', *J. Eng. Mech. Div.*, ASCE, vol. 95, no. EM4, 859-877.

Lysmer, J. and Richart, F.E. (1966). 'Dynamic reponse of footing to vertical loading.' *J. Eng. Mech. Div.*, ASCE, vol. 92, 65-91.

Lysmer, J., and Waas, G. (1972). 'Shear Waves in Plane Infinite Structures.' *J. Eng. Mech. Div.*, ASCE, vol. 98, no. EM1, 85-105.

Meynard, A. and Corte, J.-F. (1984). 'Experimental study of lateral resistance during driving.' *Second Int. Conf. on the Application of Stress-Wave Theory of Piles*, Stockholm.

Middendorp, P. and van Weele, A.F. (1986). 'Application of characteristic stress wave method in offshore practice.' *Proc. 3rd Int. Conf. on Num. Methods in Offshore Piling*, Nantes, Supplement, 6-18.

Mitwally, H. and Novak, M. (1988). 'Pile driving analysis using shaft models and FEM.' *Third Int. Conf. on the Application of Stress Wave Theory to Piles*, Ottawa.

Nguyen, T.T., Berggren, B., and Hansbo, S. (1988). 'Lateral resistance during driving and dynamic pile testing.' *Third Int. Conf. on the Application of Stress Wave Theory to Piles*, Ottawa.

Novak, M. (1977). 'Vertical vibration of floating piles.' *J. Eng. Mech. Div.*, ASCE, vol. 103, 153-168.

Novak, M., and Mitwally, H. (1988). 'Transmitting boundary for axisymmetrical dilation problems.' *J. Eng. Mech. Div.*, ASCE, vol. 114, no. 1, 181-187.

Novak, M. and Sheta, M. (1980). 'Approximate approach to contact effects of piles.' *Proc. of Session on Dynamic Response of Pile Foundations: Analytical Aspects*, ASCE National Convention, Florida, 53-79.

Novak, M., Nogami, T. and Aboul-Ella, F. (1978). 'Dynamic soil reactions for plane strain case.' *J. Eng. Mech. Div.*, ASCE, vol. 104, 953-959.

Oden, J.T. and Wellford, L.C, Jr. (1975). 'Some new finite element methods for the analysis of shock and acceleration waves in nonlinear materials.' In *Finite Element Analysis of Transient Nonlinear Structural Behaviour*, (eds Belytschoko, T., Osias, J.R., and Marcal, P.V.), ASME, Texas.

Randolph, M. F., and Pennington, D. S. (1988). 'A numerical study of dynamic cavity expansion.' *Proc. 6th Int. Conf. Num. and Anal. Meth. Geomechanics*, 329-342.

Randolph, M.F. and Simons, H.A. (1986). 'An improved soil model for one-dimensional pile driving analysis.' *Third Int. Conf. on Numerical Methods in Offshore Piling*, Nantes, 3-15.

Randolph, M.F. (1991). 'Analysis of the dynamics of pile driving.' In *Developments in Soil Mechanics IV: Advanced Geotechnical Analyses*, (eds P.K. Banerjee and R. Butterfield), Elsevier Applied Science, also *University of Western Australia Research Report No. G1001*.

Rausche, F., Goble, G.G. and Likins, G.E. (1988). 'Recent WEAP developments.' *Proc. 3rd Int. Conf. on Application of Stress-Wave Theory to Piles*, Ottawa, 164-173.

Robertson, I.A. (1966). 'Forced vertical vibration of a rigid circular disc on a semi-infinite elastic solid.' *Proc. Cambridge Phil. Soc.*, vol. 62, series A, 547-553.

Shah, P.M. (1968). *On the Dynamic Response of Foundation Systems.* PhD thesis, Rice University, Houston, Texas.

Simons, H.A. and Randolph, M.F. (1985). 'A new approach to one-dimensional pile driving analysis.' *Proc. Fifth Int. Conf. on Numerical Methods in Geomechanics*, Nagoya, vol. 3, 1457-1464.

Simons, H.A. (1985). *A Theoretical Study of Pile Driving.* PhD Thesis, University of Cambridge.

Smith, E.A.L. (1960). 'Pile driving analysis by the wave equation.' *J. Soil Mech. and Found.*, ASCE, vol. 86, 35-61.

Smith, I.M. (1982). *Programming the Finite Element Method with Application to Geomechanics.* Wiley.

Smith, I.M. and Chow, Y.K. (1982). 'Three dimensional analysis of pile drivability.' *Proc. Second Int. Conf. on Numerical Methods in Offshore Piling*, Autin, 1-9.

Smith, I.M., To, P. and Wilson, S.M. (1986). 'Plugging of pile piles.' *Third Int. Conf. on Numerical Methods in Offshore Piling*, Nantes, 53-74.

Smith, W. D. (1974). 'A non-reflecting plane boundary for wave propagation problems.' *J. Comput. Phys.*, vol. 15, 492-503.

Terzaghi, C. (1929). 'The science of foundations - its present and future.' *Trans. ASCE*, paper 1704, 270-405.

Timoshenko, S. and Goodier, J.M. (1951). *Theory of Elasticity.* Second edition, McGraw Hill.

Toki, K., Sato, T., and Miura, F. (1981). 'Separation between soil and structure during strong ground motion.' *Earthquake Engineering and Structural Dynamics*, vol. 9, 263-277.

Underwood, P., and Geers, T. L. (1981). 'Doubly asymptotic boundary-element analysis of dynamic soil-structure interaction.' *Int. J. Solids Struct.*, vol. 17, 687-697.

Warrington, D.C. (1988). 'A new type of wave equation analysis program.' *Third Int. Conf. on the Application of Stress Wave Theory to Piles*, Ottawa.

White, W., Valliappan, S., and Lee, I. K. (1977). 'Unified boundary for finite dynamic models.' *J. Eng. Mech. Div.*, ASCE, vol. 103, no. EM5, 949-964.

Whitham, G. B. (1974). *Linear and Nonlinear Waves.* Wiley, New York.

Wolf, J. P. (1986). 'A comparison of time-domain transmitting boundaries.' *Earthq. Engrg. and Struct. Dyn.*, vol. 14, 655-673.

Wolf, J.P. (1988). *Soil-Structure-Interaction Analysis in Time Domain.* Prentice-Hall, New Jersey.

Yamada, Y., Yoshimura, N., and Sakurai, T. (1968). 'Plastic stress-strain matrix and its application for the solution of elastic plastic problems.' *Int. J. Mech. Sci.*, vol. 10, 343-354.

Zaman, M., Desai, C.S., and Drumm, E.C. (1984). 'Interface model for dynamic soil-structure interaction.' *J. Geotechnical Engineering*, ASCE, vol. 110, no. 9, 1257-1273.

Zienkiewicz, O.C. (1977). *The Finite Element Method.* Third edition, McGraw-Hill.

Zienkiewicz, O.C., Best, B., Dullage, C., and Stagg, K.G. (1970). 'Analysis of non linear problems in rock mechanics with particular reference to jointed rock systems.' *Proc. 2nd Int. Conf. Soc. of Rock Mech.*, Belgrade, vol. 3, 501-509.

APPENDIX A -- SOLUTION OF RAM/CUSHION/ANVIL MODEL

The Laplace transform for the anvil velocity in the ram/cushion/anvil model is

$$L\,\dot{u}_a^* = \frac{\frac{k_c^*}{m_a^*}}{\frac{k_c^*}{m_a^*} + k_c^*\left(\frac{1}{m_a^*} + 1\right)s + \frac{1}{m_a^*}s^2 + s^3} \tag{A1}.$$

Naming the coefficients of the cubic denominator

$$a_0 = \frac{k_c^*}{m_a^*},\quad a_1 = k_c^*\left(\frac{1}{m_a^*} + 1\right),\quad a_2 = \frac{1}{m_a^*} \tag{A2},$$

equation (3.32) can be written as

$$L\,\dot{u}_a^* = \frac{a_0}{a_0 + a_1 s + a_2 s^2 + s^3} \tag{A3}.$$

Letting

$$\alpha = \frac{a_1 a_2}{6} - \frac{a_0}{2} - \frac{a_2^3}{27} \tag{A4}$$

and

$$\beta = \sqrt{\frac{a_1^3}{27} - \frac{a_1^2 a_2^2}{108} - \frac{a_0 a_1 a_2}{6} + \frac{a_0^2}{4} + \frac{a_0 a_2^3}{27}} \tag{A5},$$

if β^2 is greater than zero, the cubic denominator of equation (A1) has one real root and two imaginary roots. The inverse transform can be found readily if the following substitutions are made.

$$b_1 = \frac{a_2}{3} - (\alpha+\beta)^{1/3} - (\alpha-\beta)^{1/3} \tag{A6}$$

$$b_2 = \frac{a_2}{3} + \frac{1}{2}\left((\alpha+\beta)^{1/3} + (\alpha-\beta)^{1/3}\right) \tag{A7}$$

$$\omega = \frac{\sqrt{3}}{2}\left((\alpha+\beta)^{1/3} - (\alpha-\beta)^{1/3}\right) \tag{A8}$$

This allows the cubic denominator to be factorised, and equation (A1) becomes

$$L\,\dot{u}_a^* = \frac{a_0}{(s+b_1)\left((s+b_2)^2 + \omega^2\right)} \tag{A9},$$

which can be expanded to

$$L\,\dot{u}_a^* = \frac{a_0}{\omega^2+(b_2-b_1)^2}\left(\frac{1}{s+b_1} - \left(\frac{s+b_2}{(s+b_2)^2+\omega^2} + \frac{b_2-b_1}{(s+b_2)^2+\omega^2}\right)\right) \tag{A10}.$$

Performing the inverse Laplace transform, the anvil velocity can be found.

$$\dot{u}_a^* = \frac{a_0}{\omega^2+(b_2-b_1)^2}\left(e^{-b_1 t^*} - e^{-b_2 t^*}\left(\cos\omega t^* + \frac{b_2-b_1}{\omega}\sin\omega t^*\right)\right) \tag{A11}$$

This solution can be written in a simpler, more convenient form by making

$$c_1 = b_1\ ,\ c_2 = b_2\ -\ b_1\ ,\ \phi = \text{atan}\ \frac{c_2}{\omega}\ ,\ \text{and}\ F_p = \frac{a_0}{\omega^2 + {c_2}^2} \tag{A12}.$$

The anvil velocity and the force on the pile head are then

$$f_p^{\,*} = \dot{u}_a^{\,*} = F_p\ e^{-c_1 t^*}\left(1\ -\ e^{-c_2 t^*}\ \frac{\cos\ (\omega t^*\ -\ \phi)}{\cos\ \phi}\right) \tag{A13}.$$

The spring force can be found by using the equilibrium equation

$$f_s^{\,*} = m_a^{\,*}\ \ddot{u}_a^{\,*} + \dot{u}_a^{\,*} \tag{A14}.$$

Differentiating equation (A13), substituting into equation (A14), and simplifying, the spring force can be expressed as

$$f_s^{\,*} = F_S\left(e^{c_2 t^*}\ -\ \frac{\cos\ (\omega t^*\ -\ \theta)}{\cos\ \theta}\right) \tag{A15},$$

where

$$\theta = \text{atan}\left(\frac{c_2\ (a_2\ -\ c_1\ --\ c_2)\ -\ \omega^2}{\omega\ (a_2\ -\ c_1)}\right)\ \text{and}\ F_S = \frac{a_0\ (a_2 - c_1)}{\omega^2 + {c_2}^2} \tag{A16}.$$

For most combinations of $m_a^{\,*}$ and $k_c^{\,*}$, β^2 is greater than zero, and the solution presented above applies. For a small range of combinations, β^{*2} is less than or equal to zero, and a different solution must be used. When this is the case, the cubic denominator has three real roots, and equation (A1) can be written in the following way.

$$\text{L}\ \dot{u}_a^{\,*} = \frac{a_0}{(s\ +\ b_1)\ (s\ +\ b_2)\ (s\ +\ b_3)} \tag{A17}$$

$$b_1 = \frac{a_2}{3}\ +\ 2\sqrt{Q}\ \cos\frac{\theta}{3} \tag{A18}$$

$$b_2 = \frac{a_2}{3}\ +\ 2\sqrt{Q}\ \cos\frac{\theta + 2\pi}{3} \tag{A19}$$

$$b_3 = \frac{a_2}{3}\ +\ 2\sqrt{Q}\ \cos\frac{\theta + 4\pi}{3} \tag{A20}$$

$$Q = \frac{{a_2}^2\ -\ 3\ a_1}{9} \tag{A21}$$

$$R = \frac{2\ {a_2}^3\ -\ 9\ a_1\ a_2\ +\ 27\ a_0}{54} \tag{A22}$$

$$\theta = \text{acos}\left(\frac{R}{\sqrt{Q^3}}\right) \tag{A23}$$

If b_1, b_2, and b_3 are all distinct, equation (A18) becomes

$$\text{L}\ \dot{u}_a^{\,*} = a_0\left(\frac{1}{(s+b_1)(b_2-b_1)(b_3-b_1)} + \frac{1}{(s+b_2)(b_1-b_2)(b_3-b_2)} + \frac{1}{(s+b_3)(b_1-b_3)(b_2-b_3)}\right) \tag{A24}$$

and the solution is given by

$$f_p^{\,*} = \dot{u}_a^{\,*} = F_p\left(e^{-b_1 t^*}\ -\ A_p\ e^{-b_2 t^*}\ -\ B_p\ e^{-b_3 t^*}\right) \tag{A25}$$

with

$$F_p = \frac{a_0}{(b_2-b_1)(b_3-b_1)}, \quad A_p = \frac{b_3-b_2}{b_3-b_1}, \text{and} \quad B_p = \frac{b_2-b_1}{b_2-b_3} \tag{A26}.$$

The force in the spring is

$$f_s^* = a_0 \left(\frac{(a_2-b_1)e^{-b_1 t^*}}{(b_2-b_1)(b_3-b_1)} + \frac{(a_2-b_2)e^{-b_2 t^*}}{(b_1-b_2)(b_3-b_2)} + \frac{(a_2-b_3)e^{-b_3 t^*}}{(b_1-b_3)(b_2-b_3)} \right) \tag{A27}$$

or

$$f_s^* = F_s \left(e^{-b_1 t^*} - A_s e^{-b_2 t^*} - B_s e^{-b_3 t^*} \right) \tag{A28}$$

with

$$F_s = \frac{a_0 (a_2-b_1)}{(b_2-b_1)(b_3-b_1)}, \quad A_s = \frac{a_2-b_2}{a_2-b_1}\frac{b_3-b_2}{b_3-b_1}, \text{and} \quad B_s = \frac{a_2-b_3}{a_2-b_1}\frac{b_2-b_1}{b_2-b_3} \tag{A29}.$$

However, if two of the roots are the same, the solution is different again. When β is zero and b_3 is equal to b_2, and the solution becomes

$$f_p^* = \dot{u}_a^* = F_p e^{-c_1 t^*} \left(1 - e^{-c_2 t^*} (1 + b_2 t^*) \right) \tag{A30}$$

$$f_s^* = F_s e^{-c_1 t^*} \left(1 - e^{-c_2 t^*} (1 + b_2 A_s t^*) \right) \tag{A31}$$

$$F_p = \frac{a_0}{c_2^2}, \quad F_s = \frac{a_0}{m_a^* c_2^2}, \quad A_s = 1 - m_a^* b_2 \tag{A32}.$$

APPENDIX B -- SOLUTION OF DAMPED CUSHION MODEL

The Laplace transform of the anvil velocity for the damped cushion model is

$$\mathrm{L}\,\dot{u}_a^* = \frac{\frac{c_c^*}{m_a^*}\left(s + \frac{k_c^*}{c_c^*}\right)}{\frac{k_c^*}{m_a^*} + \left(k_c^*\left(\frac{1}{m_a^*}+1\right)+\frac{c_c^*}{m_a^*}\right)s + \left(c_c^*\left(\frac{1}{m_a^*}+1\right)+\frac{1}{m_a^*}\right)s^2 + s^3} \tag{B1}$$

Naming the coefficients of the cubic denominator as before

$$a_0 = \frac{k_c^*}{m_a^*},\quad a_1 = k_c^*\left(\frac{1}{m_a^*}+1\right)+\frac{c_c^*}{m_a^*},\quad a_2 = c_c^*\left(\frac{1}{m_a^*}+1\right)+\frac{1}{m_a^*} \tag{B2}$$

and introducing

$$c_0 = \frac{c_c^*}{m_a^*},\quad b_4 = \frac{k_c^*}{c_c^*} \tag{B3},$$

equation (B1) can be written as

$$\mathrm{L}\,\dot{u}_a^* = \frac{c_0\,(s + b_4)}{a_0 + a_1\,s + a_2\,s^2 + s^3} \tag{B4}.$$

Introducing the substitutions specified in equations (A2) to (A8), the denominator may be factorised as follows, providing β^2 is greater than zero.

$$\mathrm{L}\,\dot{u}_a^* = \frac{c_0\,(s + b_4)}{(s + b_1)\left((s + b_2)^2 + \omega^2\right)} \tag{B5}$$

This can be expanded to

$$\mathrm{L}\,\dot{u}_a^* = \frac{c_0(b_4-b_1)}{\omega^2+(b_2-b_1)^2}\left(\frac{1}{s+b_1} - \frac{s + b_2}{(s+b_2)^2+\omega^2} - \frac{b_2^2+\omega^2+b_1b_4-b_4b_2-b_2b_1}{(b_4-b_1)\left((s+b_2)^2+\omega^2\right)}\right) \tag{B6}.$$

Performing the inverse Laplace transform, the anvil velocity can be found.

$$u_a^* = \frac{c_0(b_4-b_1)}{\omega^2+(b_2-b_1)^2}\left(e^{-b_1t^*} - e^{-b_2t^*}\left(\cos\omega t^* + \frac{b_2b_1+b_4b_2-b_1b_4-b_2^2-\omega^2}{\omega\,(b_4-b_1)}\sin\omega t^*\right)\right) \tag{B7}$$

This solution can be written in a simpler form by making

$$c_1 = b_1,\ c_2 = b_2 - b_1,\ c_4 = b_4 - b_1,\ \phi = \operatorname{atan}\frac{c_2(c_4-c_2)-\omega^2}{\omega\,c_4},\ \text{and}\ F_p = \frac{c_0\,c_4}{\omega^2+c_2^2} \tag{B8}.$$

The equation for the pile head force and velocity is then in the same form as equation (A15).

$$f_p^* = u_a^* = F_p\,e^{-c_1t^*}\left(1 - e^{-c_2t^*}\frac{\cos(\omega t^* - \phi)}{\cos\phi}\right) \tag{B9}.$$

The spring force can be found by applying equation (A14).

$$f_s^* = F_s\,e^{-(c_1+c_2)t^*}\left(e^{c_2t^*} - A_s\frac{\cos(\omega t^*-\theta)}{\cos\theta}\right) \tag{B10}$$

where

$$F_S = \frac{c_0 c_4 \left(\frac{1}{m_a^*} - c_1\right)}{\omega^2 + {c_2}^2}, A_S = \frac{\frac{1}{m_a^*} - b_2 + \gamma\omega}{\frac{1}{m_a^*} - b_1}, \quad \theta = \text{atan}\left(\frac{\frac{\gamma}{m_a^*} - \omega - \gamma b_2}{\frac{1}{m_a^*} - b_2 + \gamma\omega}\right) \tag{B11}$$

and

$$\gamma = \tan\phi = \frac{(c_4 - c_2)c_2 - \omega^2}{\omega\, c_4} \tag{B12}.$$

When β^2 is less than or equal to zero, the denominator again has three real roots. Equations (A18) to (A24) define parameters b_1, b_2, and b_3.

If b_1, b_2, and b_3 are distinct, equation (B1) becomes

$$\mathrm{L}\, \dot{u}_a^* = c_0\left(\frac{(b_4 - b_1)}{(s+b_1)(b_2 - b_1)(b_3 - b_1)} + \frac{(b_4 - b_2)}{(s+b_2)(b_1 - b_2)(b_3 - b_2)} + \frac{(b_4 - b_3)}{(s+b_3)(b_1 - b_3)(b_2 - b_3)}\right) \tag{B13}$$

and the solution is given by

$$f_p^* = \dot{u}_a^* = F_p\left(e^{-b_1 t^*} - A_p\, e^{-b_2 t^*} - B_p\, e^{-b_3 t^*}\right) \tag{B14}$$

$$F_p = \frac{c_0\,(b_4 - b_1)}{(b_2 - b_1)(b_3 - b_1)}, \; A_p = \frac{b_4 - b_2}{b_4 - b_1}\,\frac{b_3 - b_1}{b_3 - b_2}, \text{ and } B_p = \frac{b_4 - b_3}{b_4 - b_1}\,\frac{b_2 - b_1}{b_2 - b_3} \tag{B15}.$$

The force in the spring is

$$f_S^* = F_S\left(e^{-b_1 t^*} + A_S\, e^{-b_2 t^*} - B_S\, e^{-b_3 t^*}\right) \tag{B16}$$

with

$$F_S = \frac{c_0\left(\frac{1}{m_a^*} - b_1\right)(b_4 - b_1)}{(b_2 - b_1)(b_3 - b_1)},$$

$$A_p = \frac{\frac{1}{m_a^*} - b_2}{\frac{1}{m_a^*} - b_1}\,\frac{b_4 - b_2}{b_4 - b_1}\,\frac{b_3 - b_1}{b_3 - b_2}, \text{ and } B_p = \frac{\frac{1}{m_a^*} - b_3}{\frac{1}{m_a^*} - b_1}\,\frac{b_4 - b_3}{b_4 - b_1}\,\frac{b_2 - b_1}{b_2 - b_3} \tag{B17}.$$

The solution for the case when β is zero and b_3 is equal to b_2 follows.

$$f_p^* = \dot{u}_a^* = F_p\, e^{-c_1 t^*}\left(1 - e^{-c_2 t^*}\,(1 + \gamma t^*)\right) \tag{B18}$$

$$f_S^* = F_S\, e^{-c_1 t^*}\left(1 - e^{-c_2 t^*}\left(A_S + \gamma\, B_S\, t^*\right)\right) \tag{B19}$$

$$F_p = \frac{c_0 c_4}{{c_2}^2}, \; F_S = \frac{c_0 c_4}{{c_2}^2}, A_S = \frac{\frac{1}{m_a^*} - b_2 + \gamma}{\frac{1}{m_a^*} - b_1}, B_S = \frac{\frac{1}{m_a^*} - b_2}{\frac{1}{m_a^*} - b_1}, \; \gamma = \frac{(c_4 - c_2)c_2}{c_4} \tag{B20}$$

FIGURES

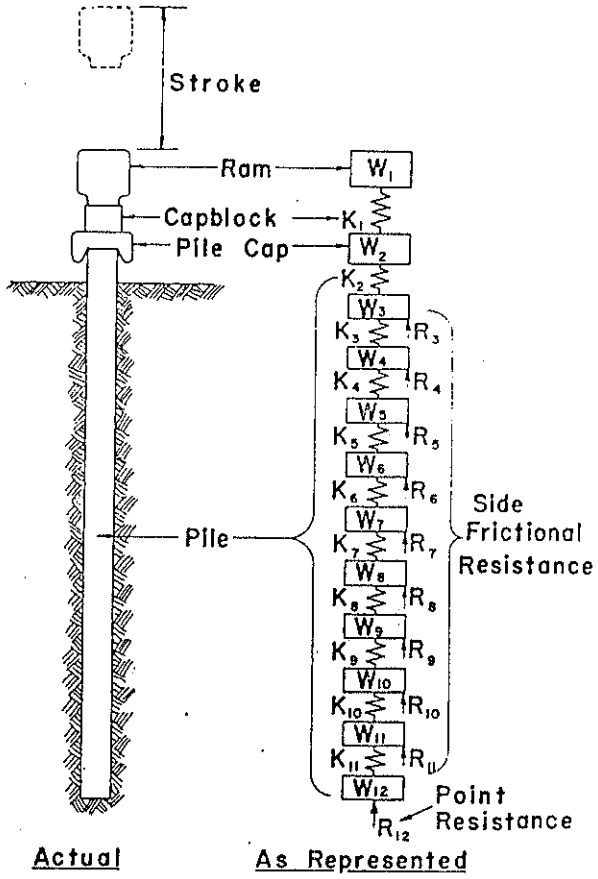

Fig 2.1. Modelling of pile system by discrete springs and dashpots (after Smith, 1960).

Soil type	Q_t in. (mm)	Q_s in. (mm)	J s/ft (s/m)	J' s/ft (s/m)	Reference
All soils	0.1 (2.5)	0.1 (2.5)	0.15 (0.492)	0.05 (0.164)	Smith (1960)
Sand	0.4 (10.2)	0.2 (5.1)	0.15 (0.492)	0.5 (1.64)	Coyle et al (1977)
Clay	0.1 (2.5)	0.1 (2.5)	0.01 (0.033)	0.2 (0.656)	Coyle et al (1977)

Table 2.1. Recommended values for quake and damping parameters.

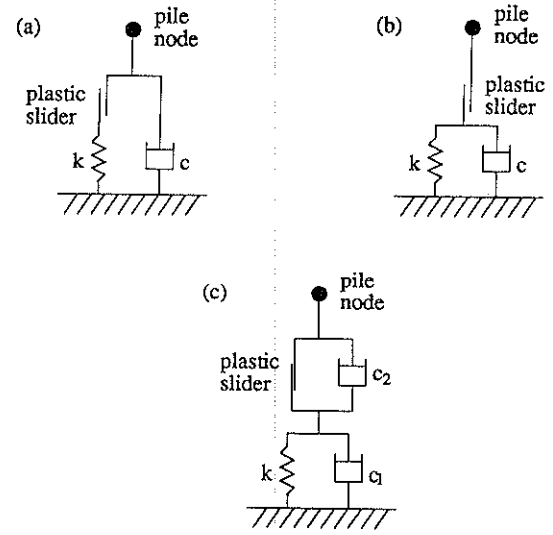

Fig 2.2. Alternative models for dynamic soil reactions.

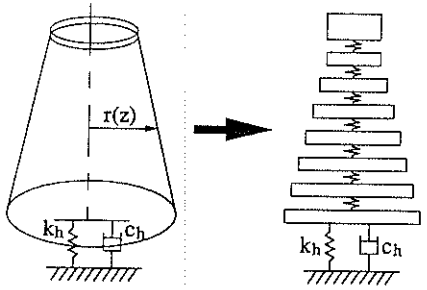

Fig 2.3. Holeyman's model for dynamic soil response at pile toe.

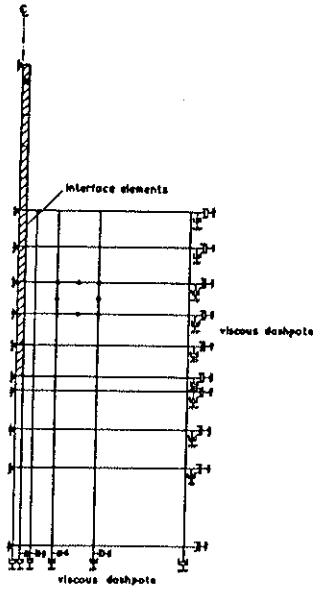

Fig 2.4. Finite element model used by Chow (after Chow, 1981).

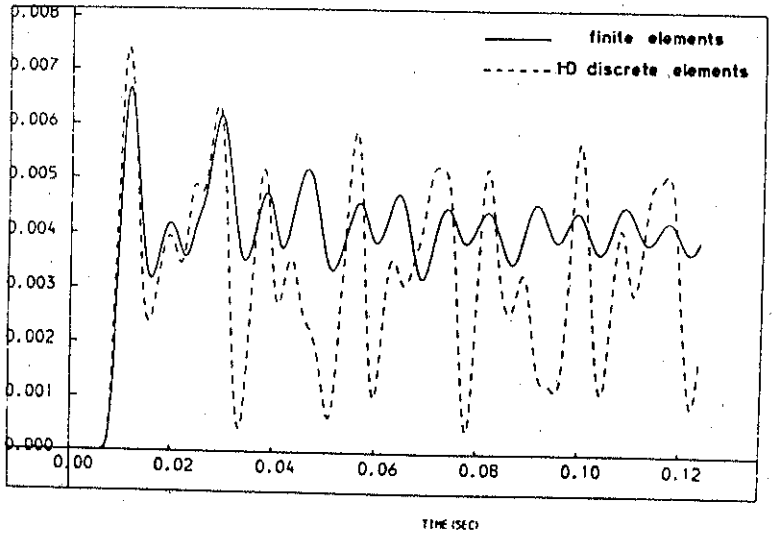

Fig 2.5. Pile toe displacement calculated by Chow (after Chow, 1981).

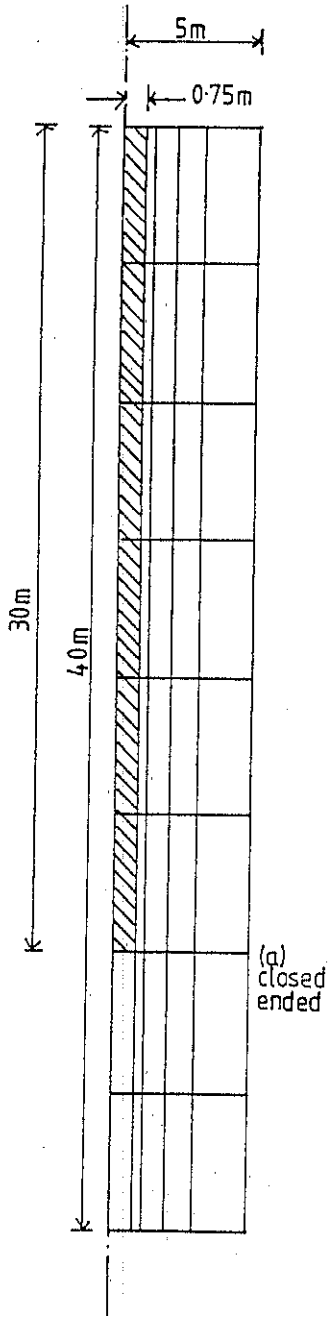

Fig 2.6. Finite element model used by Simons (after Simons, 1985).

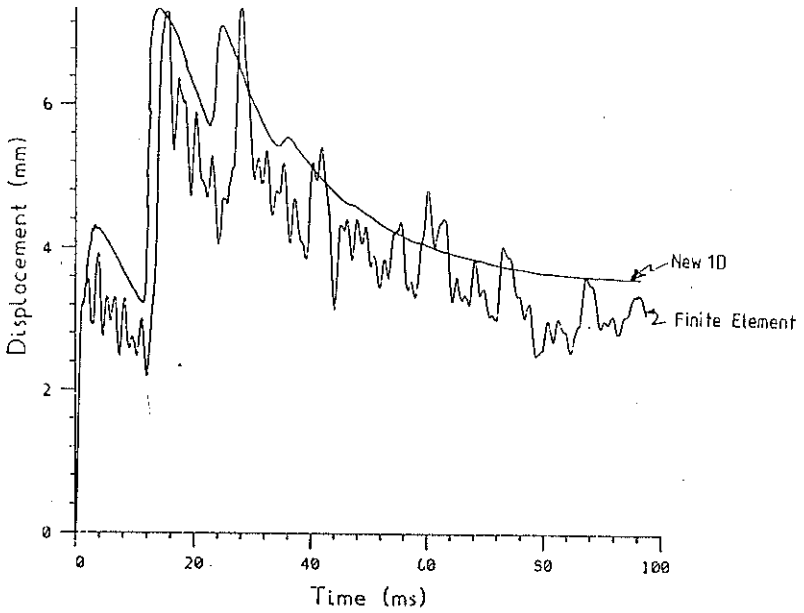

Fig 2.7. Pile head displacement calculated by Simons (after Simons, 1985).

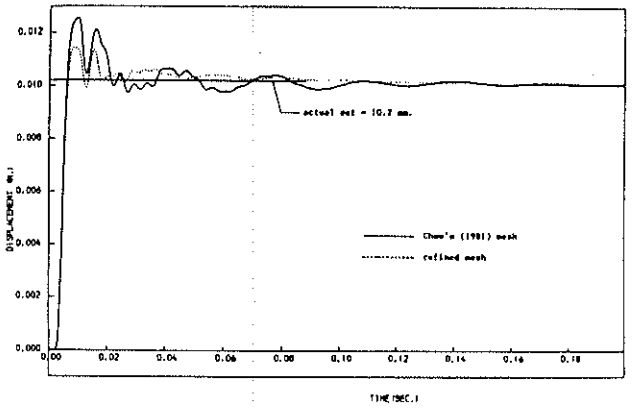

Fig 2.8. Effect of mesh refinement on pile displacement (after Smith et al, 1985).

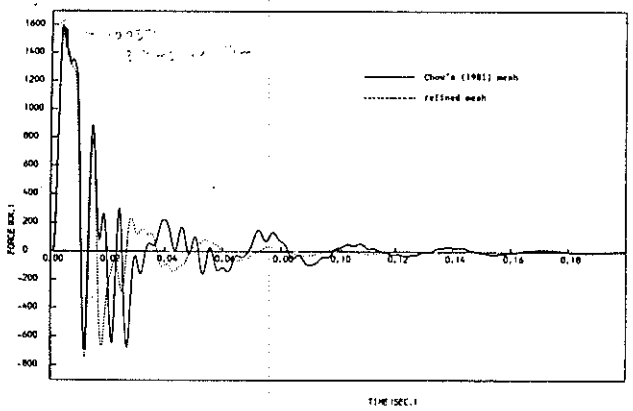

Fig 2.9. Effect of mesh refinement on pile force (after Smith et al, 1985).

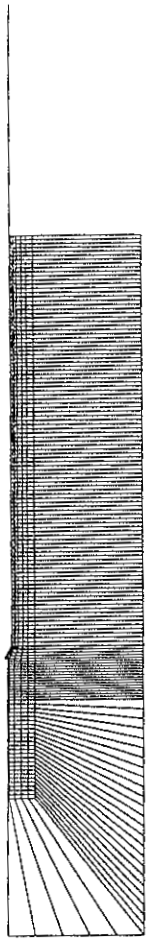

Fig 2.10. Finite element mesh used by Coutino et al (after Coutino et al, 1988).

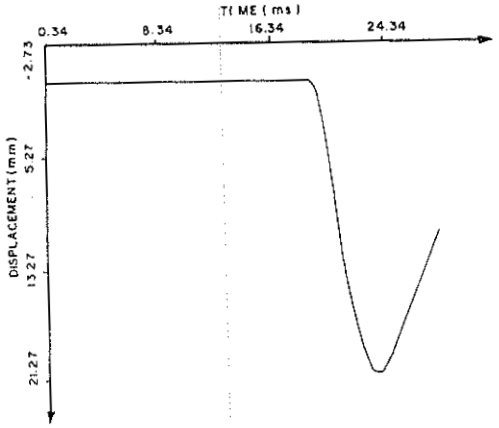

Fig 2.11(a). Pile toe displacement calculated by Coutino et al (after Coutino et al, 1988).

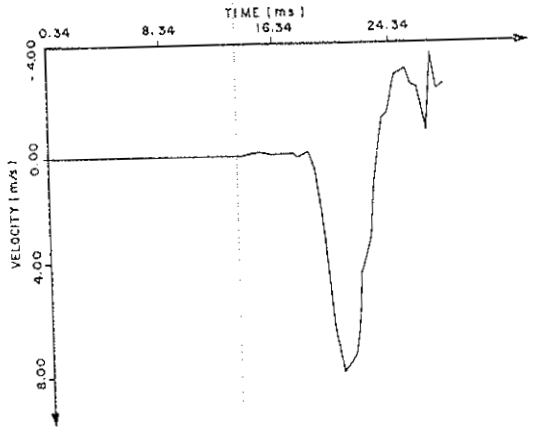

Fig 2.11(b). Pile toe velocity calculated by Coutino et al (after Coutino et al, 1988).

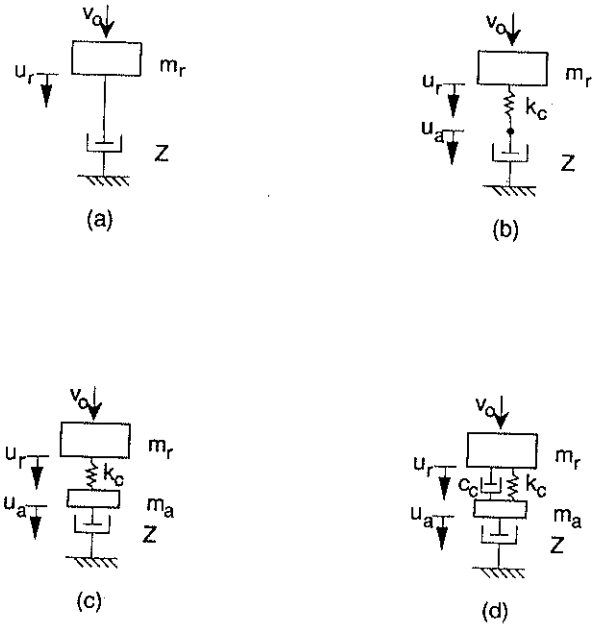

Fig 3.1. Analytical pile hammer models.

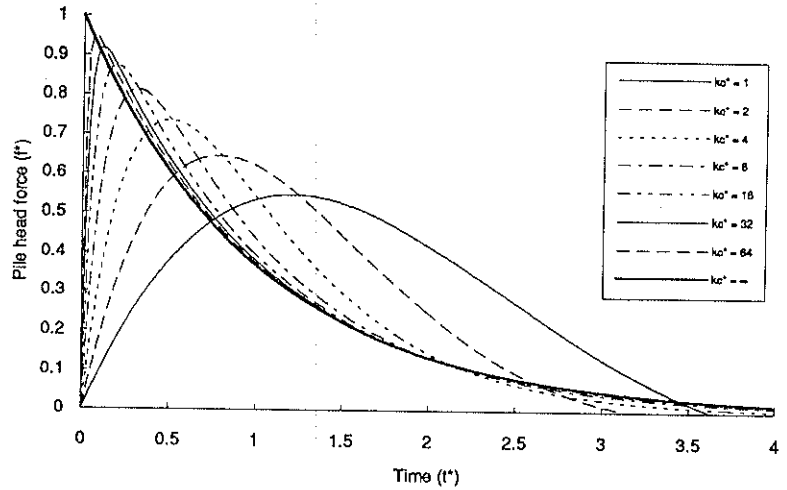

Fig 3.2. Effect of dimensionless cushion stiffness on pile head forcing function.

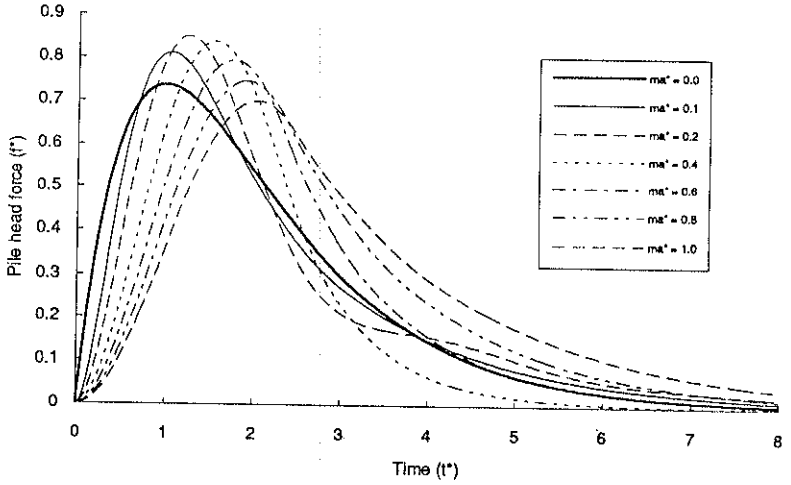

Fig 3.3. Effect of dimensionless anvil mass on pile head forcing function (kc*=4).

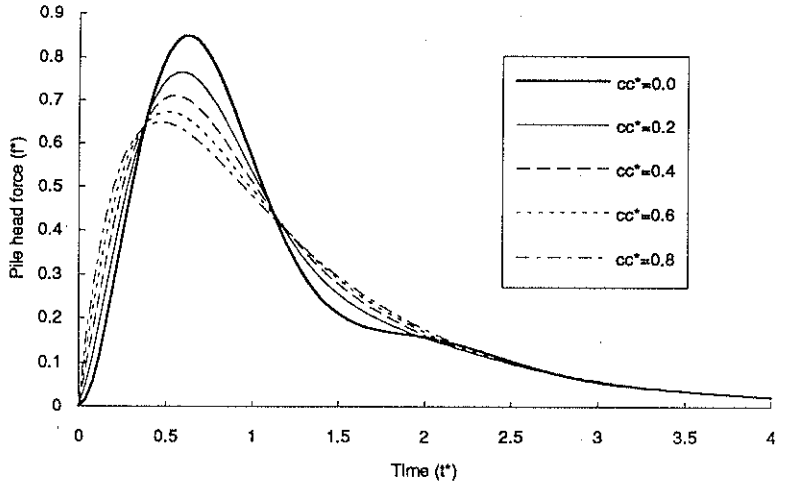

Fig 3.4. Effect of dimensionless cushion damping on pile head force (kc*=4, ma*=0.2).

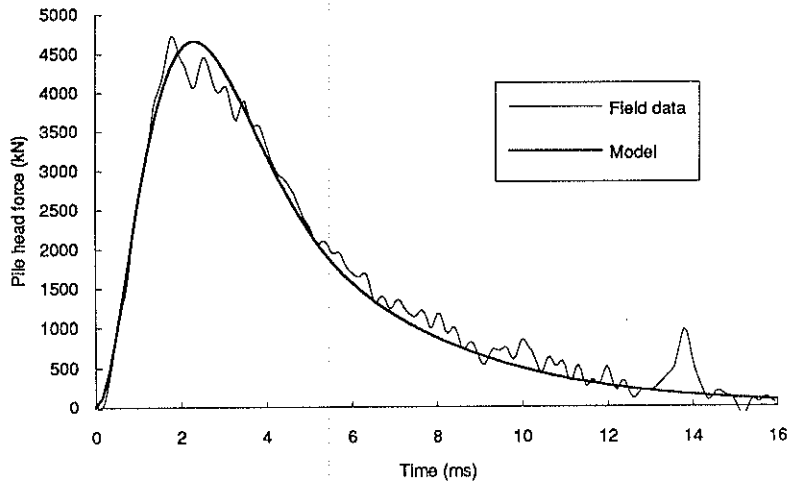

Fig 3.6. Comparison of field data and analytical solution for BSP 357 hammer.

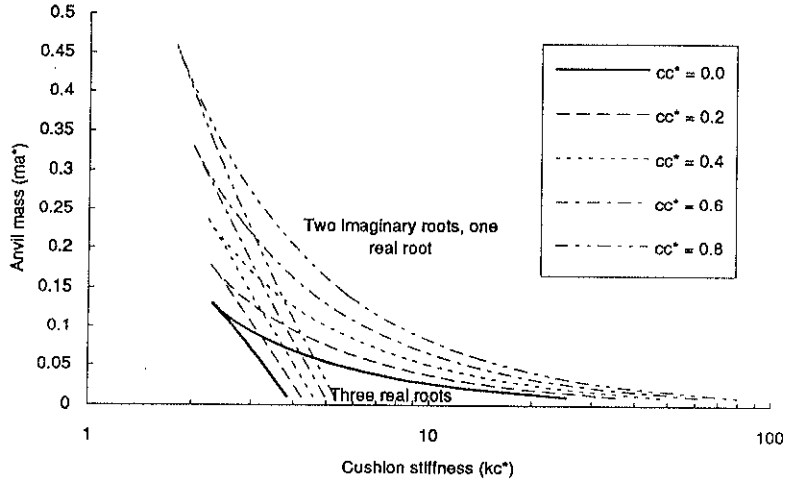

Fig 3.5. Regions in which the cubic denominator has real roots.

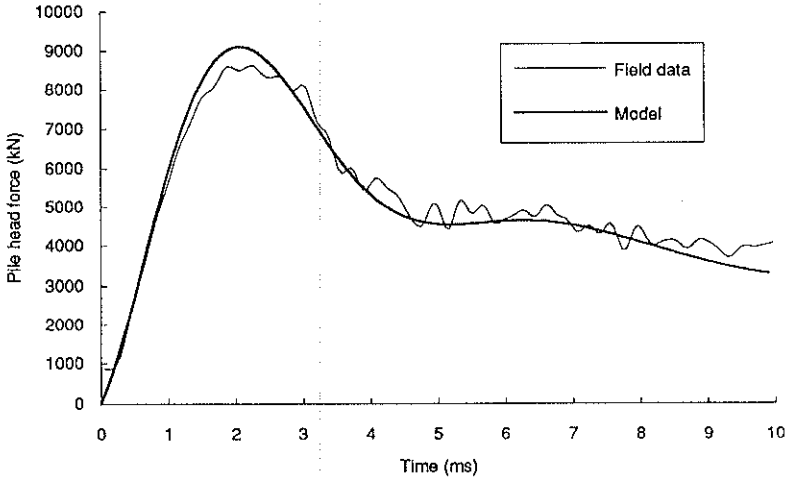

Fig 3.7. Comparison of field data and analytical solution for BSP HA40 hammer.

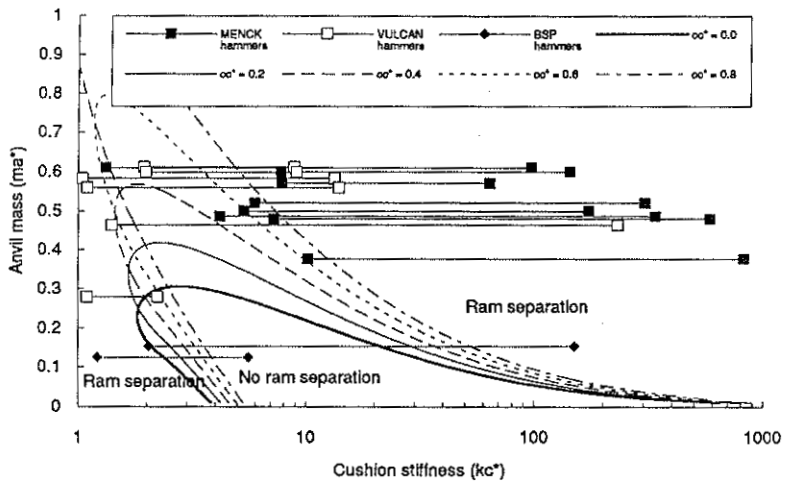

Fig 3.8. Range of parameters for a range of hammers, and regions of ram separation.

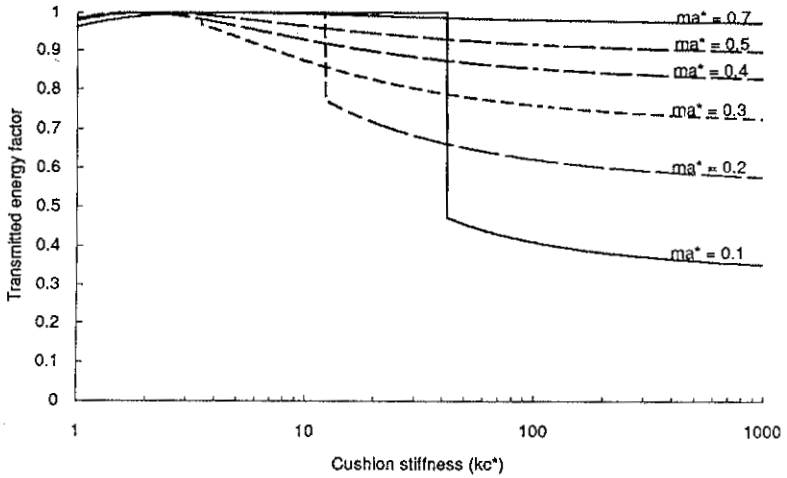

Fig 3.9. Effect of anvil mass on transmitted energy factor with no cushion damping.

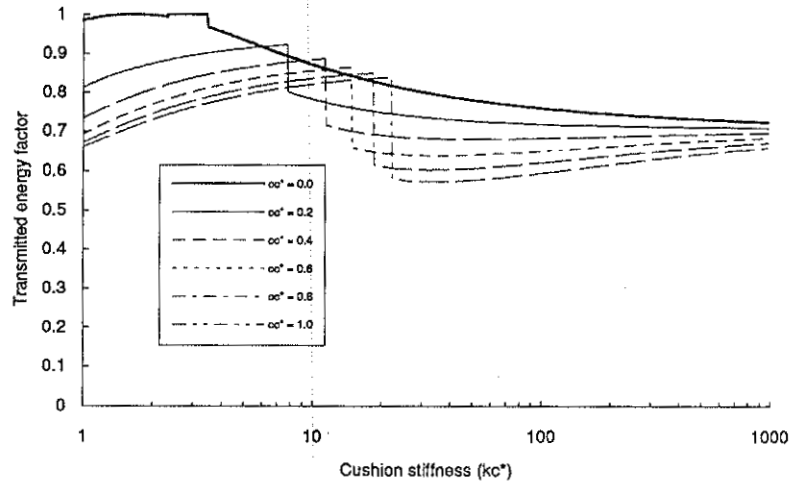

Fig 3.10. Effect of cushion damping on transmitted energy factor for ma*=0.3.

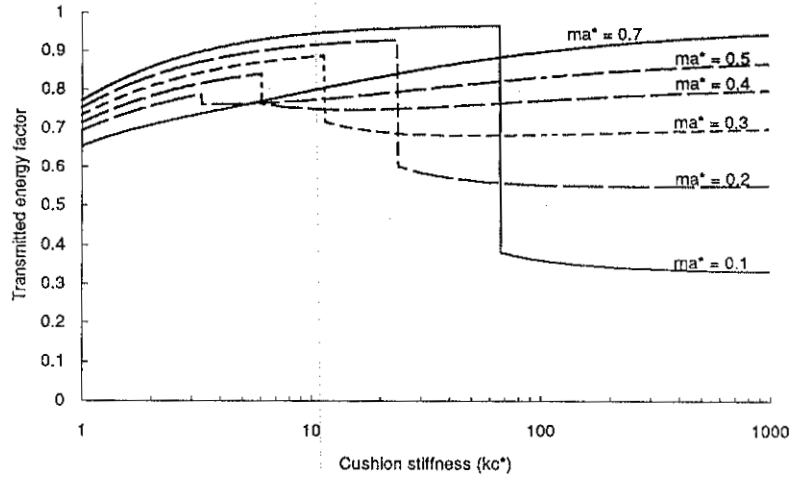

Fig 3.11. Effect of anvil mass on transmitted energy factor for cc*=0.4.

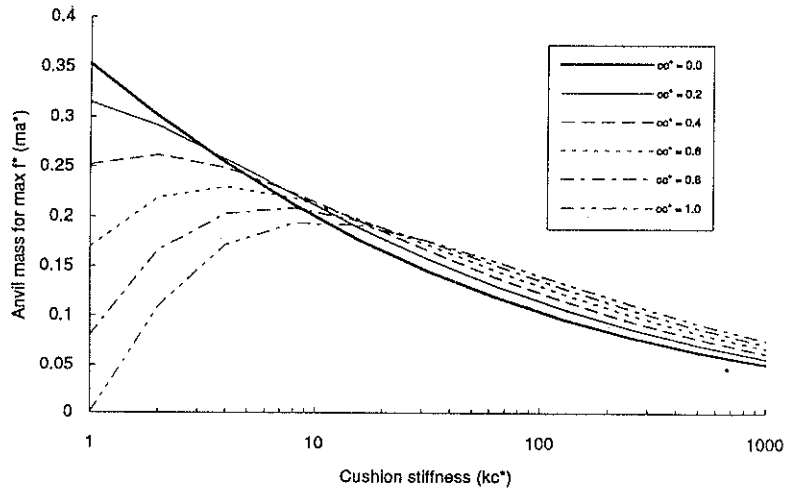

Fig 3.12. Anvil mass required to maximise pile force.

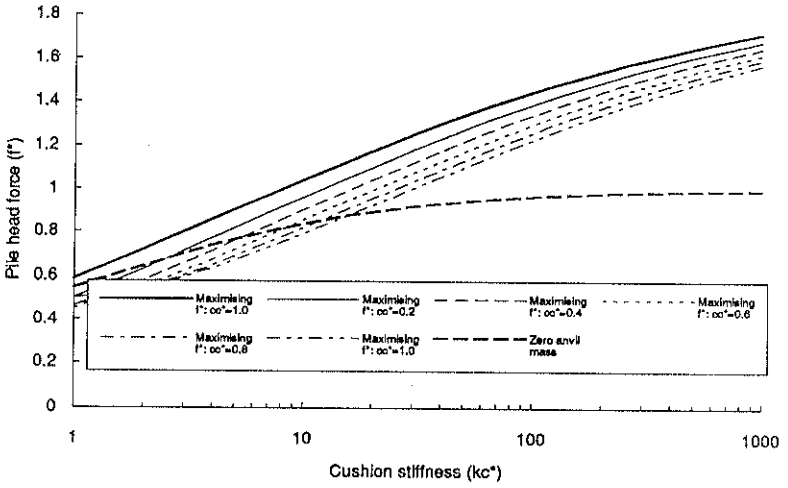

Fig 3.13. Maximum pile force obtained by varying anvil mass.

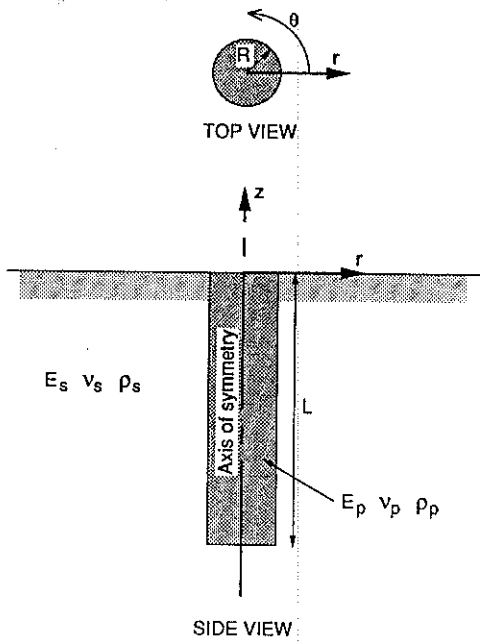

Fig 4.1. Idealisation of pile and soil, including axisymmetric axes.

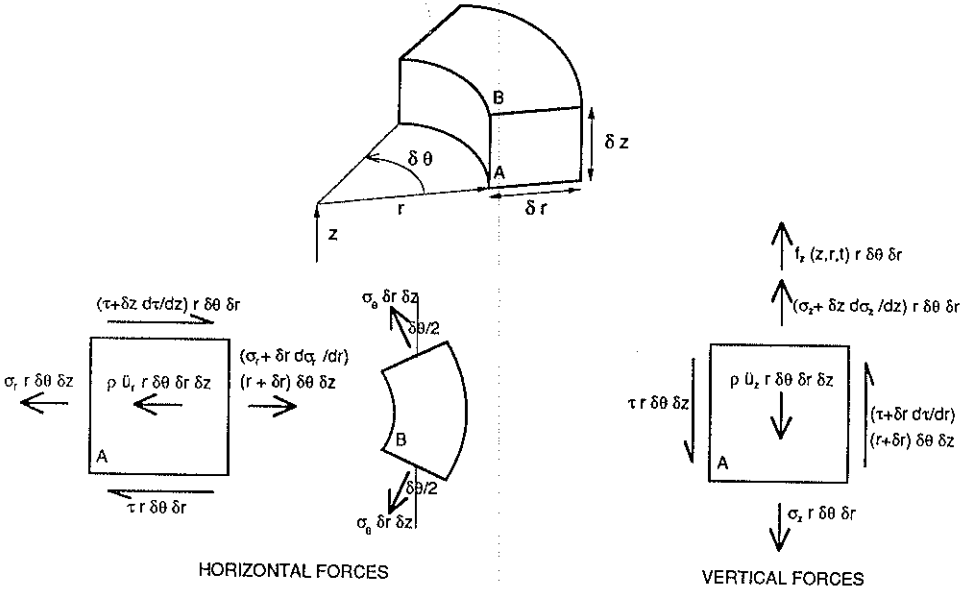

Fig 4.2. Axisymmetric stress element for derivation of equations of motion.

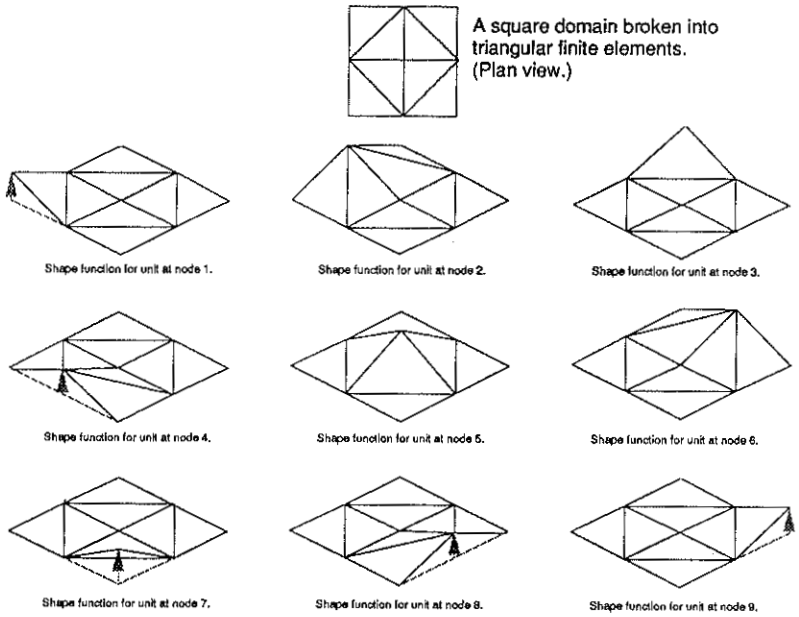

Fig 4.3. Example of finite element discretisation with corresponding shape functions.

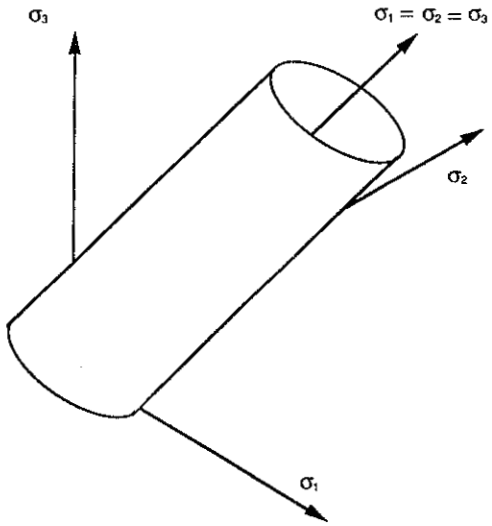

Fig 4.4. Yield surface for von Mises plasticity.

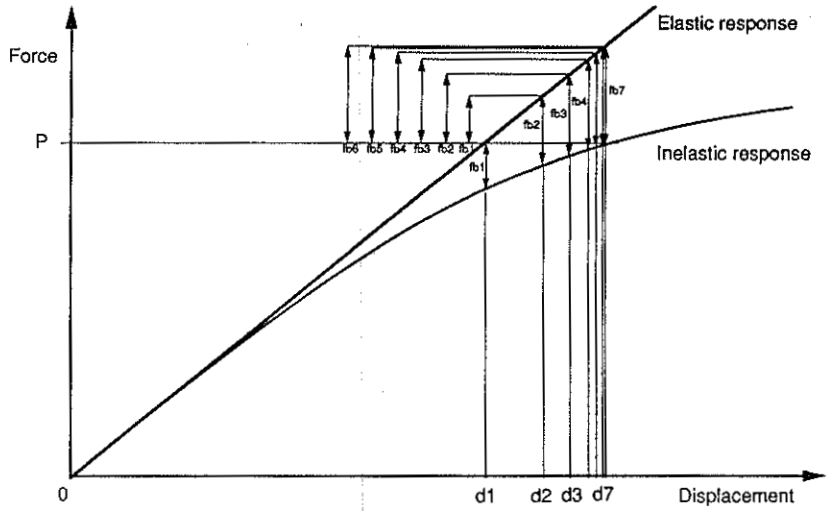

Fig 4.5(a). Graphical illustration of the Newton-Rhapson iteration method.

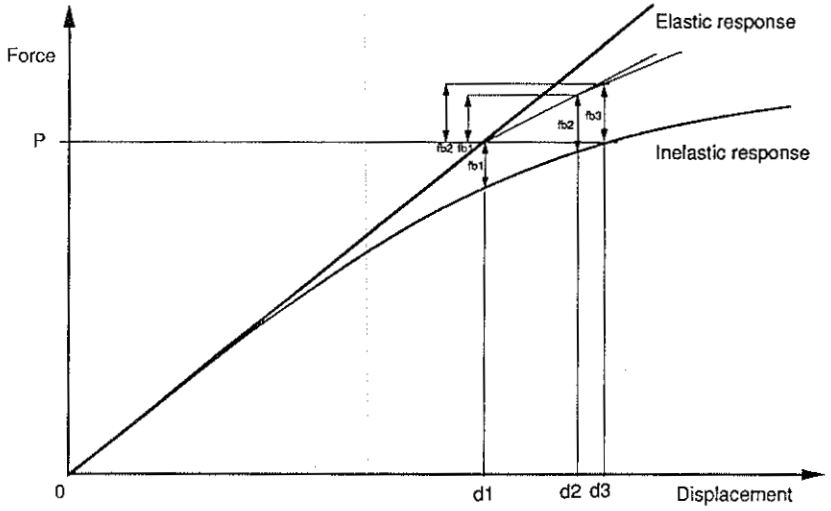

Fig 4.5(b). Graphical illustration of the modified Newton-Rhapson iteration method.

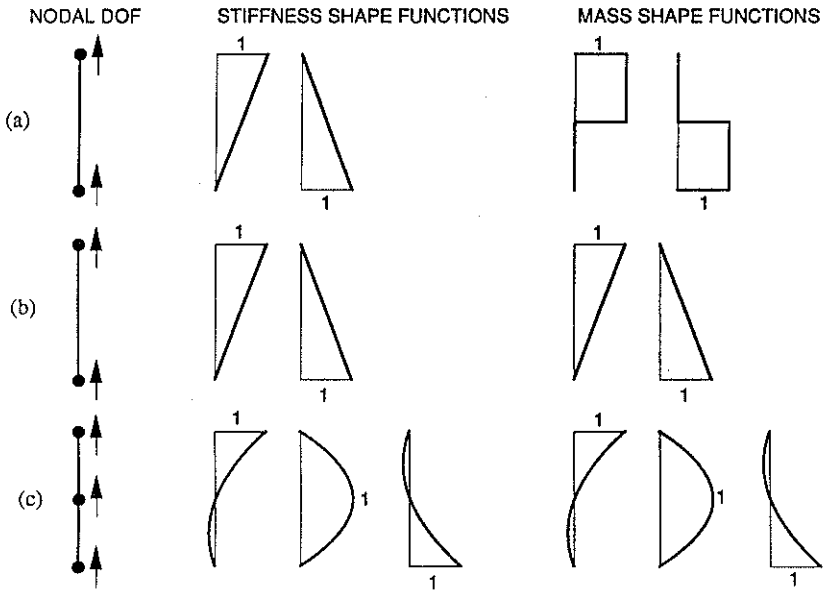

Fig 5.1. Pile element shape functions for construction of local stiffness and mass matrices.

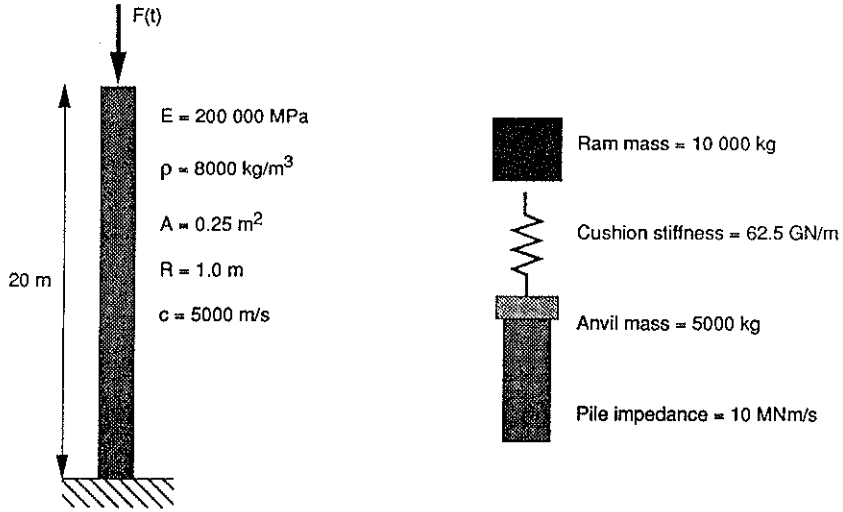

Fig 5.2. Pile and hammer properties.

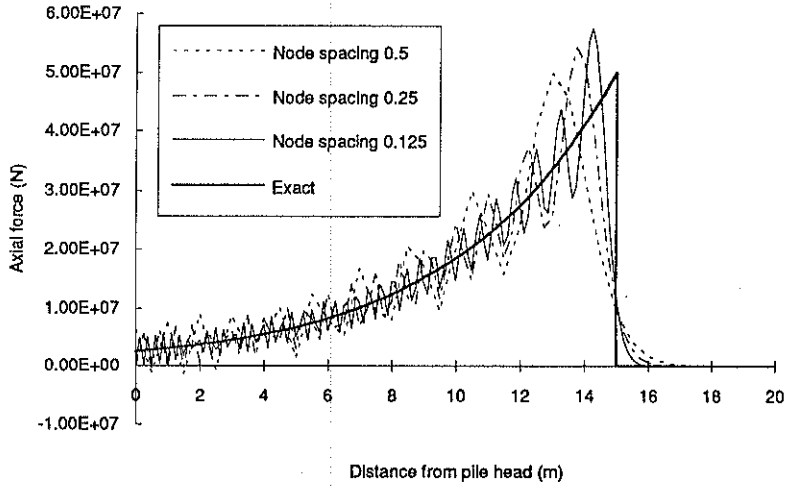

Fig 5.3. Axial force 3 ms after impact, 2 node lumped mass elements, hammer/pile impact.

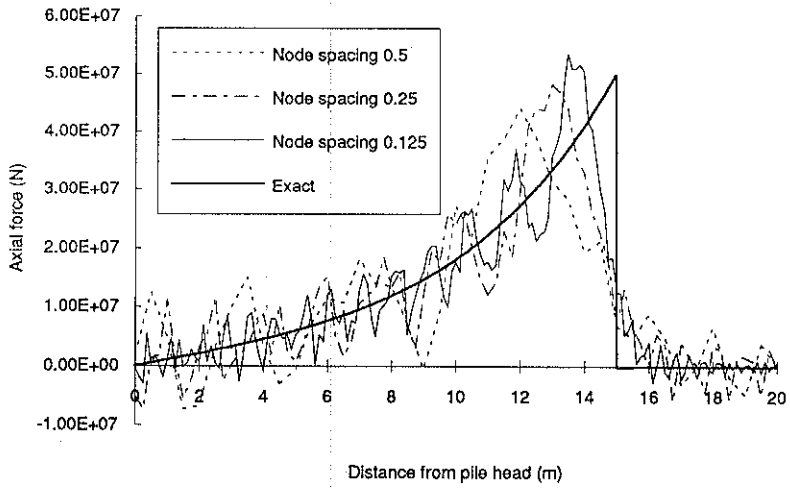

Fig 5.4. Axial force 19 ms after impact, 2 node lumped mass elements, hammer/pile impact.

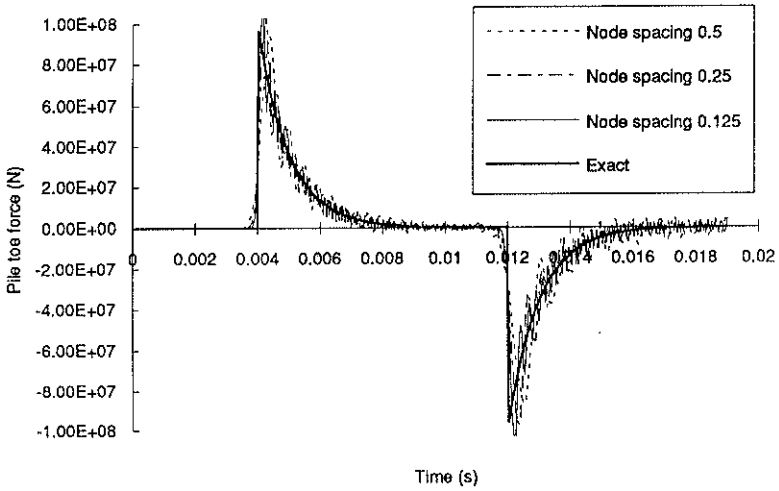

Fig 5.5. Toe force vs time, 2 node lumped mass elements, hammer/pile impact.

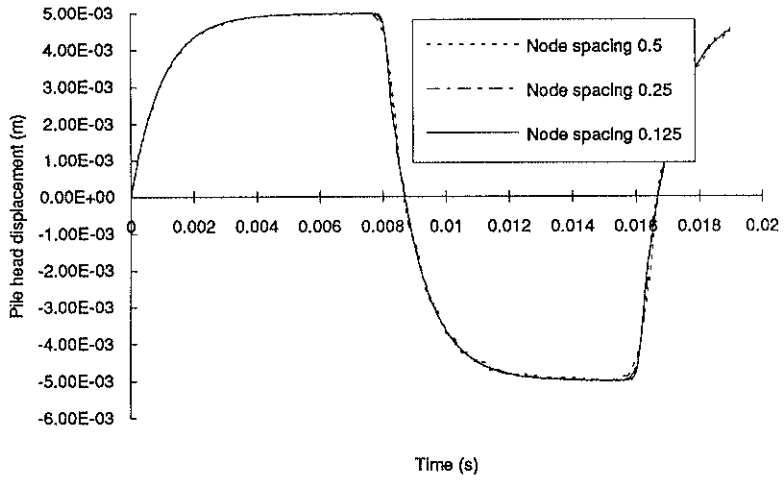

Fig 5.6. Head displacement vs time, 2 node lumped mass elements, hammer/pile impact.

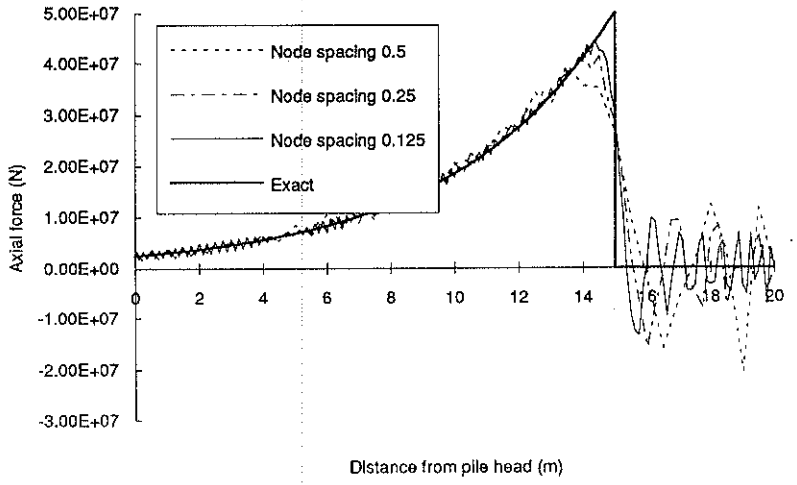

Fig 5.7. 3 ms after impact, 2 node consistent mass elements, hammer/pile impact.

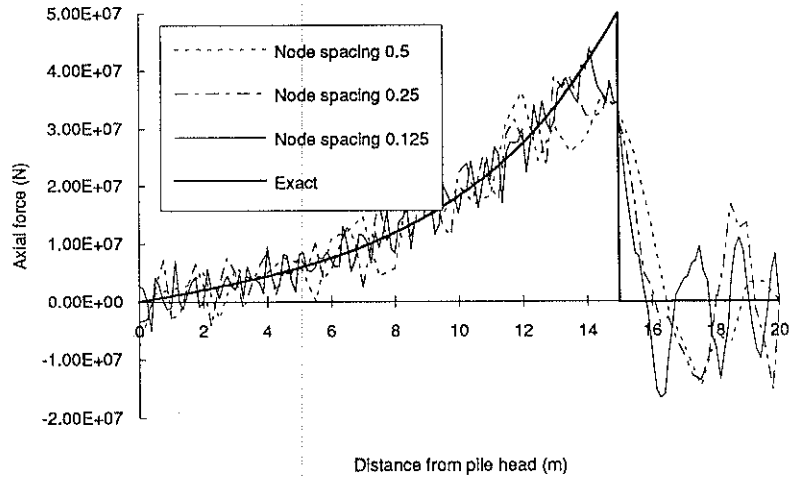

Fig 5.8. 19 ms after impact, 2 node consistent mass elements, hammer/pile impact.

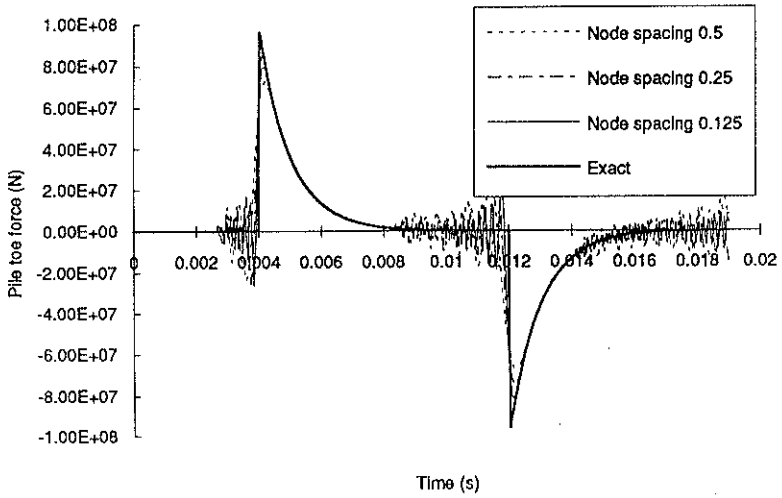

Fig 5.9. Toe force vs time, 2 node consistent mass elements, hammer/pile impact.

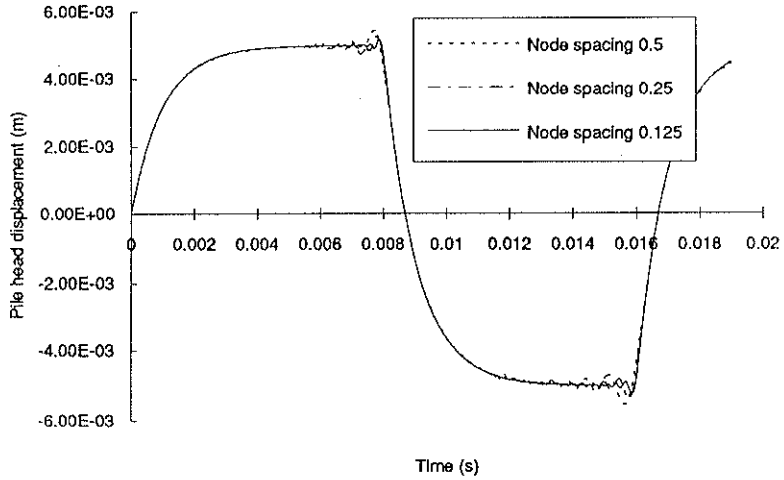

Fig 5.10. Head displacement vs time, 2 node consistent mass elements, hammer/pile impact.

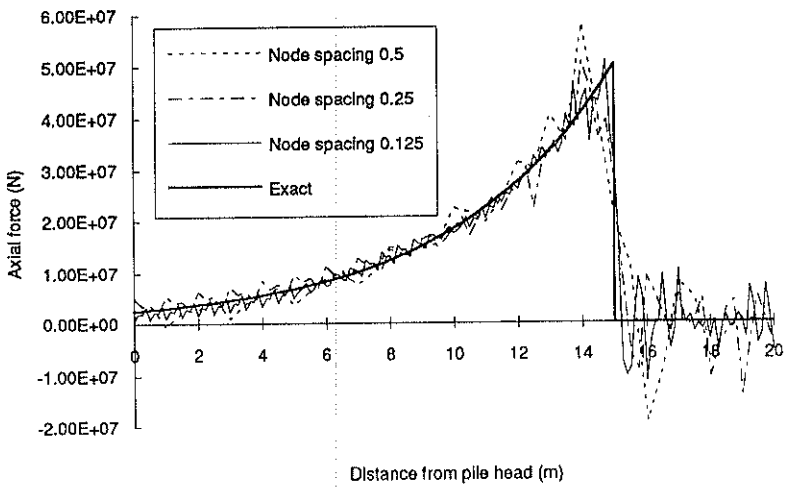

Fig 5.11. 3 ms after impact, 3 node consistent mass elements, hammer/pile impact.

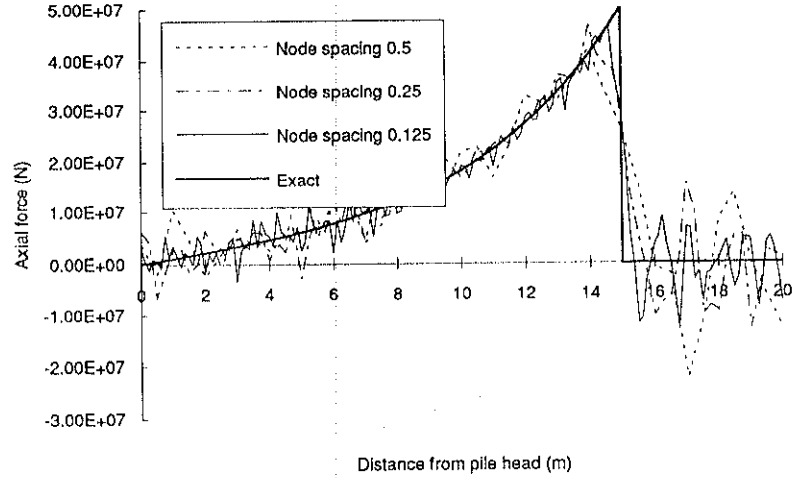

Fig 5.12. 19 ms after impact, 3 node consistent mass elements, hammer/pile impact.

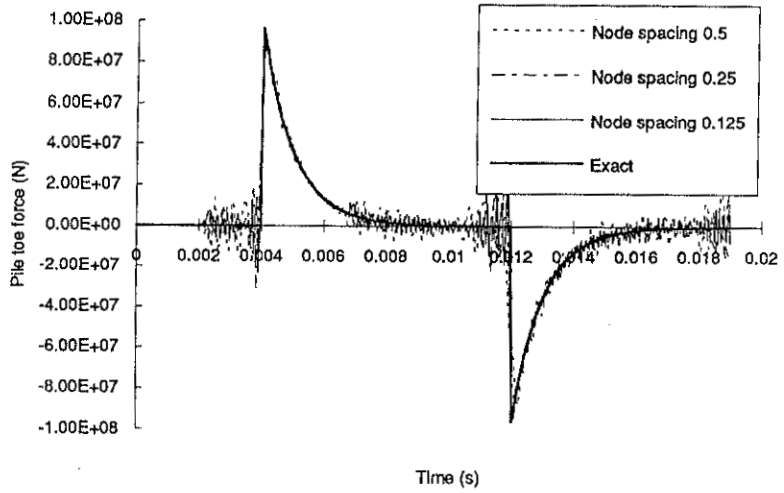

Fig 5.13. Toe force vs time, 3 node consistent mass elements, hammer/pile impact.

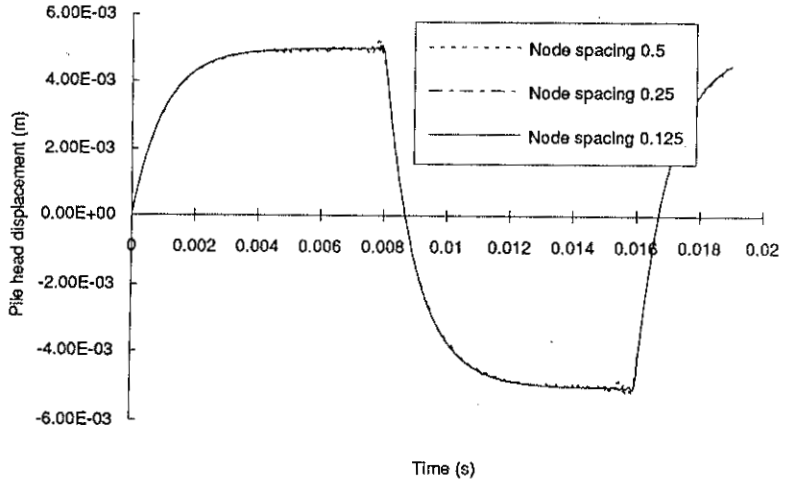

Fig 5.14. Head displacement vs time, 3 node consistent mass elements, hammer/pile impact.

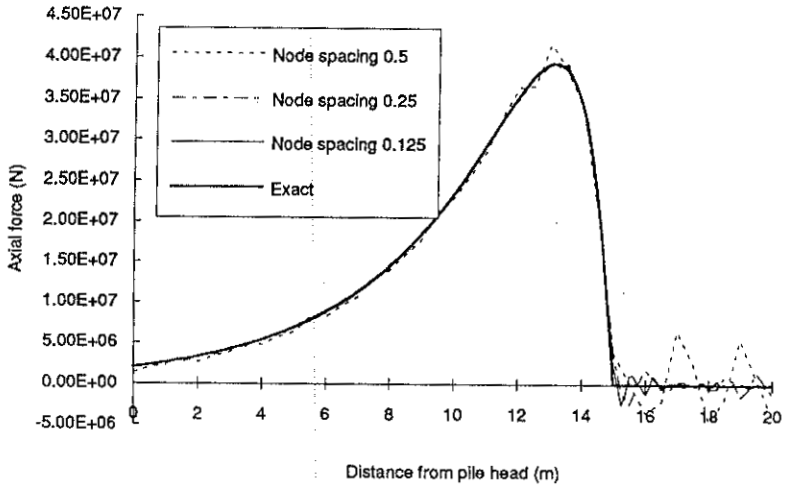

Fig 5.15. 3 ms after impact, 3 node consistent mass elements, cushioned impact.

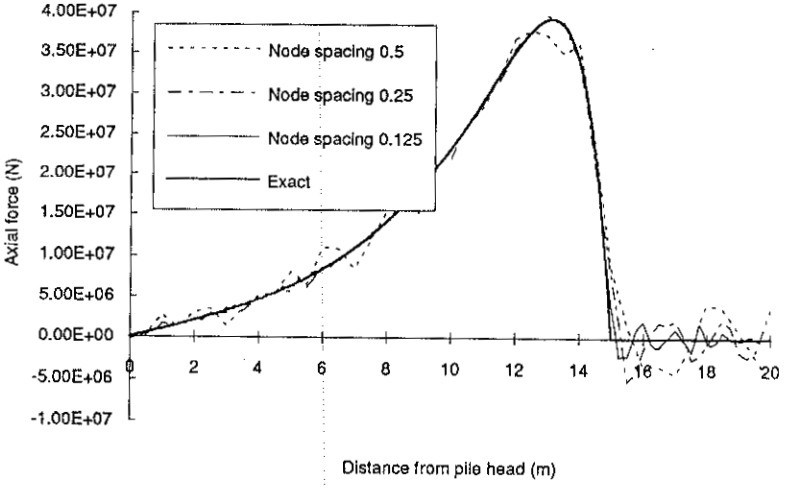

Fig 5.16. 19 ms after impact, 3 node consistent mass elements, cushioned impact.

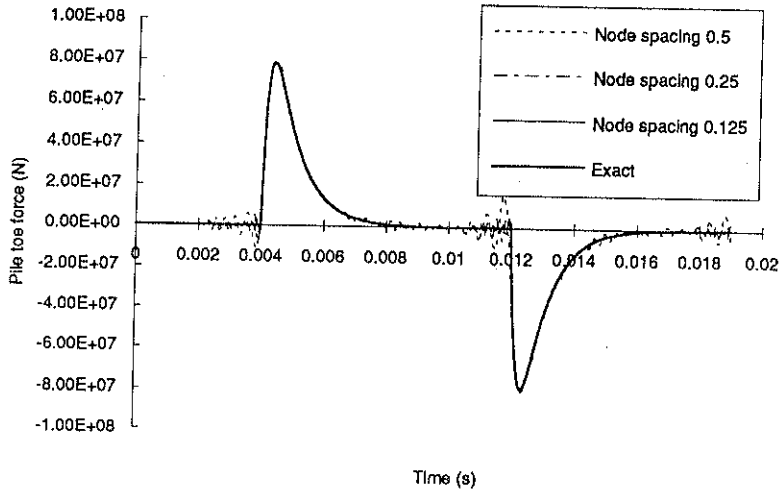

Fig 5.17. Toe force vs time, 3 node consistent mass elements, cushioned impact.

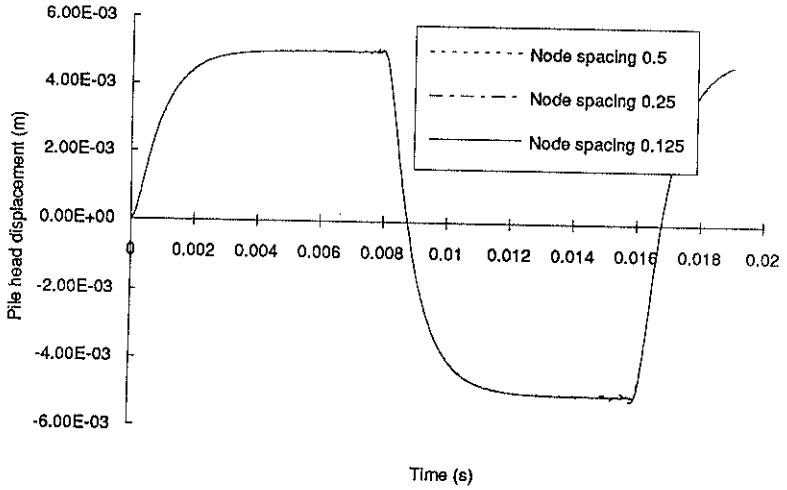

Fig 5.18. Head displacement vs time, 3 node consistent mass elements, cushioned impact.

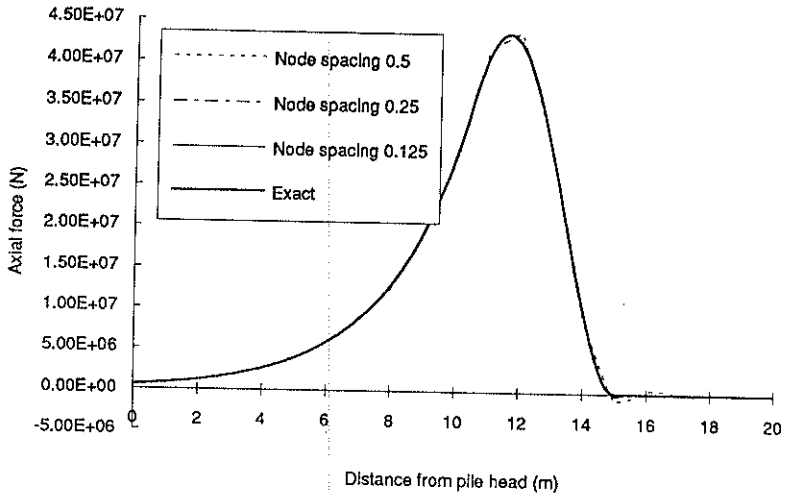

Fig 5.19. 3 ms after impact, 3 node consistent mass elements, hammer/anvil impact.

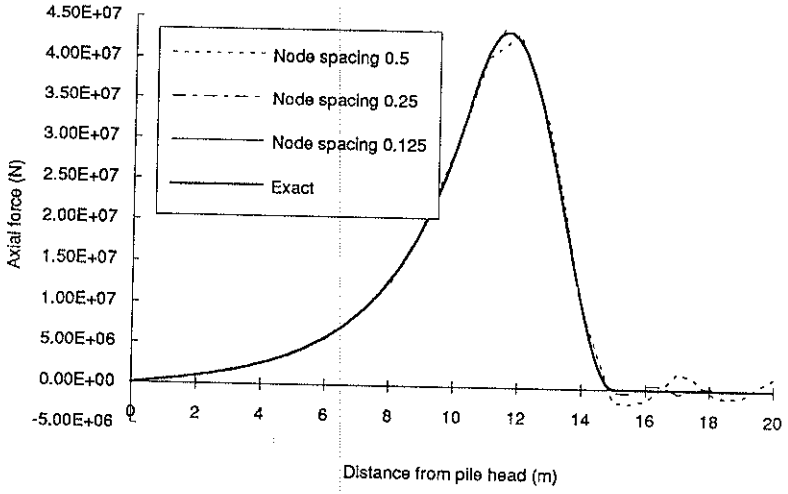

Fig 5.20. 19 ms after impact, 3 node consistent mass elements, hammer/anvil impact.

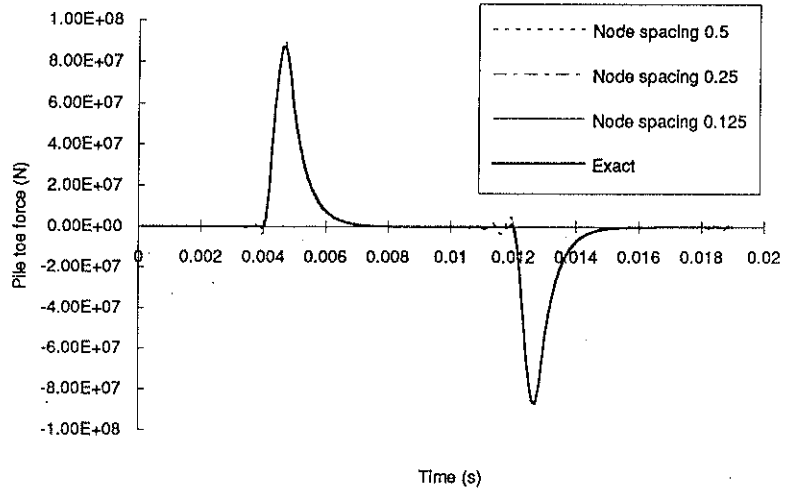

Fig 5.21. Toe force vs time, 3 node consistent mass elements, hammer/anvil impact.

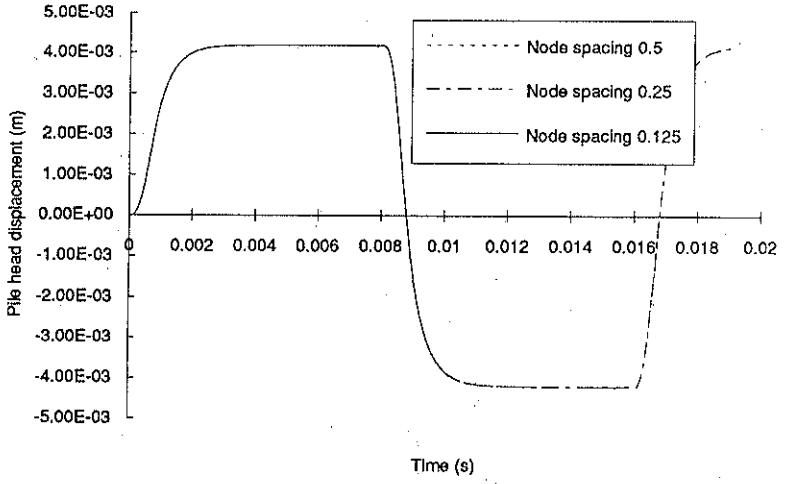

Fig 5.22. Head displacement vs time, 3 node consistent mass elements, hammer/anvil impact.

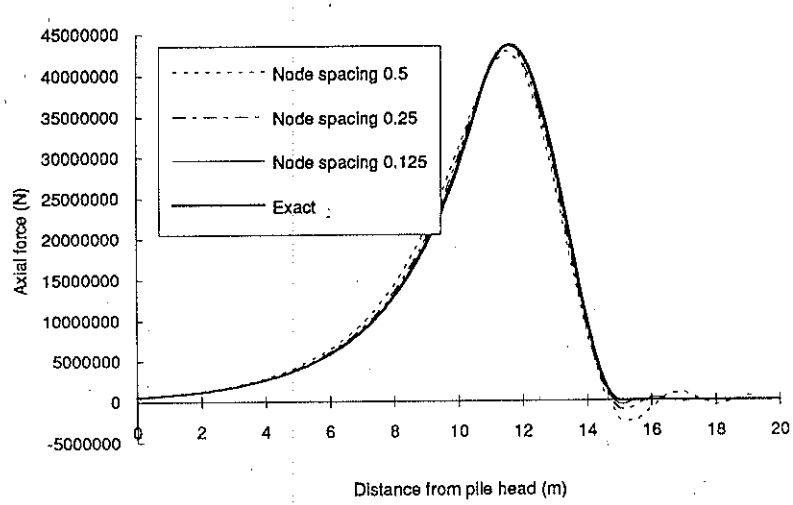

Fig 5.23. 3 ms after impact, 2 node consistent mass elements, hammer/anvil impact.

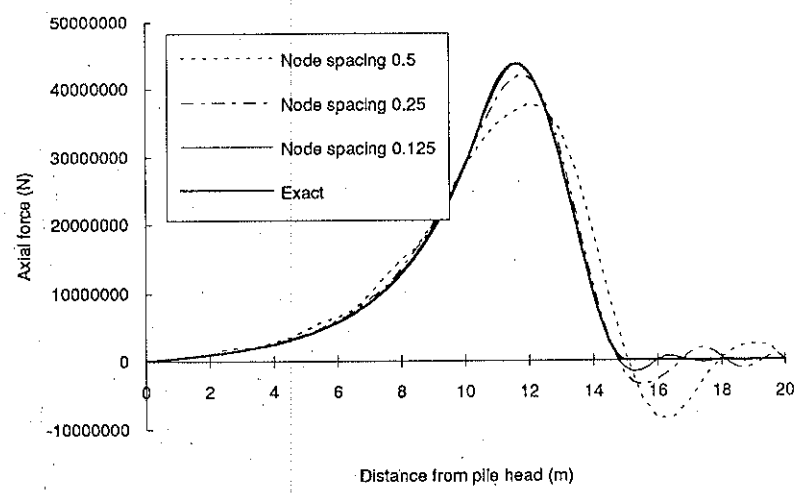

Fig 5.24. 19 ms after impact, 2 node consistent mass elements, hammer/anvil impact.

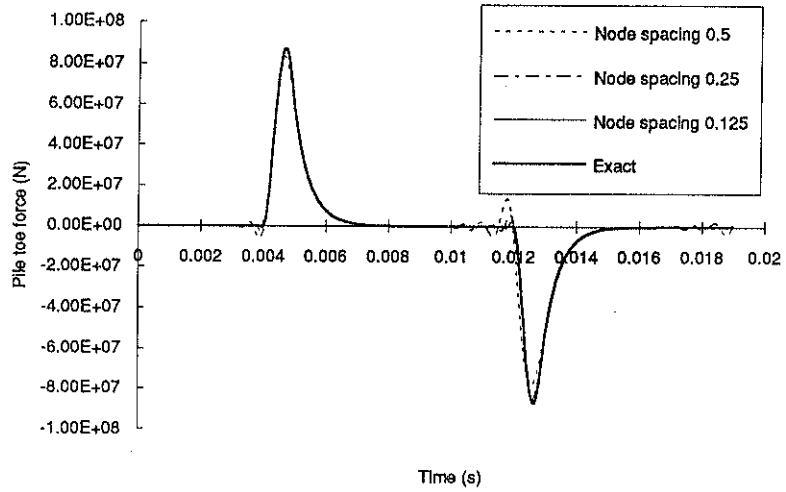

Fig 5.25. Toe force vs time, 2 node consistent mass elements, hammer/anvil impact.

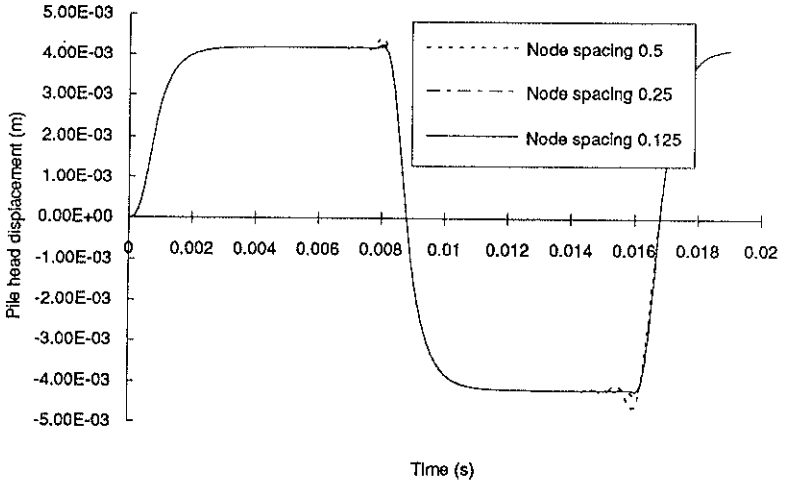

Fig 5.26. Head displacement vs time, 2 node consistent mass elements, hammer/anvil impact.

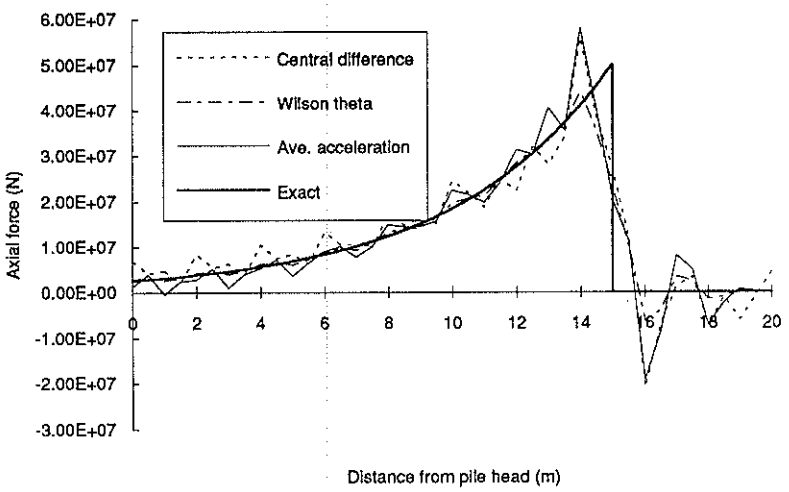

Fig 5.27. 3 ms after impact by different methods, dt = 10e-6 s, hammer/pile impact.

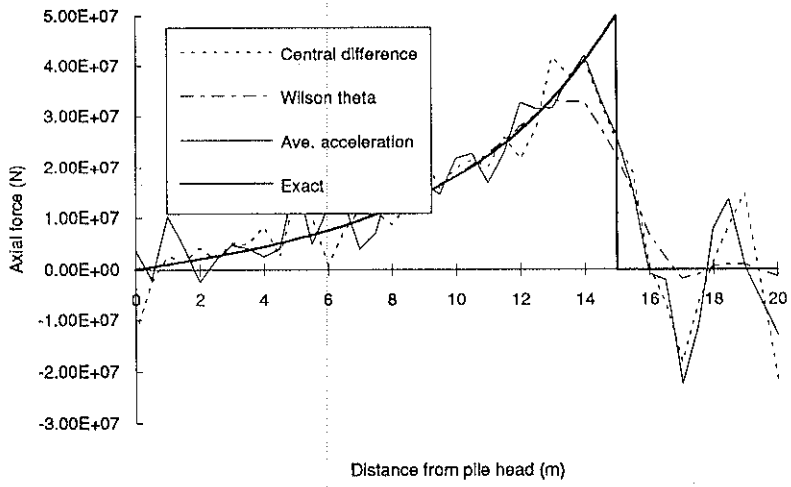

Fig 5.28. 19 ms after impact by different methods, dt = 10e-6 s, hammer/pile impact.

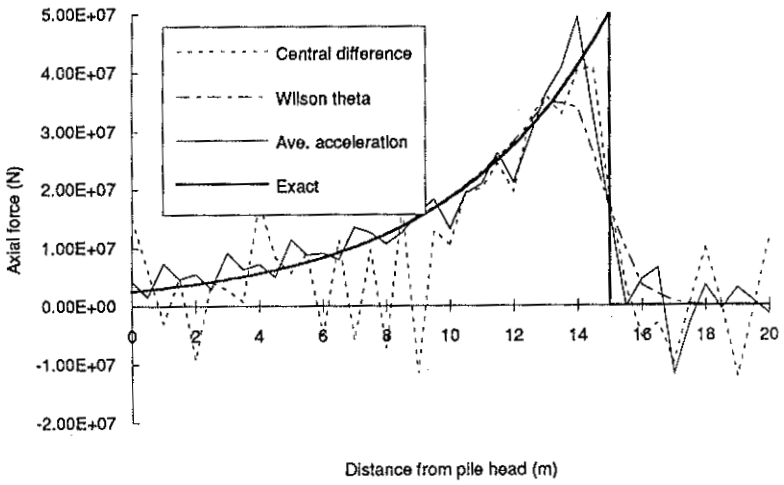

Fig 5.29. 3 ms after impact by different methods, dt = 50e-6 s, hammer/pile impact.

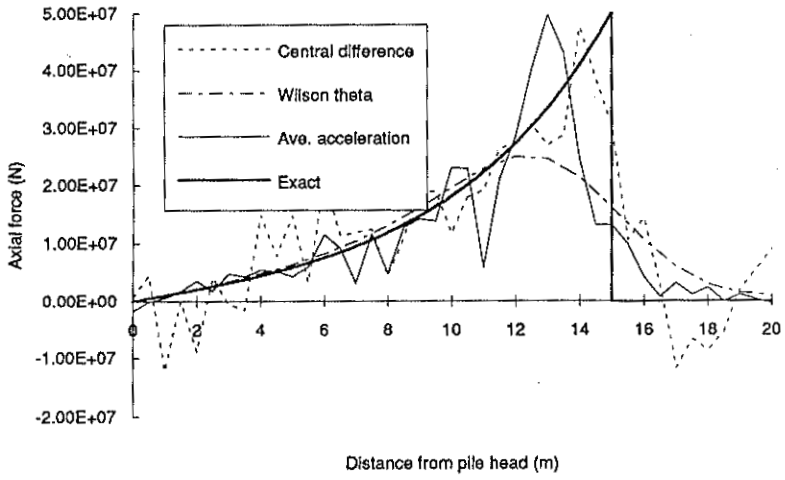

Fig 5.30. 19 ms after impact by different methods, dt = 50e-6 s, hammer/pile impact.

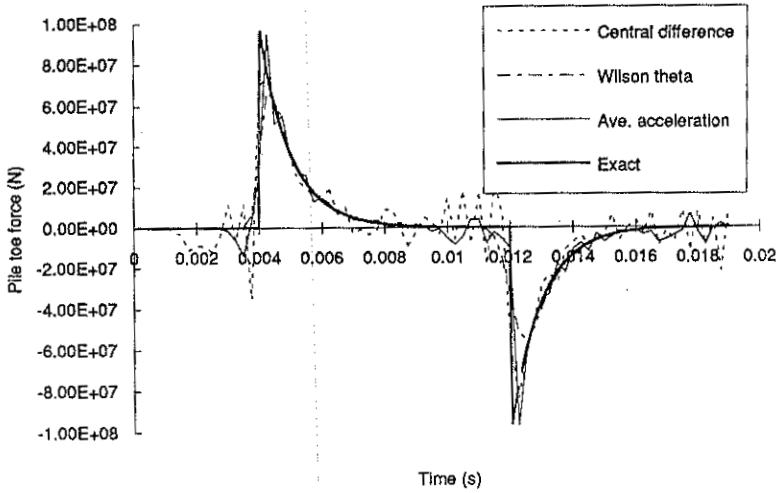

Fig 5.31. Toe force vs time by different methods, dt = 50e-6 s, hammer/pile impact.

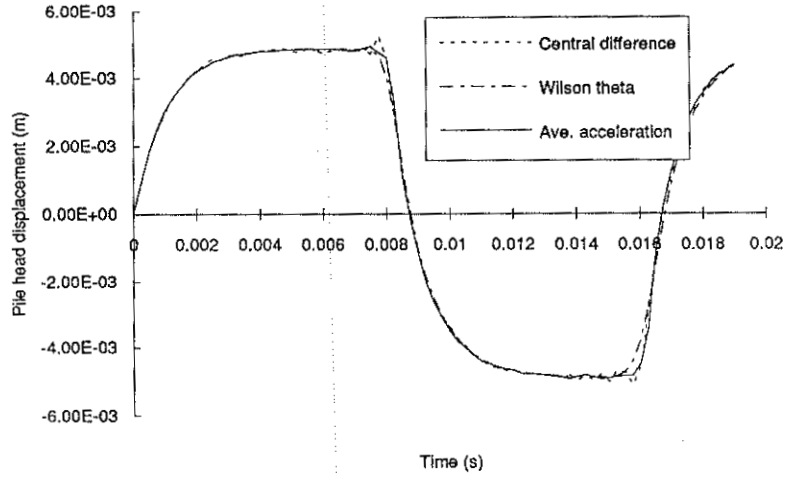

Fig. 5.32. Head displacement vs time by different methods, dt=50e-6 s, hammer/pile impact.

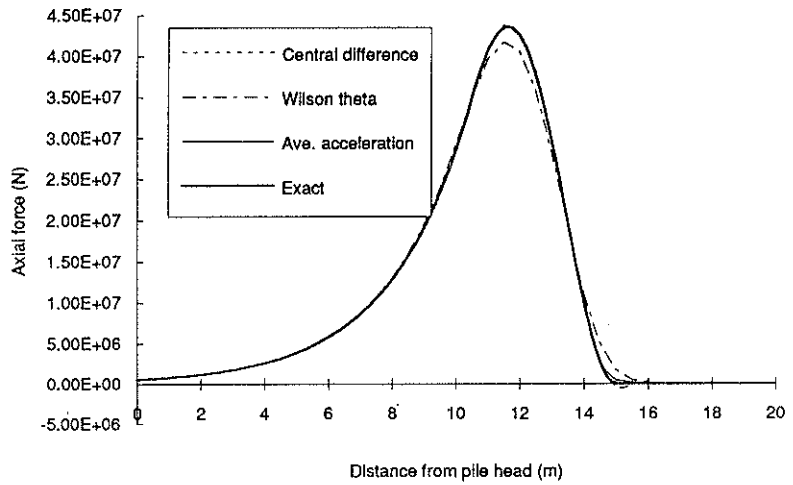

Fig 5.33. 3 ms after impact by different methods, dt = 25e-6, hammer/anvil impact.

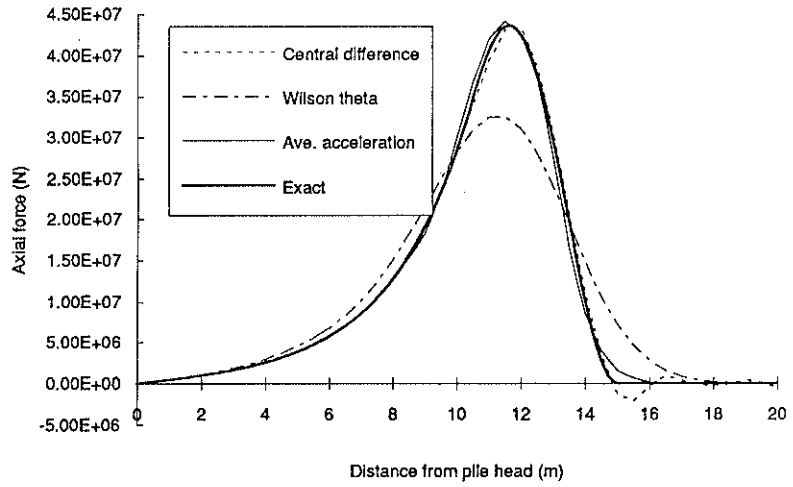

Fig 5.34. 19 ms after impact by different methods, dt = 25e-6, hammer/anvil impact.

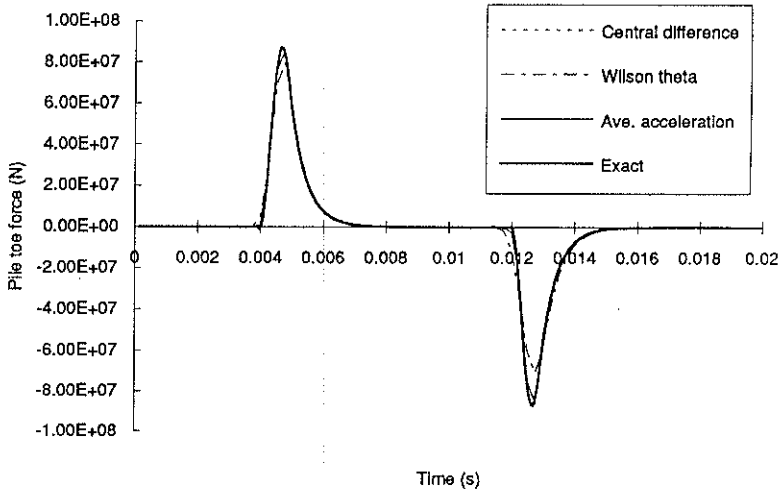

Fig 5.35. Toe force vs time by different methods, dt = 25e-6, hammer/anvil impact.

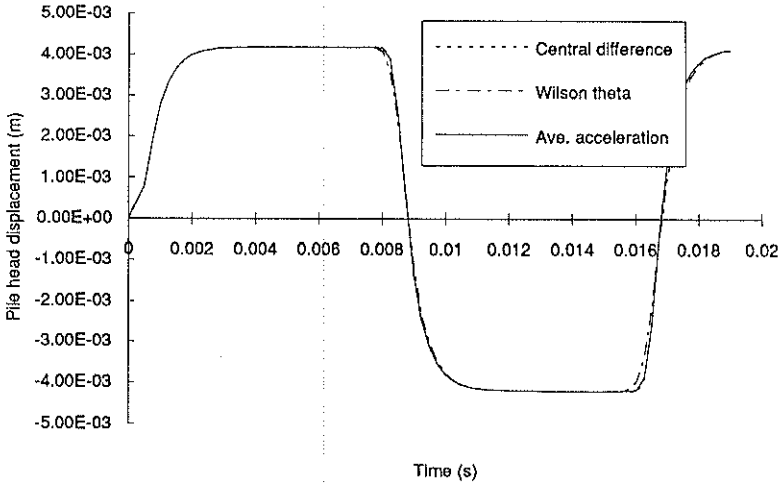

Fig. 5.36. Head displacement vs time by different methods, dt=25e-6, hammer/anvil impact.

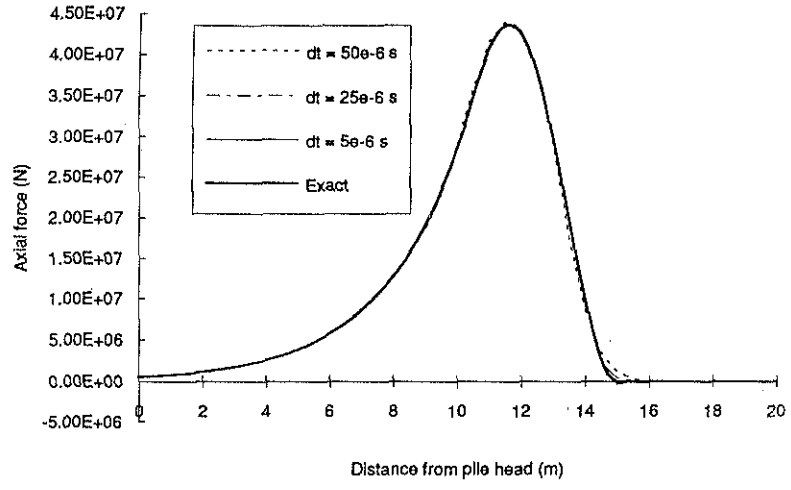

Fig 5.37. 3 ms after impact with various time steps, hammer/anvil impact.

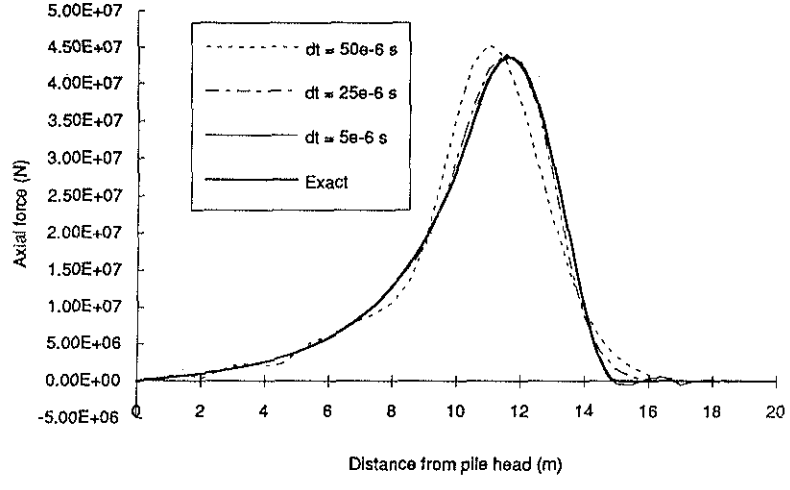

Fig 5.38. 19 ms after impact with various time steps, hammer/anvil impact.

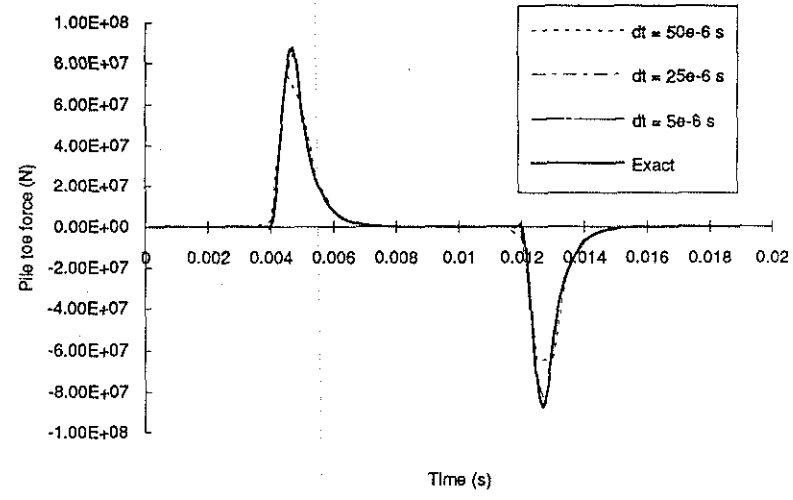

Fig 5.39. Toe force vs time with various time steps, hammer/anvil impact.

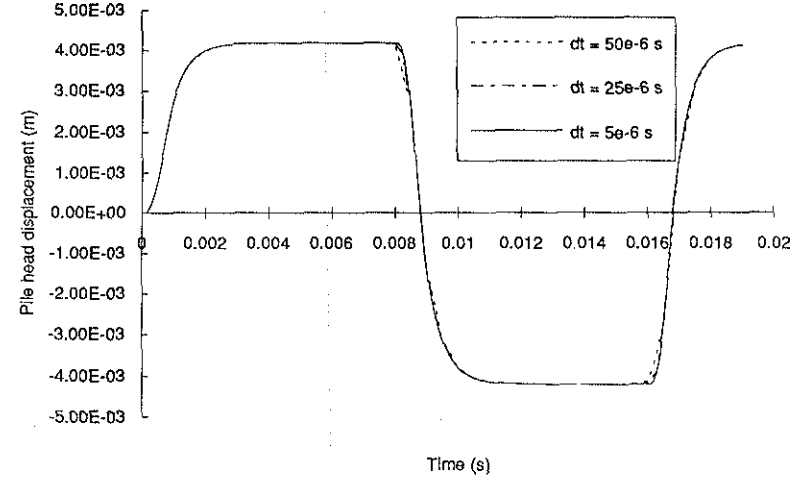

Fig 5.40. Head displacement vs time with various time steps, hammer/anvil impact.

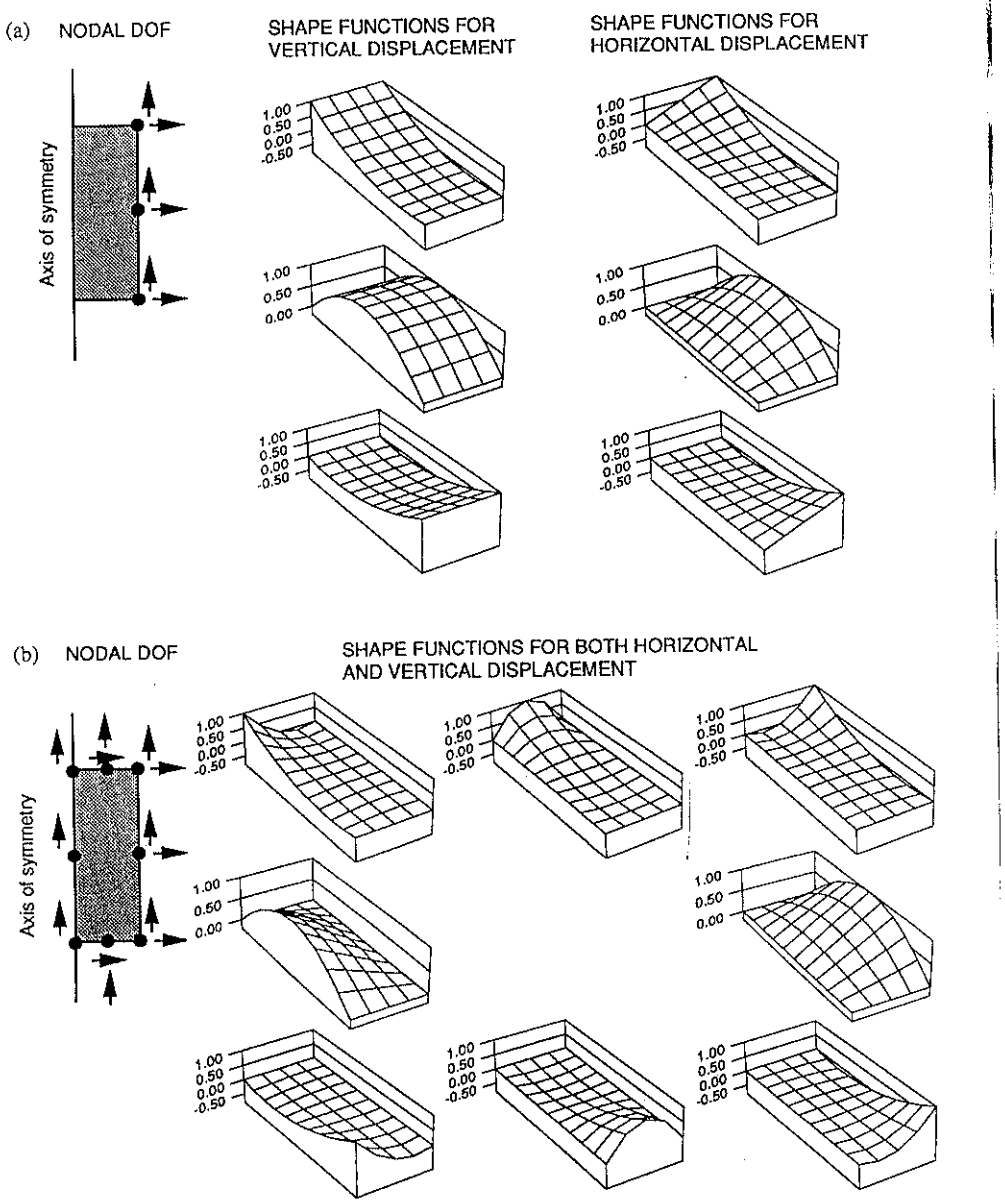

Fig 5.41. Elements for the analysis of a solid pile, including the effect of radial inertia.

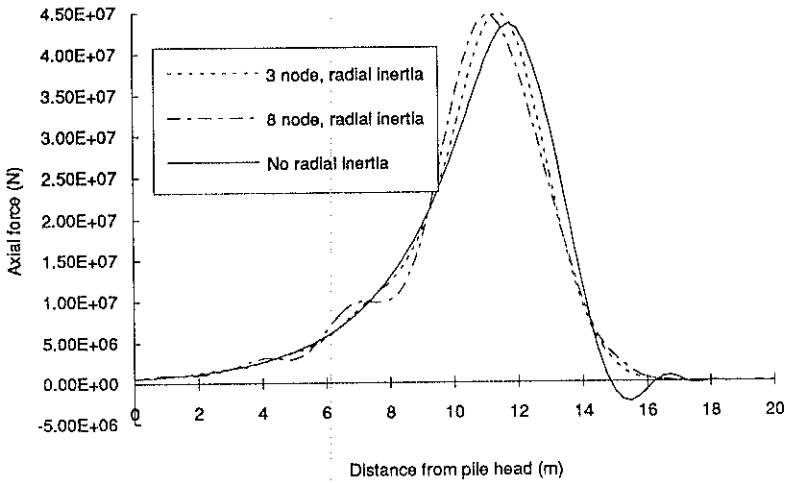

Fig 5.42. Effect of radial inertia on the axial force 3 ms after impact.

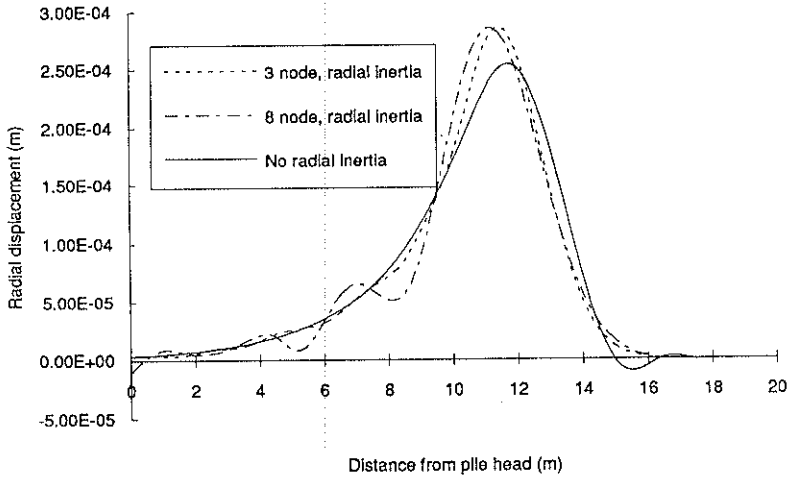

Fig 5.43. Effect of radial inertia on the radial displacement 3 ms after impact.

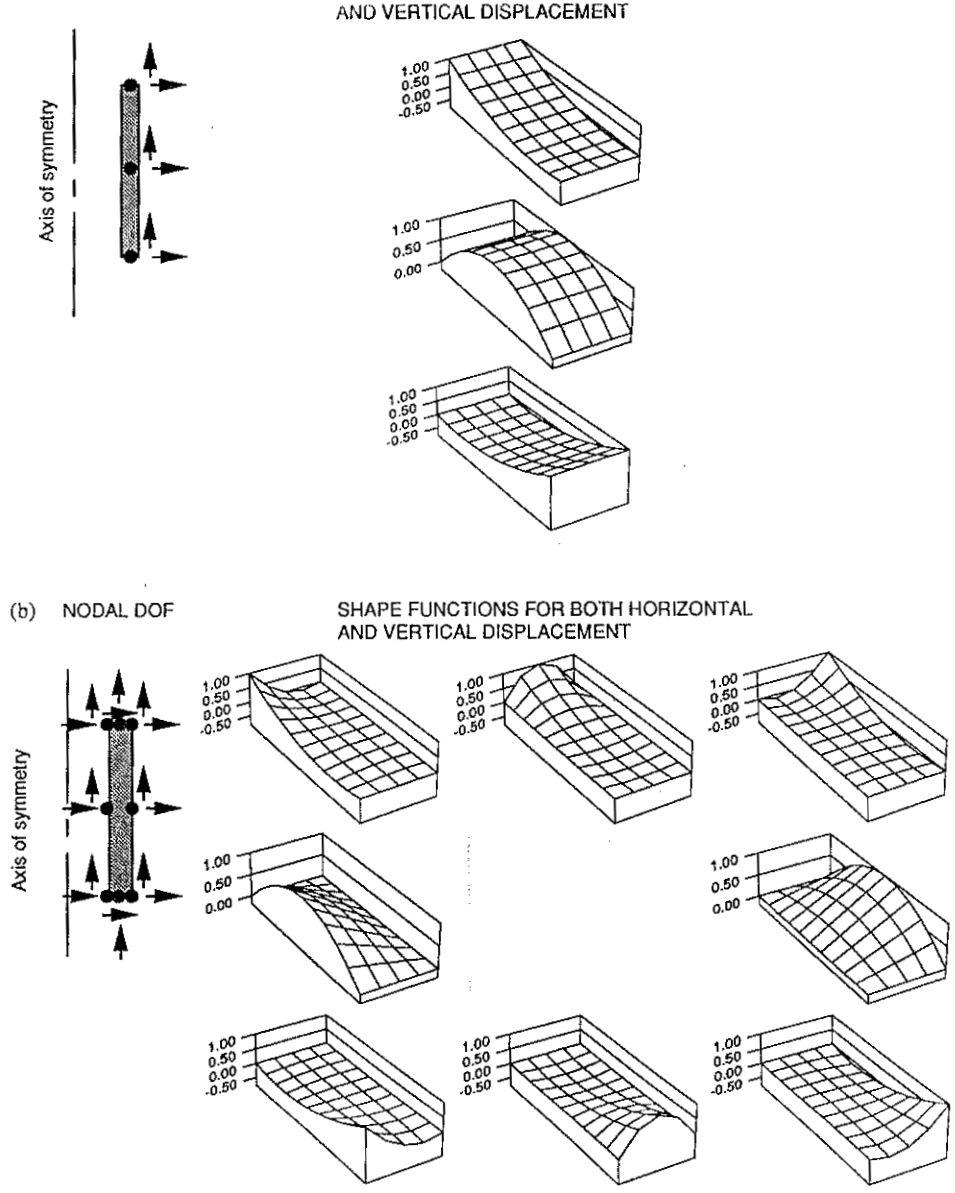

Fig 5.44. Elements for the analysis of a hollow pile, including the effect of radial inertia.

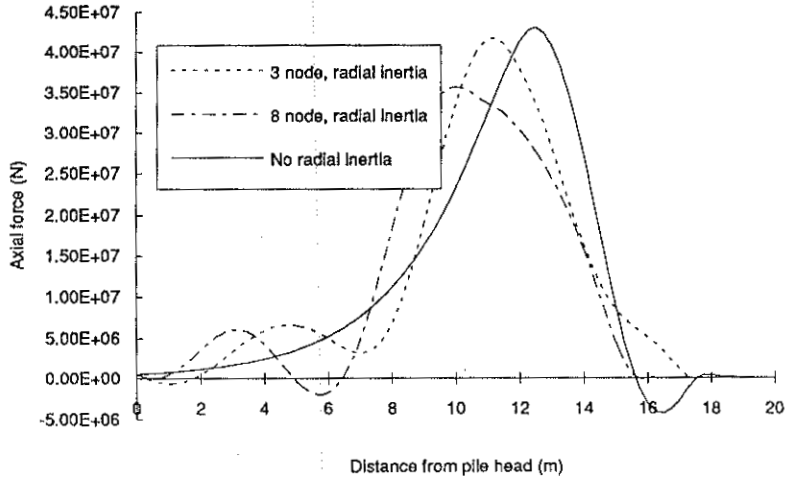

Fig 5.45. Effect of radial inertia on the axial force 3 ms after impact (tube elements).

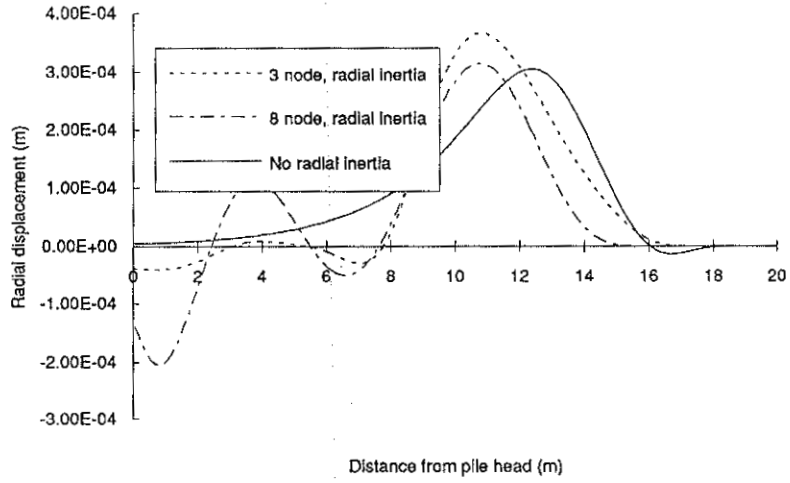

Fig 5.46. Effect of radial inertia on the radial displacement 3 ms after impact (tube elements

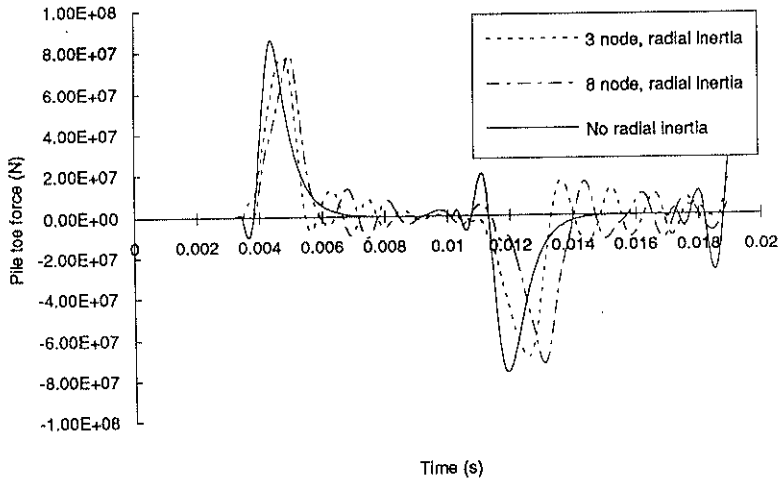

Fig 5.47. Effect of radial inertia on the toe force (tube elements).

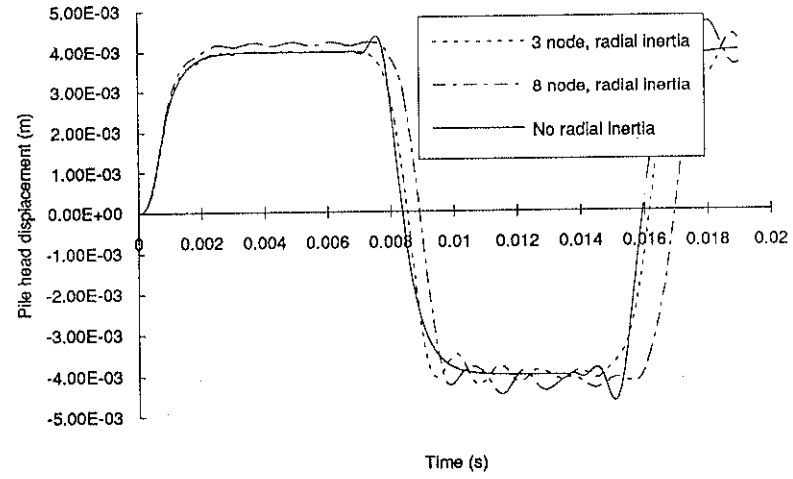

Fig 5.48. Effect of radial inertia on the head displacement (tube elements).

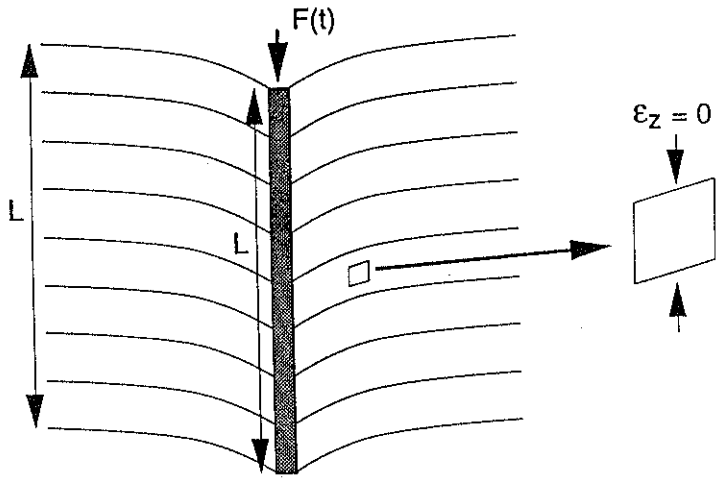

Fig 6.1. Plane strain idealisation of the soil surrounding a rigid pile.

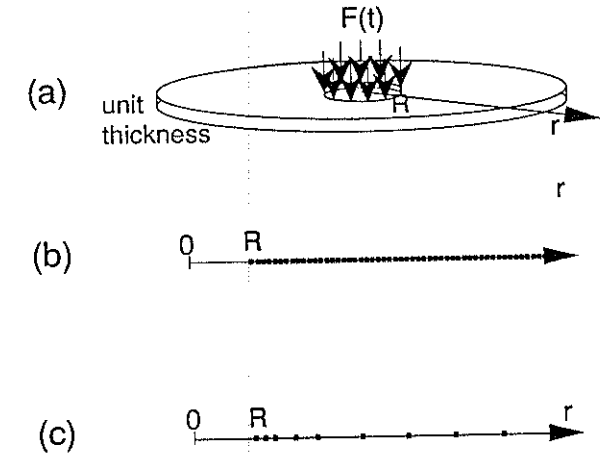

Fig 6.2. Plane strain soil disc and axisymmetric finite element meshes.

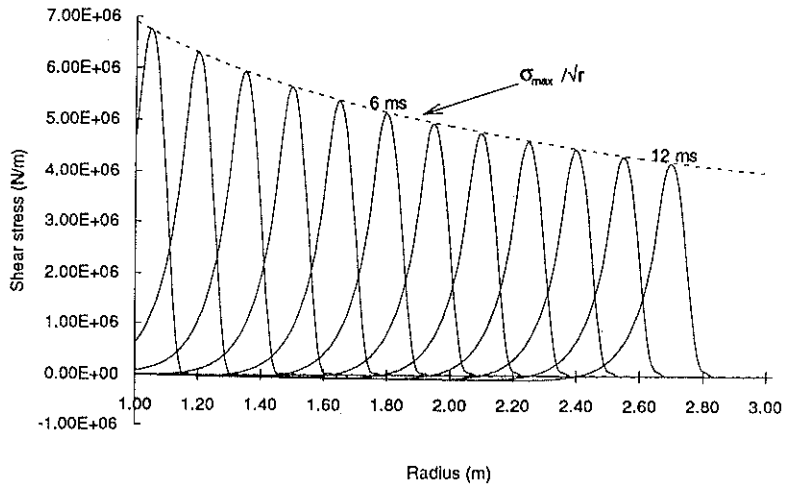

Fig 6.3. Propagation of axisymmetric shear wave in terms of stress.

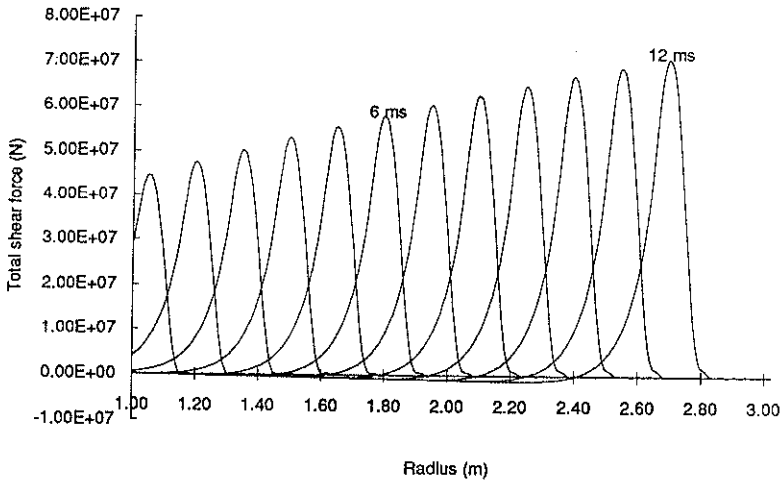

Fig 6.4. Propagation of axisymmetric shear wave in terms of total force.

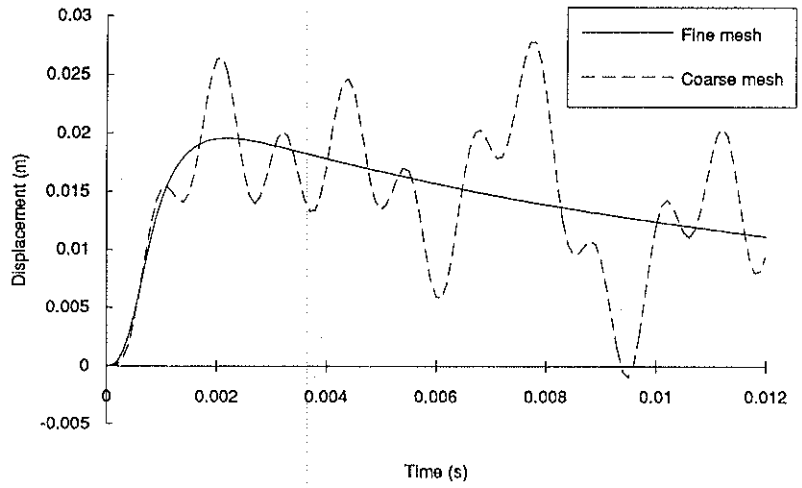

Fig 6.5. Effect of node spacing on shear displacements.

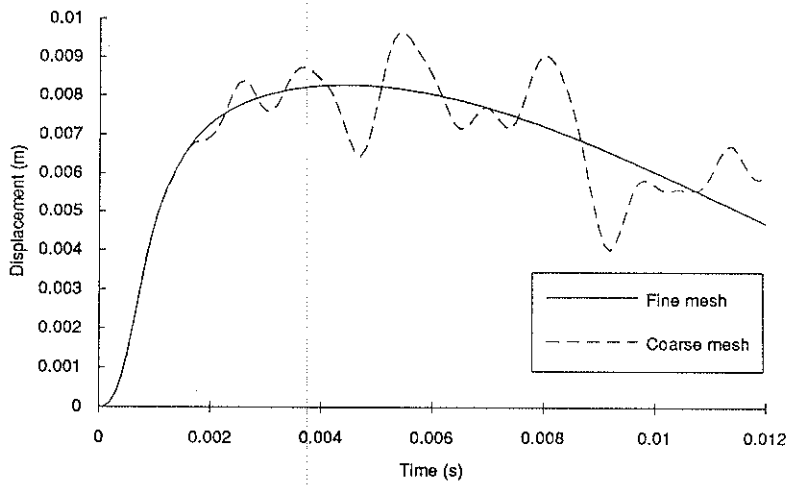

Fig 6.6. Effect of node spacing on radial displacements

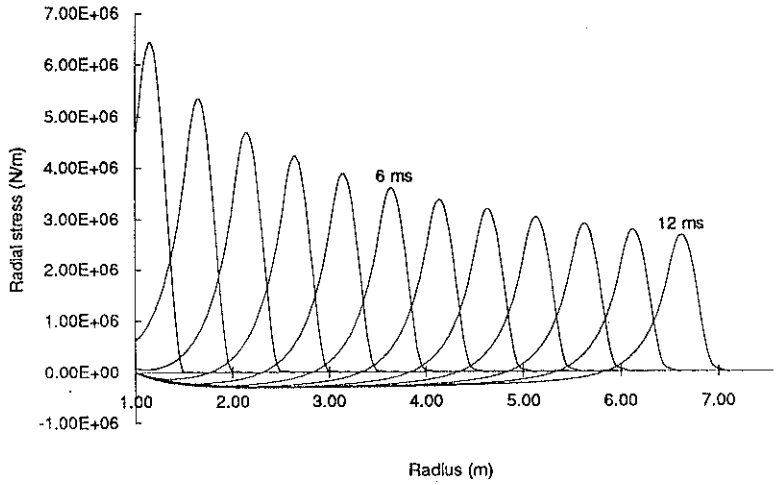

Fig 6.7. Propagation of axisymmetric dilation wave in terms of stress.

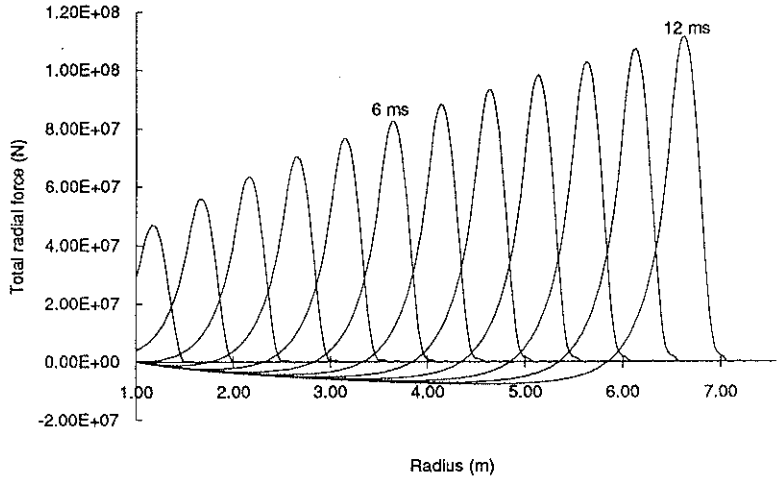

Fig 6.8. Propagation of axisymmetric dilation wave in terms of total force.

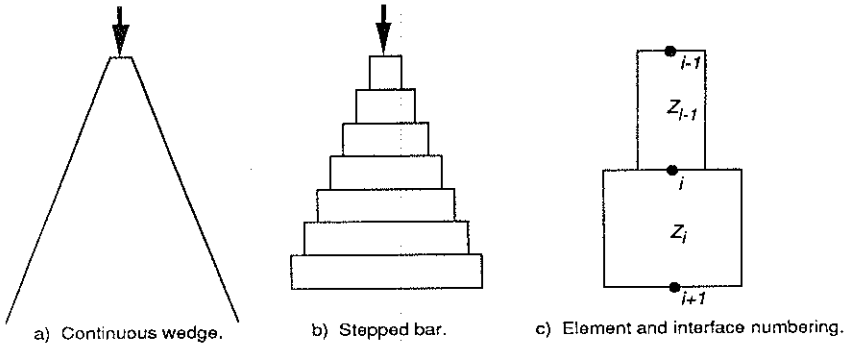

Fig 6.9. Models for axial wave propagation in a wedge.

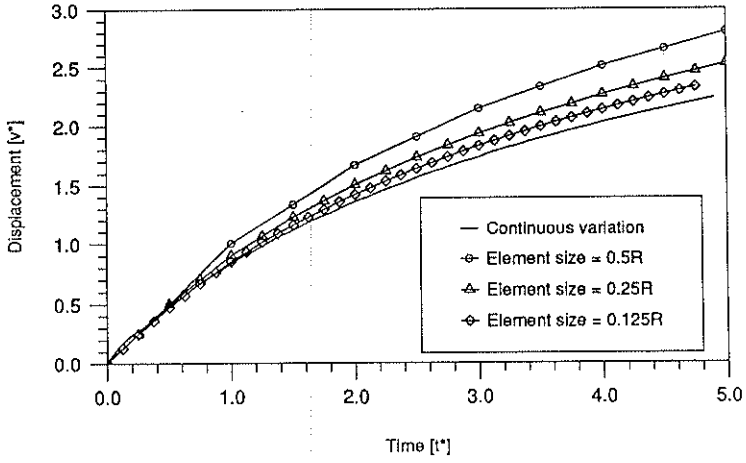

Fig 6.10. Displacement of the top of a wedge under a step load.

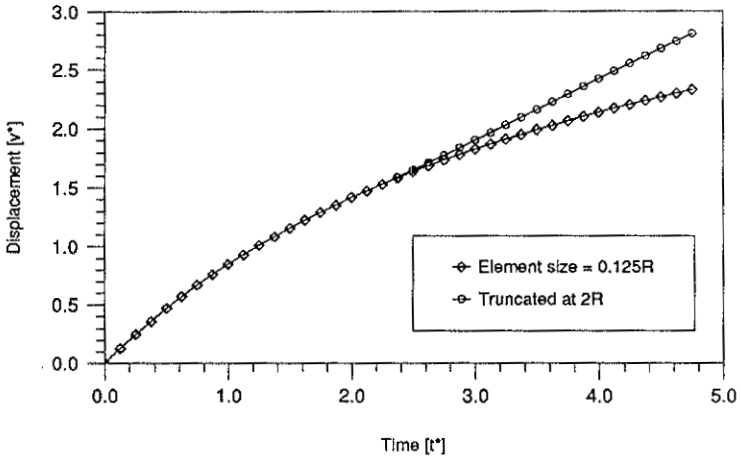

Fig 6.11. The effect of truncating the wedge with a zero reflection boundary.

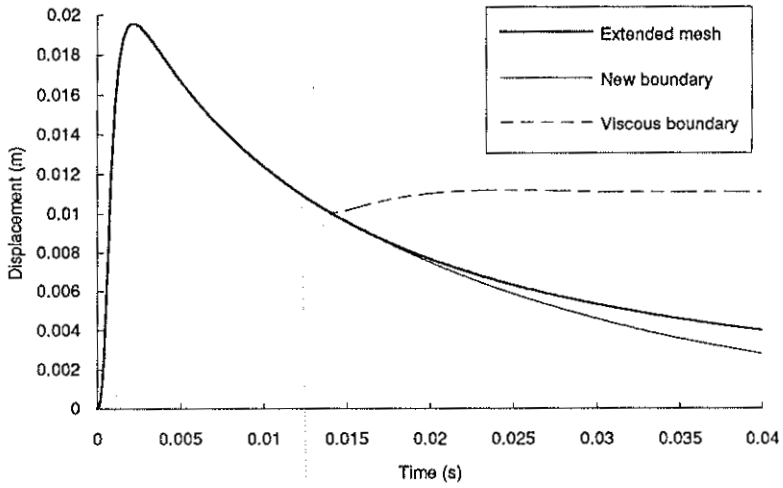

Fig 6.12. The effect of truncating the mesh at r = 2m with different shear boundaries.

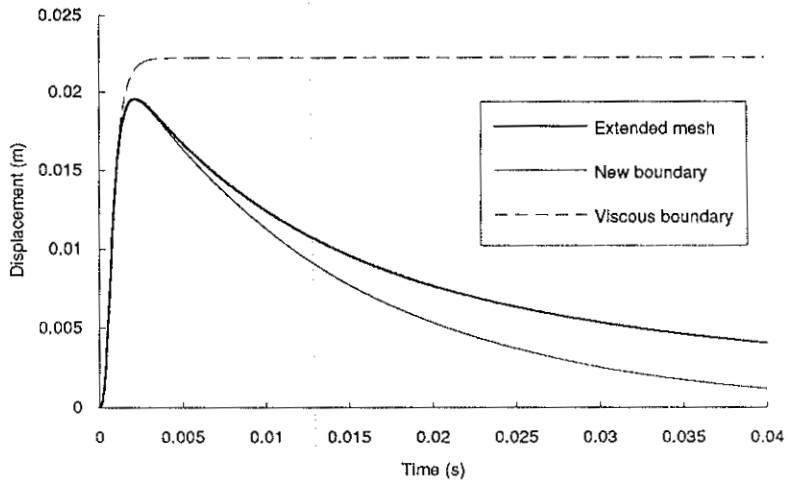

Fig 6.13. The effect of placing the shear boundaries at r = 1m.

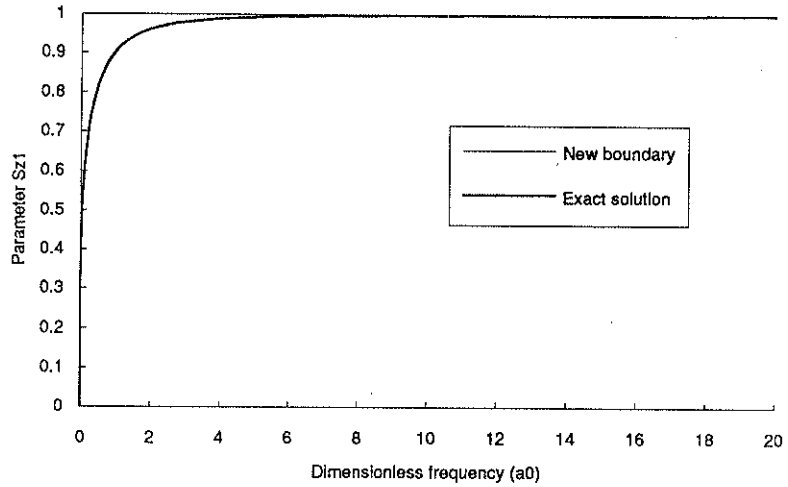

Fig 6.14. Variation of real shear stiffness with dimensionless frequency.

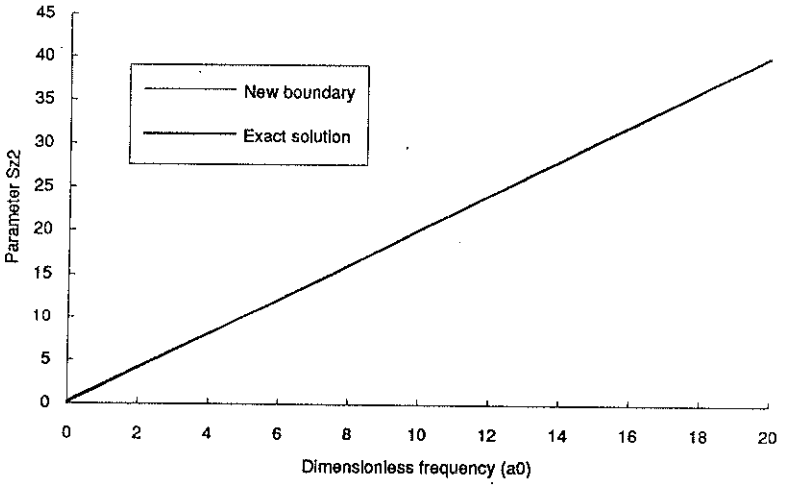

Fig 6.15. Variation of imaginary shear stiffness with dimensionless frequency.

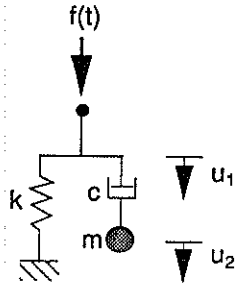

	Spherical dilation (Wolf, 1988)	Cylindrical dilation (New)
k	4 G/R	2 G/R
c	ρc_d	ρc_d
m	4 ρ R	2 ρ R

Fig 6.16. Mechanical model for dilation wave transmission from a cavity.

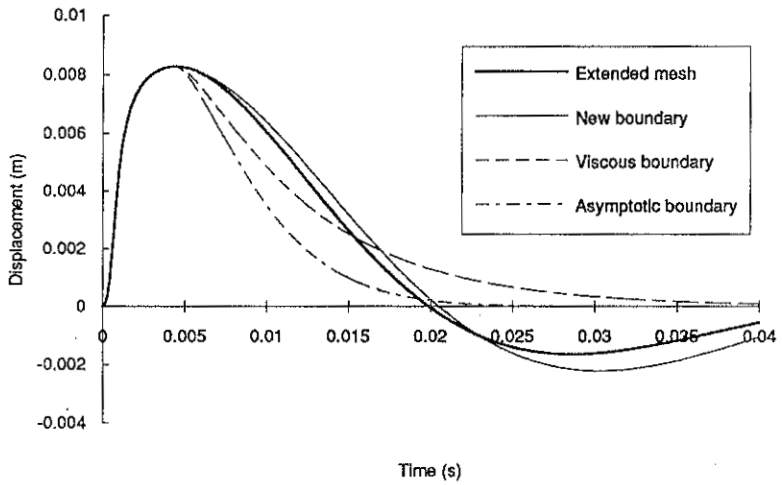

Fig 6.17. The effect of truncating the mesh at r = 2m with dilation boundaries,v = 0.45.

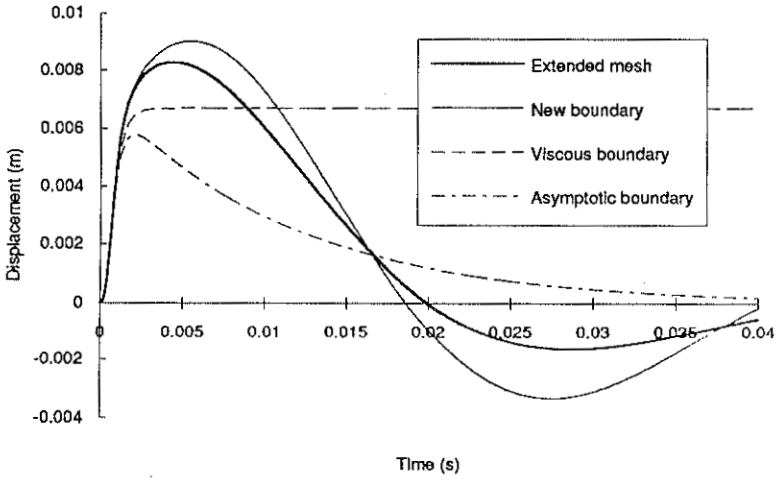

Fig 6.18. The effect of placing the dilation boundaries at r = 1m, v = 0.45.

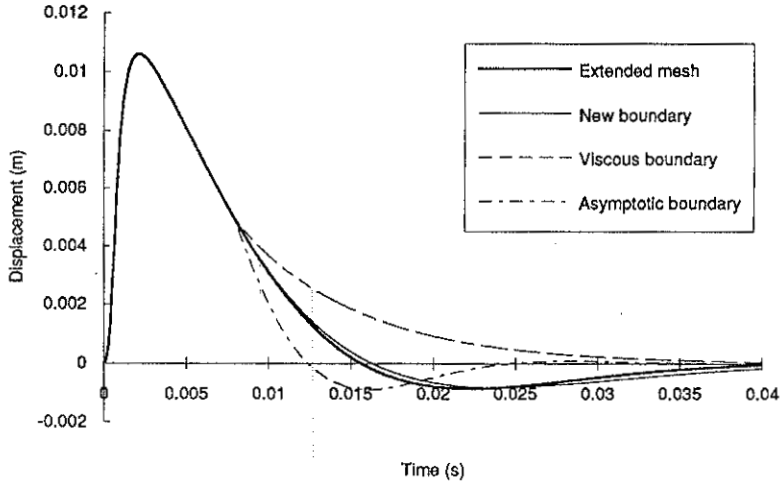

Fig 6.19. The effect of truncating the mesh at r = 2m with dilation boundaries,v = 0.25.

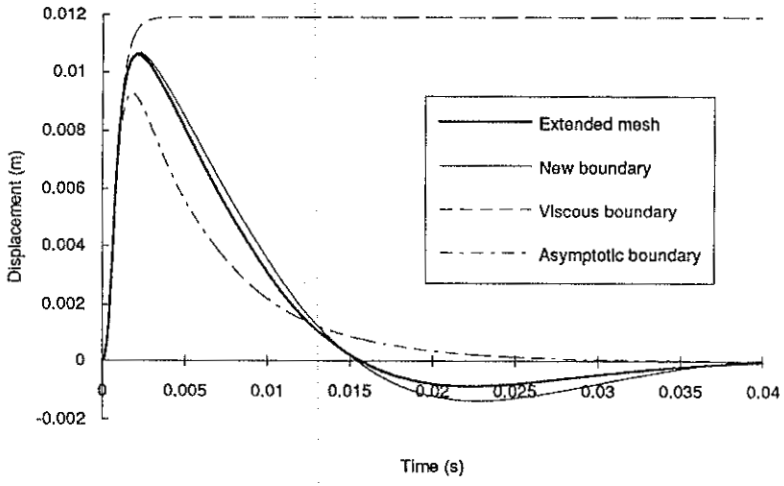

Fig 6.20. The effect of placing the dilation boundaries at r = 1m, v = 0.25.

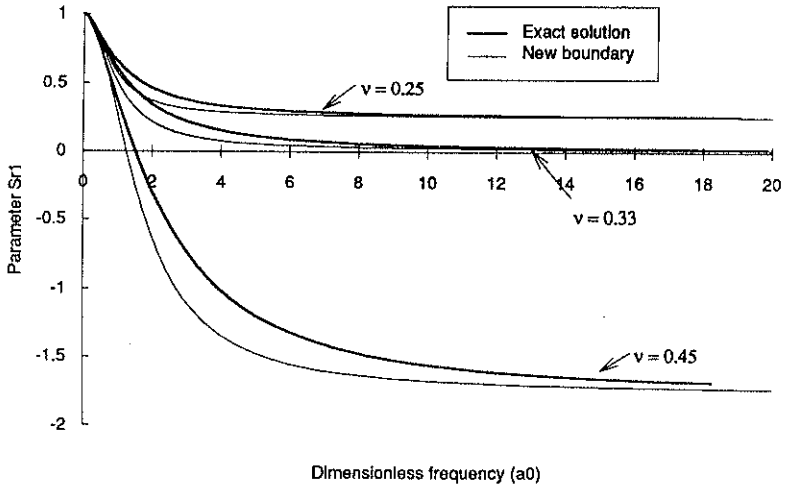

Fig 6.21. Variation of real radial stiffness with dimensionless frequency.

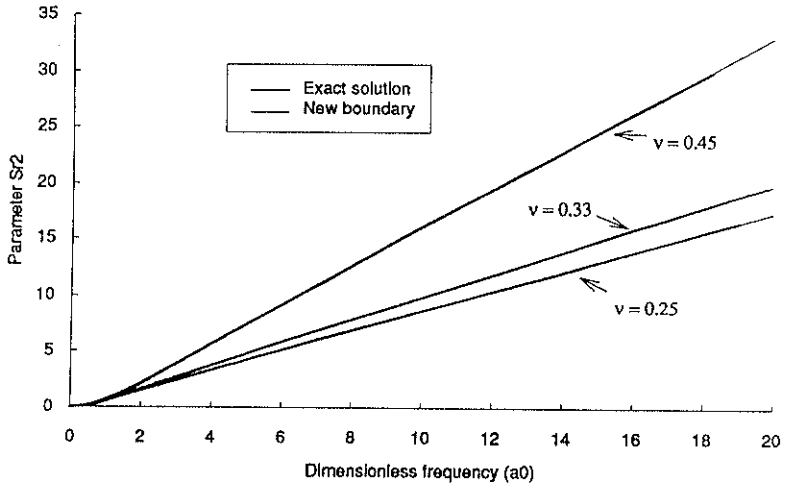

Fig 6.22. Variation of imaginary radial stiffness with dimensionless frequency.

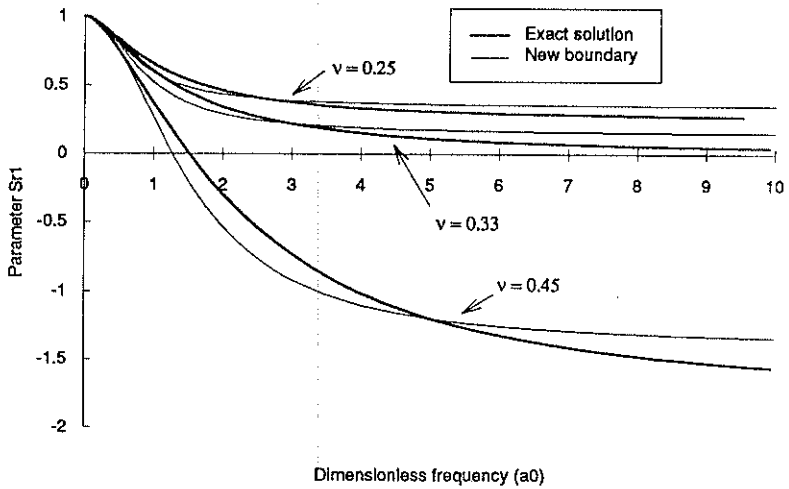

Fig 6.23. Variation of real radial stiffness with boundary matched at v=0.45, a0=5.

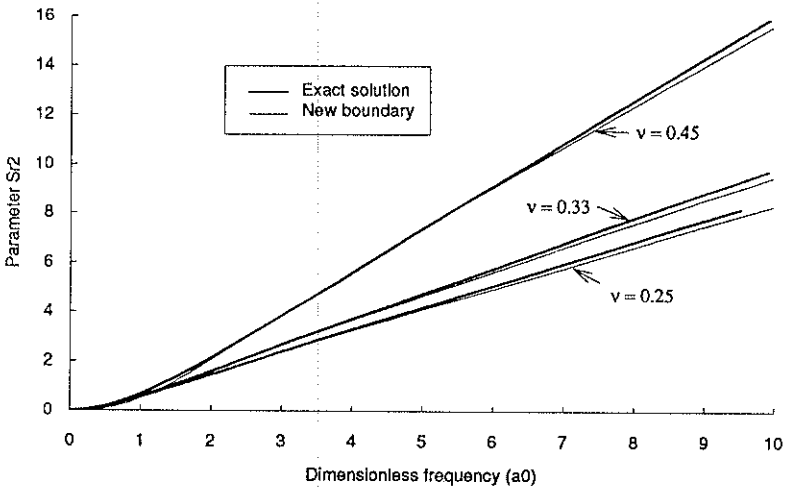

Fig 6.24. Variation of imaginary radial stiffness with boundary matched at v=0.45, a0=5.

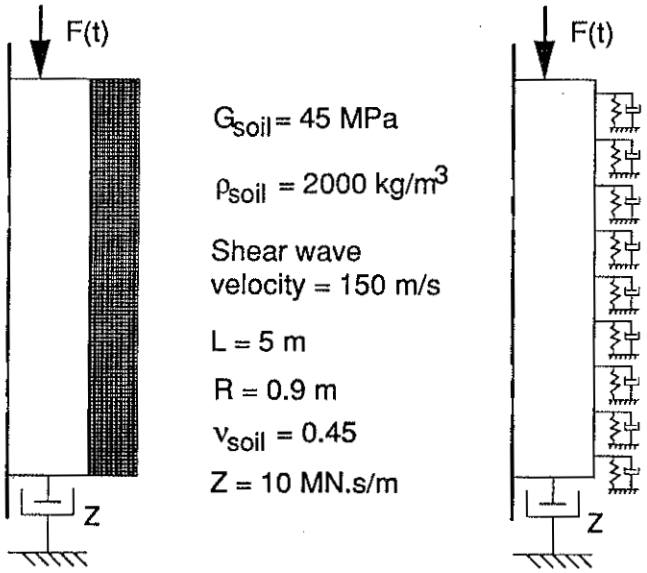

Fig 6.25. Finite element and one-dimensional semi-infinite pile models.

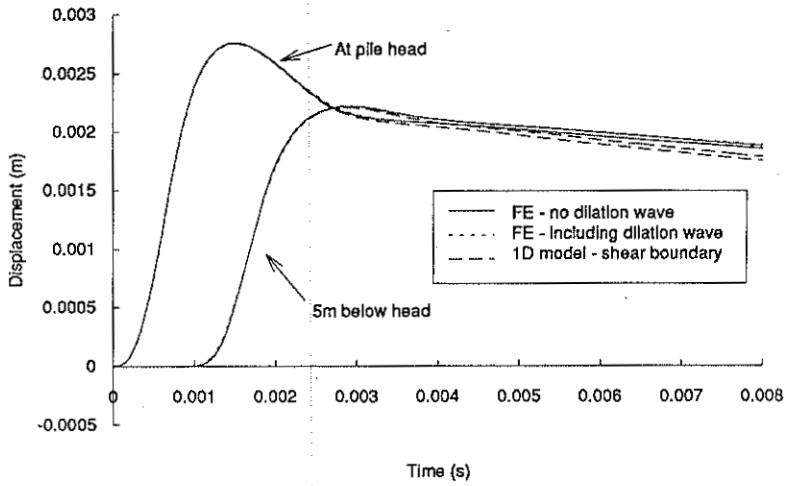

Fig 6.26. Semi-infinite pile displacements.

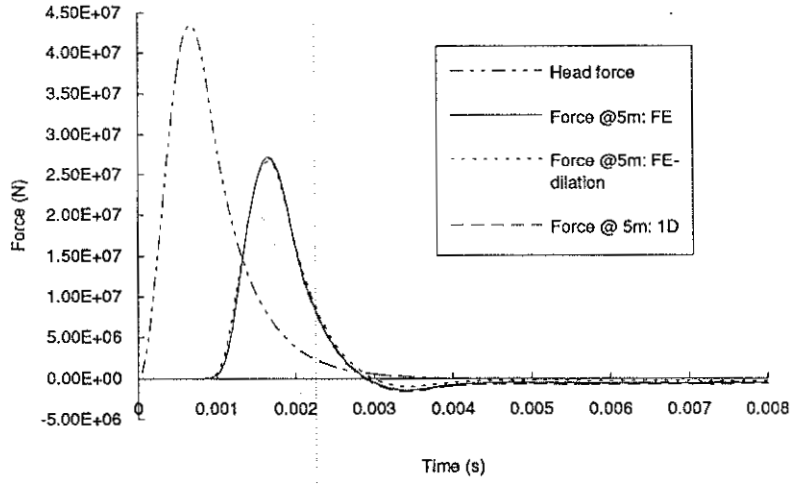

Fig 6.27. Semi-infinite pile forces.

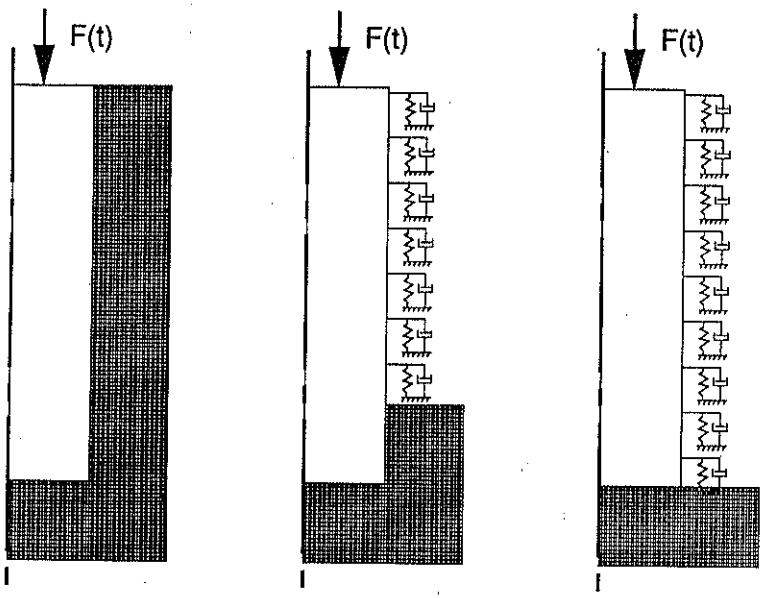

Fig 6.28. Models for evaluating interaction between the shaft and base waves.

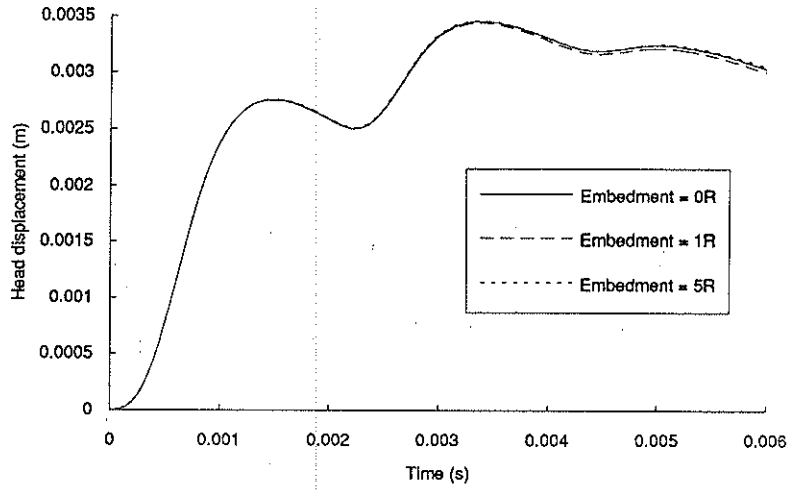

Fig 6.29. Variation of finite pile displacements with mesh embedment.

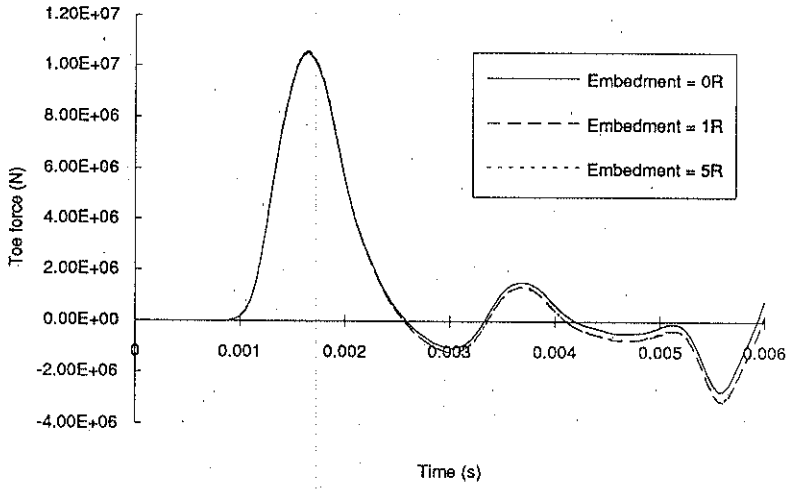

Fig 6.30. Variation of toe force with mesh embedment.

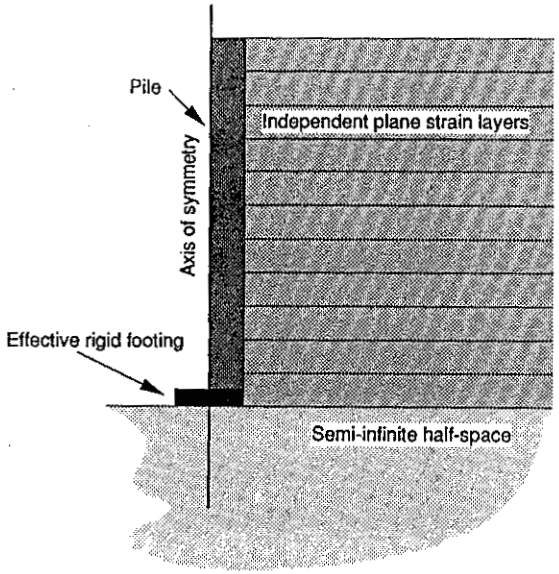

Fig 7.1. Modelling the pile toe as a rigid footing on a semi-infinite half-space.

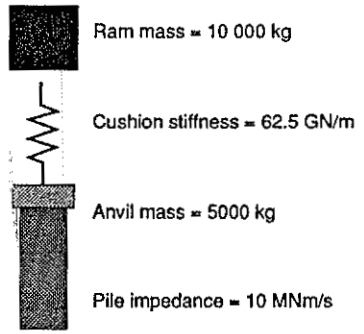

Fig 7.2(a). Hammer properties used to generate impact force applied to footing.

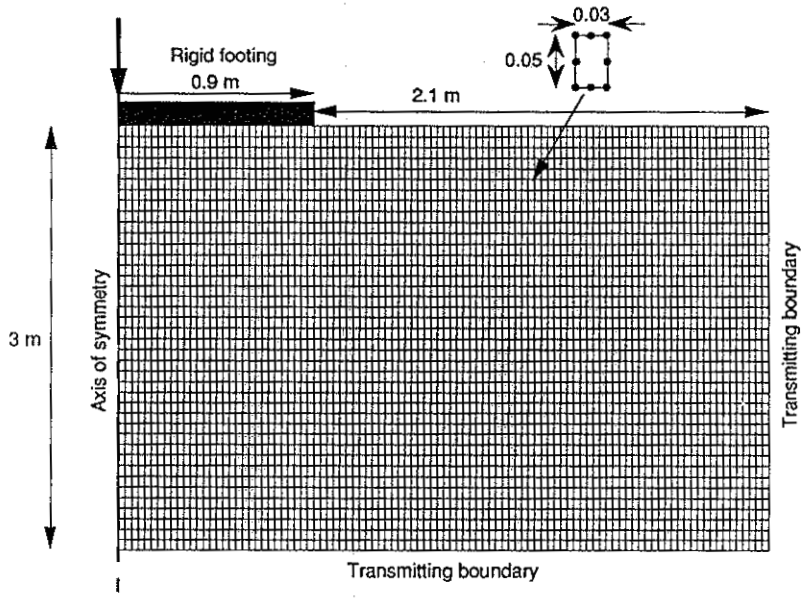

Fig 7.2(b). Finite element mesh for calculating stress waves beneath a rigid footing.

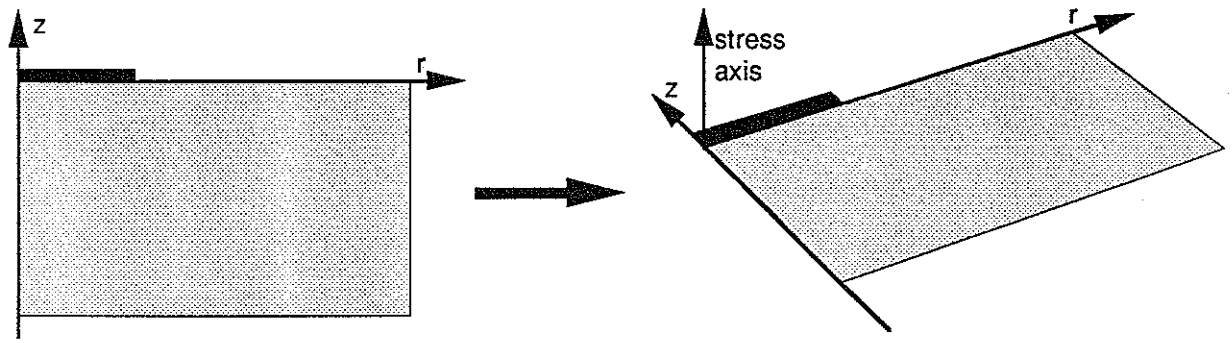

Fig 7.3. The relationship between the surface plots and the finite element mesh.

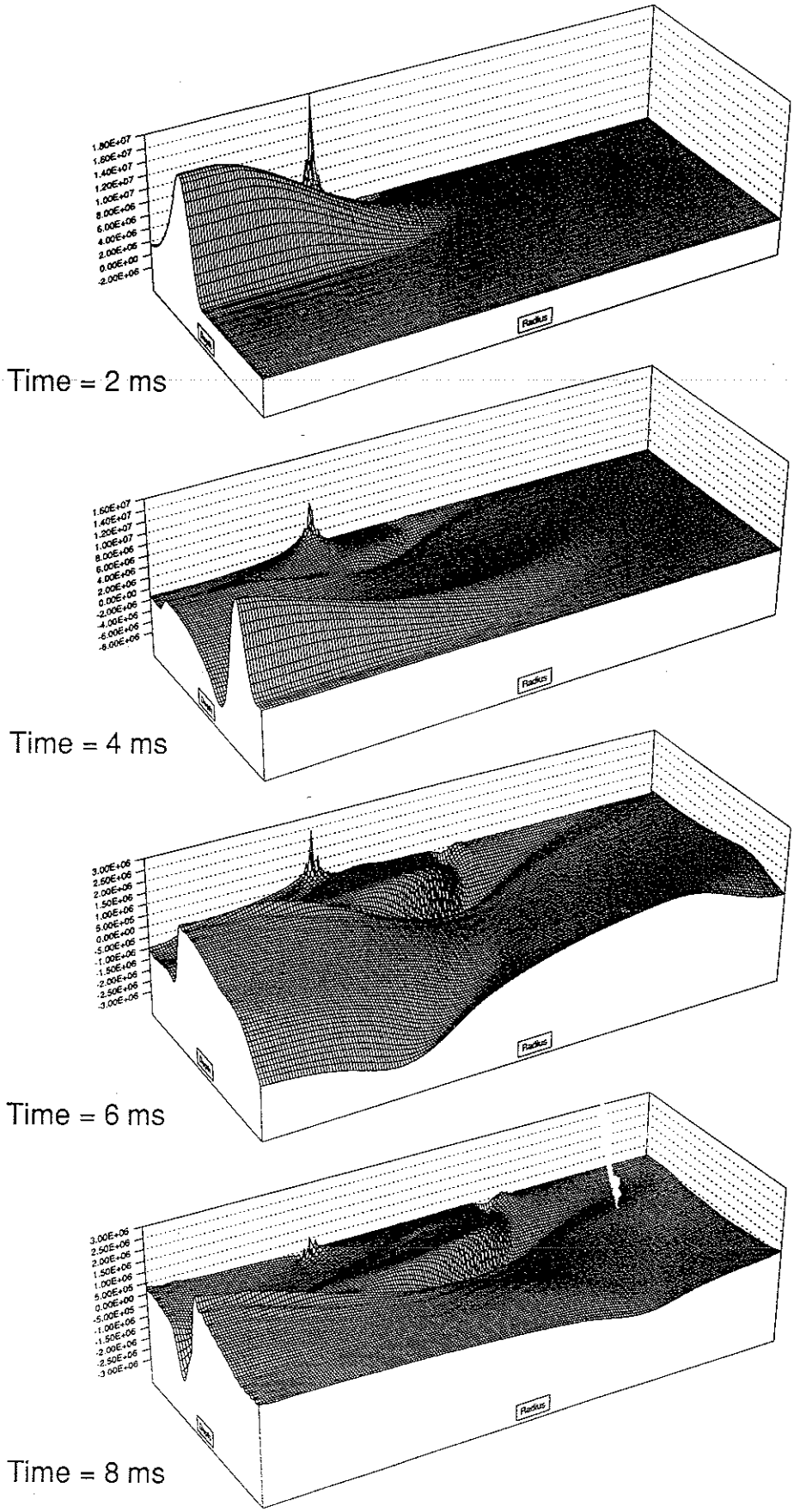

Fig 7.4. Propagation of vertical stress wave beneath a rigid footing (Pa).

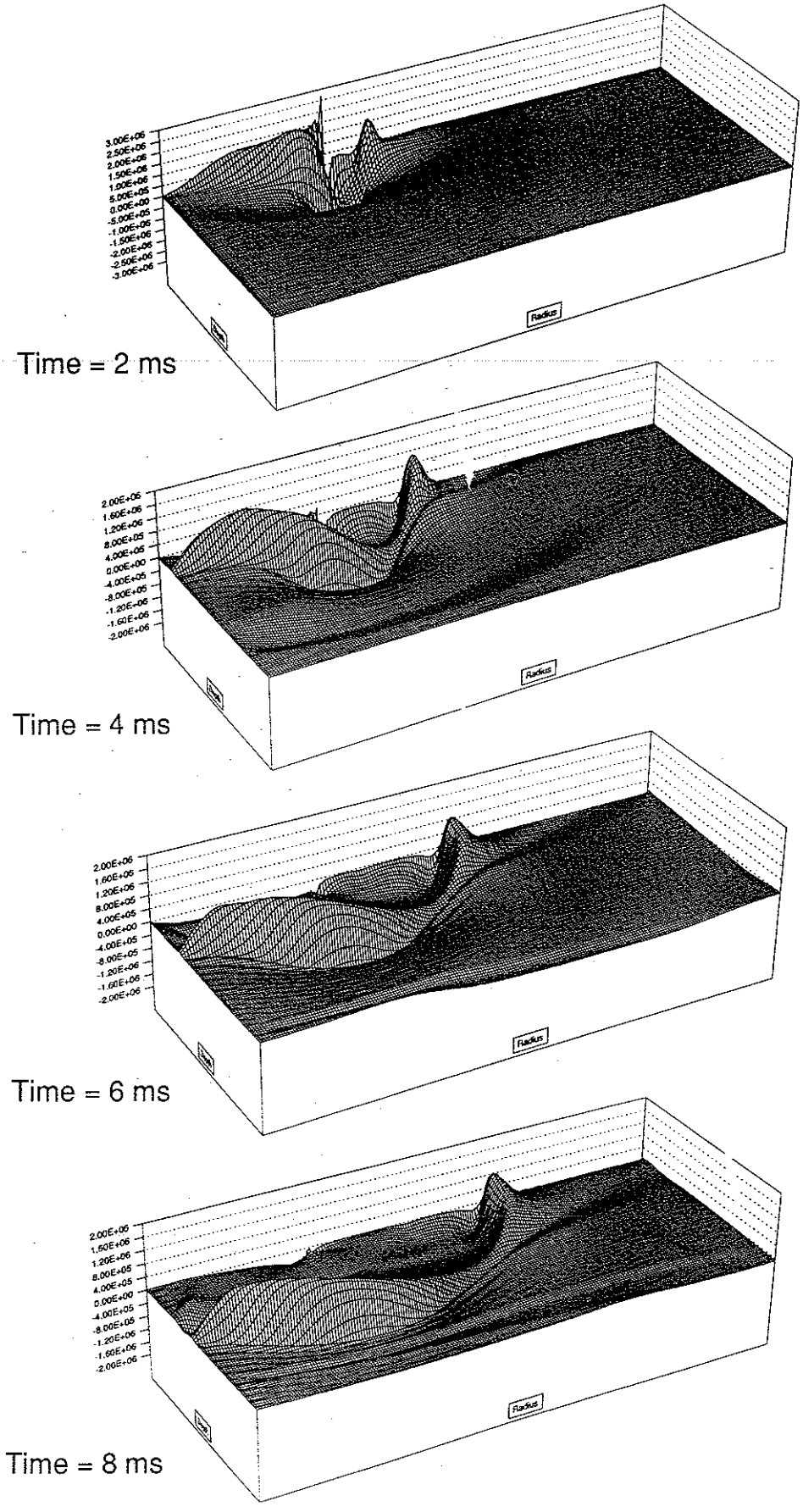

Fig 7.5. Propagation of shear stress wave beneath a rigid footing (Pa).

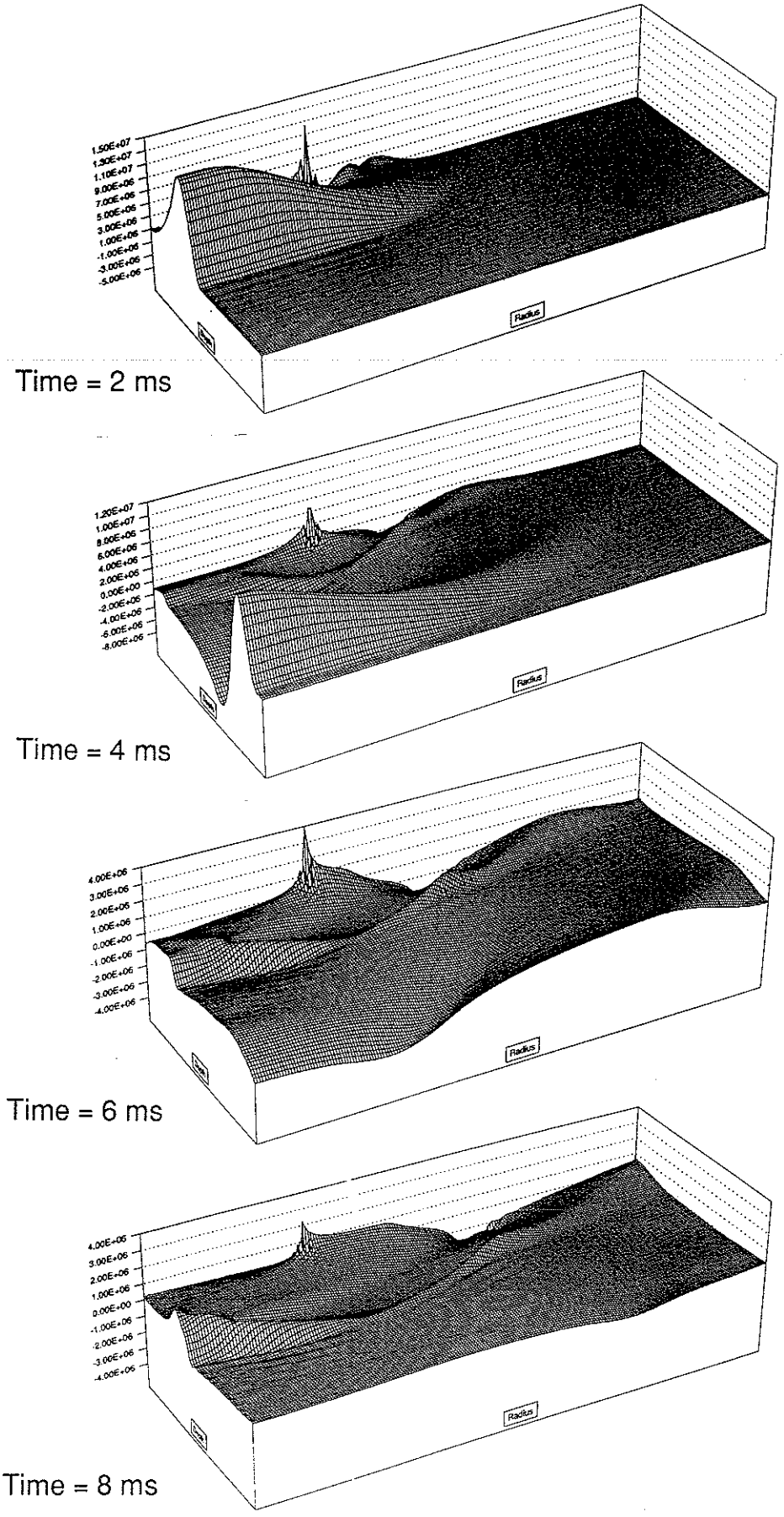

Fig 7.6. Propagation of radial stress wave beneath a rigid footing (Pa).

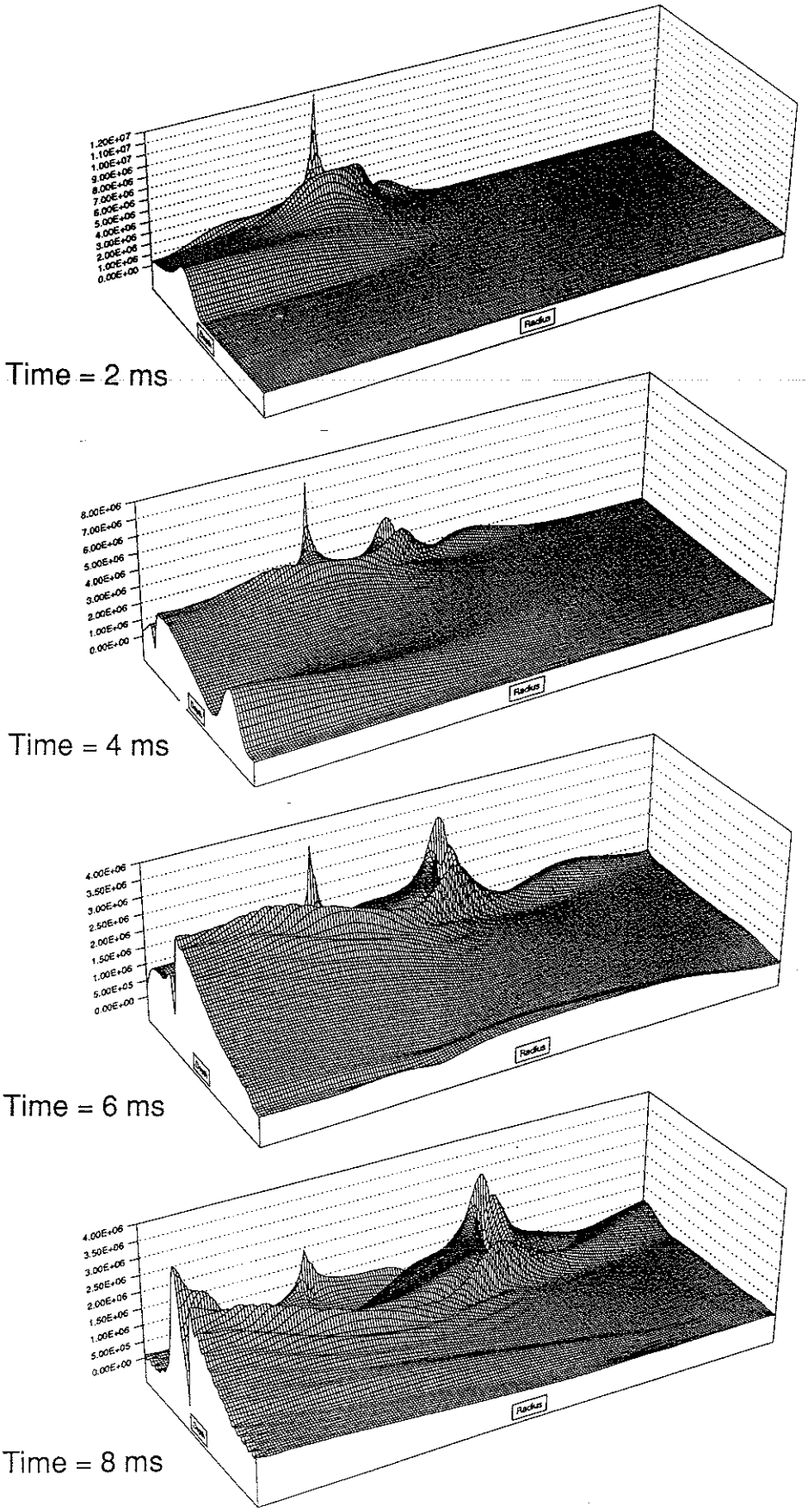

Fig 7.7. Propagation of Von Mises generalised stress wave beneath a rigid footing (Pa).

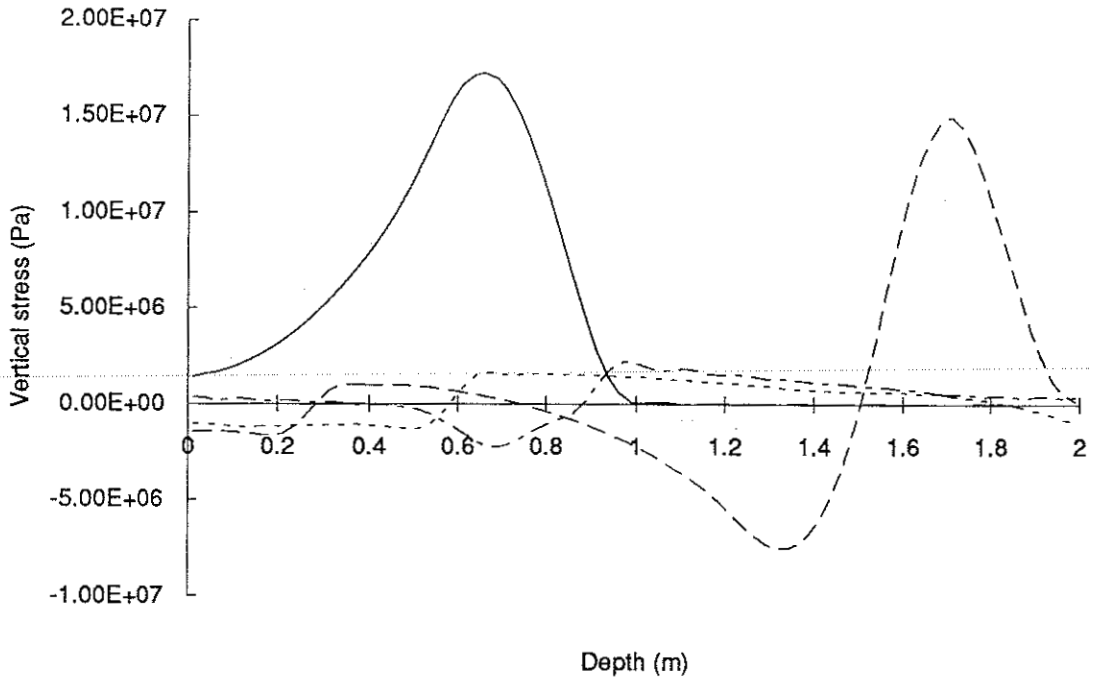

Fig 7.8. Propagation of vertical stress wave at r = 0 (legend below).

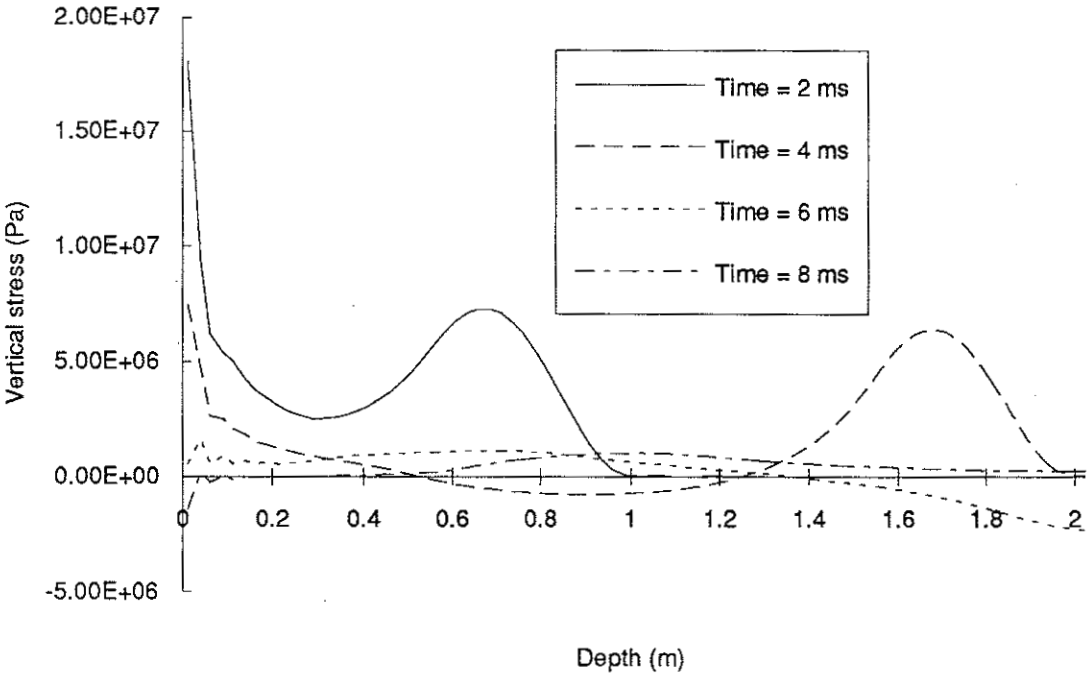

Fig 7.9. Propagation of vertical stress wave at r = R.

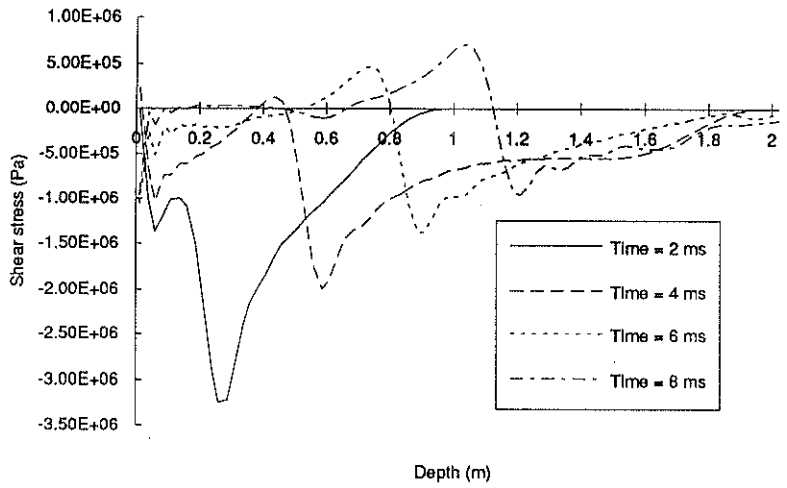

Fig 7.10. Propagation of shear stress wave at r = R.

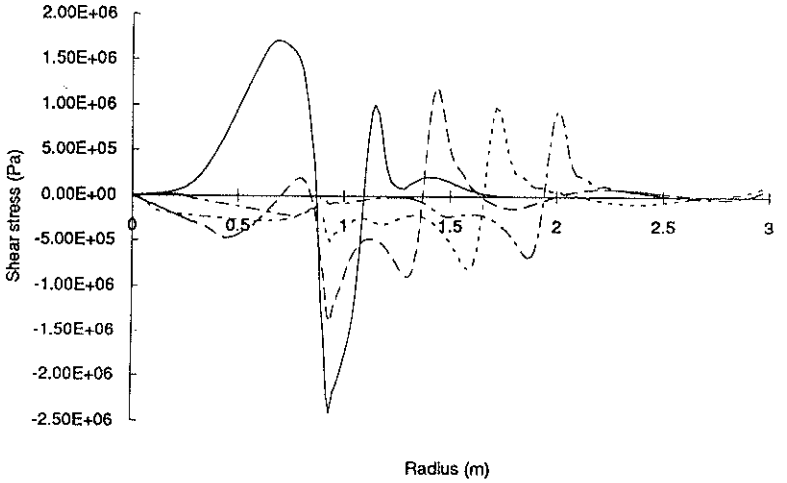

Fig 7.11. Propagation of shear stress wave at z = -0.1 m (legend above).

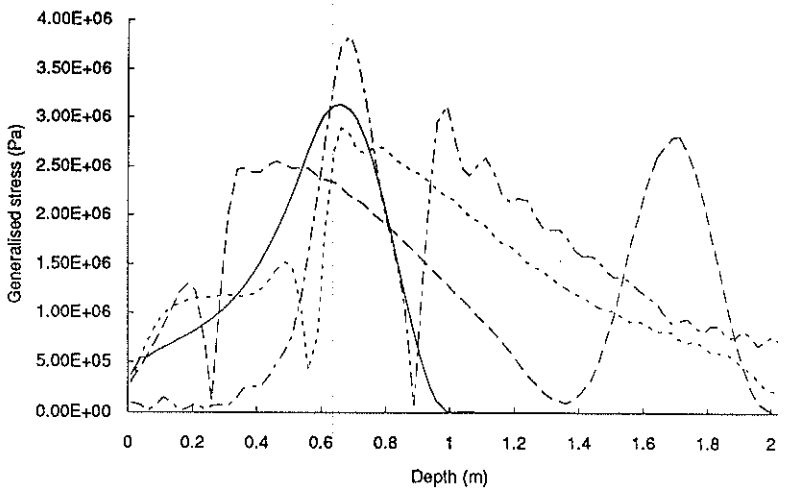

Fig 7.12(a). Propagation of generalised stress wave at r = 0 (legend below).3

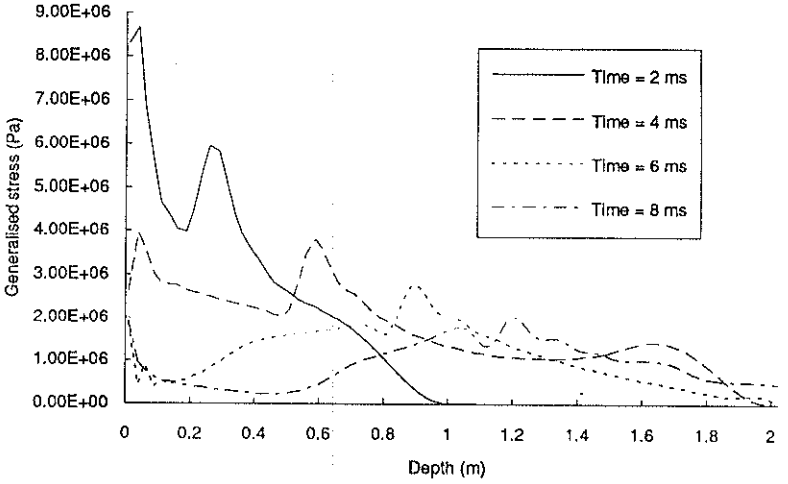

Fig 7.12(b). Propagation of generalised stress wave at r = R.

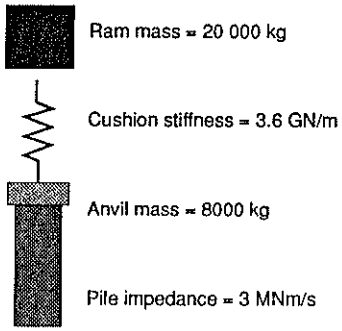

Fig 7.13. Hammer properties used to generate a less sharp impact force.

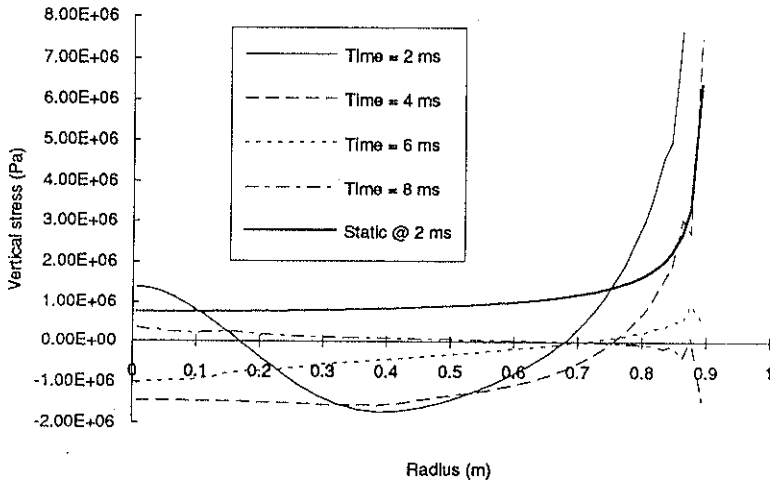

Fig 7.14. Vertical stress distribution beneath footing.

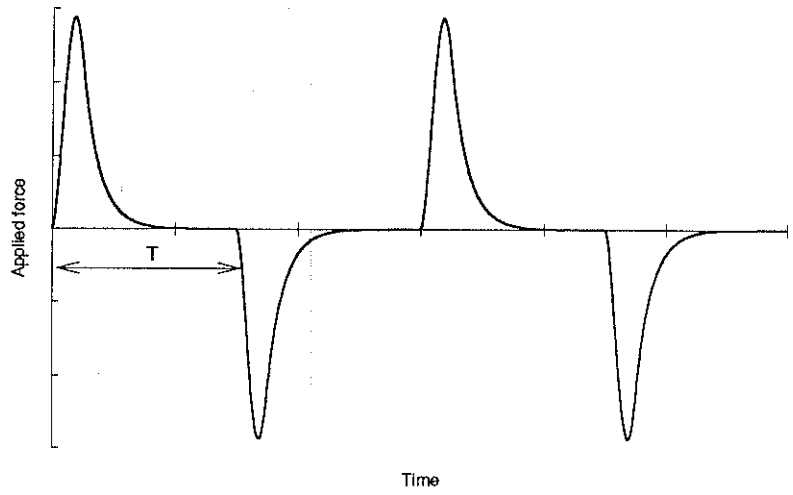

Fig 7.15(a). Continuous series of applied pulses for Fourier series analysis.

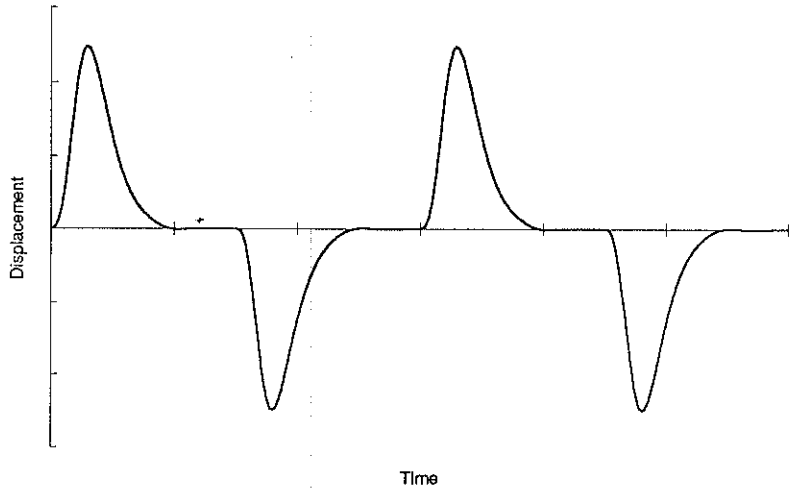

Fig 7.15(b). Corresponding displacement pulse train.

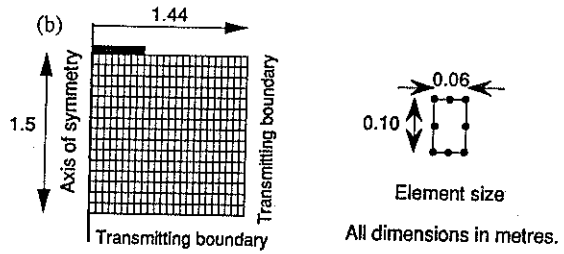

Fig 7.16(a). Finite element mesh used to compute footing complex compliance.

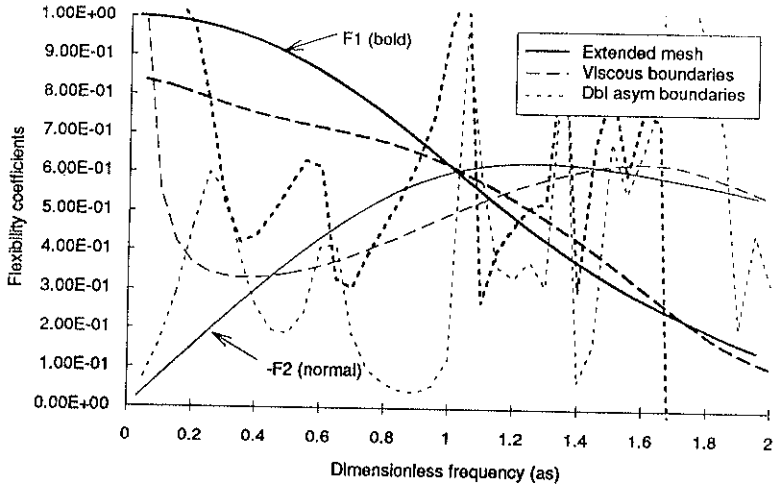

Fig 7.16(b). Effect of boundary on complex flexibility.

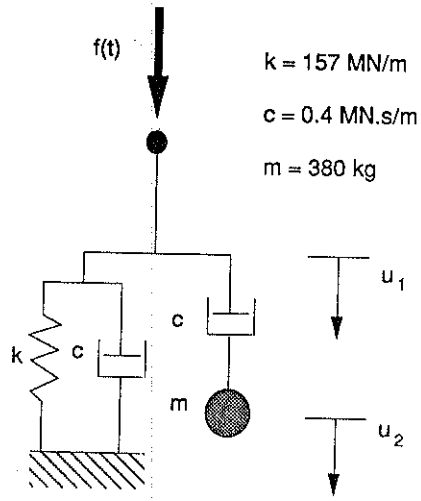

Fig 7.17(a). Mechanical system used to check compliance computation.

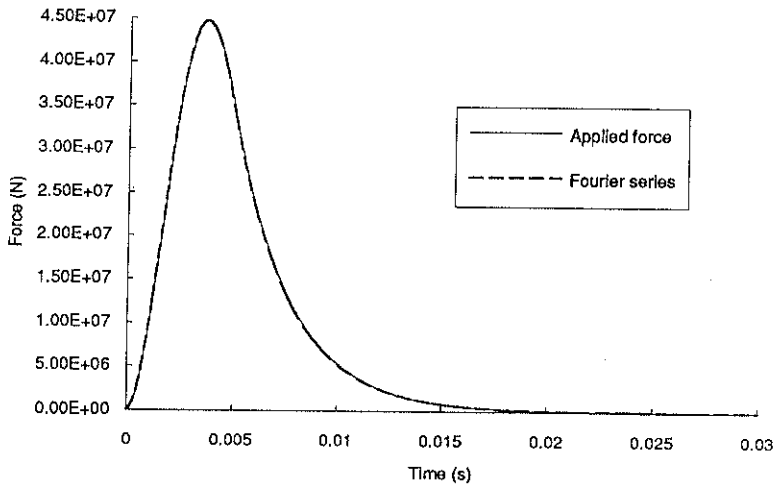

Fig 7.17(b). Force impulse used to compute compliance.

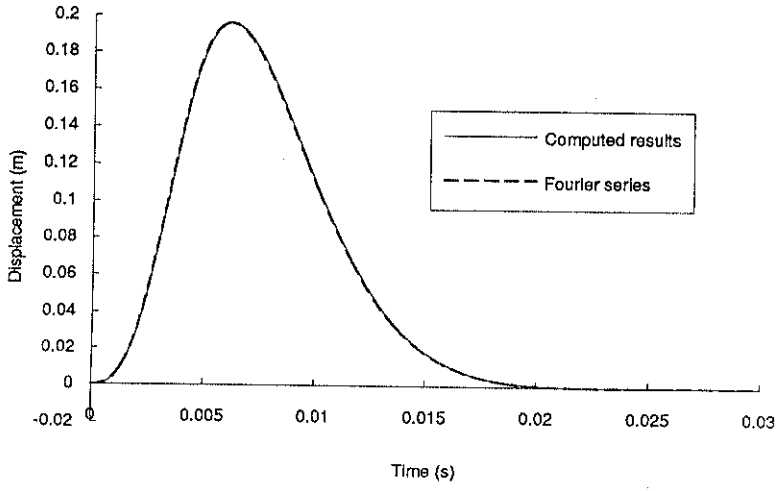

Fig 7.17(c). Model displacement under impulse force.

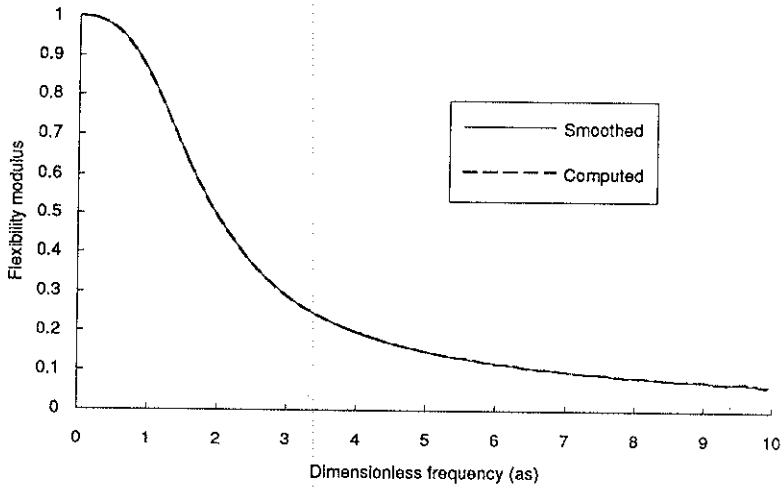

Fig 7.18(a). Computed and smoothed flexibility modulus.

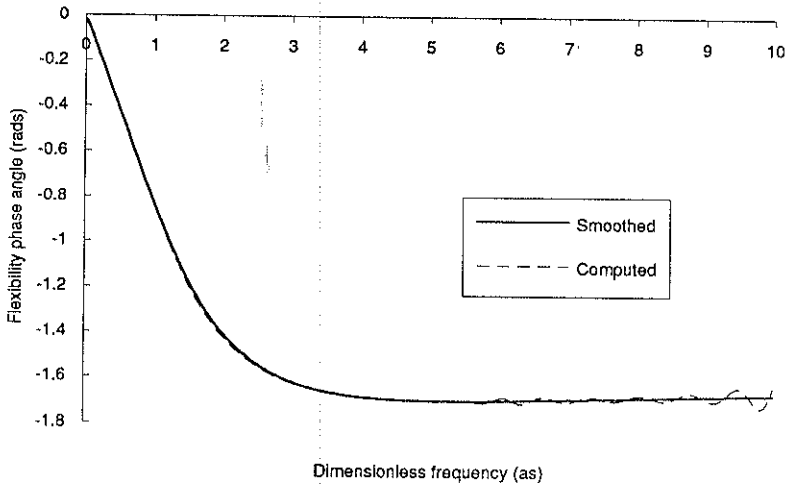

Fig 7.18(b). Computed and smoothed flexibility phase angle.

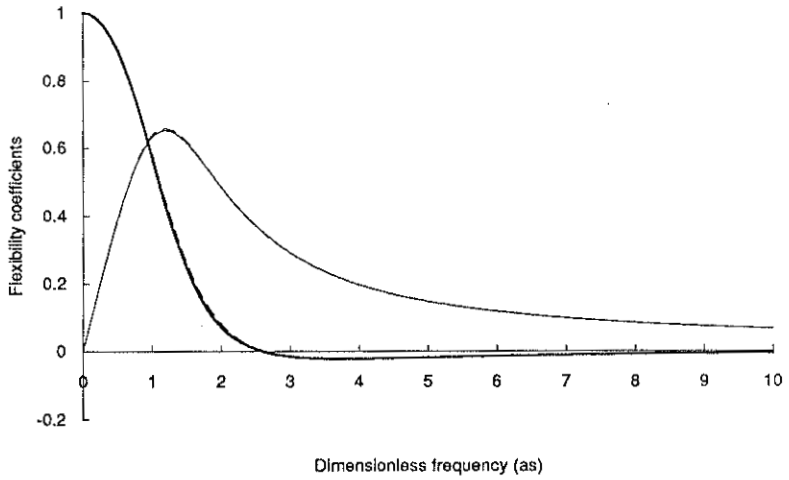

Fig 7.19. Computed and analytical flexibility coefficients for new model.

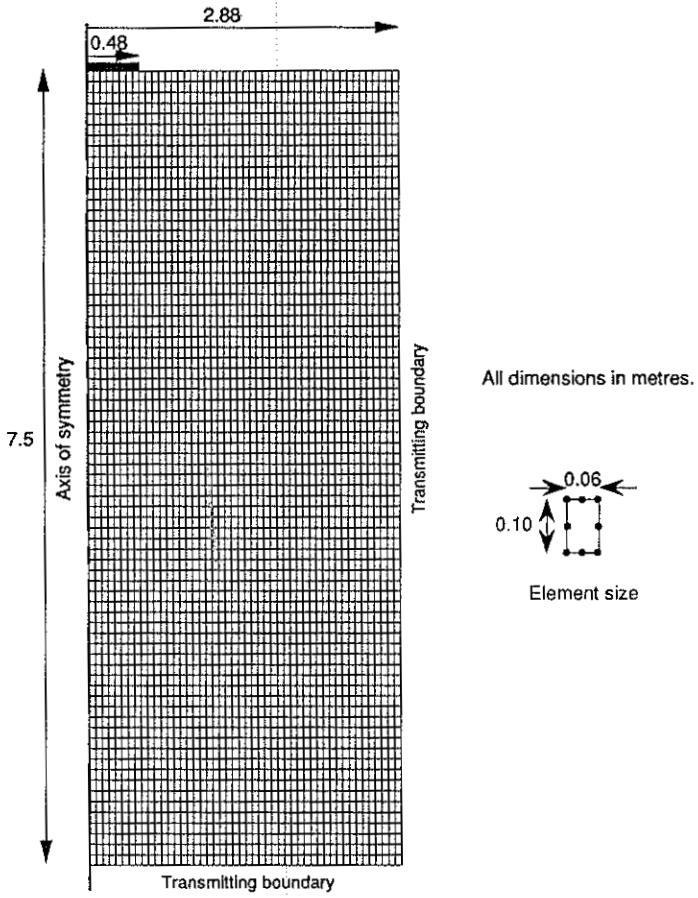

Fig 7.20. Finite element mesh used to compute the footing response to an impact load.

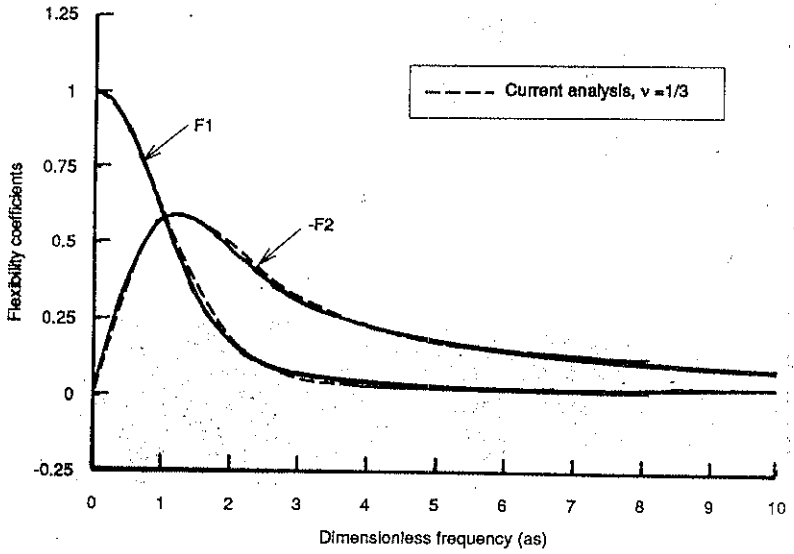

Fig 7.21. Footing compliance: present work and Luco and Westmann's (1971) analysis.

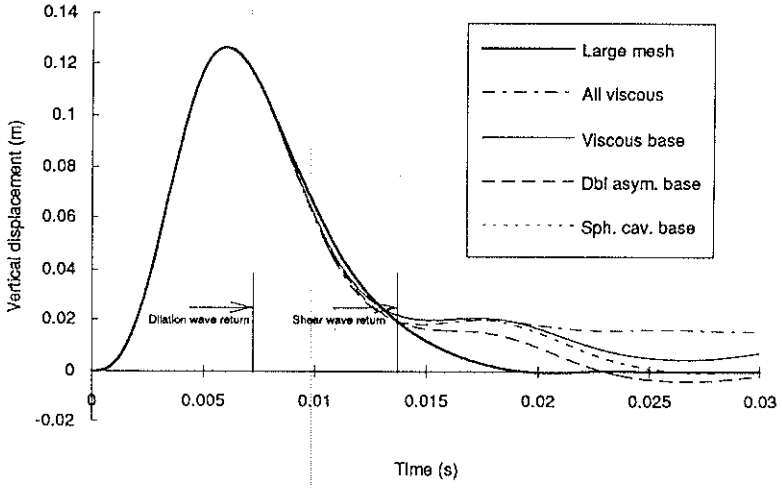

Fig 7.22. Effect of different boundaries on vertical displacement.

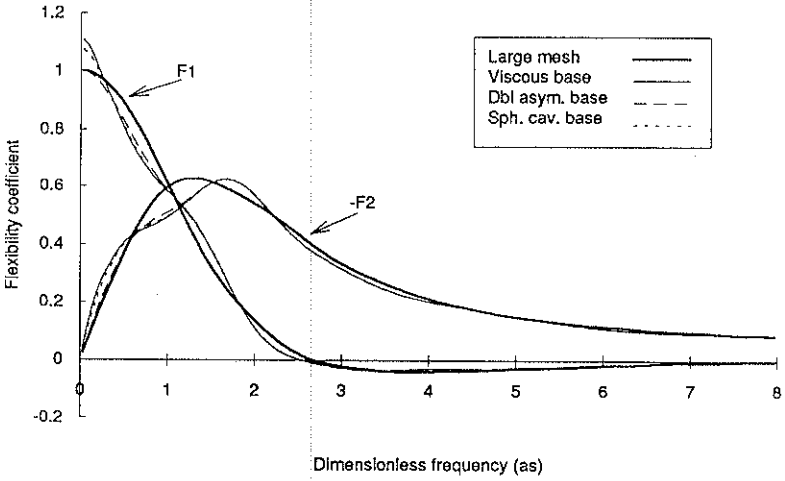

Fig 7.23. Effect of various boundaries on complex flexibility.

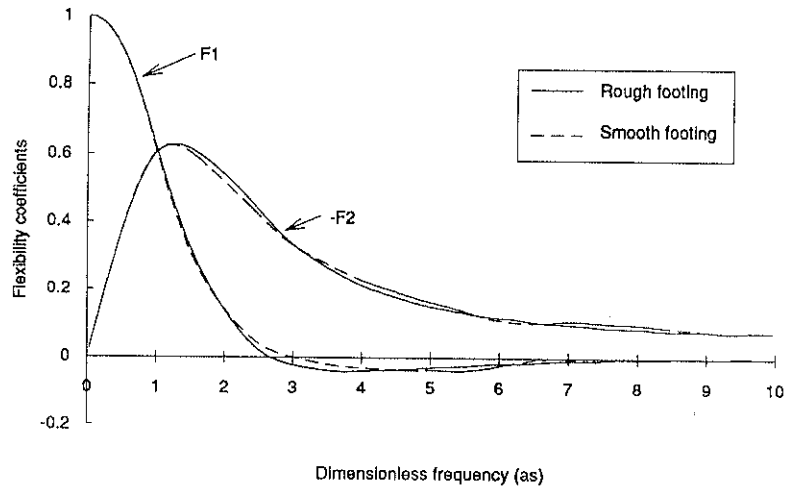

Fig 7.24. Complex flexibility of rough and smooth footings.

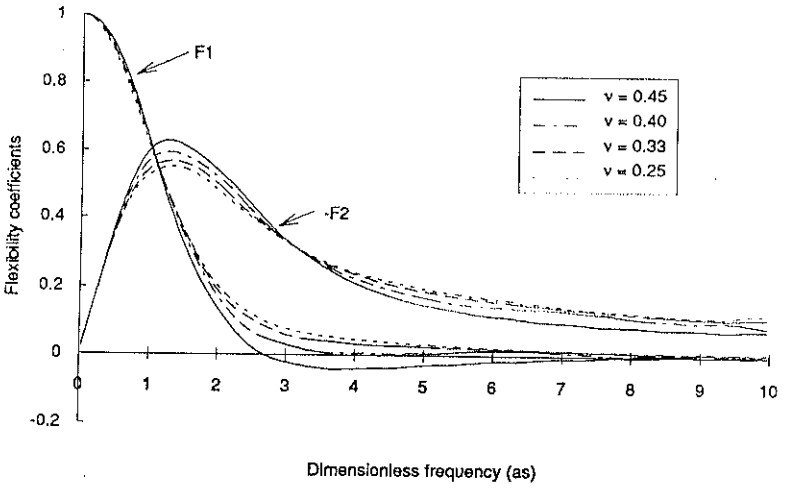

Fig 7.25. Effect of Poisson's ratio on footing flexibility.

$$k = \frac{4GR}{1-\nu}$$

$$c = 0.85\, k \frac{R}{c_s}$$

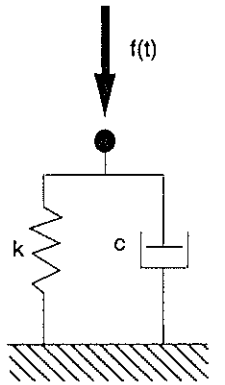

Fig 7.26(a). Lysmer's (1965) model for the dynamic response of a circular rigid footing.

$$k = \frac{4GR}{1-\nu}$$

$$c_0 = 0.8\, k \frac{R}{c_s}$$

$$c_1 = (0.34 - 4.3\,\nu^4)\, k \frac{R}{c_s}$$

$$m_0 = 0 \qquad \nu < 1/3$$

$$m_0 = 0.9(\nu - 1/3)\, k \frac{R^2}{c_s^2} \qquad \nu > 1/3$$

$$m_1 = (0.4 - 4\,\nu^2)\, k \frac{R^2}{c_s^2}$$

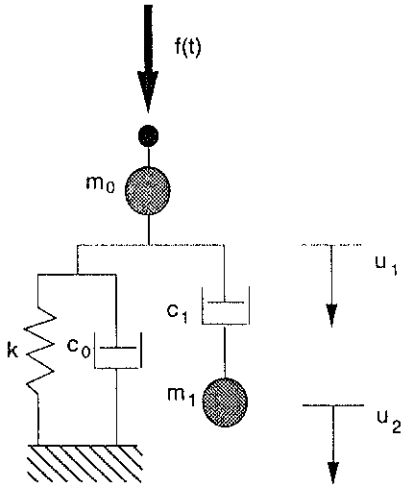

Fig 7.26(b). Wolf's (1988) model for the dynamic response of a circular rigid footing.

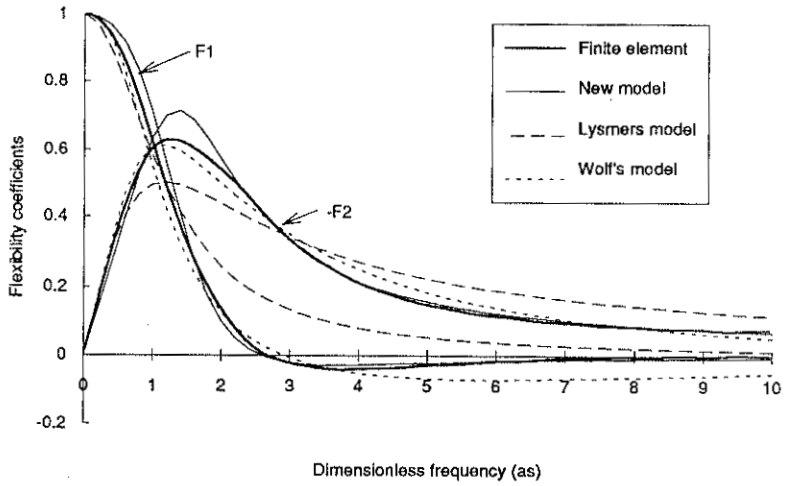

Fig 7.27. Complex frequency of base models compared with finite element solution (v=0.45)

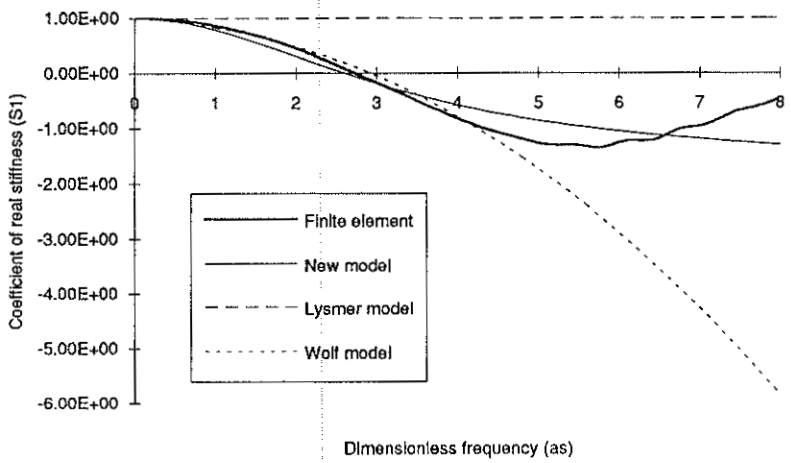

Fig 7.28. Coefficient of real stiffness for the base response (v=0.45).

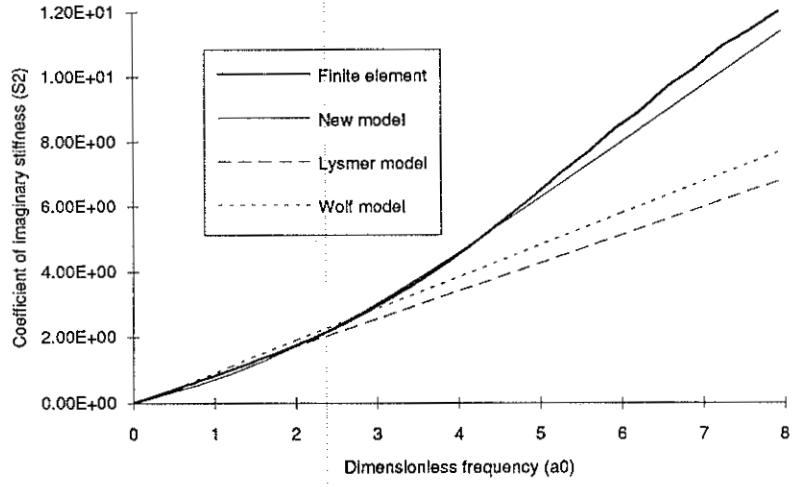

Fig 7.29. Coefficient of imaginary stiffness for the base response (v=0.45).

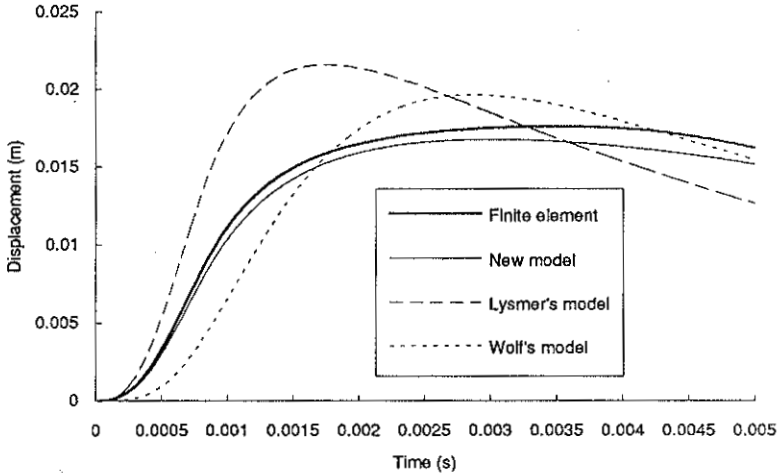

Fig 7.30. Response of base models to hammer impact (v=0.45, R=0.9m).

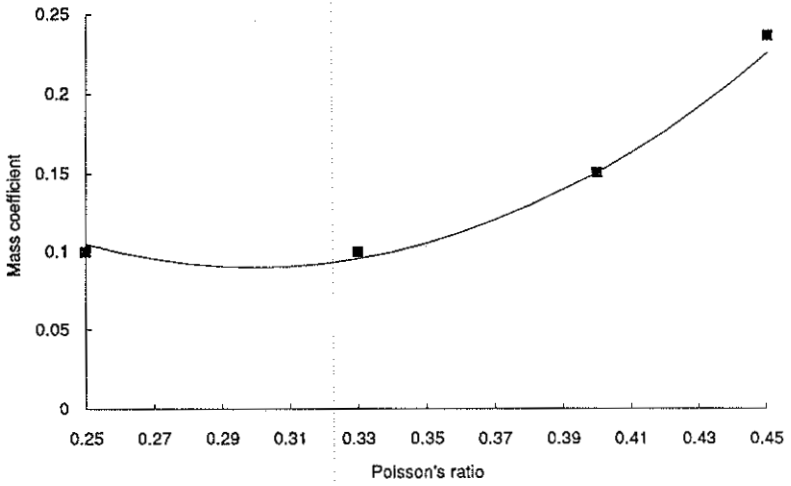

Fig 7.31. Variation of auxiliary mass coefficient with Poisson's ratio.

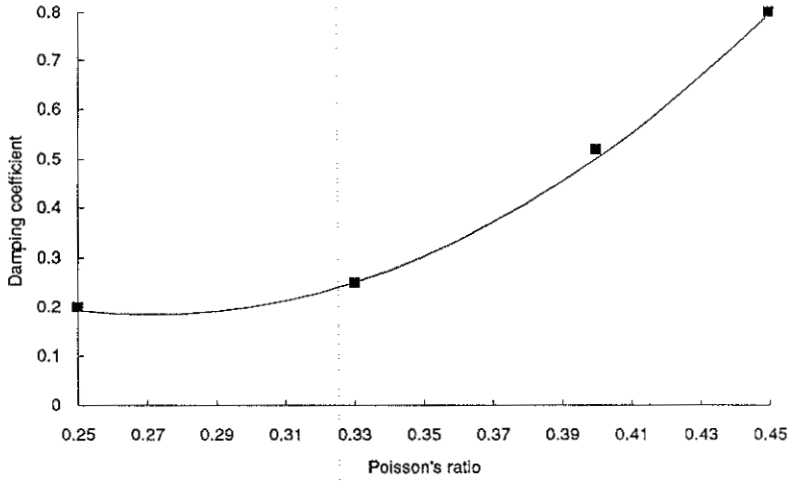

Fig 7.32. Variation of auxiliary damping coefficient with Poisson's ratio.

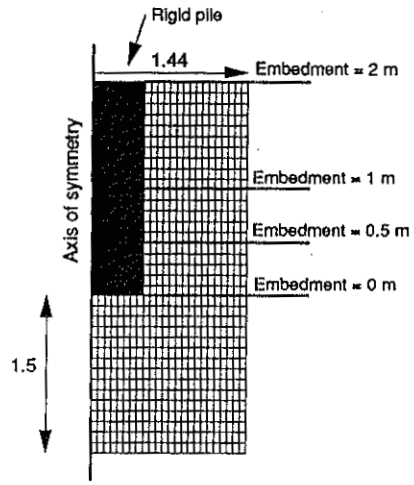

Fig 7.33(a). Finite element meshes for computing the effect of embedement.

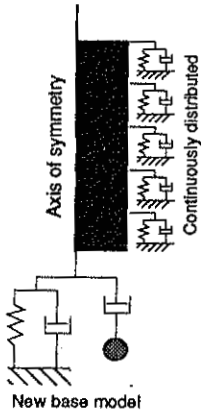

Fig 7.33(b). One-dimensional model for computing the effect of embedment.

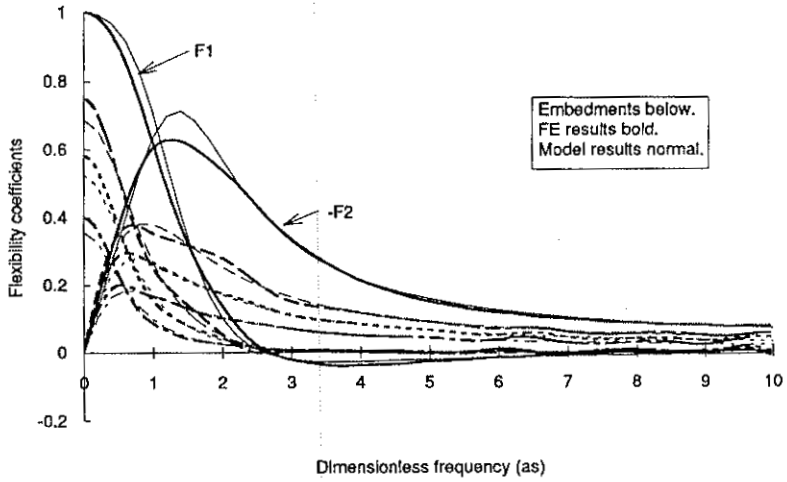

Fig 7.34. Effect of embedment on complex flexibility (v=0.45).

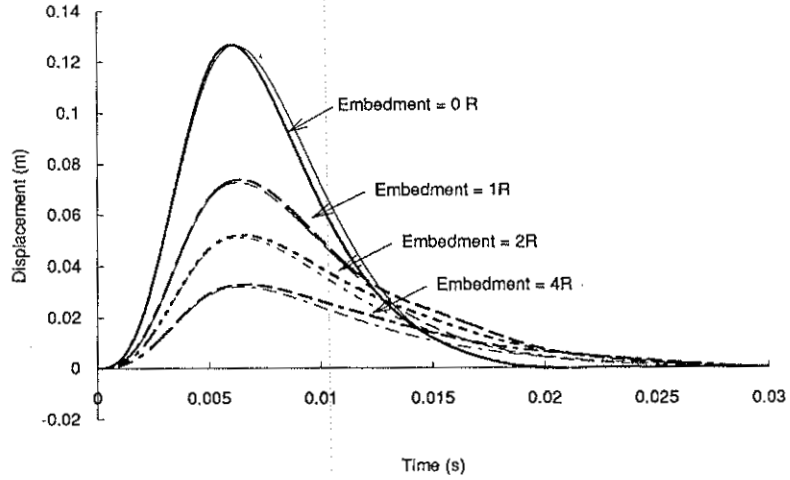

Fig 7.35. Effect of embedment on response to hammer impact (v=0.45).

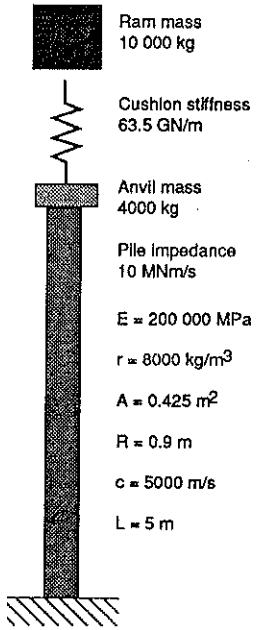

Fig 7.36. Pile example used to illustrate the effect of different base models.

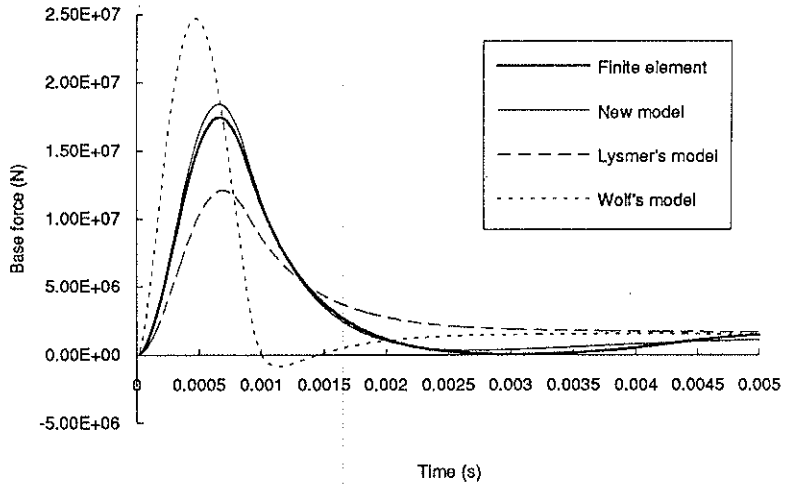

Fig 7.37(a). Comparison of base force calculated with different models.

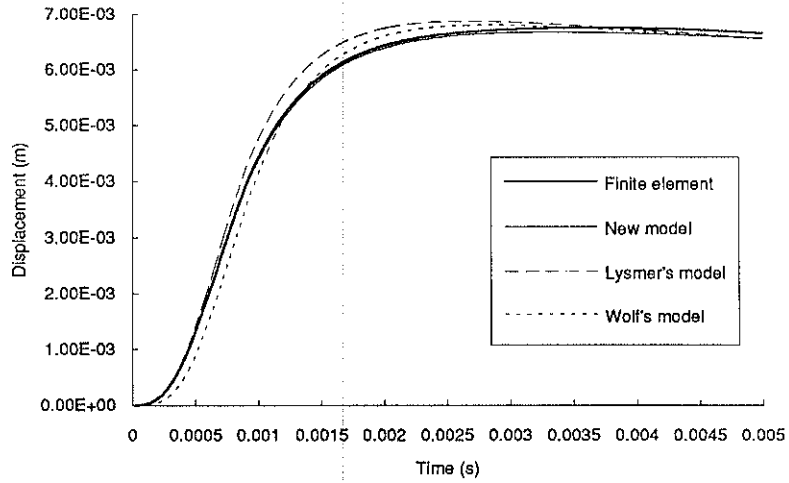

Fig 7.37(b). Comparison of base displacement calculated with different models.

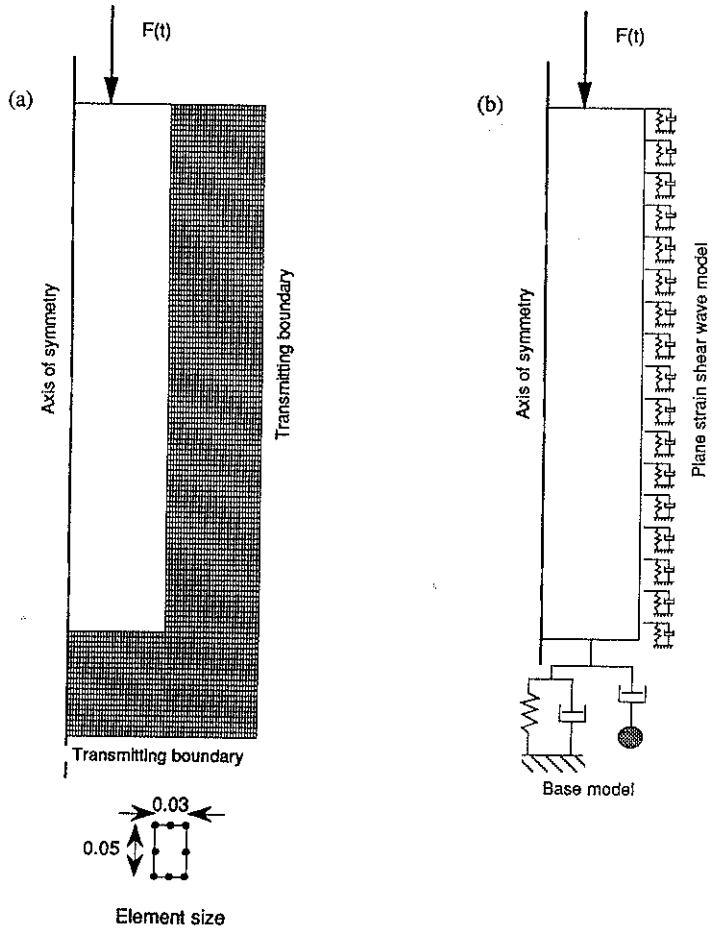

Fig 7.38. Pile models used to the compare overall response.

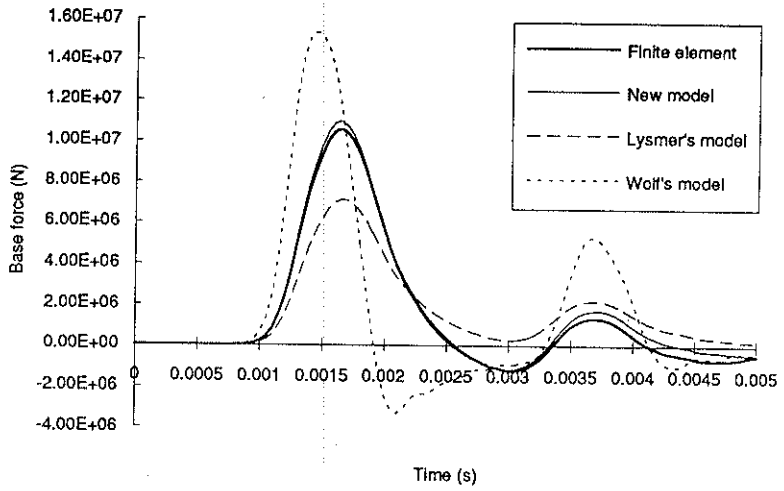

Fig 7.39. Calculated pile base force with shaft response included.

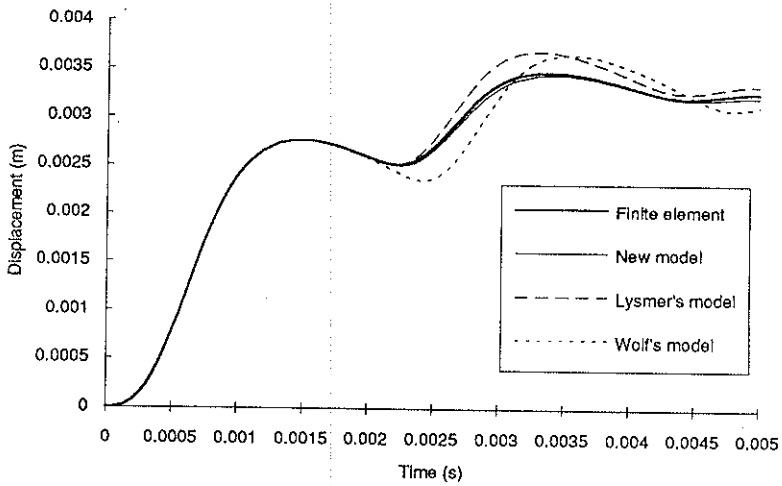

Fig 7.40. Calculated pile head displacement with shaft response included.

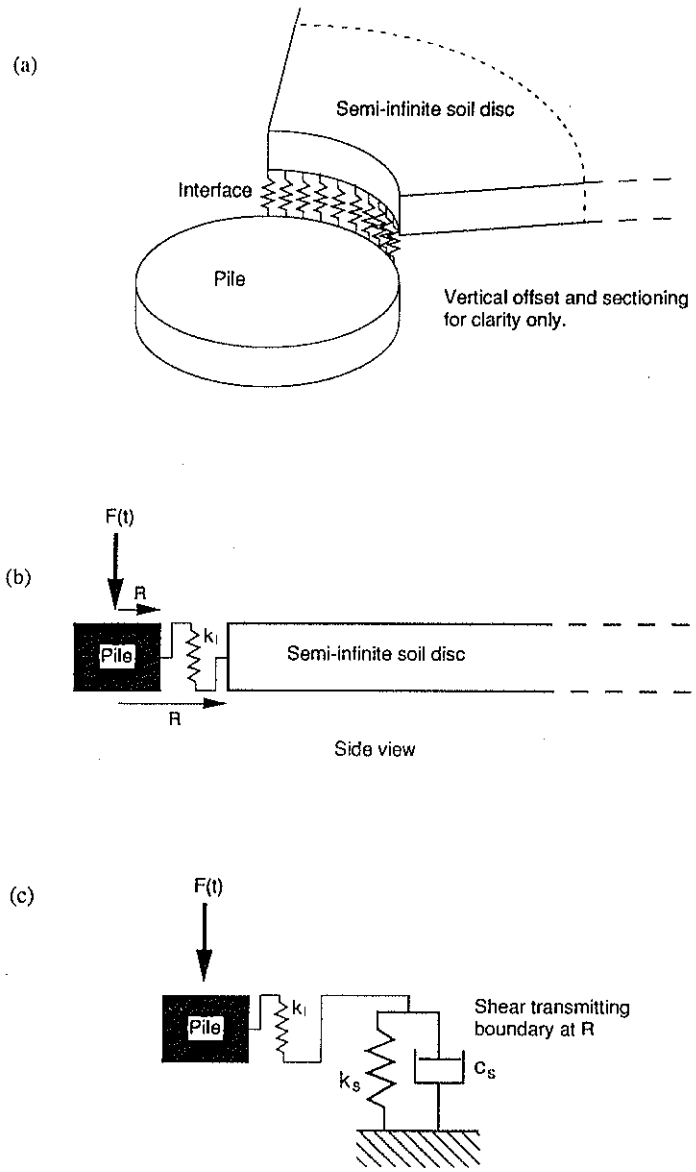

Fig 8.1. Modelling the soil/pile interface with a stiff interface element.

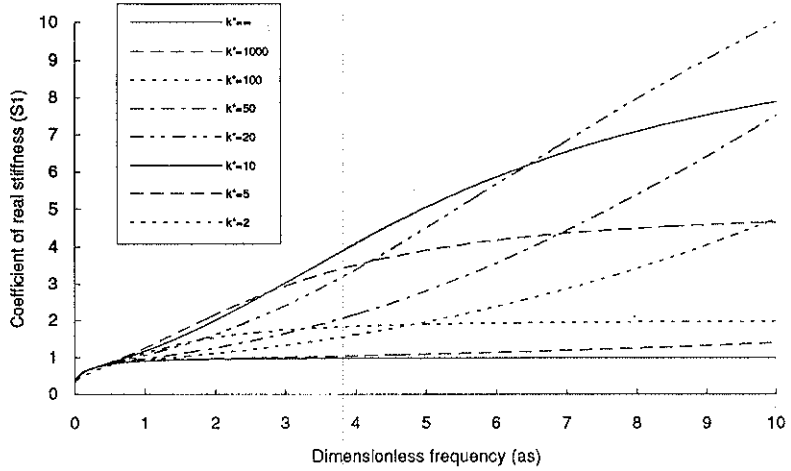

Fig 8.2(a). Effect of attached spring on real system stiffness.

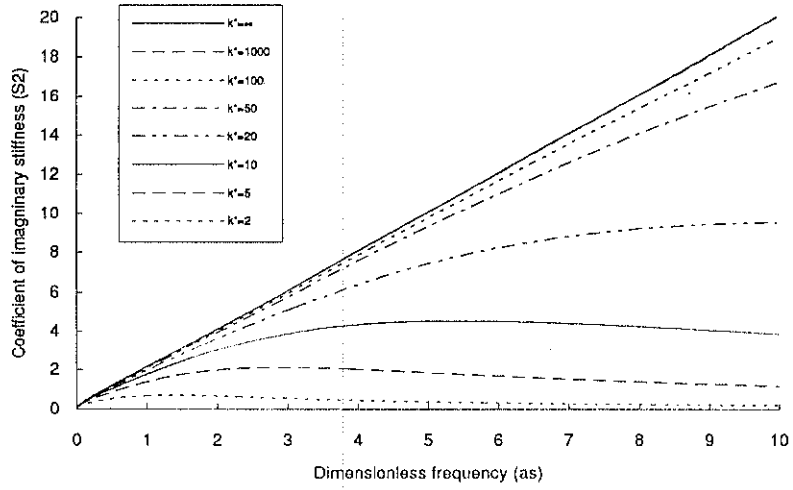

Fig 8.2(b). Effect of attached spring on imaginary system stiffness.

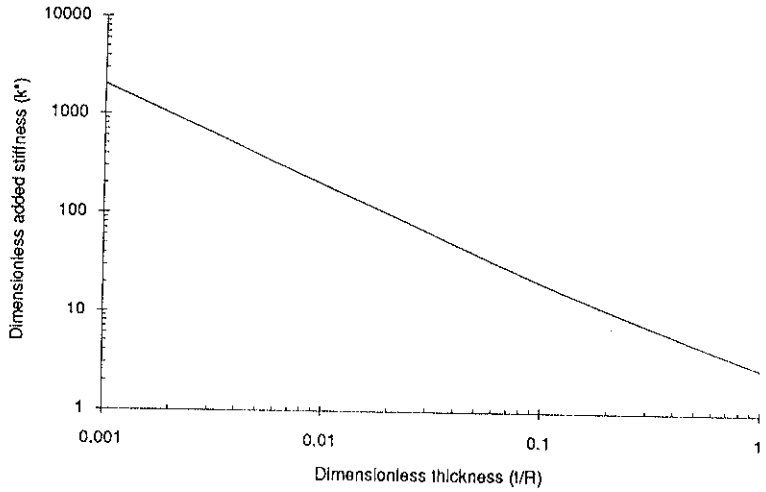

Fig 8.3. Relationship between added stiffness and interface thickness (Gm/G = 1).

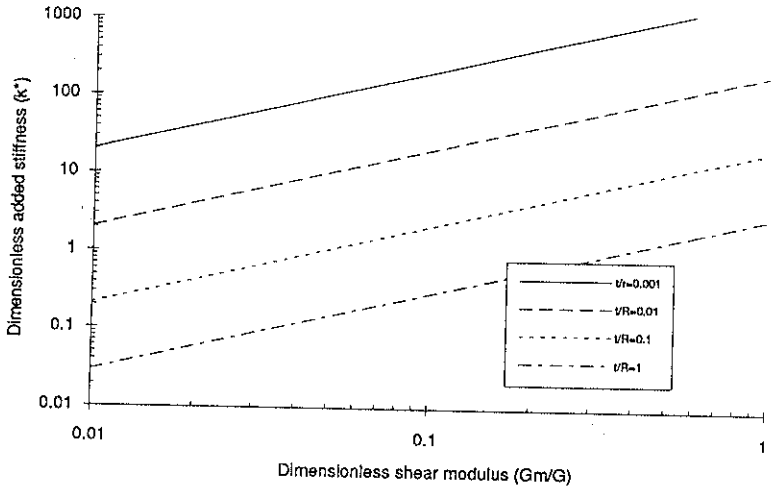

Fig 8.4. Relationship between stiffness and shear modulus for various interface thicknesses.

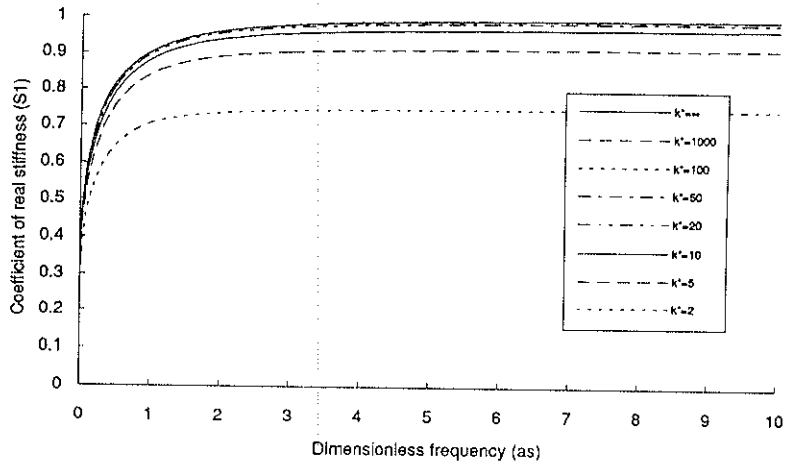

Fig 8.5(a). Effect of attached spring and dashpot on real system stiffness (c*=k*).

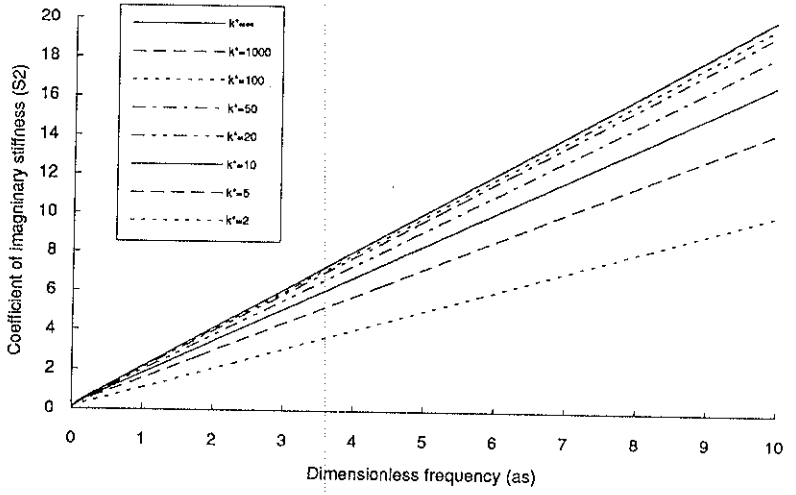

Fig 8.5(b). Effect of attached spring and dashpot on imaginary system stiffness (c*=k*).

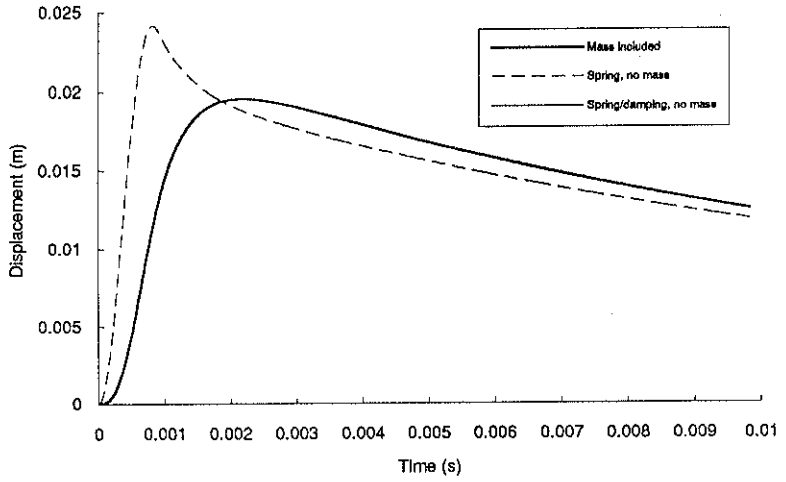

Fig 8.6. Effect of interface layer on reponse to hammer load (k*=21, t/R=0.1, Gm/G=1).

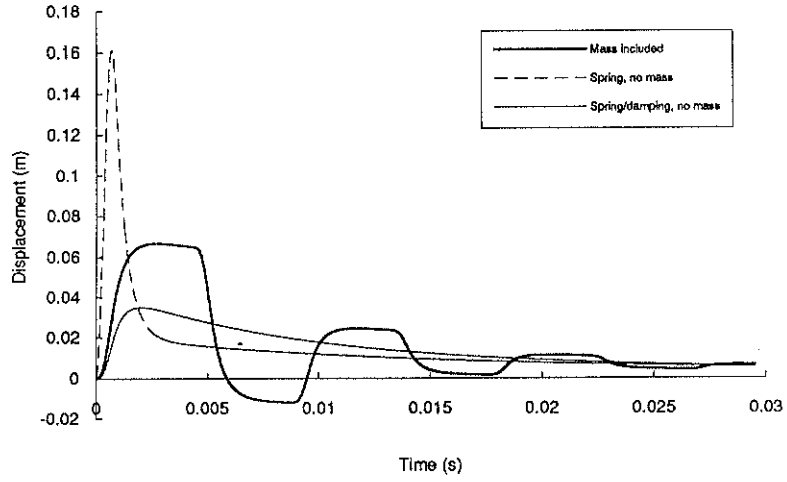

Fig 8.7. Effect of interface layer on reponse to hammer load (k*=2.1, t/R=0.1, Gm/G=0.1).

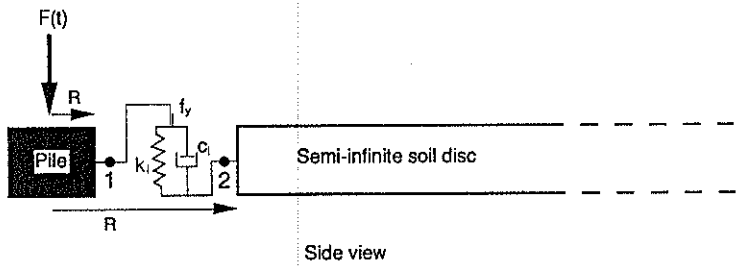

Fig 8.8. Two-node inelastic interface element for shaft/soil interaction.

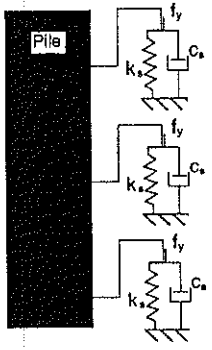

Fig 8.9. Simplified shaft model for inelastic shaft/soil interaction.

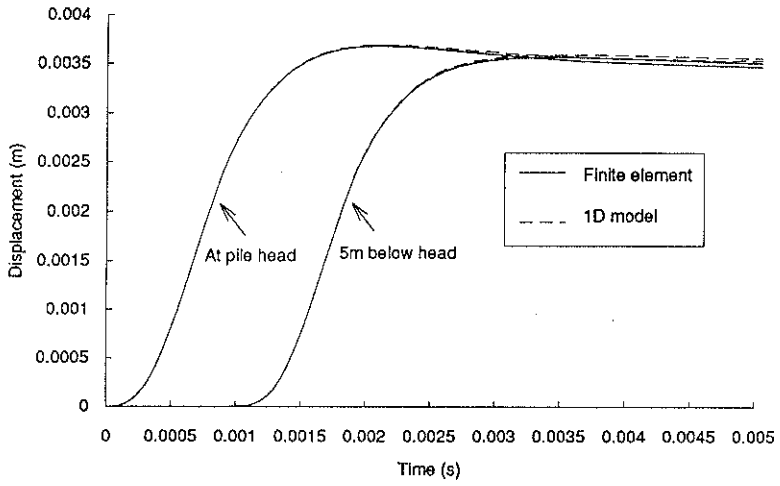

Fig 8.10. Semi-infinite pile displacements with inelastic soil.

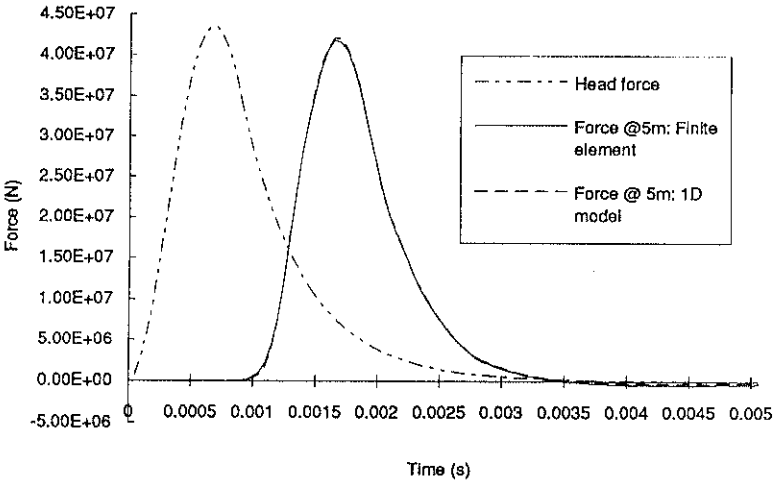

Fig. 8.11. Semi-infinite pile forces, inelastic soil.

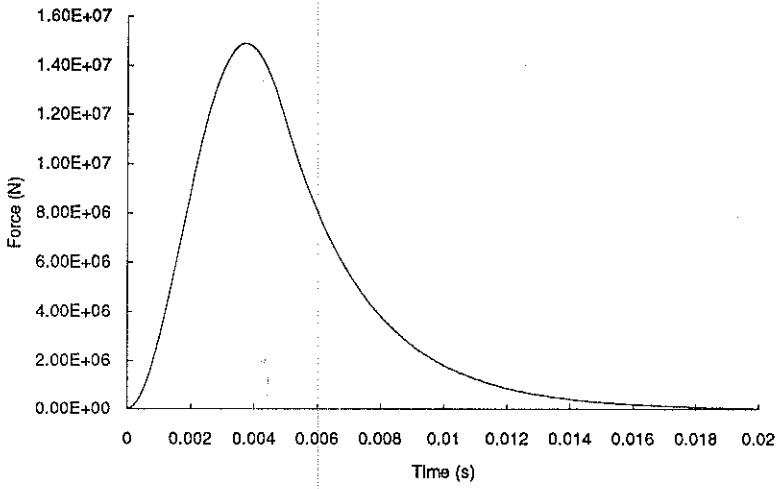

Fig 8.12(a). Hammer impact force for inelastic analyses.

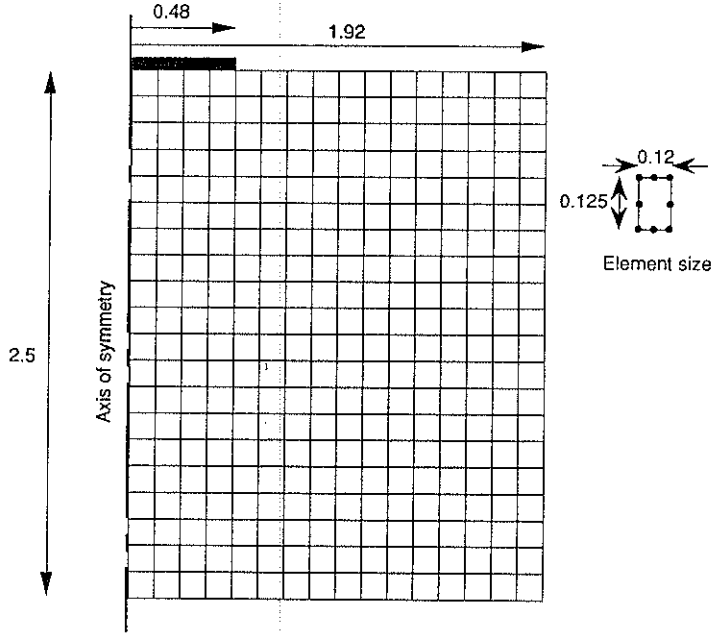

Fig 8.12(b). Finite element mesh for stress wave plots.

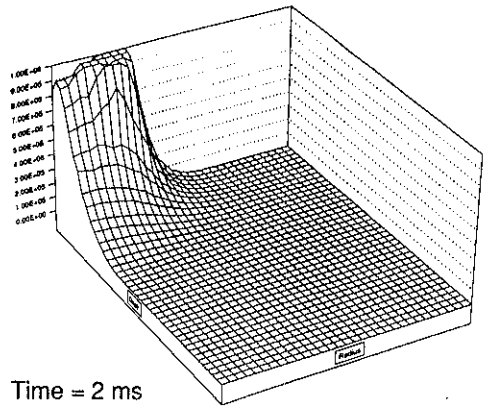

Time = 2 ms

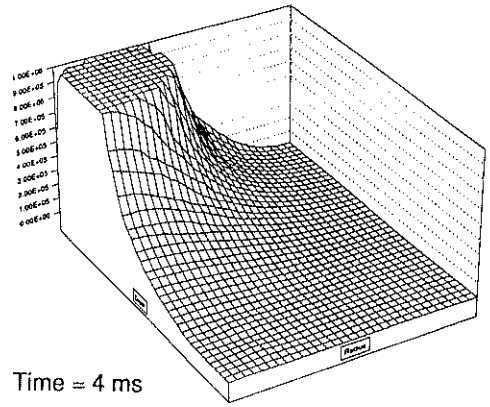

Time = 4 ms

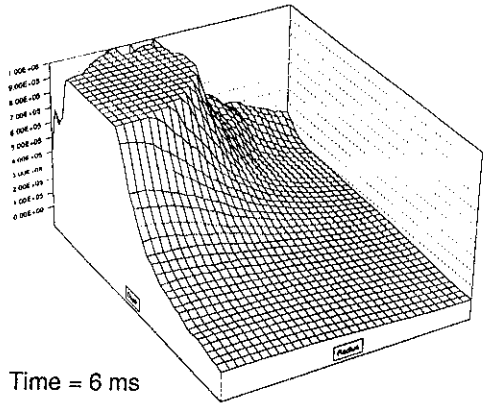

Time = 6 ms

Fig 8.13(a). Propagation of generalised shear stress wave in inelastic soil (Pa).

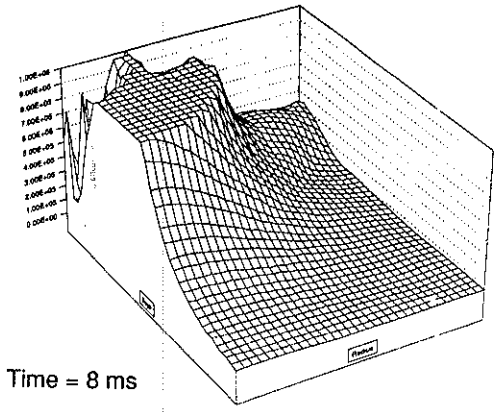

Time = 8 ms

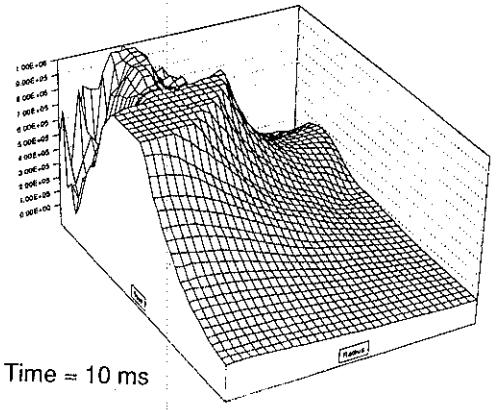

Time = 10 ms

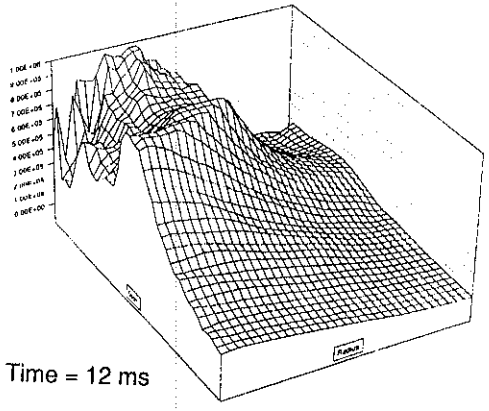

Time = 12 ms

Fig 8.13(b). Propagation of generalised shear stress wave in inelastic soil (Pa).

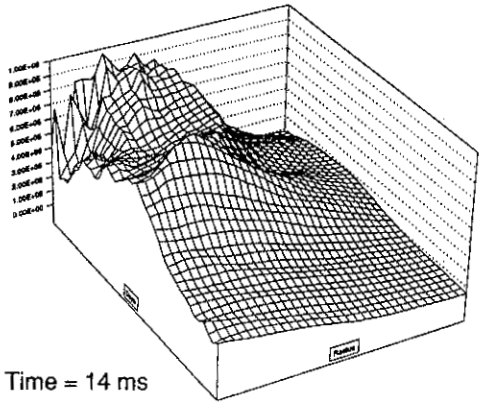

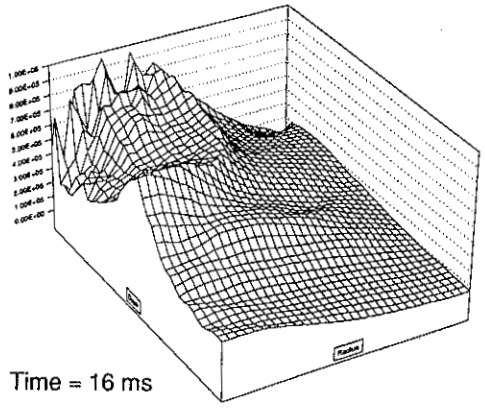

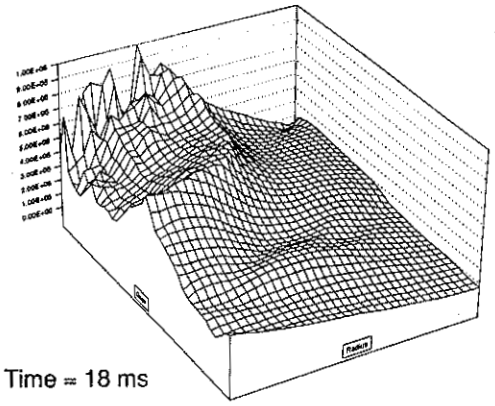

Fig 8.13(c). Propagation of generalised shear stress wave in inelastic soil (Pa).

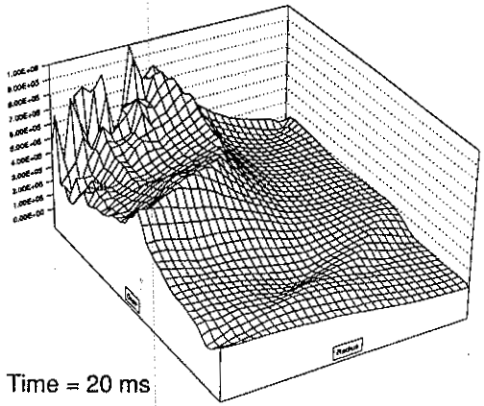

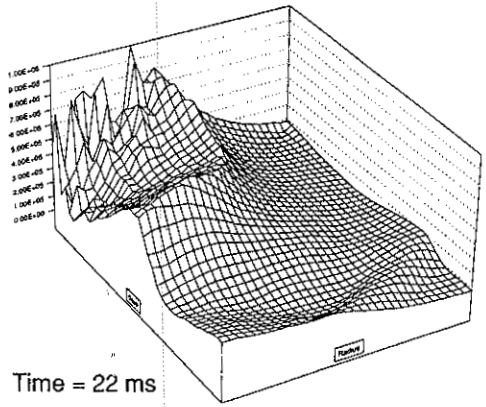

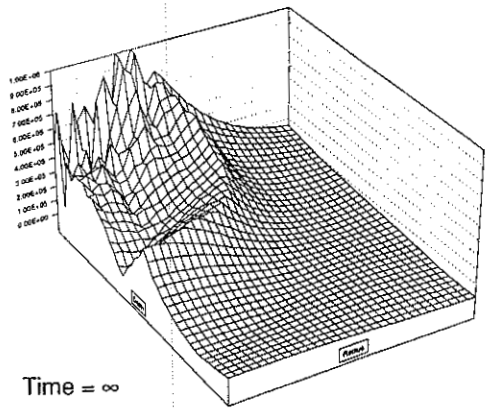

Fig 8.13(d). Propagation of generalised shear stress wave in inelastic soil (Pa).

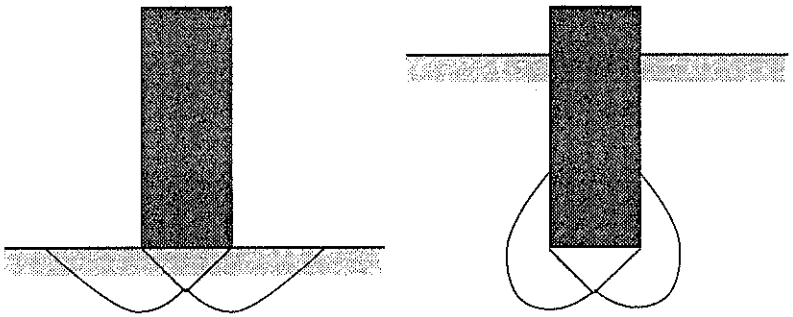

Fig 8.14(a). Approximate failure mechanisms for surface and submerged footings.

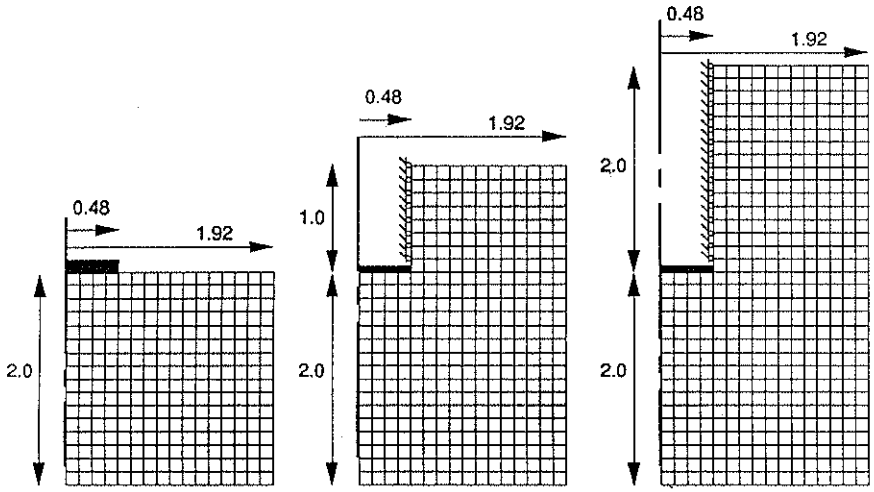

Fig 8.14(b). Finite element meshes for investigating the effect of embedment.

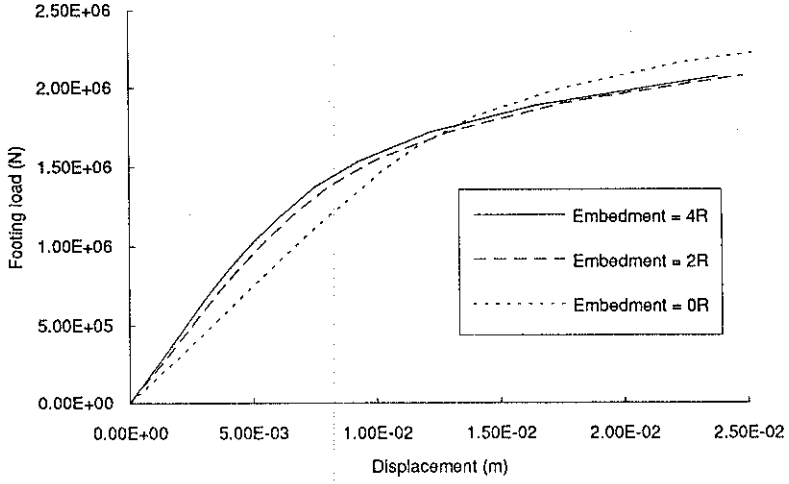

Fig 8.15. Static collapse of footings with various embedments, yield adjusted.

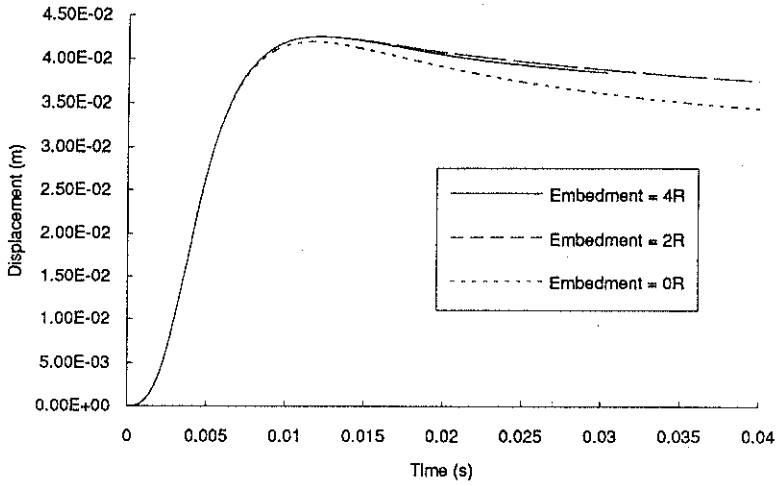

Fig 8.16(a). Effect of footing embedment on displacement (with adjusted yield stress).

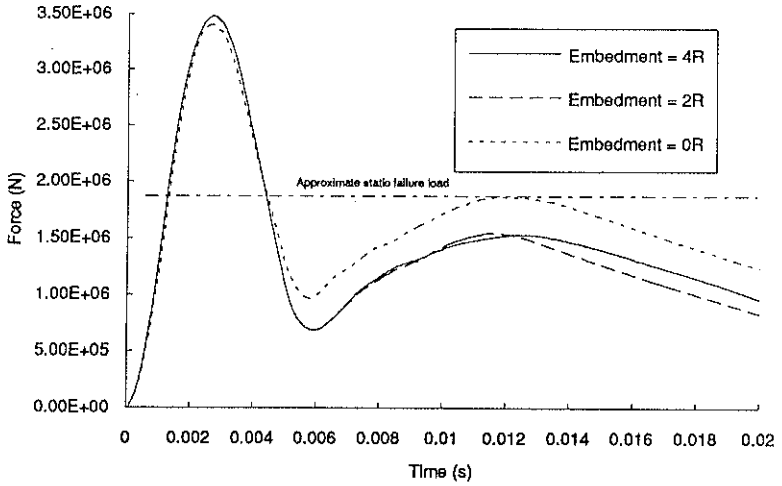

Fig 8.16(b). Effect of footing embedment on force (with adjusted yield stress).

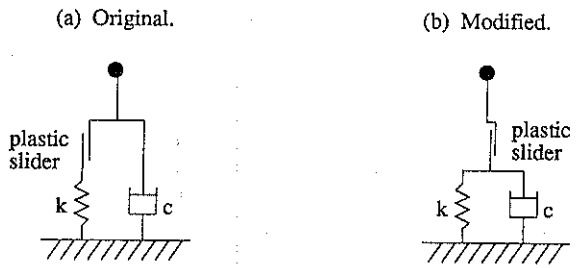

Fig 8.17. Base models derived from the Smith (1960) method and Lysmer's analogue.

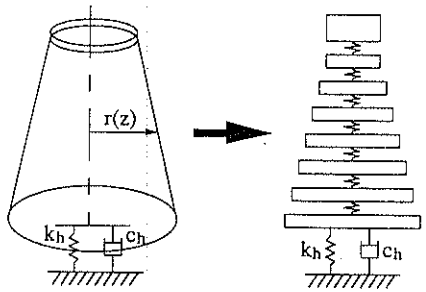

Fig 8.18. Holeyman's (1985) multiple degree of freedom base model.

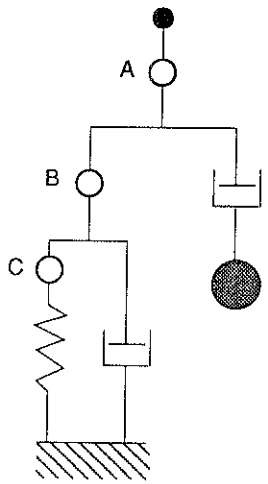

Fig 8.19(a). Alternative positions for plastic slider in new base model.

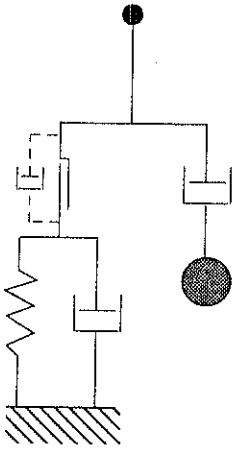

Fig 8.19(b). New base model with optional dashpot to account for soil viscosity.

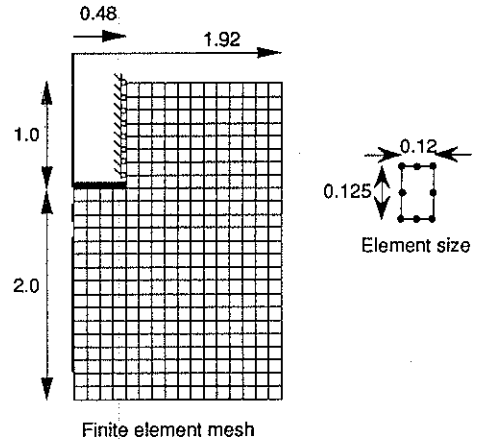

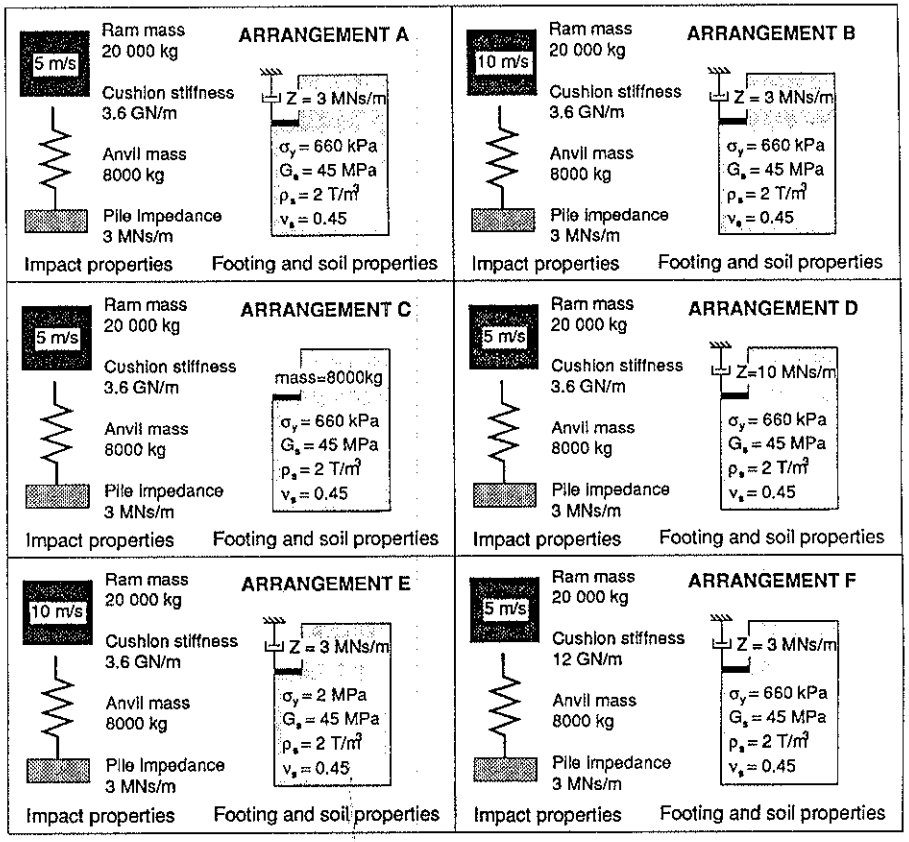

Fig 8.20. Problems used to evaluate the effectiveness of the simplified base models.

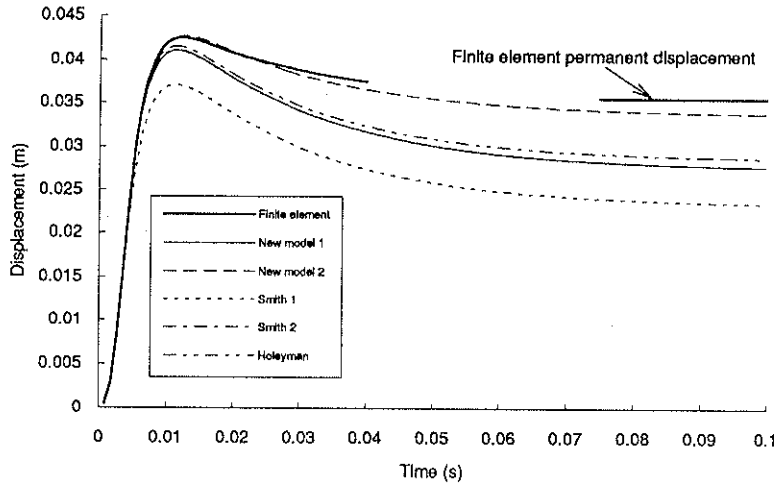

Fig 8.21(a). Displacements from different models, arrangement A.

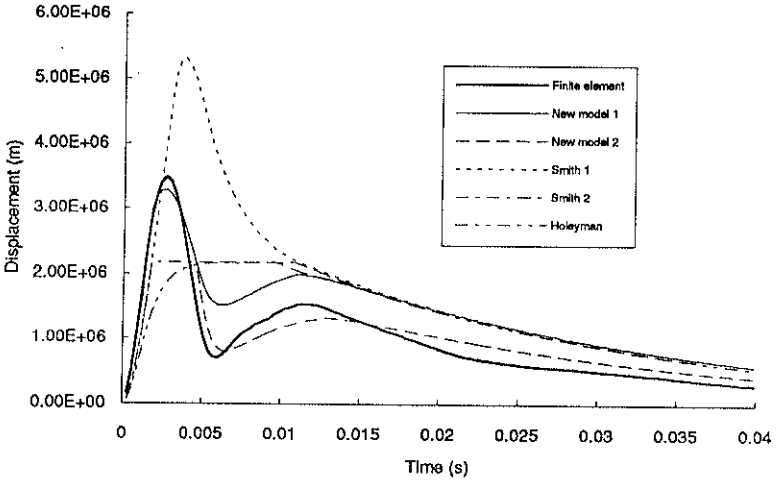

Fig 8.21(b). Forces from different models, arrangement A.

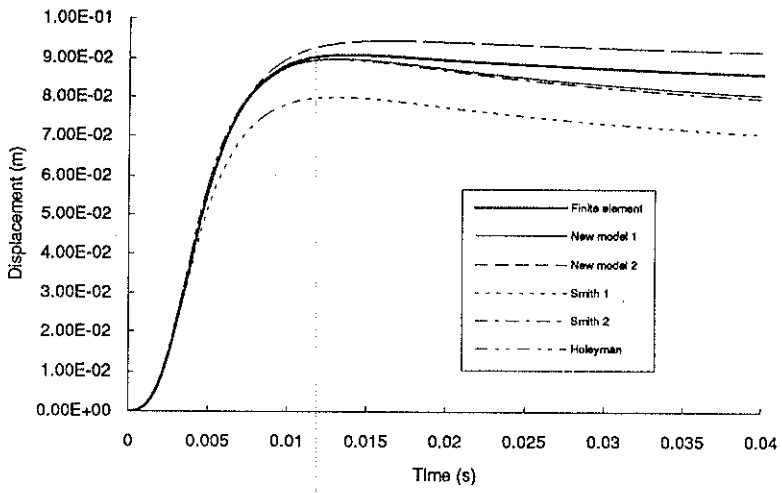

Fig 8.22(a). Displacements from different models, arrangement B.

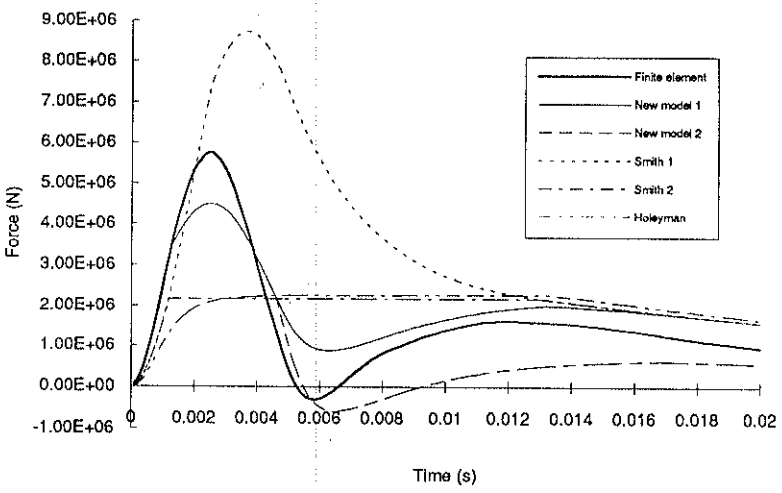

Fig 8.22(b). Forces from different models, arrangement B.

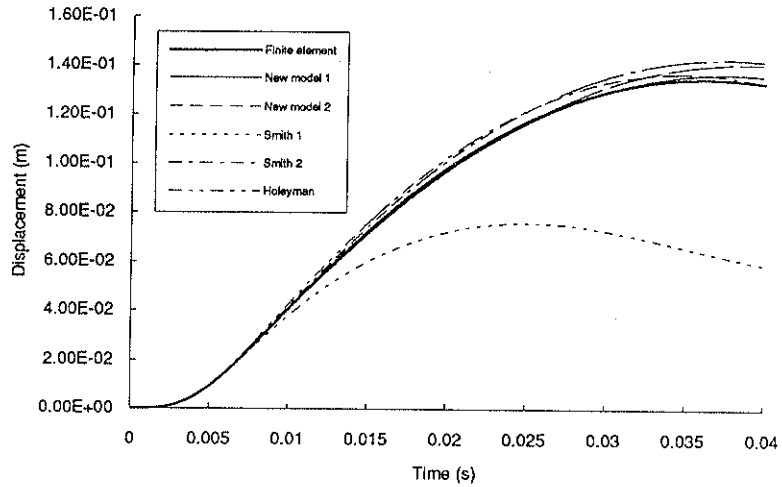

Fig 8.23(a). Displacements from different models, arrangement C.

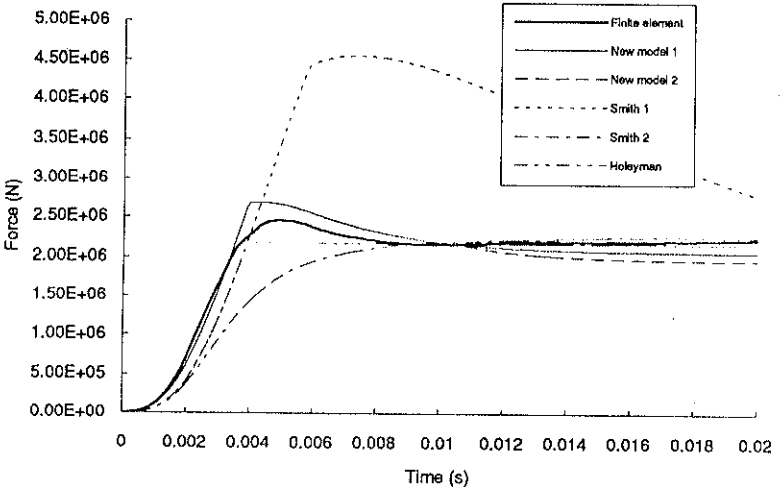

Fig 8.23(b). Forces from different models, arrangement C.

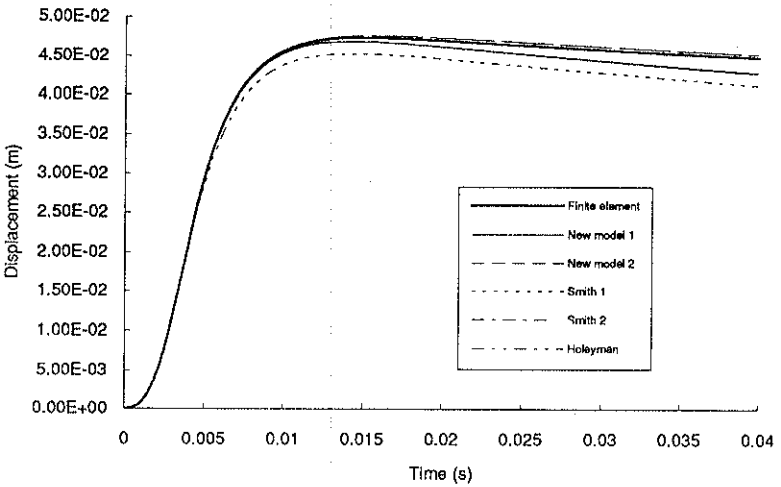

Fig 8.24(a). Displacements from different models, arrangement D.

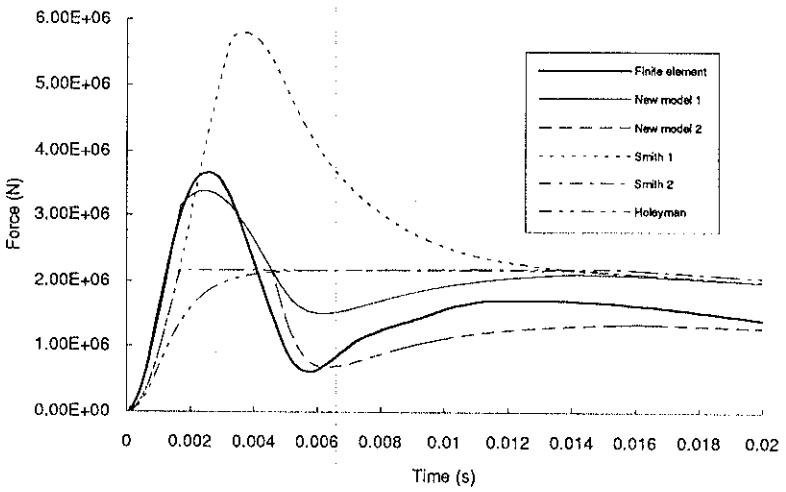

Fig 8.24(b). Forces from different models, arrangement D.

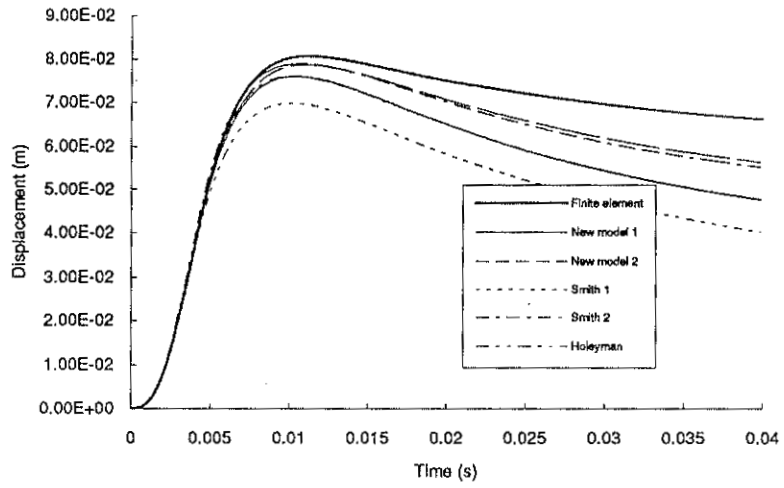

Fig 8.25(a). Displacements from different models, arrangement E.

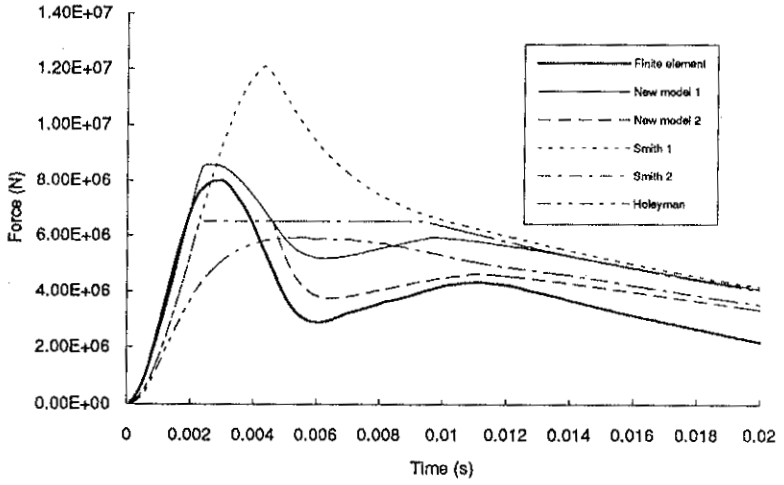

Fig 8.25(b). Forces from different models, arrangement E.

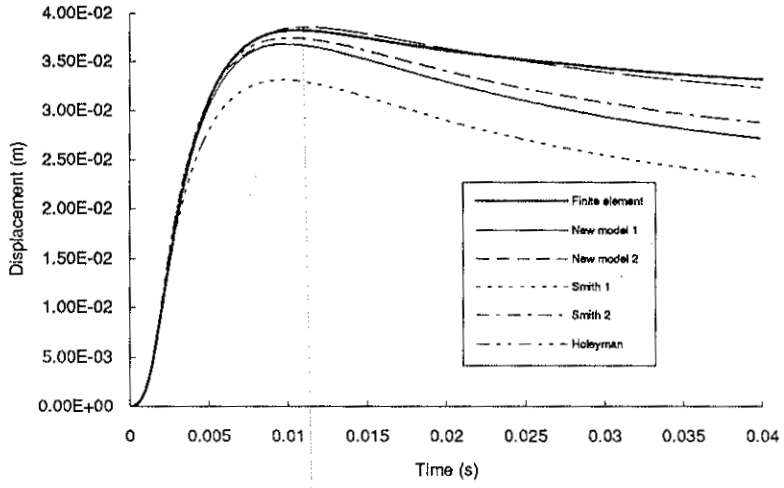

Fig 8.26(a). Displacements from different models, arrangement F.

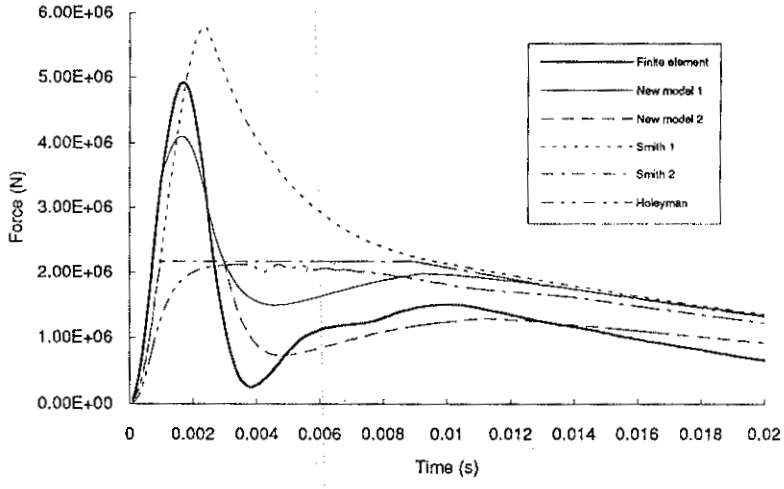

Fig 8.26(b). Forces from different models, arrangement F.

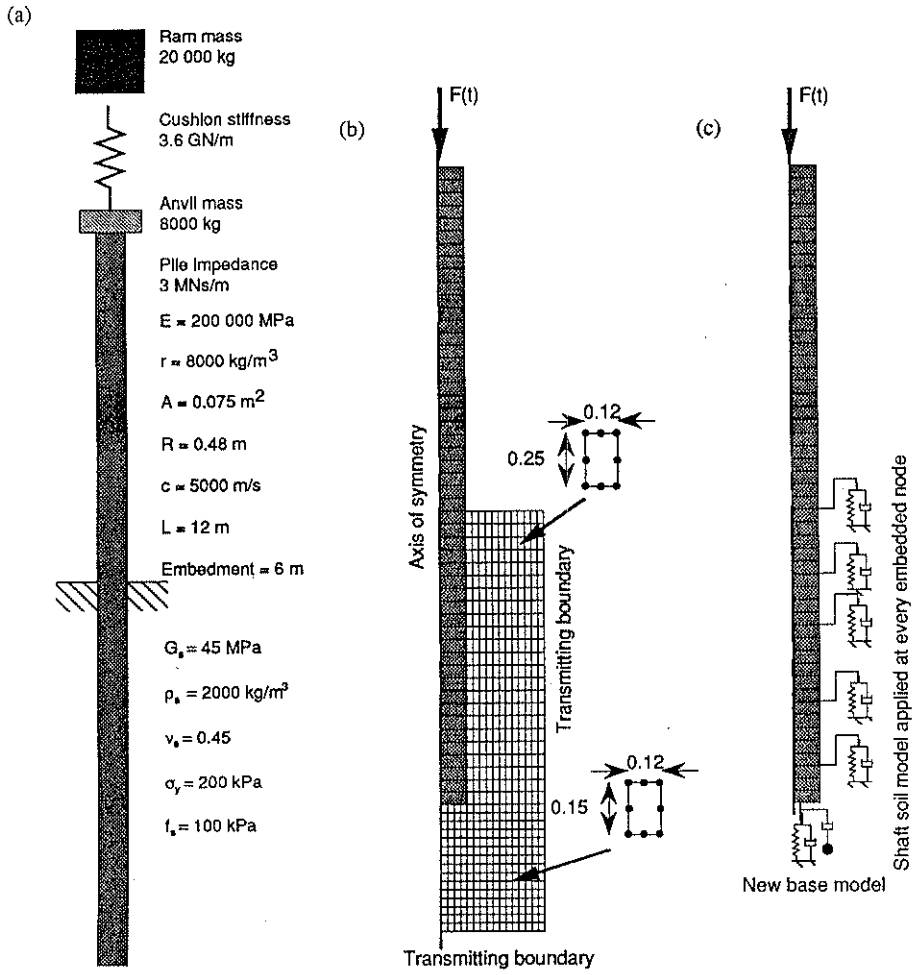

Fig 8.27. Pile and models for complete pile/soil system.

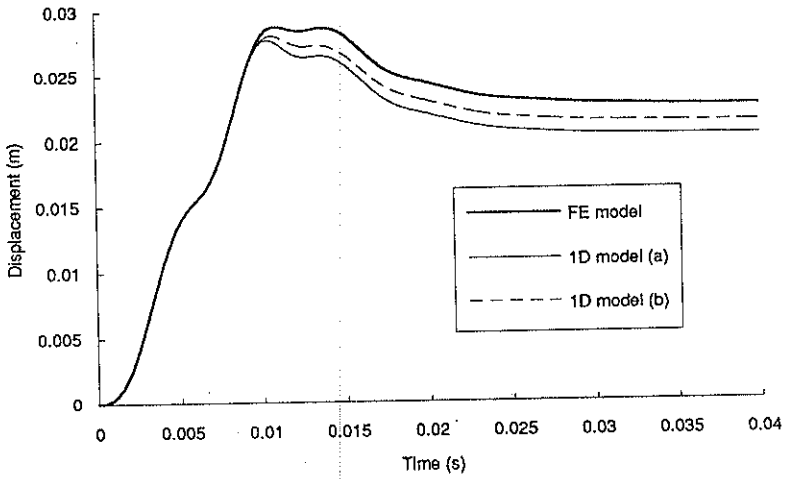

Fig 8.28(a). Pile head displacement from finite element and 1D models.

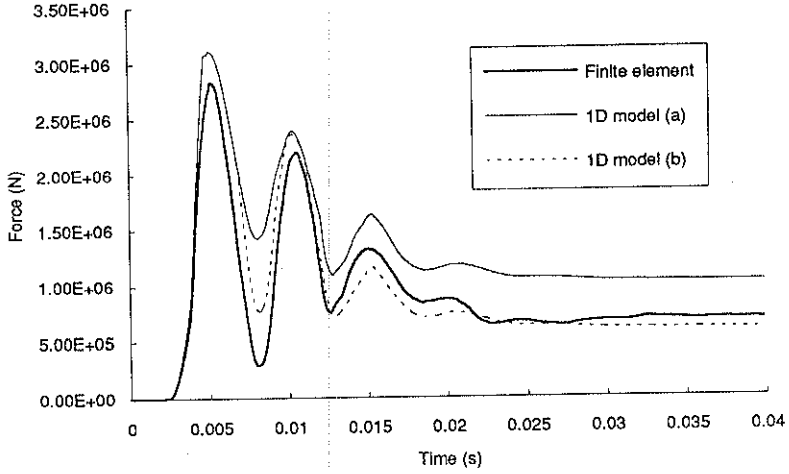

Fig 8.28(b). Pile toe force from finite element and 1D models.

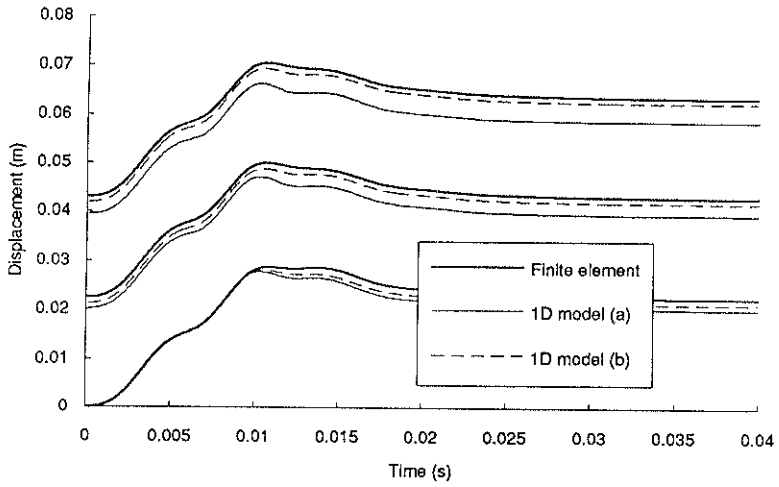

Fig 8.29(a). Pile head displacement from finite element and 1D models (repeated driving).

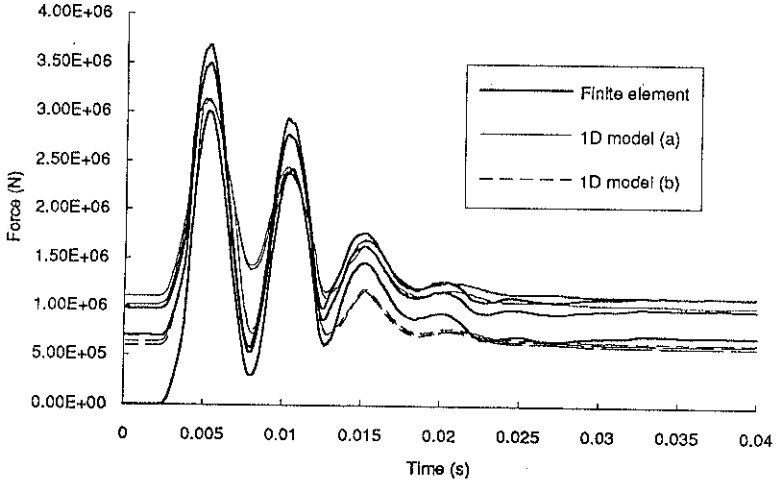

Fig 8.29(b). Pile toe force from finite element and 1D models (repeated driving).

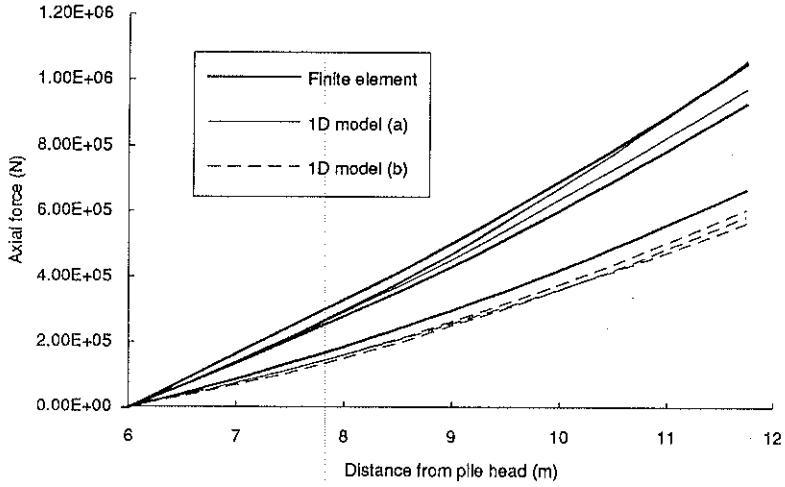

Fig 8.30. Residual axial force in pile after each blow (finite element and 1D models).

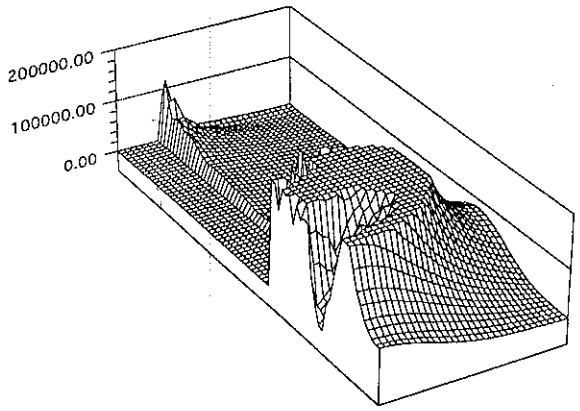

Fig 8.31. Residual generalised shear stresses calculated by the finite element model (Pa).

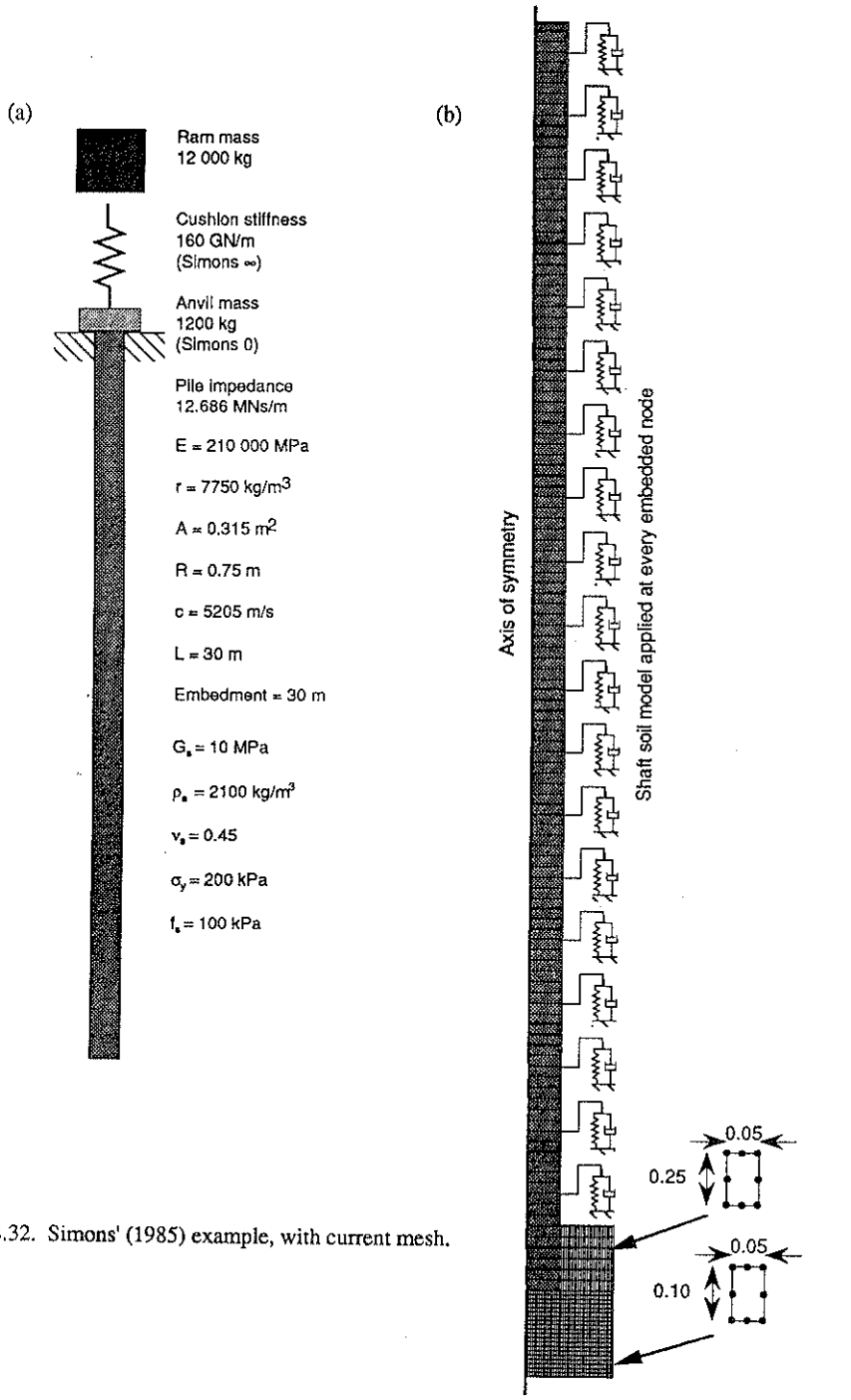

Fig 8.32. Simons' (1985) example, with current mesh.

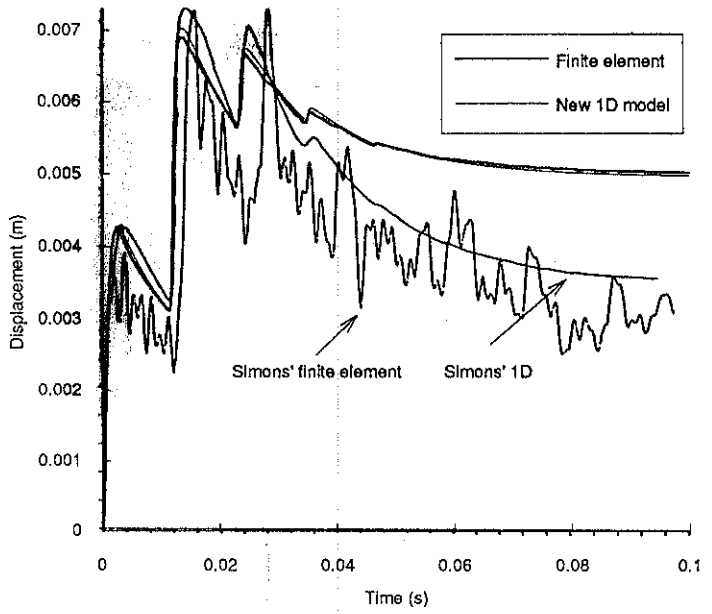

Fig 8.33. Displacements computed by Simons (1985) and by the current work.

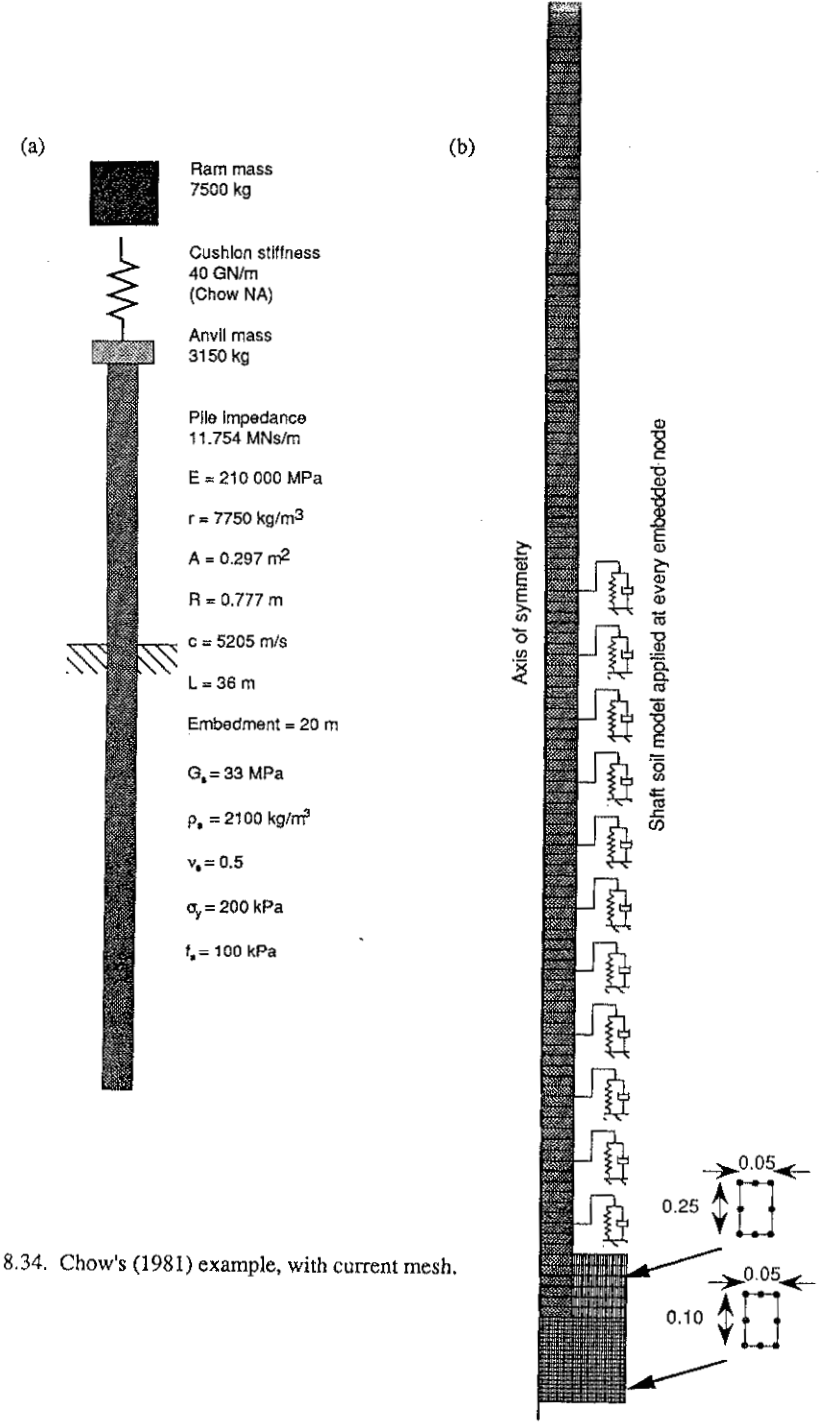

Fig 8.34. Chow's (1981) example, with current mesh.

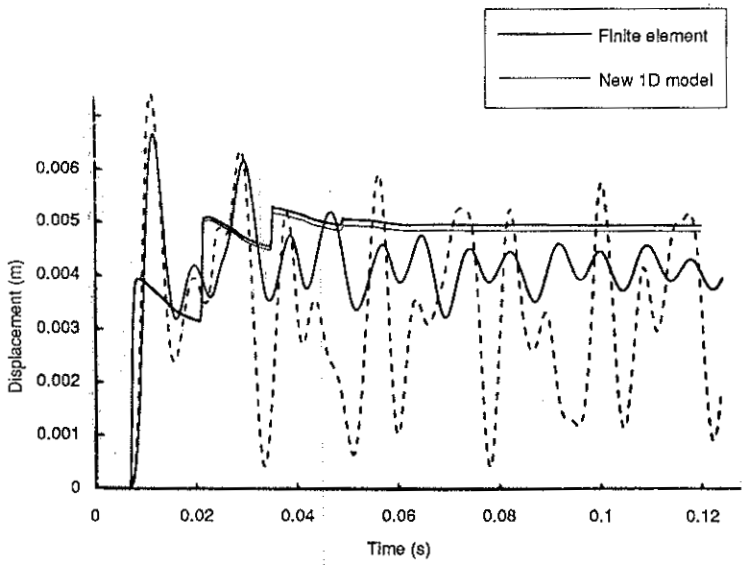

Fig 8.35. Toe displacements computed by Chow (1981) and by the current work.